



University
of Glasgow

McVicar, J. Scott G. (1993) *A generic tilt-rotor simulation model with parallel implementation*. PhD thesis.

<http://theses.gla.ac.uk/4952/>

Copyright and moral rights for this thesis are retained by the author

A copy can be downloaded for personal non-commercial research or study, without prior permission or charge

This thesis cannot be reproduced or quoted extensively from without first obtaining permission in writing from the Author

The content must not be changed in any way or sold commercially in any format or medium without the formal permission of the Author

When referring to this work, full bibliographic details including the author, title, awarding institution and date of the thesis must be given

**A Generic Tilt-Rotor Simulation Model with Parallel
Implementation**

by

J. Scott. G. McVicar, B.Sc.

Dissertation Submitted to the Faculty of Engineering, University of Glasgow, for the
Degree of Doctor of Philosophy

February 1993

© J. S. G. McVicar, 1993

Acknowledgements	i
Declaration	ii
Abstract.....	iii
Nomenclature	iv
List of Symbols.....	iv
Greek Symbols.....	xi
Sign Conventions.....	xiii
Chapter 1	1
Introduction.....	1
1.1 History of the Tilt-Rotor.....	1
1.2 The Requirement for a Tilt-Rotor Simulation Model.....	7
1.3 The GTILT Model.....	9
Chapter 2	14
Modelling.....	14
2.1 Rotor Model.....	15
2.1.1 The Tilt-Rotor Blade Element Rotor Model	16
2.1.2 Kinematics of a Flapping Blade Element With a Tilting Shaft.....	19
2.1.3 Definition of Axis Sets and Transformation Matrices	19
2.1.4 Velocity of a Blade Element	21
2.1.5 Acceleration of a Blade Element	24
2.1.6 Calculation of Aerodynamic Forces	28
2.1.7 Evaluation of Rotor Thrust	31
2.1.8 Rotor Forces and Moments in Body Axis	31
2.1.9 Blade Flapping.....	35
2.1.10 Inflow Modelling	40
2.1.10a The Glauert Model.....	40
2.1.10b The Peters - HaQuang Model	43
2.1.11 Validation of the Rotor Model.....	45
2.2 Vehicle Aerodynamics	46
2.2.1 Modelling of Wake Impingement on Vehicle Empennage	47
2.2.2 Modelling of Rotor/Wing Interaction.....	48
2.3 Control Authority.....	50
2.3.1 Rotor Control	50
2.3.2 Aerodynamic Control Surfaces	52
2.4 Locating the Vehicle Centre of Gravity	53
Chapter 3	55
Partial Periodic Trim Algorithm.....	55

3.1	Definition of Periodic Trim.....	56
3.2	Specification and Convergence of Periodic Tilt-Rotor Trim	61
Chapter 4	66
	Parallel Implementation	66
4.1	The Meiko Computing Surface	66
4.1.1	CS Tools Configuration Tools.....	68
4.1.2	CS Tools Communication Services	69
4.2	Topography Used in the Parallelisation of GTILT.....	71
4.3	Parallel Implementation of GTILT	72
4.4	Synchronisation of Communications	73
4.5	Run Time Performance of the GTILT Model.....	74
Chapter 5	76
	Results	76
5.1	Convergence of Partial Periodic Trimmer	77
5.2	Verification of GTILT	79
5.2.1a	Verification of Longitudinal Trim States Adopted by the Vehicle in Helicopter Mode.....	79
5.2.1b	Verification of Longitudinal Trim States Adopted by the Vehicle in Transitional Flight.....	81
5.2.1c	Verification of Longitudinal Trim States Adopted by the Vehicle in Aeroplane Mode.....	82
5.2.2	Verification of Trim States Adopted in Turning Flight.....	83
5.3	Response of Vehicle to a Range of Control Inputs.....	85
5.3.1a	Helicopter Mode - Doublet in Combined Collective.....	85
5.3.1b	Helicopter Mode - Doublet in Lateral Stick.....	87
5.3.1c	Helicopter Mode - Doublet in Longitudinal Stick.....	88
5.3.1d	Helicopter Mode - Doublet in Pedal	89
5.3.1e	Helicopter Mode - Doublet in Combined Lateral Cyclic	90
5.3.2a	Transitional Flight at 45° Nacelle - Doublet in Combined Collective	91
5.3.2b	Transitional Flight at 45° Nacelle - Doublet in Lateral Stick.....	92
5.3.2c	Transitional Flight at 45° Nacelle - Doublet in Longitudinal Stick	93
5.3.2d	Transitional Flight at 45° Nacelle - Doublet in Pedal	93
5.3.3a	Aeroplane Mode - Doublet in Combined Collective	94
5.3.3b	Aeroplane Mode - Doublet in Lateral Stick	95
5.3.3c	Aeroplane Mode - Doublet in Longitudinal Stick.....	95

5.3.3d	Aeroplane Mode - Doublet in Pedal	96
5.4	Transitional Time Histories	96
Chapter 6	100
Conclusions and Future Work	100
6.1	Conclusions.....	100
6.2	Suggestions for Future Research.....	102
Appendix One	105
Appendix Two	106
Appendix Three	108
Appendix Four	109
A4.1.	XV-15 Aerodynamic Data.....	109
A4.2.	XV-15 Configurational Data.....	119
A4.3.	Rotor Configurational Data.....	120
A4.4.	Control Limits and Gearings.....	121
A4.4.	Rotor Wake Impingement and Wing Downwash on Horizontal Stabiliser.....	123
References	126
Figures	131

ACKNOWLEDGEMENTS

The author wishes to express sincere gratitude to the following individuals: Professor Roy Bradley for his considerable guidance and encouragement whilst supervising this project; Dr Gareth Padfield of Flight Systems Division, Defence Research Agency, Bedford, for his assistance in the role of external supervisor; Professor Roderick M^cD Galbraith for his support; and Dr Douglas Thomson for his advice and encouragement throughout the course of this work.

Thanks are also extended to Dr Derek Higgins of Glasgow University Computing Services for his help with the Meiko Computing Surface and also Dr Stewart Houston and Dr Richard Green who proof read this manuscript.

The project was funded by the Science and Engineering Research Council CASE award with the Ministry of Defence (DRA Bedford) as the external collaborating body.

DECLARATION

The author expresses that the work presented in this Dissertation was carried out at the Department of Aerospace Engineering, University of Glasgow, between October 1989 and November 1992. It is original in content except where indicated.

February, 1993



J. Scott G. McVicar

ABSTRACT

The unique capabilities of the tilt-rotor configuration are generally accepted to provide significant potential when applied to numerous civil and military operations. A vital stage in the development of any tilt-rotor design is the simulation of its basic flying qualities which are essentially defined by the vehicle's response to a range of control inputs and the trim states it adopts. In order to carry out this simulation satisfactorily, an accurate generic mathematical model is required, however, the author is unaware of any existing tilt-rotor simulations which utilise the latest modelling techniques. A generic tilt-rotor simulation model (GTILT) which includes individual blade modelling to describe the behaviour of the rotor has been developed during this research.

One of the most significant attributes of individual blade models is that they portray the oscillatory nature of the forces and moments produced by a lifting rotor. The resulting trimmed flight path of the vehicle is periodic rather than steady in nature and consequently existing trimming algorithms, formulated for use with rotor disc representations, are inappropriate when applied to individual blade simulations. A specialised trimming algorithm capable of rapidly trimming rotorcraft simulations to a specified periodic trim state has been developed and incorporated into the GTILT model.

Individual blade modelling provides a higher level of fidelity than is possible when using a rotor disc representation but this benefit is obtained at the expense of computational burden. Hence, most sequential computing facilities are unable to provide the performance necessary to make such models practical. In order to reduce computational run-times to an acceptable level GTILT has been parallelised and implemented on a custom designed transputer network.

GTILT has been configured using XV-15 data in order to investigate the fidelity of its predicted trim states and vehicle response to a range of control inputs. During the course of this investigation, the trim algorithm is shown to be robust and capable of producing rapid convergence to a wide range of trim states. Longitudinal trims predicted by GTILT are verified against those of the similarly configured Bell C81 for a range of nacelle incidences and good correlation obtained in all cases. A qualitative verification of the trim states adopted in turning flight reveals no anomalies and the results obtained are very encouraging. The dynamic response of the vehicle is demonstrated to be qualitatively valid when a range of control inputs are applied at various nacelle incidences with the behaviour of the vehicle being explicable in all cases.

NOMENCLATURE

List of Symbols

a_0	blade lift curve slope
\mathbf{a}_a	linear acceleration of the origin of the axis set
\mathbf{a}_{bb}	acceleration of a blade element in blade axis
\mathbf{a}_{hb}	acceleration of the hub in body axis
\mathbf{a}_{hbl}	acceleration of the hub in blade axis
$a_{hblx}, a_{hbly}, a_{hblz}$	acceleration components of hub in blade axis
$a_{hbx}, a_{hbby}, a_{hbbz}$	acceleration components of hub in body axis
$a_{hblzc}, a_{hblz\beta}$	factor not multiplied by β , factor multiplied by β when calculating the acceleration of the hub in blade axis
\mathbf{a}_p	acceleration of a point
\mathbf{a}_{pb}	acceleration of pivot in body axis
\mathbf{a}_{rel}	acceleration of point relative to origin of axis set
\mathbf{c}, \mathbf{c}_t	general control vector and control vector required to produce specified periodic flight state
C_d	drag coefficient
C_{d_i}	drag coefficient of the i^{th} vehicle component
$C_d(\alpha, r_b)$	blade element drag coefficient as a function of angle of attack and spanwise location
$Ch(r_b)$	blade element chord distribution as a function of spanwise location
C_{L_i}	lift coefficient of the i^{th} vehicle component

$C_l(\alpha, r_b)$	blade element lift coefficient as a function of angle of attack and spanwise location
$C_{T_w}, C_{l_w}, C_{M_w}$	wind axis rotor aerodynamic thrust, rolling and pitching moment <i>co-efficients</i>
δ	blade profile drag coefficient
D_i	drag generated by the i^{th} vehicle component expressed in local axis
f	aerodynamic force per unit length acting on a blade element
f_{int}	internal forces acting on a blade element
fm_b	flapping moment exerted by an individual blade on the rotor hub expressed in body axis
fm_s	flapping moment exerted by an individual blade on the rotor hub expressed in shaft axis
F_x, F_y, F_z	forces acting along the x, y, z body axis
f_{xb}, f_{yb}, f_{zb}	components of aerodynamic force acting on a blade in body axis
$f_{xbl}, f_{ybl}, f_{zbl}$	components of aerodynamic force acting on a blade in blade axis
f_{xs}, f_{ys}, f_{zs}	components of aerodynamic force acting on a blade in shaft axis
f_{yble}, f_{zble}	components of aerodynamic force acting on a blade element in blade axis
g	gravitational constant
h	step size used in Runge-Kutta integration scheme and iteration scheme for Glauert inflow
I_b, I_r	blade moments of inertia in flap and rotation
i_b, j_b, k_b	unit vectors aligned with body axis set

$\mathbf{i}_{b1}, \mathbf{j}_{b1}, \mathbf{k}_{b1}$	unit vectors aligned with blade axis set
$\mathbf{i}_s, \mathbf{j}_s, \mathbf{k}_s$	unit vectors aligned with shaft axis set
$I_{xx}, I_{yy}, I_{zz}, I_{zx}$	Vehicle moments of inertia about centre of gravity
I_{yynac}	Nacelle moment of inertia
$\mathbf{J}_{11}, \mathbf{J}_{12}, \mathbf{J}_{21}, \mathbf{J}_{22}$	elements of Jacobian Matrix
K_b	equivalent spring stiffness
$[\mathbf{L}], [\mathbf{L}]_{nl}, [\mathbf{L}]_{dnl}, [\mathbf{L}]_{hnl}$	dynamic gains matrix, non-linear dynamic gains matrix, dimensional non-linear dynamic gains matrix and dimensional non-linear dynamic gains matrix expressed in hub axis
L, M, N	total roll, pitch and yaw moments acting about body axis set
L_{ab}, M_{ab}, N_{ab}	aerodynamic moments acting on a blade in blade axis
L_i	lift generated by the i^{th} vehicle component expressed in local axis
$L_{L/RRH}, M_{L/RRH}, N_{L/RRH}$	body axis moments generated by the right/left rotor acting on the corresponding hub
$L_{L/RRP}, M_{L/RRP}, N_{L/RRP}$	body axis moments generated by the right/left rotor acting on the corresponding pivot
$L_{RR}, L_{LR}, L_W,$ L_F, L_{HS}, L_{VS}	moments acting about the x-axis of the body set and generated by the right rotor, left rotor, wing, fuselage, horizontal surface and vertical surface
$l(\psi, r_b)$	lift on a blade element in blade axis
l_s	rotor shaft length
m	mass of a blade element
m_{nac}	mass of nacelle
m_v	mass of vehicle

M	moment applied by hub on a blade
M	total mass of the blade
$[M], [M]_d$	non-dimensional apparent mass matrix and dimensional apparent mass matrix
M_{trans}	body axis pitching moment generated at the pivot as the nacelle is transitioned
$M_{RR}, M_{LR}, M_W,$ M_F, M_{HS}, M_{VS}	moments acting about the y-axis of the body set and generated by the right rotor, left rotor, wing, fuselage, horizontal surface and vertical surface
M_x, M_y, M_z	rolling, pitching and yawing moments acting about body axis set
n	number of blades per rotor
$N_{RR}, N_{LR}, N_W,$ N_F, N_{HS}, N_{VS}	moments acting about the z-axis of the body set and generated by the right rotor, left rotor, wing, fuselage, horizontal surface and vertical surface
N_{Rb}	yawing moment produced by rotor transformed into body axis
N_s, N_{Rs}	shaft axis yawing moment produced by a blade and rotor
P_6	permutation matrix for a 3 bladed rotor with two flapping states per blade
p, q, r	fuselage roll, pitch and yaw rates about body axis set
$\dot{p}, \dot{q}, \dot{r}$	fuselage roll, pitch and yaw accelerations about body axis set
P_{if}, Q_{if}	body axis harmonic downwash components
P_{ih}, Q_{ih}	hub axis harmonic downwash components
P_{ifw}, Q_{ifw}	wind axis harmonic downwash components
$\dot{P}_{ih}, \dot{Q}_{ih}$	rate of change of hub axis harmonic downwash components
$\dot{P}_{ifw}, \dot{Q}_{ifw}$	rate of change of wind axis harmonic downwash components

P_v	vehicle overall permutation matrix
R	rotor radius
r	position vector
r_b	blade element spanwise location
\bar{T}_b	spanwise distance from the hub to the blade centre of mass
s	vehicle state vector
S_i	area of the i^{th} vehicle component
s_i	element of vehicle state vector
s_l, s_r, s_{if}, s_{fs}	left rotor, right rotor, induced flow and body axis flight state vectors
T_{bl}	thrust produced by a blade
T_h, l_h, M_h	hub axis rotor aerodynamic thrust, rolling moment and pitching moment
T_R	thrust produced by rotor
T_w, l_w, M_w	wind axis rotor aerodynamic thrust, rolling moment and pitching moment
t_p	time for one period of oscillation in rotor forces and moments
u_a, v_a, w_a	fuselage velocity components along x, y, z body axis
$\dot{u}_a, \dot{v}_a, \dot{w}_a$	fuselage acceleration components along x, y, z body axis
u_{hb}, v_{hb}, w_{hb}	velocity components of the hub in body axis
u_{hs}, v_{hs}, w_{hs}	velocity components of the hub in shaft axis
$u_{hsfs}, v_{hsfs}, w_{hsfs}$	local axis freestream velocity components at horizontal stabiliser
$u_{hswd}, v_{hswd}, w_{hswd}$	local axis velocity components at horizontal stabiliser after wing downwash effects have been included

u_{tac}, u_{tc}	tangential velocity component for a blade element rotating anti-clockwise and clockwise when viewed from above
u_t, u_p	tangential and normal velocity components for a blade element
$u_{wfs}, v_{wfs}, w_{wfs}$	local axis freestream velocity components at wing
$u_{wif}, v_{wif}, w_{wif}$	local velocity components at wing after rotor wake impingement has been included
[V]	mass flow parameter matrix
v_a	linear velocity of the origin of the axis set
v_{bbl}	velocity of blade element in blade axis
$v_{bblx}, v_{bbly}, v_{bblz}$	velocity components of blade element in blade axis
V_f	magnitude of vehicle speed
V_i	velocity of the i^{th} vehicle component centre of pressure
v_{hb}	velocity of the hub in body axis
v_{hbl}	velocity of the hub in blade axis
v_{if}	magnitude of rotor induced flow speed
V_M	weighted velocity component
v_p	linear velocity of a point
v_{pb}	velocity of the pivot in body axis
v_{rel}	velocity of a point relative to the origin of the axis set
V_T	total resultant flow through the rotor disc
w	weight per unit length of a blade element
w_{ifm}	momentum theory normal induced flow
w_{if}, w_{ifw}, w_{ifh}	uniform downwash component at rotor centre expressed in body, wind and hub axis

$\dot{w}_{ifw}, \dot{w}_{ifh}$	rate of change of wind axis and hub axis uniform downwash component at rotor centre
w_{ifhs}	rotor upwash component at horizontal stabiliser
w_{hsif}	local axis z-component of velocity at the horizontal stabiliser after wing downwash and rotor upwash effects have been considered
X, Y, Z	total forces aligned with the body axis set
$\dot{x}, \dot{y}, \dot{z}$	components defining relative velocity of a point moving within an axis set
$\ddot{x}, \ddot{y}, \ddot{z}$	components defining relative acceleration of a point moving within an axis set
X_{cg}, Y_{cg}, Z_{cg}	components of position vector defining the location of the vehicle centre of gravity relative to the reference point
$x_{cg}, y_{cg /r}, z_{cg}$	components of position vector of left and right pivot in body axis
X_{cgdat}, Z_{cgdat}	vehicle datum centre of gravity coordinates from reference point (taken as helicopter mode in GTILT)
X_{cgnac}, Z_{cgnac}	horizontal and vertical coordinates of the nacelle centre of gravity in helicopter mode
$\mathbf{x}_{fsCT}, \mathbf{x}_{fsCFS}, \mathbf{x}_{fsST}$	current mean trim flight state vector, current flight state vector and specified mean trim flight state vector
x_i, y_i, z_i	components of position vector of the i^{th} vehicle component
x_{ifs}	general element of flight state vector
$X_{lat}, X_{long}, X_{pedal}, X_{clc}$	Lateral, longitudinal, pedal and combined lateral cyclic stick positions
$X_{RR}, X_{LR}, X_W,$ X_F, X_{HS}, X_{VS}	components of force aligned with the x-axis of the body set and generated by the right rotor, left rotor, wing, fuselage, horizontal surface and vertical surface

$Y_{RR}, Y_{LR}, Y_W,$
 Y_F, Y_{HS}, Y_{VS} components of force aligned with the y-axis of the body set and generated by the right rotor, left rotor, wing, fuselage, horizontal surface and vertical surface

$Z_{RR}, Z_{LR}, Z_W,$
 Z_F, Z_{HS}, Z_{VS} components of force aligned with the z-axis of the body set and generated by the right rotor, left rotor, wing, fuselage, horizontal surface and vertical surface

Greek Symbols

α relative angular acceleration of rotating axis set

α angle of attack, blade incidence

$\beta_i, \dot{\beta}_i$ blade flapping angle, rate of change of blade flapping angle

β_f fuselage sideslip angle in trajectory axis

χ rotor wake angle

$\partial_a, \partial_e, \partial_r$ aileron, elevator and rudder deflections

ϵ_w wing wake downwash angle at horizontal stabiliser

ϕ blade angle of attack

ϕ_f fuselage bank angle in trajectory axis

$\gamma, \dot{\gamma}, \ddot{\gamma}$ shaft angle of tilt, angular velocity and acceleration

γ_f fuselage angle of climb in trajectory axis

θ blade pitch

θ_f fuselage pitch attitude in trajectory axis

$\theta_{tw}(r_b)$ blade twist distribution as a function of spanwise location

θ_{0c}, θ_{0d} combined and differential collective inputs

θ_{0l}, θ_{0r} collective blade pitch input to left and right rotors

$\theta_{1sc}, \theta_{1sd}$	combined and differential longitudinal cyclic inputs
$\theta_{1sl}, \theta_{1sr}$	longitudinal cyclic input to left and right rotors
θ_{1cc}	combined lateral cyclic input
$\theta_{1cl}, \theta_{1cr}$	lateral cyclic input to left and right rotors
$\lambda_{0w}, \lambda_{1sw}, \lambda_{1cw}$	normalised, wind axis induced flow components
$\dot{\lambda}_{0w}, \dot{\lambda}_{1sw}, \dot{\lambda}_{1cw}$	rate of change of normalised, wind axis induced flow components
ρ	air density
ζ, ζ_t	general initial state vector and initial state vector required to produce specified periodic trim state
ω	angular velocity of rotating axis
ω_{bl}	angular velocity of blade axis set
$\psi, \dot{\psi}, \ddot{\psi}$	blade azimuthal position, angular velocity and acceleration
ψ_f	fuselage track angle in trajectory axis
ψ_r	amount of rotor revolution from initial position
ψ_w	rotor sideslip angle
Ω_f	fuselage turn rate in trajectory axis
$\omega_1, \omega_2, \omega_3$	angular velocity components of blade axis set in body axis, shaft axis and blade axis
$\omega_x, \omega_y, \omega_z$	angular velocity components of blade axis set in blade axis
$\dot{\omega}_x, \dot{\omega}_y, \dot{\omega}_z$	angular acceleration components of blade axis set in blade axis
$\omega_{xc}, \omega_{x\beta}$	factor not multiplied by β , factor multiplied by β when calculating the pitch rate of the blade axis set in blade axis

$\omega_{zc}, \omega_z\beta$ factor not multiplied by β , factor multiplied by β when calculating the yaw rate of the blade axis set in blade axis

ω_{yc} factor not multiplied by β when calculating the acceleration in roll of the blade axis set in blade axis

Sign Conventions

Fuselage Attitude

Pitch	+ve	nose up
Roll	+ve	bank to right
Azimuth	+ve	yaw to right

Stick Positions

Longitudinal	+ve	stick forward
Lateral	+ve	stick right
Pedal	+ve	pedal right
Combined Lateral Cyclic	+ve	stick right

Graph Labels and Dimensions

All time histories plotted from GTILT are given in seconds with the following dimensions being associated with the physical parameters:-

Root Pitch	collective blade root pitch	degrees
lat	lateral Stick position	Percentage right
long	longitudinal stick position	Percentage forward
Pedal	pedal position	Percentage right
Com. Lat.	combined lateral cyclic stick position	Percentage right
V_{fp} / Speed	magnitude of vehicle speed	Knots
Beta	fuselage sideslip angle	degrees
Gamma	fuselage angle of climb	degrees
Omega	fuselage turn rate	degrees per second
Phi	fuselage bank angle	degrees
Theta	fuselage pitch angle	degrees
Psi	fuselage track angle	degrees

u_a, v_a, w_a	body axis translational velocities	metres per second
p, q, r	body axis angular velocities	radians per second
F_x, F_y, F_z	forces aligned with the body axis set	Newtons
M_x, M_y, M_z	moments about the body axis set	Newton metres

Chapter 1

INTRODUCTION

Simulation represents a vital stage in the evolution of any rotorcraft design as this enables a rapid evaluation of the proposed vehicle's basic flight mechanic properties such as trim, performance and response to be carried out over a wide range of flight conditions. This is particularly true of the tilt-rotor which utilises a unique blend of aerodynamic and rotor control states to exert control authority and also has a relatively unexplored flight envelope. A generic tilt-rotor model would therefore provide an invaluable insight into the basic handling qualities of the proposed design and assist in the development of suitable control strategies and configurational parameters necessary to produce acceptable handling qualities. Despite this importance, the author is unaware of any tilt-rotor simulation which has been formulated from first principles and utilises the latest generation of rotor modelling techniques. The aim of this project has been the development of a generic tilt-rotor simulation model which utilises advanced modelling techniques and is also suitable for use as a design tool. In order to achieve this aim, it is evident that the model must be capable of rapidly evaluating a wide range of valid tilt-rotor trim states whilst also accurately portraying the dynamic response of the vehicle. Before this work is introduced, it is felt appropriate to familiarise the reader with the tilt-rotor concept by means of a historical perspective.

1.1 History of the Tilt-Rotor

The potential offered by a vehicle whose flight envelope combines a Vertical Take-Off Landing (VTOL) capability with long range and high speed cruising performance has been generally established for some time (Mark 1987, Norwine 1990, Lane and Alton 1991). The attributes of such a vehicle would be directly exploited when performing missions that necessitate a sequence of hovering tasks which are linked together by a series long range transits. Military operations of this type could include troop deployment, search and rescue, anti-submarine warfare, covert operations and maritime early warning and electronic warfare missions (Norwine 1990). Civil operations which have this profile can be found in long distance transportation between city centres, accessing remote areas, linking of distant hubs and rapid response search and rescue missions (Norwine 1990, Lane and Alton, 1991 and The Bell-Boeing Study Team, 1987). Hence, a vehicle with this blend of characteristics would be attractive to both military and civil operators.

In order to establish the desired VTOL capability some form of powered lifting device is necessary. However, this technique sacrifices a large percentage of the available engine power in carrying the vehicle's weight and therefore only limited cruising performance can be obtained. Furthermore, the most common powered lift device, the helicopter rotor, has poor characteristics when operating at high advance ratios (defined as the ratio of the resultant hub velocity to rotor blade tip speed). In this regime, losses are incurred due to compressibility effects (on the advancing side of the disc) and reversed flow or blade stall effects (on the retreating side of the disc). Reichart (1973) demonstrates that these losses severely restrict the lifting capacity of the rotor and therefore limit the top speed of the vehicle. Additionally, greater lift is generated on the advancing side of the rotor disc than on the retreating side and the resultant adverse moments must be opposed by inputs of cyclic blade pitch, therefore, top speed is further restricted by the control limits. Hence, powered lift alone cannot yield the required VTOL capabilities in conjunction with long range, high speed cruising performance. If these characteristics are to be encapsulated in one vehicle, then powered lift must be used in combination with some form of aerodynamic lifting surface. Numerous design concepts have been proposed in an attempt to achieve this alliance and the most significant of these will now be discussed.

Perhaps the most well known technique is the use of thrust vectoring to generate powered lift on fixed wing aircraft. This method utilises directional control over the efflux of a gas turbine engine in order to produce powered lift at low forward speeds. Thrust vectoring yields its optimal performance in the high speed cruising regime but requires large amounts of energy to produce powered lift. Thus, it is evident that vectored thrust is most ideally suited towards high performance aircraft which also require some limited capacity for low speed flight, eg the British Aerospace Harrier combat aircraft. Vectored thrust does not, however, demonstrate the correct characteristics for use in vehicles which require a more balanced compromise between VTOL capabilities and cruising performance. For such vehicles the helicopter rotor represents a more attractive propulsion system because it requires less energy during the hovering phase (Mark 1987). Considerable research effort has been committed towards producing a vehicle which could efficiently convert from rotor-borne to wing-borne flight and, arguably, the most significant proposals in this arena are:-

1. The compound helicopter.
2. The advancing blade concept.
3. The X-wing concept.
4. The tilt-wing concept.
5. The tilt-rotor concept.

The first three proposals on this list all maintain the "edge-on" orientation of the rotor disc throughout the flight envelope. This fixed orientation leads to significant problems in terms of handling qualities and aeroelastic considerations during high speed flight (Reichart, 1973). In an attempt to avoid these problems, solutions such as the stopping or stowing of the rotor during high speed flight have been investigated. However, the structural requirements necessary to stop and stow the rotor under such conditions are prohibitively complex and such concepts are generally thought to be impractical.

The tilt-wing and the tilt-rotor concepts provide similar, more elegant, solutions to the problem of conversion from rotor-borne to wing-borne flight. In these concepts, conversion is achieved by tilting the orientation of the rotor discs during a transition phase. Low speed flight is obtained using a near horizontal orientation of the rotor discs with rotor thrust providing lift. During transitional flight the rotor discs are tilted forward and the rotor thrust is increasingly dedicated towards providing propulsion whilst the wing supports progressively more of the vehicle's weight. On completion of the transition the rotor discs are inclined to the vertical and the thrust produced is used purely for propulsion with the wing sustaining all of the vehicle's weight. The elegance of this solution lies in the fact that vehicles of this type enjoy the low speed handling qualities of the conventional helicopter and the cruising performance of the conventional turbo-prop without incurring the penalties of the previous three concepts.

Tilt-wing and tilt-rotor vehicles both flew for the first time during the 1950's in the United States and neither encountered significant difficulties which would preclude full scale development (Ishida and Nakatani, 1990). However, the tilt-rotor emerged as the favoured candidate for continued development after an extended debate between protagonists at NASA Ames and NASA Langley Research Centres (Mark 1987). It should be noted that interest in the tilt-wing concept has recently been rekindled by the Japanese who aim to have a civil tilt-wing aircraft flying in 1994 and certified by 1997 (Nakatani 1991, Ishida and Nakatani 1990). However, the large majority of recent effort has been devoted towards the development of the tilt-rotor concept. A detailed account describing this work is given by Mark (1987), Norwine (1990) and Brown et al (1992) and a brief summary of the salient information contained within these publications will now be given.

The first tilt-rotor design was produced in the United Kingdom during the period 1937 to 1938. This project was called the Baynes Heliplane and did not

progress to the manufacturing stage, however, the design was well conceived and provided enough detailed information to be of value to future designers.

During World War 2 a tilt-rotor type vehicle, the Focke-Wulf Achgelis 269, was developed in Germany. The rotors on this aircraft were positioned beneath the wings for take-off and rotated upwards to become pusher propellers during the cruising phase. A full scale mock up of the Achgelis FA 269 was constructed but was destroyed in an allied air raid.

The first convertible tilt-rotor vehicle to be flown successfully was the Transcendental Model 1-G; this was a small vehicle of 1750 lbs gross weight and was conceived by Dr Robert Lichten in the United States. Between 1954 and 1955 two aircraft of this type were constructed and 23 hours of flight testing were obtained in approximately 100 flights using private funding. Full conversion to aeroplane mode was never achieved and the programme was abandoned after a fatal crash involving one of the vehicles.

The first aircraft to prove the viability of the tilt-rotor concept was the Bell XV-3 which was a design project undertaken by Bell Helicopters in 1952 using funding supplied by the United States Army. The XV-3 was again a small vehicle with a maximum gross weight of around 5000 lb, power was supplied by a single air cooled piston engine which was mounted on the fuselage centreline. This engine was linked to the two wing tip mounted rotors by means of a system of drive shafts and gearboxes. The XV-3 flying programme commenced in 1953 and the vehicle was successfully used to prove the viability of the tilt-rotor concept by performing full transitions to and from helicopter mode. During this programme, the XV-3 was used to define and explore the conversion envelope from rotor borne to wing borne flight, also, the ability of the tilt-rotor to perform a safe autorotation in the event of an engine failure was demonstrated. However, the XV-3 suffered from a number of significant problems, mainly due to lack of power, which resulted in a serious crash in 1956. The limited power produced by the single engine forced the use of lightweight construction and this led to serious structural problems - in particular an aeroelastic coupling between rotor and pylon which led to a catastrophic failure in hovering flight. On completion of the flight test programme the XV-3 project was concluded in 1966.

During the late 1960's there was a growing interest within NASA to perform research into various forms of powered lift in an attempt to establish the United States as a world leader in that field. As a result of this interest and the success of the XV-3 programme, a project was initiated at NASA Ames Research Centre to develop a tilt-rotor research vehicle. The aim of this project was to design and construct a tilt-

rotor which could demonstrate the military utility of the tilt-rotor concept. The tilt-rotor designed was called the XV-15 and two examples were to be built under a \$50 million budget; a diagrammatical representation of this vehicle is provided in Figure 1.1.

After competition between the Bell Helicopter Company and Boeing Vertol the contract to build these vehicles was awarded to Bell. The design requirements were based on search and rescue/medical evacuation experienced gained in Vietnam, in particular, long range and high speed performance were to be combined with a VTOL capability. From this requirement, the XV-15 was to have a gross weight of 15000 lbs and have the capability to carry payloads of 4000 lbs over a range of 1000 miles at a top speed of 350 Knots. The XV-15 first flew in 1977 and a detailed and extensive flight test programme was undertaken. During this programme, 750 hours flying time were logged during which 2000 transitions were performed and the flight envelope of the vehicle was fully explored with many technical capabilities such as engine out performance being established. The main reason for the improved performance of the XV-15 relative to that of the XV-3 was the use of more powerful propulsion units, the structure of the XV-15 could therefore be heavier and the previously encountered aeroelastic problems were avoided.

On completion of the technical flight test programme the XV-15 was used to demonstrate the military capabilities of the tilt-rotor particularly in the search and rescue role. Attempts were made to interest the United States Army and Airforce in a vehicle based on the XV-15 but unfortunately all attempts failed.

In 1982 the United States Marines became interested in the tilt-rotor as a potential replacement for their Sikorsky CH-53 and CH-46 assault helicopters. This interest was partly generated in response to the advent of the latest generation "smart" missiles, for example the Exocet, which can be shore launched and are an extreme threat to shipping at ranges of up to 50 miles. It is therefore desirable to deploy troops into battle from greater distances in order to ensure the safety of the assault ships. Due to the restrictions in the conventional helicopter's range it was suspected that it could no longer adequately fulfil this role, therefore, interest in the tilt-rotor increased as it was seen to offer a potential solution to this problem.

To satisfy this requirement the specification laid down was for a tilt-rotor capable of carrying 24 battle ready troops or 6000 lbs of cargo over a range of 430 nautical miles at a cruising speed of 275 Knots. In 1985 the Bell Helicopter Company and Boeing Vertol were paired together in a contract to design such a vehicle - from this contract the V-22 Osprey was developed and this vehicle is depicted in Figure 1.2.

The first flight of the V-22 took place in March 1989 with the first full transition being completed in August of the same year. Since then 6 prototype vehicles have been constructed and in excess of 600 flying hours logged during some 550 flights. The V-22 flight test programme carried out using these vehicles has been exhaustive and is described in detail by Cooper (1992), Thomason (1990), Dunford (1990) and Martin and Ostlund (1989). A lengthy description of this programme is not appropriate here, however, the main point of interest is that a large portion of the vehicle flight envelope has been explored in all modes of flight with a top speed of 292 Knots, a ceiling of 26000 ft and a maximum external payload of 4000 lbs all being attained. Unfortunately, two of the test vehicles have been lost during this programme, however, both accidents have been thoroughly investigated and neither has been attributed to fundamental design defects.

Continued funding for the V-22 project has been under threat for some time and has been the cause of extended debate in the United States Government. However, the future of this project now seems assured with \$550 million being made available under a Navy contract to construct five production representative V-22 vehicles.

Another military application of the tilt-rotor which is currently under development is that of a remotely piloted Unmanned Aerial Vehicle (UAV) whose role would be found in long range reconnaissance, gunfire support, target designation, communications and electronic countermeasures. Much work has been carried out by Bell Textron (Brown et al, 1992) in the development of a tilt-rotor UAV and a prototype has been successfully flown under remote control with over 30 hours being logged. A demonstrator vehicle is currently being developed and it is hoped that this will lead to a full scale production version.

Whilst the majority of expenditure accrued on the tilt-rotor project has been devoted towards the development of a military vehicle considerable effort is also being carried out in the investigation of possible civil variants. In 1980 the Federal Aviation Authority (FAA) sponsored a programme to explore means by which improvements could be made to the United States national transportation network. In this study, the tilt-rotor was identified as offering a potential means by which airport capacity could be expanded without adding large and expensive infrastructure (Lane and Alton 1991). The conclusions drawn by this programme led to a jointly funded FAA/NASA/DoD programme whose aim was to document the potential of civil tilt-rotor vehicles. This work resulted in a report which illustrates in detail possible applications for a series of civil tilt-rotor configurations ranging from an unpressurized 8 seat vehicle based on the XV-15 to a new pressurised 75 seat design (Bell-Boeing Study Team 1987). The main

conclusions of this report are that the civil tilt-rotor offers unique capabilities and is superior to multi-engine helicopters under most conditions, however, its success is dependent on the continued military development of the V-22.

The potential of the civil tilt-rotor has also been recognised in Europe and a consortium was formed in 1988 in an attempt to design and produce a vehicle of this type. The consortium consists of six rotorcraft manufacturers from five European countries and was formed in 1988 under the European Future Advanced Rotorcraft (Eurofar) project. The first stage of this project was to investigate the feasibility of a European tilt-rotor aircraft and produce a baseline tilt-rotor design based on the results of a market survey. In light of the findings of this survey the baseline configuration selected was for a 30 seat pressurized vehicle with a range of 600 nautical miles at a cruising speed of 300 Knots (Andres and Monti 1988). On completion of the initial design study the Eurofar project has been continued to a simulation phase in order to assess the handling qualities and operational requirements of the tilt-rotor (Rollet and Thibaudat 1992). It is hoped to continue this work into the second phase of the project which would ultimately lead to the development of an operational tilt-rotor by the year 2000.

1.2 The Requirement for a Tilt-Rotor Simulation Model

From the preceding discussion it is apparent that the tilt-rotor offers excellent potential by successfully combining good low speed handling qualities with efficient cruising performance and that this concept has now been developed to a mature stage. Numerous roles which would exploit this potential have been suggested, and hence, it can be seen that future tilt-rotor aircraft will vary widely in terms of size and configuration in order to perform these missions (The Bell-Boeing Study Team 1987). As more diverse tilt-rotor configurations evolve, it is important that an evaluation of their stability and control characteristics is carried out at an early stage in the design process so that satisfactory flying characteristics can be obtained at minimal cost during subsequent development. One recognised method for performing such an evaluation is the use of a generic mathematical model, Padfield (1981), as this can provide invaluable insight into the behaviour of a new design before resources are committed during the development phase. This is particularly true of the tilt-rotor whose handling qualities and flight envelope are relatively unexplored when compared to those of the conventional helicopter and fixed wing aircraft, however, few tilt-rotor simulation models currently exist world wide.

The novel technique utilised to exert control authority on the tilt-rotor configuration further promotes the requirement for a simulation model in order to assist

in the development of suitable control laws. In low speed flight, control forces are applied by means of collective and cyclic blade root pitch deflections in a similar manner to a conventional helicopter. During the cruising phase authority is exerted through displacements of aerodynamic surfaces such as ailerons, elevator and rudder as witnessed on a conventional fixed wing aircraft. During transitional flight, the rotor controls are progressively washed out as the nacelles are tilted forward from helicopter mode with the gearing of the aerodynamic surfaces being a function of both dynamic pressure and nacelle incidence. A detailed description of this technique is given by Churchill and Dugan (1981) and in the Bell-Boeing Tilt-Rotor Handling Qualities Short Course Notes. One facet of this technique is that it produces a redundancy in control, for example, in helicopter mode a rolling moment can be generated by means of either an aileron deflection or by increasing the collective of one rotor relative to the other, and this type of redundancy is not experienced by conventional fixed wing aircraft or helicopters. The control issue is further clouded because the axis round which the rotor states exert their authority alters as the nacelles are transitioned, for example, a differential collective input would generate a yawing moment in aeroplane mode as opposed to a rolling moment in helicopter mode. A mathematical model would provide an ideal tool for use in the development of control laws by which these characteristics could be exploited to yield a performance that is optimised according to some specified criteria.

From the preceding discussion, it is perhaps evident that the simulation model should accurately predict the dynamic response of the vehicle to a wide range of control inputs. However, Reichart (1973) identifies that accurate replication of the vehicle's trim states is also particularly important when modelling the tilt-rotor configuration because of significant non-linearities in its behaviour. Such non-linear characteristics are primarily attributable to rotor wake impingement effects on the horizontal stabiliser and strong cross-coupling between rotor control states (Marr and Roderick 1974). A detailed description of these effects is provided in Chapter 5 but they will now be illustrated qualitatively for the purposes of the current discussion. This type of non-linearity is exemplified graphically in Figure 1.3 (adapted from Reichart, 1973) which shows qualitatively the trim curves obtained for the longitudinal stick displacements against trimmed forward airspeed in both helicopter mode and aeroplane mode. From this figure it can be seen that the shape of these trim curves is strongly dependent on nacelle incidence and that a stick reversal (shown here in the mid-speed range) is evident in the helicopter mode trim curve. A representation of a transitional trim curve is also depicted in Figure 1.3. and it can be seen that this exhibits two stick reversals with the exact location and magnitude being dependent on the configuration of the vehicle being considered. Stick reversals such as those depicted in

this figure are undesirable and, if excessive, could lead to unacceptable handling qualities. Thus, it is of great significance that the simulation model should be capable of accurately capturing such facets of the vehicle behaviour. Strategies (such as controlling the tailplane incidence) could then be explored to eliminate these undesirable effects early in the design process in order to avoid incurring the expense of producing a vehicle with unacceptable handling qualities.

The observations made in the preceding discussion highlight the requirement for a generic tilt-rotor simulation model for use in the design of future configurations. If this model is to offer significant benefits as a design tool, it should faithfully capture the dynamic response of the vehicle to a range of control inputs. Of equal importance from a design viewpoint is that this model should be capable of predicting the trim states adopted by that vehicle throughout the flight envelope. The aim of the current research has been to develop a novel generic tilt-rotor simulation model which has the facility of realising these goals. A detailed description of the Generic TILT-rotor (GTILT) simulation model produced by this research is given in Chapters 2, 3 and 4 and is also documented in earlier publications (McVicar and Bradley, 1990, McVicar and Bradley, 1991, McVicar and Bradley, 1992a, McVicar and Bradley 1992b). However, it is felt appropriate that GTILT's salient features (in the context of the arguments put forward in this section) should be introduced at this stage and it is convenient to use the modelling of the rotor as a start point to this discussion.

1.3 The GTILT Model

The modelling of the rotor forces and moments is of key importance to any rotorcraft simulation, in fact, Padfield (1988) defines three levels into which these simulations can be categorised dependant primarily on the techniques utilised to model the behaviour of the rotor. In the Level 1 category the rotor disc is modelled as a whole and the spanwise aerodynamic loads are integrated analytically with compressibility effects being neglected. Padfield (1988) states that such models are useful when applied to regimes where the aerodynamic blade loadings can be evaluated satisfactorily by analytic integration. The rotor blades incorporated on the tilt-rotor configuration are highly twisted and have substantial chord variations from root to tip, therefore, accurate analytic integration of the blade loads would be impractical and it was decided to employ numerical techniques to perform this integration. The loadings produced by each blade are therefore evaluated individually and these factors drive the GTILT model towards the Level 2 category as defined by Padfield (1988). However, it should be noted that the GTILT model does not extend fully into the Level 2 category because it

does not include nonlinear three dimensional aerodynamics, effects of blade vortex interaction or any elastic blade modes.

It was decided that a Level 3 model was inappropriate as this requires detailed elastic blade modelling and a free wake analysis of the rotor induced flow. Padfield (1988) describes the inclusion of this amount of detail as being generally unnecessarily complex for a flight mechanics model.

One drawback of individual blade modelling is that it is numerically intensive and represents a large computational burden which can produce prohibitively long run times. For this reason a large number of existing rotorcraft simulations sacrifice modelling fidelity by using Level 1 techniques (Thomson 1992, Padfield 1981, Harendra et al 1973). In fact, the author is unaware of any existing generic tilt-rotor simulation models which have been derived from first principles with sufficient modelling detail to merit Level 2 status, therefore, GTILT is unique in its class.

Advanced rotorcraft simulations (such as Level 2 models) have primarily been developed in order to extend high levels of modelling fidelity to the arenas of control law development and piloted simulation. Before this goal can be fully realised and the enhanced fidelity fully exploited, computational run times must be reduced to an acceptable level so that such models are of practical use in these arenas. Generally, the evaluation of a specified trim state forms the start point for any simulation and it is therefore vitally important that the associated trimming algorithm should be reliable and capable of rapidly obtaining a wide range of vehicle trim states. From the discussion at the beginning of Chapter 3, it is evident that the trimmed forces and moments produced by an individual blade rotor model are periodic rather than steady in nature. This periodicity, in combination with the inherent instabilities experienced by all rotorcraft configurations, creates difficulties when attempting to trim such simulations. Existing trim algorithms developed for use with Level 2 models tend to suffer from stability problems and yield slow convergence, therefore, significant computational effort is required to produce a specified periodic trim and this is also discussed in Chapter 3. From the preceding observations it is evident that a superior trimming methodology must be developed if the latest advanced rotorcraft simulations are to yield true practical benefits for a wide range of applications. As this requirement has emerged, research has been carried out in the development of an efficient means by which a periodic, standalone rotor model (Peters and Izadpanah) can be trimmed. However, the author is unaware of any existing technique which can efficiently and reliably trim a complete rotorcraft simulation to a specified periodic trim state. The development of such a trimming technique would therefore represent a significant contribution to the important

and developing field of Level 2 rotorcraft simulation. The solution of the trim problem was therefore identified as a key area during the formulation of GTILT and this was successfully addressed by the innovative trimming methodology which is derived in Chapter 3. This unique algorithm is capable of rapidly ascertaining the correct set of initial conditions and control displacements necessary to produce a wide range of specified trim states. The attributes of this trimmer are further extended because it is capable of evaluating trim states for a vehicle with the tilt-rotor's novel control characteristics and strongly non-linear behaviour (as previously discussed). From the sample iteration histories provided in Chapter 5 it is evident that this algorithm is indeed capable of producing rapid convergence for a wide range of tilt-rotor trim states even in adverse areas of the flight envelope. It is felt that this trim algorithm provides an elegant and robust solution to the problem of trimming advanced rotorcraft simulation models and this makes the advanced fidelity offered by such models more accessible to control system designers and simulationists. This work, therefore, represents a significant contribution to the field of rotorcraft modelling.

Inverse simulation is a technique which is recognised to be of value when assessing vehicle handling qualities or developing pilot strategies (Thomson and Bradley 1988, Thomson and Bradley 1993). This technique is particularly valuable when considering vehicles which exhibit severe non-linear characteristics (Smith and Meyer 1987) as witnessed in the tilt-rotor configuration. Essentially, the trim algorithm derived in Chapter 3 performs a model inversion because it predicts the set of control inputs necessary to produce a prescribed, trimmed, flight path. As discussed in Section 5.4, a manoeuvre can therefore be divided into discrete intervals and this trim algorithm used to predict the control inputs necessary to recreate that manoeuvre at discrete points through its history. The resulting sequence of control displacements can subsequently be linked together and the vehicle forced to follow the prescribed flight path during a forward simulation. The unique attributes of the periodic trim algorithm can therefore be exploited in order to perform studies into the characteristic behaviour of the tilt-rotor configuration whilst performing detailed manoeuvring flight. This technique is of value because it can be used to quickly obtain an insight into the behaviour of the tilt-rotor configuration when following relatively complex flight paths. Two examples are given in Chapter 5 where the trimming algorithm is used to predict the control inputs necessary to perform full transitions to and from helicopter mode. The results obtained are discussed in Section 5.4 and provide an enlightening impression into the behaviour of the tilt-rotor configuration during transitional flight.

As stated previously, the large amount computational effort required to implement Level 2 simulations has made them unattractive for use in control law design

and piloted simulation. Until recently, it has been necessary to use models with lower levels of fidelity for these purposes and hence a degree of modelling detail is lost. However, the recent advent of advanced computational hardware has made individual blade modelling more attractive to rotorcraft simulationists and some of the latest generation helicopter models have provided real-time performance on such machines (Du Val 1989, Meerwijk and Brouwer 1991). One such technique for reducing computational run time is that of parallel processing whereby the model is divided into separate sequential sections, or threads, which can be run autonomously from each other in parallel on dedicated processors called transputers. This technique lends itself to Level 2 rotorcraft modelling because dedicated transputers can be used to evaluate the forces and moments acting on each rotor blade and the vehicle airframe concurrently, therefore, significant savings in run time are possible. The GTILT model has been parallelised and implemented on a customised transputer network in order to reduce computational run time and the methodology used is discussed in Chapter 4. It is fully expected that the unique capabilities of GTILT could be further enhanced by structuring the software implementation in a more efficient manner in order to yield real-time performance and this is discussed in Section 4.5.

The technique used to model the aerodynamic forces and moments acting on the vehicle airframe is described in Section 2.2. Each major component of the airframe (wing, fuselage, horizontal surfaces and vertical fin) is considered separately and has its own associated look-up table defining a set of aerodynamic force and moment coefficients. This technique gives the user greatest freedom in the specification of the vehicle configuration and best facilitates the modelling of wake impingement on the empennage and wing. As stated in the preceding section of this chapter, accurate modelling of the wake impingement on the empennage is essential if GTILT is to fully portray the important non-linear characteristics of the tilt-rotor vehicle. This effect has been included by imposing an equivalent induced upwash at the horizontal stabiliser using wind-tunnel data published by Marr and Sambell (1973) and a detailed discussion on this subject is given in Section 2.2.1.

From the discussion in Section 1.2 it is apparent that the GTILT model must include a combination of rotor control states and aerodynamic control surfaces if it is to be of benefit as a control system design tool. In order to achieve this goal, 5 rotor control states and 4 aerodynamic surfaces have been included as part of the GTILT model with the gearing between piloted stick displacement and control deflection being defined in the form of look-up tables. This technique extends to the user a large amount of flexibility in the definition of control laws and is discussed in detail in Section 2.3.

The author recognises that verification of GTILT must be obtained if it is to be used with confidence as a design tool. Considerable effort has been expended towards achieving a quantitative verification for both the dynamic response of this model and the trim states it predicts. GTILT was configured using XV-15 data and a range of predicted trim states were then verified against those of the Bell C81 (Van Gaasbeek, 1981) which is of established merit for use in tilt-rotor simulations (Schillings et al 1990). The results of this exercise promoted a large amount of confidence in the modelling fidelity produced by GTILT and a detailed appraisal is provided in Chapter 5. Despite considerable effort, it was not possible to obtain flight test data or established model data depicting the dynamic response of the tilt-rotor configuration. However, a range of control inputs were applied to GTILT at various nacelle incidences and a detailed qualitative verification of the predicted behaviour produced extremely encouraging results; these are discussed in Chapter 5.

Chapter 2

MODELLING

Accurate prediction of vehicle flying characteristics is the principal aim of any flight mechanics model. Such characteristics are generated in response to the forces and moments acting on the vehicle and these must therefore be accurately predicted if high levels of fidelity are to be obtained. Once the forces and moments have been defined the equations of motion can be integrated and the vehicle's dynamic behaviour modelled. The vehicle equations of motion incorporated in GTILT are the commonly used Euler rigid body equations (Etkin 1972) which take the form:-

$$\dot{u}_a = \frac{X}{m_v} - (q w_a - r v_a) - g \sin\theta_f$$

$$\dot{v}_a = \frac{Y}{m_v} - (r u_a - p w_a) + g \cos\theta_f \sin\phi_f$$

$$\dot{w}_a = \frac{Z}{m_v} - (p v_a - q u_a) + g \cos\phi_f \cos\theta_f$$

$$I_{xx}\dot{p} = (I_{yy} - I_{zz})qr + I_{xz}(\dot{r} + pq) + L$$

$$I_{yy}\dot{q} = (I_{zz} - I_{xx})rp + I_{xz}(r^2 - p^2) + M$$

$$I_{zz}\dot{r} = (I_{xx} - I_{yy})pq + I_{xz}(\dot{p} - qr) + N$$

The rate of change of the Euler angles θ_f , ϕ_f , ψ_f are related to the body axis angular velocity components by the following differential equations:-

$$\dot{\phi}_f = p + q \sin\phi_f \tan\theta_f + r \cos\phi_f \tan\theta_f$$

$$\dot{\theta}_f = q \cos\phi_f - r \sin\phi_f$$

$$\dot{\psi}_f = q \sin\phi_f \sec\theta_f + r \cos\phi_f \sec\theta_f$$

The orientation of the vehicle body axis set relative to an earth fixed frame can be defined by a sequence of transformations through the Euler angles. To move from earth fixed axis to body axis the transformation is carried out by the following sequence of rotations; firstly, through the heading angle, ψ_f , then the pitch angle, θ_f , before, finally, the bank angle, ϕ_f and this is shown graphically in Figure 2.1.

As stated previously, the forces and moments acting on the vehicle must be accurately evaluated if its flying characteristics are to be authentically portrayed. Consequently, a large amount of effort has been expended in the derivation of expressions which define the external forces and moments X, Y, Z, L, M and N. The most convenient strategy for this is to reduce the vehicle into its constituent components and evaluate the corresponding force and moment contributions from each. The individual contributions are then summed to produce the overall forces and moments acting on the vehicle:-

$$\begin{aligned}
 X &= X_{RR} + X_{LR} + X_W + X_F + X_{HS} + X_{VS} \\
 Y &= Y_{RR} + Y_{LR} + Y_W + Y_F + Y_{HS} + Y_{VS} \\
 Z &= Z_{RR} + Z_{LR} + Z_W + Z_F + Z_{HS} + Z_{VS} \\
 L &= L_{RR} + L_{LR} + L_W + L_F + L_{HS} + L_{VS} \\
 M &= M_{RR} + M_{LR} + M_W + M_F + M_{HS} + M_{VS} \\
 N &= N_{RR} + N_{LR} + N_W + N_F + N_{HS} + N_{VS}
 \end{aligned}$$

where the above subscripts denote the following:-

- RR:- right rotor
- LR:- left rotor
- W:- wing
- F:- fuselage
- HS:- horizontal surface
- VS:- vertical surface

The derivation of expressions which define the above force and moment components will now be presented.

2.1 Rotor Model

A major component of any rotorcraft simulation is the modelling of the rotor itself as it is this which provides the propulsive forces and moments on which the characteristic behaviour of the vehicle is formed. Many rotor models exist for helicopter applications but these are often based on a quasi steady analytical solution carried out in multi-blade coordinates, for example, Thomson 1992 and Padfield 1981. In order to restrict the complexity of the analytic solutions only relatively simple blade parameters describing twist, chord and aerodynamic properties can be included. Such a limitation is acceptable when investigating helicopter flight mechanics because the rotor blades encountered are generally relatively simple in form. However, tilt-rotor blades have a geometry designed to yield an optimum compromise of performance when used

throughout a flight envelope extending from low speed helicopter mode operations to high speed fixed wing flight. As a result the blades are highly twisted with substantial chord variations from root to tip and consequently a simplified analytic solution would sacrifice fidelity by failing to model these characteristics. Existing tilt-rotor simulations, such as that of Harendra et al (1973), devised for flight mechanics studies and real-time simulation pay this penalty by incorporating multi-blade disc models in order to reduce computational requirements to a realisable level (Churchill and Dugan 1982).

One method of improving fidelity is the use of numerical techniques to model each blade individually because this permits the inclusion of more complex blade geometries and aerodynamic properties. Additionally, the oscillatory behaviour of the rotor is now reflected because the disc is not modelled as a whole but instead the contribution from each blade is considered separately. Recent advances in supercomputer technology have made models of this type attractive for use in flight mechanics studies because, as discussed in Chapter 4, they are ideally suited for implementation in parallel on a computing surface. Helicopter simulations such as those of Du Val (1989) and Meerwijk and Brouwer (1991) have been formulated around an individual blade model and real-time performance achieved when implemented on a computing surface. However, no such model is known to be available in the United Kingdom for tilt-rotor handling qualities analysis. Given the availability of a parallel computing resource at the University of Glasgow and the improved integrity offered by individual blade modelling it was decided to include such a model as part of this simulation.

2.1.1 The Tilt-Rotor Blade Element Rotor Model

When formulating this model three main aspects have been included:-

1. Blade Flapping -this is the angle through which the blade has rotated in a direction parallel to the rotor shaft as shown in Figure 2.2. This motion is essential if the rolling and pitching moments generated by the rotating blades are to be balanced at the rotor hub. A detailed discussion of blade flapping is given in Prouty (1990) but essentially equilibrium is obtained through an interaction between local angle of attack and dynamic pressure variations around the rotor disc. Flapping motion forms a key role in forming the behaviour of the rotor and therefore must be included if this is to be accurately portrayed. Flapping is included in this model by assuming that the rotor is composed of rigid blades which are hinged at the hub and have a stiffness in flap; such a technique is widely used and its validity is investigated by Padfield (1981). The

differential equation describing blade flapping behaviour for a for a centre sprung tilting rotor is derived in section 2.1.9.

Tilt-rotor vehicles incorporate gimbal mounted rotors in order to reduce disc loading sensitivity to blade flap and alleviate Coriolis forces at the hub (Edenborough 1972). Such rotors cannot transmit moments about the pitch or roll axis and also have a flap frequency close to one; this can be modelled using a centre spring representation by including a low equivalent spring stiffness. An alternative method of modelling gimballed rotors would be to derive the equations of motion for the hub, these could then be solved by integration if the hub were massive or by iteration if no mass were associated with the hub. It is proposed that such work would be beneficial to investigate the integrity of the centre sprung approximation when modelling gimballed rotors, however, this has been outwith the scope of the current research.

2. Rotor Induced Flow -this is the velocity imparted to the column of air drawn through the rotor disc. The rotor thrust is generated in reaction to the accelerating force which produces this velocity and therefore the induced flow must be modelled accurately before the rotor performance can be predicted. The earliest research centred on the evaluation of the induced velocity produced by a loaded rotor is attributable to Glauert (1926) where momentum theory is applied across a uniformly loaded rotor disc with an infinite number of blades. The inaccuracy inherent in the assumption of uniform disc loading was recognised and Glauert enhanced the momentum approximation by superimposing harmonic contributions onto the original theory to portray longitudinal and lateral variations in velocity. The Glauert model forms the most basic inflow model generally used in rotorcraft simulation and a discussion of this work is given in Prouty (1990), Johnson (1980b) and Bramwell (1976). It is interesting to note that although this theory has never been proved, its validity is generally accepted.

The main attributes of the Glauert model are its ease of use and minimal computing requirements - however it suffers from some inadequacies. The algorithm assumes that the mass of air flowing through the rotor can be accelerated instantaneously in response to control inputs or changes in flight condition. This is not the case due to inertial considerations and in fact there is a lag associated with the induced flow reaching its new steady state following a change in flight condition or control perturbation. Additionally, the effects of aerodynamic rotor pitching and rolling moments on the induced flow are not included. Gaonkar and Peters (1988) highlight that these neglected effects are of significant importance when attempting correlation between predicted induced flow with that of measured data. In the light of this

information, a considerable amount of research has been carried out since the 1950's in an attempt to model induced flow more accurately and this work is summarised by Chen (1990). Typical of the latest generation of these models is that of Peters and HaQuang (1988) which uses a three state first order differential equation to characterise induced flow behaviour. This methodology was developed using unsteady actuator disc theory and includes the elements missing from the Glauert model.

Both the Glauert and Peters-HaQuang induced flow models have been incorporated as part of the blade element model derived in this chapter and will be discussed in greater detail in Section 2.1.10.

3. Rotor Forces and Moments - individual blade components are obtained by integration along the span then summed together to produce the overall rotor forces and moments. Once transformed into body axis these parameters can be input into the overall vehicle equations of motion. Expressions defining individual blade forces and moments are derived in Section 2.1.6.

After consideration it was decided to neglect the following:-

1. Lag degree of freedom:- to reduce in plane stresses generated at the hub due to Coriolis and inertial forces articulated rotors include lag hinges and dampers which allow the blades to lag in the plane of rotation. On teetering and gimbaled rotors the blades are underslung below the hinge so that variations in the radial velocity components of the flapping blades cancel to produce zero net in plane stress at the hub. Lag hinges are therefore not required and any lagging motion produced will be purely due to aeroelastic bending of the blade. Therefore it was decided that the effect of lagging motion would be negligible when compared with that of blade flap and that the added complexity involved precluded its inclusion.

2. Aeroelasticity:- modelling of blade flexibility leads to the solution of highly complex mathematical expressions which influence the behaviour of the rotor across a range of frequencies. The higher frequency effects are generally thought of as being too fast for the pilot to perceive and beyond the bandwidth of present flight controllers, therefore, they are considered of little significance for piloted simulation and handling qualities analyses. It is recognised that blade aeroelastics can also alter the lower frequency characteristics of the rotor, for example, in torsion which changes the effective blade pitch and consequently the collective input required to produce a specified trim or manoeuvre. If facets such as this are to be accurately captured by an aeroelastic model then a large amount of detailed design data would be required (Simpson 1991), no such data is currently available for existing tilt-rotor aircraft. It

was therefore concluded that the complexity of aeroelastic modelling and the lack of necessary design data precluded the inclusion of blade flexibility in the current model.

3. Blade weight :- gravitational acceleration has been considered negligible when compared to the other accelerating forces acting on the blade.

4. Outward tilt of nacelles:- axis transformations are simplified by assuming that the rotor shaft tilts in a plane parallel to that defined by the x and z body axis sets.

5. Dynamic stall:- effects have been considered negligible. There is the facility to include retreating blade stall by definition of a look-up table for lift co-efficient, C_l , against angle of attack, α .

6. Compressibility:- at present the blade lift coefficient implemented is considered as constant along the span and assumes two dimensional flow over the airfoil section. This is purely due to lack of data and it is proposed that look-up tables for sectional lift coefficients which include Mach number and three dimensional flow corrections should be incorporated at a later date.

2.1.2 Kinematics of a Flapping Blade Element With a Tilting Shaft

Before the forces and moments produced by a blade element can be ascertained the velocity and acceleration of that element must be evaluated, in order to do this a convenient axis system is defined.

2.1.3 Definition of Axis Sets and Transformation Matrices

The axis sets used in the derivation of this model are shown diagrammatically in Figure 2.3. As can be seen three axis sets are used and these are:-

1. Body axis, centred at the vehicle centre of gravity with the x-axis aligned along the vehicle centreline, the z-axis pointing downward and the y-axis making up the right handed set.

2. Shaft axis, centred at the shaft pivot with the orientation being obtained by a rotation of γ , the shaft angle, about the body y-axis.

3. Blade axis, centred at the rotor hub with the orientation being obtained by a rotation of ψ , the blade azimuthal angle, about the shaft z-axis.

To move from body to shaft axis the following transformation is used to tilt the axis set through the prescribed angle:-

$$\begin{bmatrix} i_s \\ j_s \\ k_s \end{bmatrix} = \begin{bmatrix} \cos\gamma & 0 & \sin\gamma \\ 0 & 1 & 0 \\ -\sin\gamma & 0 & \cos\gamma \end{bmatrix} \begin{bmatrix} i_b \\ j_b \\ k_b \end{bmatrix}$$

Now, to transform into blade axis a rotation about the z-shaft axis followed by a rotation about the y-blade axis is performed:-

$$\begin{bmatrix} i_H \\ j_{bl} \\ k_{bl} \end{bmatrix} = \begin{bmatrix} \cos\beta & 0 & -\sin\beta \\ 0 & 1 & 0 \\ \sin\beta & 0 & \cos\beta \end{bmatrix} \begin{bmatrix} -\cos\psi & \sin\psi & 0 \\ -\sin\psi & -\cos\psi & 0 \\ 0 & 0 & 1 \end{bmatrix} \begin{bmatrix} i_s \\ j_s \\ k_s \end{bmatrix} \quad (\text{eqn 2.1})$$

assuming β is suitably small that:-

$$\begin{aligned} \cos\beta &= 1 \\ \sin\beta &= \beta \end{aligned}$$

then eqn 2.1 becomes:-

$$\begin{bmatrix} i_H \\ j_{bl} \\ k_{bl} \end{bmatrix} = \begin{bmatrix} 1 & 0 & -\beta \\ 0 & 1 & 0 \\ \beta & 0 & 1 \end{bmatrix} \begin{bmatrix} -\cos\psi & \sin\psi & 0 \\ -\sin\psi & -\cos\psi & 0 \\ 0 & 0 & 1 \end{bmatrix} \begin{bmatrix} i_s \\ j_s \\ k_s \end{bmatrix}$$

Thus, to move from body to blade axis two transformations are carried out, firstly into shaft axis, then into blade axis:-

$$\begin{bmatrix} i_H \\ j_{bl} \\ k_{bl} \end{bmatrix} = \begin{bmatrix} 1 & 0 & -\beta \\ 0 & 1 & 0 \\ \beta & 0 & 1 \end{bmatrix} \begin{bmatrix} -\cos\psi & \sin\psi & 0 \\ -\sin\psi & -\cos\psi & 0 \\ 0 & 0 & 1 \end{bmatrix} \begin{bmatrix} \cos\gamma & 0 & \sin\gamma \\ 0 & 1 & 0 \\ -\sin\gamma & 0 & \cos\gamma \end{bmatrix} \begin{bmatrix} i_b \\ j_b \\ k_b \end{bmatrix}$$

to give:-

$$\begin{bmatrix} i_H \\ j_{bl} \\ k_{bl} \end{bmatrix} = \begin{bmatrix} -\cos\psi\cos\gamma + \beta\sin\gamma & \sin\psi & -\cos\psi\sin\gamma - \beta\cos\gamma \\ -\sin\psi\cos\gamma & -\cos\psi & -\sin\psi\sin\gamma \\ -\beta\cos\psi\cos\gamma - \sin\gamma & \beta\sin\psi & -\beta\cos\psi\sin\gamma + \cos\gamma \end{bmatrix} \begin{bmatrix} i_b \\ j_b \\ k_b \end{bmatrix} \quad (\text{eqn 2.2})$$

To move in the opposite direction, from blade to body axis, the individual rotation matrices are transposed and the order of multiplication reversed.

2.1.4 Velocity of a Blade Element

In order to evaluate the aerodynamic forces acting on a blade element it is first necessary to determine the absolute velocity of that element in local axis. It is shown in Meriam (1980) that the absolute velocity, \mathbf{v}_p , of a point moving in a co-ordinate system with rotating axis is given by:-

$$\mathbf{v}_p = \mathbf{v}_a + \frac{d\mathbf{r}}{dt}$$

$$\mathbf{v}_p = \mathbf{v}_a + \dot{x}\mathbf{i} + \dot{y}\mathbf{j} + \dot{z}\mathbf{k} + (\boldsymbol{\omega} \times \mathbf{r}) \quad (\text{eqn 2.3})$$

where:-

\mathbf{v}_a :- is the linear velocity of the origin of the axis set.

\mathbf{r} :- is the position vector of the point in the axis set.

$\dot{x}, \dot{y}, \dot{z}$:- are the linear velocity components of the point in the axis set.

$\boldsymbol{\omega}$:- is the angular velocity of the reference frame.

To calculate the absolute velocity of a blade element in local axis it is first necessary to evaluate the velocities of two intermediate points; the pivot and the hub, both in body axis. Therefore to evaluate the velocity of the left or right hand pivot in body axis:-

$$\left. \begin{aligned} \mathbf{v}_a &= u_a \mathbf{i}_b + v_a \mathbf{j}_b + w_a \mathbf{k}_b \\ \mathbf{r} &= -x_{cg} \mathbf{i}_b + y_{cg1/r} \mathbf{j}_b - z_{cg} \mathbf{k}_b \\ \boldsymbol{\omega} &= p \mathbf{i}_b + q \mathbf{j}_b + r \mathbf{k}_b \\ \dot{x} = \dot{y} = \dot{z} = 0 &\Rightarrow \mathbf{v}_{rel} = 0 \end{aligned} \right\} \quad (\text{eqns 2.4})$$

Applying Equations 2.4 to Equation 2.3 gives:-

$$\mathbf{v}_{pb} = \begin{bmatrix} u_a - qz_{cg} - ry_{cg1/r} \\ v_a + pz_{cg} - rx_{cg} \\ w_a + py_{cg1/r} + qx_{cg} \end{bmatrix}$$

For the velocity of the hub in body axis:-

$$\left. \begin{aligned} \mathbf{v}_a &= \mathbf{v}_{pb} \\ \mathbf{r} &= l_s \sin\gamma \mathbf{i}_b - l_s \cos\gamma \mathbf{k}_b \\ \boldsymbol{\omega} &= p \mathbf{i}_b + q \mathbf{j}_b + r \mathbf{k}_b \\ \dot{x} &= l_s \dot{\gamma} \cos\gamma \\ \dot{y} &= 0 \\ \dot{z} &= l_s \dot{\gamma} \sin\gamma \end{aligned} \right\} \quad (\text{eqns 2.5})$$

Substituting Equations 2.5 into Equation 2.3 gives the velocity of the hub in body axis:

$$\mathbf{v}_{hb} = \begin{bmatrix} u_a - qz_{cg} - ry_{cg}/r + (\dot{\gamma} - q)l_s \cos\gamma \\ v_a + pz_{cg} - rx_{cg} + l_s p \cos\gamma + l_s r \sin\gamma \\ w_a + py_{cg}/r + qx_{cg} + (\dot{\gamma} - q)l_s \sin\gamma \end{bmatrix} \quad (\text{eqn 2.6})$$

The following notation is now adopted for simplicity:-

$$\mathbf{v}_{hb} = \begin{bmatrix} u_{hb} \\ v_{hb} \\ w_{hb} \end{bmatrix}$$

Transforming the hub velocity into blade axis using Equation 2.2 :-

$$\mathbf{v}_{hbl} = \begin{bmatrix} -u_{hb}(\cos\psi \cos\gamma - \beta \sin\gamma) + v_{hb} \sin\psi - w_{hb}(\cos\psi \sin\gamma + \beta \cos\gamma) \\ -(u_{hb} \sin\psi \cos\gamma + v_{hb} \cos\psi + w_{hb} \sin\psi \sin\gamma) \\ -u_{hb}(\beta \cos\psi \cos\gamma + \sin\gamma) + v_{hb} \beta \sin\psi + w_{hb}(-\beta \cos\psi \sin\gamma + \cos\gamma) \end{bmatrix}$$

To obtain the velocity of a blade element at radius $r_b \mathbf{i}_{bl}$ from the hub calculated in blade axis with origin centred at the hub:-

$$\left. \begin{aligned} \mathbf{v}_a &= \mathbf{v}_{hbl} \\ \mathbf{r} &= r_b \mathbf{i}_{bl} \\ \dot{x} = \dot{y} = \dot{z} = 0 &\Rightarrow \mathbf{v}_{rel} = 0 \end{aligned} \right\} \quad (\text{eqns 2.7})$$

The angular velocity of blade axis set is given by:-

$$\omega_{bl} = \omega_1 + \omega_2 + \omega_3$$

where:-

ω_1 is the component of rotation about the body axis.

ω_2 is the component of rotation about the shaft axis.

ω_3 is the component of rotation about the blade axis.

hence:-

$$\omega_1 = p \mathbf{i}_b + (q - \dot{\gamma}) \mathbf{j}_b + r \mathbf{k}_b$$

$$\omega_2 = -\dot{\psi} \mathbf{k}_s$$

$$\omega_3 = -\dot{\beta} \mathbf{j}_{bl}$$

Transforming the body and shaft axis components into blade axis using the appropriate rotation matrices gives:-

$$\omega_1 = \begin{bmatrix} p(-\cos\psi\cos\gamma + \beta\sin\gamma) + (q - \dot{\gamma})\sin\psi - r(\cos\psi\sin\gamma + \beta\cos\gamma) \\ -p\sin\psi\cos\gamma - (q - \dot{\gamma})\cos\psi - r\sin\psi\sin\gamma \\ -p(\beta\cos\psi\cos\gamma + \sin\gamma) + (q - \dot{\gamma})\beta\sin\psi + r(-\beta\cos\psi\sin\gamma + \cos\gamma) \end{bmatrix}$$

$$\omega_2 = \begin{bmatrix} \beta\dot{\psi} \\ 0 \\ -\dot{\psi} \end{bmatrix}$$

Therefore the angular velocity of the blade axis set, in local axis, is given by:-

$$\omega_{bl} = \begin{bmatrix} p(-\cos\psi\cos\gamma + \beta\sin\gamma) + (q - \dot{\gamma})\sin\psi - r(\cos\psi\sin\gamma + \beta\cos\gamma) + \beta\dot{\psi} \\ -p\sin\psi\cos\gamma - (q - \dot{\gamma})\cos\psi - r\sin\psi\sin\gamma + \dot{\beta} \\ -p(\beta\cos\psi\cos\gamma + \sin\gamma) + (q - \dot{\gamma})\beta\sin\psi + r(-\beta\cos\psi\sin\gamma + \cos\gamma) - \dot{\psi} \end{bmatrix}$$

....(eqn 2.8)

For simplicity the following notation is now adopted:-

$$\omega_{bl} = \begin{bmatrix} \omega_x \\ \omega_y \\ \omega_z \end{bmatrix} \quad (\text{eqn 2.9})$$

Expressions 2.7 and 2.9 are now applied to Equation 2.3 and the local axis velocity of a blade element evaluated as:-

$$v_{bbl} = \begin{bmatrix} -u_{hb}(\cos\psi\cos\gamma - \beta\sin\gamma) + v_{hb}\sin\psi - w_{hb}(\cos\psi\sin\gamma + \beta\cos\gamma) \\ -(u_{hb}\sin\psi\cos\gamma + v_{hb}\cos\psi + w_{hb}\sin\psi\sin\gamma) + r_b\omega_z \\ -u_{hb}(\beta\cos\psi\cos\gamma + \sin\gamma) + v_{hb}\beta\sin\psi + w_{hb}(-\beta\cos\psi\sin\gamma + \cos\gamma) - r_b\omega_y \end{bmatrix} \quad \dots(\text{eqn 2.10})$$

For simplicity say:-

$$v_{bbl} = \begin{bmatrix} v_{bblx} \\ v_{bbly} \\ v_{bblyz} \end{bmatrix}$$

This expression defines the local axis absolute velocity of a blade element and is used in section 2.1.6 when the blade elemental aerodynamic forces are evaluated.

2.1.5 Acceleration of a Blade Element

In order to evaluate the inertial loads acting on a blade element it is first necessary to calculate the absolute acceleration of that element in local axis. It is shown in Meriam (1980) that the absolute acceleration, \mathbf{a}_p , of a point moving in a co-ordinate system with rotating axis is given by the following:-

$$\mathbf{a}_p = \mathbf{a}_a + \frac{d^2\mathbf{r}}{dt^2}$$

$$\mathbf{a}_p = \mathbf{a}_a + \mathbf{a}_{rel} + 2\boldsymbol{\omega} \times \mathbf{v}_{rel} + \boldsymbol{\omega} \times (\boldsymbol{\omega} \times \mathbf{r}) + \boldsymbol{\alpha} \times \mathbf{r} \quad (\text{eqn 2.11})$$

where:-

\mathbf{a}_a :- is the linear acceleration of the origin of the axis set.

\mathbf{r} :- is the position vector of the point in the axis set.

$\mathbf{a}_{rel} = \frac{\partial^2 \mathbf{r}}{\partial t^2}$:- is the acceleration of the point relative to the origin of the axis set.

$\mathbf{v}_{rel} = \frac{\partial \mathbf{r}}{\partial t}$:- is the velocity of the point relative to the origin of the axis set.

ω :- is the angular velocity of the reference frame.

$\alpha = \frac{\partial \omega}{\partial t}$:- is the relative angular acceleration of the origin of the axis set.

To evaluate the acceleration of a blade element in local axis it is first necessary to evaluate the absolute acceleration of two intermediate points, the pivot and the hub in body axis. To calculate the acceleration of the left and right hand pivot in body axis the following expressions are applied to Equation 2.11:-

$$\begin{aligned}\mathbf{a}_a &= \dot{u}_a \mathbf{i}_b + \dot{v}_a \mathbf{j}_b + \dot{w}_a \mathbf{k}_b \\ \mathbf{r} &= -x_{cg} \mathbf{i}_b + y_{cg1/r} \mathbf{j}_b - z_{cg} \mathbf{k}_b \\ \omega &= p \mathbf{i}_b + q \mathbf{j}_b + r \mathbf{k}_b \\ \dot{x} = \dot{y} = \dot{z} = 0 &\Rightarrow \mathbf{v}_{rel} = 0 \\ \ddot{x} = \ddot{y} = \ddot{z} = 0 &= 0 \Rightarrow \mathbf{a}_{rel} = 0 \\ \alpha &= \dot{p} \mathbf{i}_b + \dot{q} \mathbf{j}_b + \dot{r} \mathbf{k}_b\end{aligned}$$

this gives the acceleration of the pivot in body axis as:-

$$\mathbf{a}_{pb} = \begin{bmatrix} \dot{u}_a + (q^2 + r^2)x_{cg} + (pq - \dot{r})y_{cg1/r} - (rp + \dot{q})z_{cg} \\ \dot{v}_a - (p^2 + r^2)y_{cg1/r} - (pq + \dot{r})x_{cg} - (rq - \dot{p})z_{cg} \\ \dot{w}_a + (p^2 + q^2)z_{cg} - (\dot{q} - rp)x_{cg} + (rq + \dot{p})y_{cg1/r} \end{bmatrix}$$

The acceleration of the hub can now be obtained in body axis by applying the following expressions to Equation 2.11:-

$$\mathbf{a}_a = \mathbf{a}_{pb}$$

$$\mathbf{r} = l_s \sin\gamma \mathbf{i}_b - l_s \cos\gamma \mathbf{k}_b$$

$$\boldsymbol{\omega} = p \mathbf{i}_b + q \mathbf{j}_b + r \mathbf{k}_b$$

$$\mathbf{v}_{rel} = l_s \dot{\gamma} \cos\gamma \mathbf{i}_b + l_s \dot{\gamma} \sin\gamma \mathbf{k}_b$$

$$\mathbf{a}_{rel} = (l_s \ddot{\gamma} \cos\gamma - l_s \dot{\gamma}^2 \sin\gamma) \mathbf{i}_b + (l_s \ddot{\gamma} \sin\gamma + l_s \dot{\gamma}^2 \cos\gamma) \mathbf{k}_b$$

$$\boldsymbol{\alpha} = \dot{p} \mathbf{i}_b + \dot{q} \mathbf{j}_b + \dot{r} \mathbf{k}_b$$

and this gives:-

$$\begin{aligned} \mathbf{a}_{hb} = \mathbf{a}_{pb} + & \begin{bmatrix} l_s \ddot{\gamma} \cos\gamma - l_s \dot{\gamma}^2 \sin\gamma \\ 0 \\ l_s \ddot{\gamma} \sin\gamma + l_s \dot{\gamma}^2 \cos\gamma \end{bmatrix} + \begin{bmatrix} 2 q l_s \dot{\gamma} \sin\gamma \\ -2 p l_s \dot{\gamma} \sin\gamma + 2 r l_s \dot{\gamma} \cos\gamma \\ -2 q l_s \dot{\gamma} \cos\gamma \end{bmatrix} \\ & + \begin{bmatrix} -q^2 l_s \sin\gamma - p r l_s \cos\gamma - r^2 l_s \sin\gamma \\ -(-p q l_s \sin\gamma + r q l_s \cos\gamma) \\ p^2 l_s \cos\gamma + p r l_s \sin\gamma + q^2 l_s \cos\gamma \end{bmatrix} + \begin{bmatrix} -\dot{q} l_s \cos\gamma \\ \dot{p} l_s \cos\gamma + \dot{r} l_s \sin\gamma \\ -\dot{q} l_s \sin\gamma \end{bmatrix} \end{aligned}$$

Adopting the following notation for simplicity:-

$$\mathbf{a}_{hb} = \begin{bmatrix} a_{hbx} \\ a_{hb y} \\ a_{hbz} \end{bmatrix}$$

where:-

$$\begin{aligned} a_{hbx} = \dot{u}_a + (q^2 + r^2)x_{cg} + (pq - \dot{r})y_{cg|/r} - (rp + \dot{q})z_{cg} + \\ (2ql_s\dot{\gamma} - q^2l_s - rl_s - l_s\dot{\gamma}^2)\sin\gamma + (l_s\ddot{\gamma} - \dot{q}l_s - prl_s)\cos\gamma \end{aligned}$$

$$\begin{aligned} a_{hb y} = \dot{v}_a - (p^2 + r^2)y_{cg|/r} - (pq + \dot{r})x_{cg} - (rq + \dot{p})z_{cg} + \\ (pq l_s + \dot{r} l_s - 2p l_s \dot{\gamma}) \sin\gamma + (2r l_s \dot{\gamma} - r q l_s + \dot{p} l_s) \cos\gamma \end{aligned}$$

$$a_{hbz} = \dot{w}_a + (p^2 + q^2)z_{cg} + (\dot{q} - rp) x_{cg} + (rq + p) y_{cg} + (l_s \ddot{\gamma} + pr l_s - \dot{q} l_s) \sin \gamma + (l_s \dot{\gamma}^2 - 2q l_s \dot{\gamma} + p^2 l_s + q^2 l_s) \cos \gamma$$

Transforming into blade axis using Equation 2.2 gives:-

$$\mathbf{a}_{hbl} = \begin{bmatrix} -a_{hbx}(\cos \psi \cos \gamma - \beta \sin \gamma) + a_{hbz}(\cos \psi \sin \gamma + \beta \cos \gamma) \\ -(a_{hbx} \sin \psi \cos \gamma + a_{hbz} \sin \psi \sin \gamma) \\ -a_{hbx}(\beta \cos \psi \cos \gamma - \sin \gamma) + a_{hbz}(-\beta \cos \psi \sin \gamma + \cos \gamma) \end{bmatrix}$$

The following notation is again adopted for simplicity:-

$$\mathbf{a}_{hbl} = \begin{bmatrix} a_{hblx} \\ a_{hbly} \\ a_{hblz} \end{bmatrix}$$

The local axis acceleration of a blade element at radius r_b \mathbf{i}_{bl} can now be evaluated by applying the following expressions to Equation 2.11:-

$$\mathbf{a}_a = \mathbf{a}_{hbl}$$

$$\mathbf{r} = r_b \mathbf{i}_{bl}$$

$$\boldsymbol{\omega} = \omega_x \mathbf{i}_{bl} + \omega_y \mathbf{j}_{bl} + \omega_z \mathbf{k}_{bl}$$

$$\dot{x} = \dot{y} = \dot{z} = 0 \Rightarrow \mathbf{v}_{rel} = 0$$

$$\ddot{x} = \ddot{y} = \ddot{z} = 0 \Rightarrow \mathbf{a}_{rel} = 0$$

$$\boldsymbol{\alpha} = \dot{\omega}_x \mathbf{i}_{bl} + \dot{\omega}_y \mathbf{j}_{bl} + \dot{\omega}_z \mathbf{k}_{bl}$$

and this gives the acceleration of a blade element in blade axis as:-

$$\mathbf{a}_{bbl} = \begin{bmatrix} a_{hblx} - \omega_y^2 r_b - \omega_z^2 r_b \\ a_{hbly} + \omega_x \omega_y r_b + \dot{\omega}_z r_b \\ a_{hblz} + \omega_x \omega_z r_b - \dot{\omega}_y r_b \end{bmatrix} \quad (\text{eqn 2.12})$$

where:-

$$\begin{aligned} \dot{\omega}_y = & -(\dot{p} + r \dot{\gamma}) \sin \psi \cos \gamma + (p \dot{\gamma} - \dot{r}) \sin \psi \sin \gamma - p \dot{\psi} \cos \psi \cos \gamma - \\ & (\dot{q} - \dot{\gamma}) \cos \psi + \psi (q - \dot{\gamma}) \sin \psi - r \dot{\psi} \cos \psi \sin \gamma + \ddot{\beta} \end{aligned}$$

$$\begin{aligned} \dot{\omega}_z = & -(\dot{p}\dot{\beta} + \dot{p}\dot{\beta} + r\dot{\beta}\dot{\gamma})\cos\psi\cos\gamma + (q - \dot{\gamma})\beta\psi\cos\psi + (\dot{r} - p\dot{\gamma})\cos\gamma + \\ & p\beta\psi\sin\psi\cos\gamma + (p\beta\dot{\gamma} - \dot{r}\dot{\beta} - r\dot{\beta})\cos\psi\sin\gamma - (\dot{p} + r\dot{\gamma})\sin\gamma + \\ & (\dot{q}\dot{\beta} - \dot{\gamma}\dot{\beta} + q\dot{\beta} - \dot{\gamma}\dot{\beta})\sin\psi + r\beta\psi\sin\psi\sin\gamma - \ddot{\psi} \end{aligned}$$

Equation 2.12 defines the absolute acceleration of a blade element in local axis and is utilised in Section 2.19 when the elemental inertial forces are evaluated.

2.1.6 Calculation of Aerodynamic Forces

The local axis absolute velocity of a blade element is derived in Section 2.1.4 and is given by Equation 2.10 this will now be used to evaluate the aerodynamic forces acting on a blade element. The force and velocity components acting on a blade element rotating in an anti-clockwise direction when viewed from above are shown in Figure 2.4 with the corresponding diagram for a blade rotating in the opposite direction being given by Figure 2.5. With reference to these figures it can be seen that the same right hand axis set is used in both cases. Thus, for the anti-clockwise rotating blade, the y-axis points from the leading to trailing edge and the tangential component of velocity is given by:-

$$u_{tac} = -v_{bbly}$$

For the clockwise rotating blade the y-axis points from trailing to leading edge and the tangential component of velocity is now given by:-

$$u_{tc} = v_{bbly}$$

It is more convenient to define one expression which describes the the tangential velocity component of a blade element regardless of direction of rotation therefore the parameter N_{clock} is now introduced:-

$$u_t = -N_{clock} v_{bbly}$$

whereby:-

$N_{clock} = 1$ for blades rotating anti-clockwise when viewed from above.

$N_{clock} = -1$ for blades rotating clockwise when viewed from above.

For both directions of rotation the normal velocity component, u_p , is given by :-

$$u_p = v_{bbly} - w_{if} - \frac{r_b}{R} (q_{if} \cos\psi - p_{if} \sin\psi) \quad (\text{eqn 2.13})$$

Where the blade element velocity components, v_{bbl_y} and v_{bbl_z} , are expressed in local axis and are given by Equation 2.10. The uniform, longitudinal and lateral inflow components, w_{if} , q_{if} and p_{if} , are as defined in section 2.1.10.

The blade angle of attack, ϕ , is given by:-

$$\phi = \sin^{-1} \left(\frac{\psi}{\sqrt{u_t^2 + u_p^2}} \right)$$

In helicopter modelling it is appropriate to assume that $u_t \gg u_p$ and therefore the small angle approximation can be made for ϕ (Padfield 1981). As tilt-rotor vehicles operate in regimes where the inflow experienced can produce blade tip angles of attack reaching approximately 40° such a simplification cannot be made for this application.

Now the blade incidence, α , is given by:-

$$\alpha = \theta + \phi$$

$$\alpha = \theta + \sin^{-1} \left(\frac{\psi}{\sqrt{u_t^2 + u_p^2}} \right)$$

Where θ , the blade pitch angle is given by:-

$$\theta = \theta_0 + \theta_{1c} \cos\psi + \theta_{1s} \sin\psi + \theta_{tw}(r_b)$$

and:-

θ_0 , θ_{1c} , θ_{1s} are the collective, longitudinal and lateral cyclic blade pitch control inputs respectively.

$\theta_{tw}(r_b)$ is the function which defines the blade twist geometry.

The lift on a blade element is given by:-

$$l(\psi, r_b) = \frac{1}{2} \rho V^2 Ch(r_b) C_l(\alpha, r_b)$$

$$l(\psi, r_b) = \frac{1}{2} \rho (u_t^2 + u_p^2) Ch(r_b) C_l(\alpha, r_b) \quad (\text{eqn 2.14})$$

where:-

ρ is air density.

$Ch(r_b)$ is the spanwise function defining the blade chord geometry.

$C_l(\alpha)$ is the function in terms of blade incidence and spanwise location defining the elemental lift co-efficient.

The drag on a blade element is given by:-

$$d(\psi, r_b) = \frac{1}{2} \rho V^2 C_h(r_b) C_d(\alpha, r_b)$$

$$d(\psi, r_b) = \frac{1}{2} \rho (u_t^2 + u_p^2) C_h(r_b) C_d(\alpha, r_b) \quad (\text{eqn 2.15})$$

where:-

$C_d(\alpha, r_b)$ is the elemental drag co-efficient as a function of spanwise location and angle of attack.

Resolving the lift and drag forces shown in Figures 2.4 and 2.5 into blade axis, noting the requirement for N_{clock} to provide the correct resolution of lift and drag in the y_{blade} direction, gives :-

$$f_{y\text{ble}} = N_{\text{clock}} d(\psi, r_b) \cos\phi - N_{\text{clock}} l(\psi, r_b) \sin\phi \quad (\text{eqn 2.16})$$

$$f_{z\text{ble}} = -l(\psi, r_b) \cos\phi - d(\psi, r_b) \sin\phi \quad (\text{eqn 2.17})$$

Substituting Equations 2.14 and 2.15 into Equations 2.16 and 2.17 gives:-

$$f_{y\text{ble}} = \frac{1}{2} \rho (u_t^2 + u_p^2) C_h(r_b) (N_{\text{clock}} C_d(\alpha, r_b) \cos\phi - N_{\text{clock}} C_l(\alpha, r_b) \sin\phi)$$

$$f_{z\text{ble}} = \frac{1}{2} \rho (u_t^2 + u_p^2) C_h(r_b) (-C_d(\alpha, r_b) \sin\phi - C_l(\alpha, r_b) \cos\phi)$$

Integrating to give the forces acting on the whole blade:-

$$f_{y\text{bl}} = \frac{1}{2} \rho N_{\text{clock}} \int_0^R (u_t^2 + u_p^2) C_h(r_b) (C_d(\alpha, r_b) \cos\phi - C_l(\alpha, r_b) \sin\phi) dr_b$$

...(eqn 2.18)

$$f_{zbl} = \frac{1}{2} \rho \int_0^R (u_t^2 + u_p^2) Ch(r_b) (-C_d(\alpha, r_b) \sin\phi - C_l(\alpha, r_b) \cos\phi) dr_b$$

...(eqn 2.19)

2.1.7 Evaluation of Rotor Thrust

Rotor thrust is the force generated in the opposite direction to the shaft z-axis and, as discussed in section 2.1.1, is of importance when evaluating the velocity of the air induced through the rotor. To obtain the thrust produced by a blade it is necessary to resolve the forces given by Equations 2.18 and 2.19 into shaft axis, thus, using the appropriate transformation matrix:-

$$\begin{bmatrix} f_{xs} \\ f_{ys} \\ f_{zs} \end{bmatrix} = \begin{bmatrix} -\cos\psi & -\sin\psi & 0 \\ \sin\psi & -\cos\psi & 0 \\ 0 & 0 & 1 \end{bmatrix} \begin{bmatrix} 1 & 0 & \beta \\ 0 & 1 & 0 \\ -\beta & 0 & 1 \end{bmatrix} \begin{bmatrix} f_{xbl} \\ f_{ybl} \\ f_{zbl} \end{bmatrix}$$

The thrust generated by an individual blade is given by:-

$$T_{bl} = -f_{zs} = -f_{zbl} + \beta f_{xbl}$$

Where f_{xbl} is the spanwise aerodynamic force acting on the blade and, as 2-dimensional aerodynamics are utilised, :-

$$f_{xbl} = 0$$

therefore:-

$$T_{bl} = -f_{zs}$$

Overall rotor thrust is obtained by summing the individual contributions of each blade:-

$$\text{Overall rotor thrust, } T_R = \sum_{i=1}^n -f_{zsi}$$

2.1.8 Rotor Forces and Moments in Body Axis

The main purpose of the rotor model is to evaluate the rotor forces and moments in body axis as these can then be input into the overall vehicle equations of motion.

The blade forces are transformed from local to body axis by applying the appropriate rotation matrix to Equations 2.18 and 2.19, the body axis blade forces are then found to be:-

$$\begin{aligned} f_{xb} &= (-f_{ybl} \sin\psi - f_{zbl} \beta \cos\psi) \cos\gamma - f_{zbl} \sin\gamma \\ f_{yb} &= -f_{ybl} \cos\psi + f_{zbl} \beta \sin\psi \\ f_{zb} &= (-f_{ybl} \sin\psi - f_{zbl} \beta \cos\psi) \sin\gamma + f_{zbl} \cos\gamma \end{aligned}$$

The force components generated by each individual blade are now summed to give the overall rotor forces in body axis:-

$$\begin{aligned} X_{R/LR} &= \sum_{i=1}^n ((-f_{ybl_i} \sin\psi_i - f_{zbl_i} \beta_i \cos\psi_i) \cos\gamma_i - f_{zbl_i} \sin\gamma_i)_{L/R} \\ Y_{R/LR} &= \sum_{i=1}^n (-f_{ybl_i} \cos\psi_i + f_{zbl_i} \beta_i \sin\psi_i)_{L/R} \\ Z_{R/LR} &= \sum_{i=1}^n ((-f_{ybl_i} \sin\psi_i - f_{zbl_i} \beta_i \cos\psi_i) \sin\gamma_i + f_{zbl_i} \cos\gamma_i)_{L/R} \end{aligned}$$

Rotor moments acting on the hub are generated as a result of two factors, firstly blade flapping behaviour and, secondly, blade forces acting in the y_{shaft} direction.

Blade flapping causes rolling and pitching moments to be exerted on the rotor hub as the blade advances round the azimuth . A pictorial representation of the centre spring equivalent blade model is given in Figure 2.2 and it can be seen that the flapping moment exerted by an individual blade on the hub is given by the following (in shaft axis):-

$$f_{m_s} = K_b \beta j_s$$

This is transformed into body axis by use of the appropriate rotation matrices giving:-

$$f_{m_b} = \begin{bmatrix} -K_b \beta \sin\psi \cos\gamma \\ -K_b \beta \cos\psi \\ -K_b \beta \sin\psi \cos\gamma \end{bmatrix} \quad (\text{eqn 2.20})$$

The blade forces acting in a direction parallel to the y_{shaft} axis generate a yawing moment at the rotor hub. As the transformation from blade to shaft axis is performed by a rotation about the y_{shaft} axis then:-

$$f_{ys} = f_{ybl}$$

This force consists of aerodynamic, inertial and internal components, with the aerodynamic contribution being as given in Equation 2.18, therefore, for a blade element:-

$$f_{yble} = d(\psi, r_b) \cos \phi - l(\psi, r_b) \sin \phi - m a_{bbly} + \text{internal forces}$$

The blade axis y-component of acceleration, a_{bbly} , is given in Equation 2.12 as:-

$$a_{bbly} = a_{hbly} + \omega_x \omega_y r_b + \dot{\omega}_z r_b$$

and, assuming that the rotor angular acceleration is responsible for the major contribution to the inertial force component, the blade elemental force parallel to the y_{shaft} axis becomes:-

$$f_{yble} = d(\psi, r_b) \cos \phi - l(\psi, r_b) \sin \phi - m \ddot{\psi} r_b + \text{internal forces}$$

Noting that the internal forces, when integrated over the span, equate to zero the yawing moment produced by an individual blade becomes:-

$$N_s = \int_0^{r_b} r_b (d(\psi, r_b) \cos \phi - l(\psi, r_b) \sin \phi) dr_b + \int_0^{r_b} m \ddot{\psi} r_b^2 dr_b$$

Further noting that rotational moment of inertia, I_r , is given by:-

$$I_r = \int_0^{r_b} m r_b^2 dr_b$$

the yawing moment produced by an individual blade is given by:-

$$N_s = \frac{1}{2} \rho \int_0^R r_b (u_t^2 + u_p^2) Ch(r_b) (C_d(\alpha, r_b) \cos \phi - C_l(\alpha, r_b) \sin \phi) dr_b + I_r \ddot{\psi}$$

The overall rotor yawing moment in shaft axis is therefore:-

$$N_{Rs} = \frac{1}{2}\rho \sum_{i=1}^n \left(\int_0^R r_b (u_t^2 + u_p^2) Ch(r_b) (C_d(\alpha, r_b) \cos\phi - C_l(\alpha, r_b) \sin\phi) dr_b + I_r \dot{\psi} \right)_i$$

Transforming into body axis by pre-multiplication of the appropriate rotation matrix gives:-

$$N_{Rb} = \begin{bmatrix} -N_{Rs} \sin\gamma \\ 0 \\ N_{Rs} \cos\gamma \end{bmatrix} \quad (\text{eqn 2.21})$$

The body axis moments generated by the rotor acting on the hub are obtained by summing Equations 2.20 and 2.21 to give:-

$$L_{L/RRH} = -K_B \beta \sin\psi \cos\gamma - N_{Rs} \sin\gamma$$

$$M_{L/RRH} = -K_B \beta \cos\psi$$

$$N_{L/RRH} = -K_B \beta \sin\psi \sin\gamma + N_{Rs} \cos\gamma$$

The body axis moment generated by the left or right hand rotor and acting on the corresponding pivot is now given by:-

$$\begin{bmatrix} L_{L/RRP} \\ M_{L/RRP} \\ N_{L/RRP} \end{bmatrix} = \begin{bmatrix} L_{L/RRH} \\ M_{L/RRH} \\ N_{L/RRH} \end{bmatrix} + \begin{vmatrix} \mathbf{i}_b & \mathbf{j}_b & \mathbf{k}_b \\ I_s \sin\gamma & 0 & I_s \cos\gamma \\ X_{L/RR} & Y_{L/RR} & Z_{L/RR} \end{vmatrix}$$

The overall body axis moment generated by the left or right rotor and acting on the vehicle centre of gravity can now be evaluated by the following:-

$$\begin{bmatrix} L_{L/RR} \\ M_{L/RR} \\ N_{L/RR} \end{bmatrix} = \begin{bmatrix} L_{L/RRP} \\ M_{L/RRP} \\ N_{L/RRP} \end{bmatrix} + \begin{vmatrix} \mathbf{i}_b & \mathbf{j}_b & \mathbf{k}_b \\ x_{cg} & y_{cg|/r} & z_{cg} \\ X_{L/RR} & Y_{L/RR} & Z_{L/RR} \end{vmatrix}$$

As the nacelles are transitioned, a pitching moment is generated at the pivot in reaction to the accelerating torque acting on the nacelle, it is convenient to include this effect at this stage. The pitching moment generated at the pivot during a transition of the nacelle is given by:-

$$\mathbf{M}_{trans} = \ddot{\gamma} I_{YY_{nac}} \mathbf{j}_b$$

The body axis moment generated by the rotors acting at the vehicle centre of gravity is now given by:-

$$\begin{bmatrix} L_{L/RR} \\ M_{L/RR} \\ N_{L/RR} \end{bmatrix} = \begin{bmatrix} L_{L/RRP} + Z_{L/RR} y_{cgl/r} - Y_{L/RR} z_{cg} \\ M_{L/RRP} + X_{L/RR} z_{cg} - Z_{L/RR} x_{cg} + \dot{\gamma}_{l/r} I_{YY_{nac}} \\ N_{L/RRP} + Y_{L/RR} x_{cg} - X_{L/RR} y_{cgl/r} \end{bmatrix}$$

2.1.9 Blade Flapping

As stated in section 2.1.1 blade flapping motion is of significant importance when modelling the behaviour of a rotor. In this model the flapping behaviour is described by a second order differential equation whose derivation is based on the blade element shown in Figure 2.6, as can be seen, this element has the following forces acting on it:

w = weight per unit length ≈ 0

f = aerodynamic force per unit length

f_{int} = internal reactions from neighbouring elements

If:-

$$f_{int} = - \frac{dF_{int}}{dr_b}$$

Then:-

$$m_{a_{bb1}} = f - \frac{dF_{int}}{dr_b}$$

Integrating along the span:-

$$\int_0^R m_{a_{bb1}} dr_b = \int_0^R f dr_b - \int_0^R \frac{dF_{int}}{dr_b} dr_b$$

Taking moments about the hub:-

$$\int_0^R r_b i_{b1} \times m_{a_{bb1}} dr_b = \int_0^R r_b i_{b1} \times f dr_b - \int_0^R r_b i_{b1} \times \frac{dF_{int}}{dr_b} dr_b + M$$

where M is the moment applied by the hub on the blade.

Now:-

$$r_b \mathbf{i}_b \times m \mathbf{a}_{bb1} = \begin{bmatrix} 0 \\ -r_b m a_{bb1z} \\ r_b m a_{bb1y} \end{bmatrix}$$

where the acceleration vector of the blade element, \mathbf{a}_{bb1} , is derived in section 2.1.5 and is given by Equation 2.12, therefore:-

$$r_b \mathbf{i}_b \times m \mathbf{a}_{bb1} = \begin{bmatrix} 0 \\ m(-a_{hblz} r_b - \omega_x \omega_z r_b^2 + \dot{\omega}_y r_b^2) \\ m(a_{hbly} r_b + \omega_x \omega_y r_b^2 + \dot{\omega}_z r_b^2) \end{bmatrix}$$

Noting that:-

$$\int_0^R m r_b^2 dr_b = I_b$$

$$\int_0^R m r_b dr_b = M \bar{r}_b$$

where:-

I_b is the blade moment of inertia.

M is the total mass of the blade.

\bar{r}_b is the distance from the hub to the blade centre of mass.

gives:-

$$\begin{bmatrix} 0 \\ \int_0^R m(-a_{hblz} r_b - \omega_x \omega_z r_b^2 + \dot{\omega}_y r_b^2) dr_b \\ 0 \\ \int_0^R m(a_{hbly} r_b + \omega_x \omega_y r_b^2 + \dot{\omega}_z r_b^2) dr_b \\ 0 \end{bmatrix} = \begin{bmatrix} 0 \\ -a_{hblz} M \bar{r}_b - I_b(-\omega_x \omega_z + \dot{\omega}_y) \\ 0 \\ a_{hbly} M \bar{r}_b + I_b(\omega_x \omega_y + \dot{\omega}_z) \\ 0 \end{bmatrix}$$

...(eqn 2.22)

$$\Rightarrow \int_0^R r_b \mathbf{i}_b \times m \mathbf{a}_{bb} dr_b = \begin{bmatrix} 0 \\ a_{hb} I_b M \bar{r}_b - I_b (-\omega_x \omega_z + \omega_y) \\ a_{hb} I_b M \bar{r}_b + I_b (\omega_x \omega_y + \omega_z) \end{bmatrix}$$

Now for the moment acting on the blade due to the aerodynamic forces:-

$$r_b \mathbf{i}_b \times \mathbf{f} = \begin{bmatrix} 0 \\ -r_b f_{zble} \\ r_b f_{yble} \end{bmatrix}$$

The aerodynamic forces acting on the blade element are derived in section 2.1.6 and are described by Equations 2.16 and 2.17, therefore, the corresponding aerodynamic moments acting on the blade element are given by:-

$$r_b \mathbf{i}_b \times \mathbf{f} =$$

$$\begin{bmatrix} 0 \\ -r_b \frac{1}{2} \rho (u_t^2 + u_p^2) Ch(r_b) (N_{clock} C_d(\alpha, r_b) \cos \phi - N_{clock} C_l(\alpha, r_b) \sin \phi) \\ r_b \frac{1}{2} \rho (u_t^2 + u_p^2) Ch(r_b) (-C_d(\alpha, r_b) \sin \phi - C_l(\alpha, r_b) \cos \phi) \end{bmatrix}$$

Integrating along the span to give the total aerodynamic moment acting on the blade:-

$$\int_0^R r_b \mathbf{i}_b \times \mathbf{f} dr_b =$$

$$\begin{bmatrix} 0 \\ \int_0^R -r_b \frac{1}{2} \rho (u_t^2 + u_p^2) Ch(r_b) (N_{clock} C_d(\alpha, r_b) \cos \phi - N_{clock} C_l(\alpha, r_b) \sin \phi) dr_b \\ \int_0^R r_b \frac{1}{2} \rho (u_t^2 + u_p^2) Ch(r_b) (-C_d(\alpha, r_b) \sin \phi - C_l(\alpha, r_b) \cos \phi) dr_b \end{bmatrix}$$

For future convenience the aerodynamic moments acting on the blade are denoted by the following notation:-

$$\int_0^R r_b \mathbf{i}_b \times \mathbf{f} dr_b = \begin{bmatrix} L_{ab} \\ M_{ab} \\ N_{ab} \end{bmatrix}$$

Where L_{ab} , M_{ab} and N_{ab} represent the aerodynamic rolling, pitching and yawing moments acting on the blade respectively and are expressed in the local axis set.

For the moment acting on the blade due to the internal forces:-

$$-\int_0^R r_b \mathbf{i}_b \times \frac{d\mathbf{F}_{int}}{dr_b} dr_b = -[\mathbf{i}_b \times \mathbf{F}_{int}]_0^R + \int_0^R \mathbf{i}_b \times \mathbf{F}_{int} dr_b$$

At the blade root $r_b = 0$ and, for a free tip, $\mathbf{F}_{int} = 0$ at $r_b = R$, therefore:-

$$[\mathbf{i}_b \times \mathbf{F}_{int}]_0^R = 0$$

Also, the internal forces when integrated across the span, equate to zero:-

$$\int_0^R \mathbf{i}_b \times \mathbf{F}_{int} dr_b = 0$$

Thus:-

$$\int_0^R r_b \mathbf{i}_b \times \frac{d\mathbf{F}_{int}}{dr_b} dr_b = 0$$

For the centre sprung blade element shown in Figure 2.2 the moment, \mathbf{M} , applied by the hub on the blade is given by:-

$$\mathbf{M} = \begin{bmatrix} 0 \\ K_b \beta \\ 0 \end{bmatrix}$$

Therefore, Equation 2.22 becomes:-

$$\begin{bmatrix} 0 \\ -ahblyM\bar{r}_b - I_b f(-\omega_x \omega_z + \omega_y) \\ ahblz M\bar{r}_b + I_b l(\omega_x \omega_y + \omega_z) \end{bmatrix} = \begin{bmatrix} L_{ab} \\ M_{ab} + K_b \beta \\ N_{ab} \end{bmatrix}$$

where:-

\mathbf{i}_b terms form an expression describing blade torsional behaviour.

\mathbf{j}_b terms form an expression describing blade flapping behaviour.

\mathbf{k}_b terms form an expression describing blade lead/lag behaviour.

Therefore, the expression describing blade flapping behaviour is now given by:-

$$-a_{hblz}M\bar{r}_b - I_b(-\omega_x\omega_z + \dot{\omega}_y) = M_{ab} + K_B\beta$$

In order to reformulate this expression in terms of the blade flap states the following notation is introduced:-

$$a_{hblz} = a_{hblzc} + a_{hblz\beta} \beta$$

$$\omega_x = \omega_{xc} + \omega_{x\beta} \beta$$

$$\omega_z = \omega_{zc} + \omega_{z\beta} \beta$$

$$\dot{\omega}_y = \dot{\omega}_{yc} + \ddot{\beta}$$

where:-

$$a_{hblzc} = \frac{M\bar{r}_b}{I_b} [-a_{hbxc}\sin\gamma + a_{hbzc}\cos\gamma]$$

$$a_{hblz\beta} = \frac{M\bar{r}_b}{I_b} [-a_{hbxc}\cos\psi\cos\gamma + a_{hbys}\sin\psi - a_{hbzc}\cos\psi\sin\gamma]$$

$$\omega_{xc} = -p\cos\psi\cos\gamma + (q - \dot{\gamma})\sin\psi - r\cos\psi\sin\gamma$$

$$\omega_{x\beta} = p\sin\gamma - r\cos\gamma + \dot{\psi}$$

$$\omega_{zc} = -p\sin\gamma + r\cos\gamma - \dot{\psi}$$

$$\omega_{z\beta} = -p\cos\psi\cos\gamma + (q - \dot{\gamma})\sin\psi - r\cos\psi\sin\gamma$$

$$\begin{aligned} \dot{\omega}_{yc} = & -(p + r\dot{\gamma})\sin\psi\cos\gamma + (p\dot{\gamma} - \dot{r})\sin\psi\sin\gamma - \\ & p\dot{\psi}\cos\psi\cos\gamma - (\dot{q} - \ddot{\gamma})\cos\psi + \dot{\psi}(q - \dot{\gamma})\sin\psi - \\ & r\dot{\psi}\cos\psi\sin\gamma \end{aligned}$$

Giving a flapping equation of:-

$$\begin{aligned} \ddot{\beta} - \omega_{x\beta} \omega_{z\beta} \beta^2 - \left(\omega_{z\beta} \omega_{xc} + \omega_{zc} \omega_{x\beta} + a_{hblz\beta} - \frac{K_B}{I_b} \right) \beta \\ = \left(\omega_{zc} \omega_{xc} + a_{hblzc} - \dot{\omega}_{yc} \right) + M_{ab} \quad (\text{eqn 2.23}) \end{aligned}$$

This expression is integrated using the fourth order Runge-Kutta scheme described in Appendix 1 to give the blade flap states at each time step.

2.1.10 Inflow Modelling

As stated in Section 2.1.1 both the Glauert and Peters-HaQuang inflow models have been incorporated as part of GTILT and these shall now be described.

2.1.10a The Glauert Model

This model is based on momentum theory and assumes a uniformly loaded rotor with harmonic contributions superimposed to portray lateral and longitudinal variations in the induced velocity. The Glauert model takes the form:-

$$v_{if} = w_{if} + \frac{T_R}{R}(q_{if}\cos\psi + p_{if}\sin\psi)$$

where the uniform component normal to the rotor disc is given by:-

$$w_{if} = \frac{T_R}{2\rho\pi R^2\sqrt{(u_{hs}^2 + v_{hs}^2 + (w_{hs} - w_{if})^2)}} \quad (\text{eqn 2.24})$$

The rotor disc experiences an upwash at the leading edge and a downwash at the trailing edge in a similar manner to a wing producing lift (Bramwell 1976) and the longitudinal harmonic component of induced flow, q_{ifw} , is included in an attempt to model this effect. The evaluation of this component is most conveniently carried out in a hub wind axis set where the x-axis is aligned parallel to the resultant velocity vector of the rotor hub. As shown in Figure 2.7 the orientation of this axis set is obtained by a rotation about the z_{shaft} axis through the hub sideslip angle, ψ_w . Therefore:-

$$\begin{aligned} q_{if} &= q_{ifw}\cos\psi_w - p_{ifw}\sin\psi_w \\ p_{if} &= q_{ifw}\sin\psi_w + p_{ifw}\cos\psi_w \end{aligned}$$

where the rotor sideslip angle ψ_w is given by:-

$$\psi_w = \tan^{-1}\left(\frac{v_{hs}}{u_{hs}}\right)$$

It is stated in Bramwell (1976) that the slope of the ratio v_{if}/w_{if} is a function of the wake angle, χ , and is equal to $\tan(\chi/2)$ at the rotor centre; the wind axis longitudinal harmonic induced flow component can therefore be written as:-

$$\begin{aligned} q_{ifw} &= w_{if} \tan\left(\frac{\chi}{2}\right) & \left(\chi < \frac{\pi}{2}\right) \\ q_{ifw} &= w_{if} \cot\left(\frac{\chi}{2}\right) & \left(\chi > \frac{\pi}{2}\right) \end{aligned}$$

where the rotor wake angle, χ , is shown in Figure 2.8 and is given by:-

$$\tan\chi = \frac{\sqrt{u_{hs}^2 + v_{hs}^2}}{w_{if} - w_{hs}}$$

By transforming into hub-wind axis the lateral velocity component experienced by the rotor disc tends to zero and consequently the wind axis lateral harmonic downwash component is also zero:-

$$p_{ifw} = 0$$

The uniform component of induced flow is directly related to the rotor thrust through Equation 2.24 and consequently, the normal component of induced flow and rotor thrust are closely coupled. Also, from Equation 2.13, it can be seen that the induced velocity strongly influences the magnitude of the normal velocity component acting on the rotor disc and consequently has a significant effect on the individual blade forces and moments. It is therefore evident that the induced flow through the rotor will play a significant role in the amount of thrust produced by that rotor and also the level of flapping behaviour exhibited by its blades. As these parameters are closely coupled and many of the expressions involved are non-linear, it is most convenient to perform their evaluation iteratively using the following scheme:-

$$w_{ifj+1} = w_{ifj} - \frac{f(w_{ifj})}{f'(w_{ifj})}$$

where $f(w_{ifj})$ is approximated numerically by the following:-

$$f'(w_{ifj}) = \frac{f(w_{ifj} + h) - f(w_{ifj})}{h}$$

and the iteration function is given by :-

$$f(w_{ifj}) = 2\rho\pi R^2 w_{if} \sqrt{(u_{hs}^2 + v_{hs}^2 + (w_{hs}^2 - w_{if}^2))} - T_R$$

The solution algorithm for the above iteration scheme is depicted in Figure 2.9.

The Glauert model has been in existence for some time and is rudimentary in nature but is still attractive to rotorcraft simulationists (Thomson 1992 and Padfield 1981) due to its ease of use. However, as discussed in Section 2.1.1, this model contains two notable inadequacies which adversely effect its performance. Firstly, it is assumed that the mass of air flowing through the rotor can be accelerated instantaneously in response to a change in flight condition or control perturbation and,

secondly, the effects of rotor pitching and rolling moments are neglected. A further deficiency is the necessity for the iteration loop when evaluating blade flap, rotor thrust and inflow. As the expressions involved are evaluated numerically they are computationally intensive and therefore the repeated evaluation of these parameters greatly increases computational run-time. These limitations are generally accepted and since the 1950's a considerable amount of research has been devoted to induced flow modelling in an attempt to improve fidelity and reduce its computational burden; this work is summarised by Chen (1990).

Perhaps the most comprehensive methodology for modelling rotor induced flow is that of free-wake analysis and this has been incorporated in the CAMRAD model (Johnson 1980b). However, free-wake modelling is numerically intensive and therefore requires a considerable amount of computational effort which makes such techniques impractical for flight mechanics studies and real-time simulation purposes. For such applications a finite state, non-uniform induced flow model similar to that of Glauert is most suitable because this can be implemented with realisable levels of computational effort and produces results which are more easy to interpret than those yielded by a free-wake approach (Chen 1990).

In an effort to produce such a model Curtiss and Shupe (1971) expanded the Glauert model by adopting a perturbational approach using momentum theory to include the effects of rotor pitching and rolling moments on the induced flow. Pitt and Peters (1981), using actuator disc theory, further extended the Glauert model to include a dynamic lag associated with the acceleration of a mass of air through the rotor following a change in flight state or perturbation in control. This work produced a three state first order differential equation to describe the behaviour of the induced flow and included the previously described elements which are missing from the original Glauert model. This dynamic inflow model is quoted by Gaonkar and Peters (1988) in the following form:-

$$[M] \begin{bmatrix} \dot{\lambda}_{0w} \\ \dot{\lambda}_{1sw} \\ \dot{\lambda}_{1cw} \end{bmatrix} + [L]^{-1} \begin{bmatrix} \lambda_{0w} \\ \lambda_{1sw} \\ \lambda_{1cw} \end{bmatrix} = \begin{bmatrix} \delta C_{Tw} \\ \delta C_{lw} \\ \delta C_{Mw} \end{bmatrix}_{\text{aerodynamic}} \quad (\text{eqn 2.25})$$

where $[M]$ is the apparent mass matrix which associates a dynamic lag with the response of the inflow states following a control displacement or change in flight condition. $[L]$ is the gains matrix which relates the induced flow components to the aerodynamic rotor thrust, rolling and pitching moment coefficients.

The dynamic gains matrix included in Equation 2.25 is developed directly from perturbational analysis and consequently it is necessary to utilise perturbed thrust and moment co-efficients when using this model. For the purposes of flight mechanics simulation it is often more convenient to use total values for these coefficients (Chen and Hindson 1987) and a non-linear version of Equation 2.25 is therefore more suitable for such applications. A model of this type is described by Peters and HaQuang (1988) and has been adapted and incorporated into GTILT.

2.1.10b The Peters - HaQuang Model

This model is based on an equation of a similar form to that quoted in Equation 2.25:-

$$[M] \begin{bmatrix} \dot{\lambda}_{0w} \\ \dot{\lambda}_{1sw} \\ \dot{\lambda}_{1cw} \end{bmatrix} + [L]_{nl}^{-1} \begin{bmatrix} \lambda_0 \\ \lambda_{1sw} \\ \lambda_{1cw} \end{bmatrix} = \begin{bmatrix} C_{T_w} \\ -C_{l_w} \\ -C_{M_w} \end{bmatrix}_{\text{aerodynamic}} \quad (\text{eqn 2.26})$$

where the matrix $[L]_{nl}$ is the non-linear version of the dynamic gains matrix and the rotor thrust and moment coefficients are the total rather than perturbed values.

As can be seen Equation 2.26 is quoted in a non-dimensional form, GTILT utilises dimensional parameters throughout, therefore, Equation 2.26 should be stated in dimensional form:-

$$[M]_d \begin{bmatrix} \dot{w}_{ifw} \\ \dot{q}_{ifw} \\ \dot{p}_{ifw} \end{bmatrix} + [L]_{dnl}^{-1} \begin{bmatrix} w_{ifw} \\ q_{ifw} \\ p_{ifw} \end{bmatrix} = \begin{bmatrix} T_w \\ l_w \\ M_w \end{bmatrix}_{\text{aerodynamic}} \quad (\text{eqn 2.27})$$

where, for twisted blades, the apparent mass matrix, $[M]_d$, is given by:-

$$[M]_d = \begin{bmatrix} \rho R^3 & 0 & 0 \\ 0 & \rho R^4 & 0 \\ 0 & 0 & \rho R^4 \end{bmatrix} \begin{bmatrix} \frac{128}{75} & 0 & 0 \\ 0 & -\frac{16}{45} & 0 \\ 0 & 0 & -\frac{16}{45} \end{bmatrix}$$

and the dynamic gains matrix $[L]_{dnl}$ is given by:-

$$[L]_{dnl} = [L][V]^{-1}$$

where:-

$$[L] = \begin{bmatrix} \frac{1}{2} & 0 & \frac{15\pi}{64} \left(\frac{1 - \sin\chi}{1 + \sin\chi} \right)^{\frac{1}{2}} \\ 0 & \frac{-4}{1 + \sin\chi} & 0 \\ \frac{15\pi}{64} \left(\frac{1 - \sin\chi}{1 + \sin\chi} \right)^{\frac{1}{2}} & 0 & \frac{-4\sin\chi}{(1 + \sin\chi)} \end{bmatrix} \begin{bmatrix} \frac{1}{\rho\pi R^2} & 0 & 0 \\ 0 & \frac{1}{\rho\pi R^3} & 0 \\ 0 & 0 & \frac{1}{\rho\pi R^3} \end{bmatrix}$$

In this case the wake angle, χ , is complimentary to that of the Glauert model and is defined as:-

$$\tan\chi = \frac{w_{hs} - w_{ifm}}{\sqrt{(u_{hs}^2 + w_{hs}^2)}}$$

Where w_{ifm} is the momentum theory normal induced flow resulting from the rotor thrust. The mass flow parameter matrix, $[V]$, is given by:-

$$[V] = \begin{bmatrix} V_T & 0 & 0 \\ 0 & V_M & 0 \\ 0 & 0 & V_M \end{bmatrix}$$

Where V_T is the total resultant flow through the rotor disc:-

$$V_T = \sqrt{u_{hs}^2 + v_{hs}^2 + (w_{hs} - w_{if})^2}$$

The mass flow parameter, V_M , can be interpreted as a weighted velocity component (Gaonkar and Peters 1988) and is given by:-

$$V_M = \frac{d(V_T \cdot w_{ifm})}{dw_{ifm}} = \frac{u_{hs}^2 + v_{hs}^2 + (w_{hs} - 2w_{ifm})(w_{hs} - w_{ifm})}{V_T}$$

It is more convenient to evaluate the rotor forces and moments in hub axis, therefore transforming from wind to hub axis:-

$$\begin{bmatrix} T_w \\ -L_w \\ -M_w \end{bmatrix} = [T] \begin{bmatrix} T_h \\ -L_h \\ -M_h \end{bmatrix}$$

$$\begin{bmatrix} w_{ifw} \\ q_{ifw} \\ p_{ifw} \end{bmatrix} = [T] \begin{bmatrix} w_{ifh} \\ q_{ifh} \\ p_{ifh} \end{bmatrix}$$

where the rotation matrix, [T], is given by:-

$$[T] = \begin{bmatrix} 1 & 0 & 0 \\ 0 & \cos\psi_w & \sin\psi_w \\ 0 & -\sin\psi_w & \cos\psi_w \end{bmatrix}$$

Therefore, in hub axis, Equation 2.27 becomes:-

$$[M] \begin{bmatrix} \dot{w}_{ifh} \\ \dot{q}_{ifh} \\ \dot{p}_{ifh} \end{bmatrix} + [L]_{hnl}^{-1} \begin{bmatrix} w_{ifh} \\ q_{ifh} \\ p_{ifh} \end{bmatrix} = \begin{bmatrix} T_h \\ L_h \\ M_h \end{bmatrix}_{\text{aerodynamic}} \quad (\text{eqn 2.28})$$

where:-

$$[L]_{hnl}^{-1} = [V] [T]^T [L]^{-1} [T]$$

$$[L]_{hnl}^{-1} = [V] [\tilde{L}]$$

The components of $[\tilde{L}]$ have been evaluated using the symbolic algebraic manipulation package, Mathematica, and are as given in Appendix 2.

The normal induced flow component resulting from the rotor thrust, w_{ifm} , can now be defined in terms of the first row of the matrix $[\tilde{L}]$:-

$$w_{ifm} = \frac{1}{2\rho\pi R^2} \begin{bmatrix} 1 \\ 0 \\ 0 \end{bmatrix}^T [\tilde{L}] \begin{bmatrix} w_{ifh} \\ q_{ifh} \\ p_{ifh} \end{bmatrix}$$

Equation 2.28 is integrated using the fourth order Runge-Kutta scheme described in Appendix 1 to give the induced flow at each time step.

2.1.11 Validation of the Rotor Model

As the model developed in the preceding sections of this chapter is novel it was important to ensure its validity at an early stage. In order to do this, the rotor model was configured using Westland Lynx data and the predicted blade flap, forces, moments and inflow produced for a range of flight conditions and control displacements verified against those of an established rotorcraft model, Helistab (Padfield 1981). The levels of agreement obtained were extremely encouraging and are documented by McVicar and Bradley (1990).

2.2 Vehicle Aerodynamics

As stated at the beginning of this chapter it is most convenient to consider the constituent parts of the vehicle separately when evaluating the aerodynamic forces and moments acting on the airframe. The vehicle has therefore been broken down into the following components:-

1. Wing and Nacelles
2. Horizontal Stabiliser
3. Vertical Fins
4. Fuselage

Where the aerodynamic characteristics of each are defined by a set of force and moment coefficients generally obtained from wind-tunnel tests. A detailed description of the technique used to evaluate the aerodynamic forces and moments in this manner is given in Appendix 3. With reference to this appendix it can be seen that the local dynamic pressure, angle of attack and sideslip angle must be accurately evaluated if a good prediction of the aerodynamic forces and moments is to be obtained. When calculating these parameters it is important to consider the effects of rotor wake impingement as this influences the local velocity vectors acting on the vehicle airframe.

Analytic modelling of the total vehicle flowfield perhaps represents the most accurate method of including the effects of rotor wake impingement on the vehicle airframe (Clark 1985, Clark and McVeigh 1985, Lesching and Wagner 1990). However, the level of complexity inherent in such models promotes the requirement for levels of computational effort which currently precludes them from use in flight mechanics studies. Additionally, these analytic models produce detailed information about the vehicle flowfield which may not be of direct concern when used as part of a flight mechanics model. In this case, the forces and moments acting on the airframe are of greater interest as it is these which directly influence the vehicle's handling qualities. Therefore it was felt that the complexity inherent in analytically modelling the vehicle flowfield was outwith the scope of the current research and another more suitable methodology should be sought.

McVeigh et al (1988) demonstrate that the nature of rotor/airframe interaction experienced by tilt-rotor aircraft is strongly dependent upon nacelle incidence and airspeed, these authors summarise rotor/airframe interactions occurring in the three primary flight modes as follows:-

1. Low speed flight in helicopter mode where a large portion of the wing is impinged upon by the rotor flowfield and consequently a download is experienced. In this flight mode the empennage is unaffected.
2. Transitional flight, depending on airspeed and nacelle incidence, sections of the wing and empennage are immersed in the rotor wake and therefore the forces and moments acting on these components are affected.
3. Cruising flight in aeroplane mode where a large section of the wing lies within the rotor slipstream and thus the performance of the wing is altered from that experienced in the freestream.

In GTILT the aerodynamic forces and moments acting on the wing/nacelles, horizontal stabiliser, vertical fins and fuselage are considered separately, therefore, it is possible to evaluate the influence of the rotor wake on these components independently. From the description of rotor wake impingement given by McVeigh et al (1988) it is evident that the components primarily influenced by the rotor flowfield are the empennage, wing and nacelles; the methodology used to model impingement on these components will now be discussed.

2.2.1 Modelling of Wake Impingement on Vehicle Empennage

After conducting wind-tunnel tests using a 1/5th scale tilt-rotor model Marr and Sambell (1973) have shown that rotor wake impingement on the vehicle empennage could best be modelled by adding equivalent induced velocity components to the freestream velocity of the horizontal stabiliser and vertical fins. The results obtained from these tests fall naturally into two categories, longitudinal flight and sideslipping flight, and are discussed in detail by Marr and Sambell (1973) and Marr and Roderick (1974). The salient observations can be summarised in the following manner.

In longitudinal flight it was found that impingement on the horizontal surfaces is best described by an equivalent induced velocity which takes the form of an upwash throughout the range of airspeeds and nacelle incidences researched. The upwash distribution obtained by Marr and Sambell (1973) is given in Table A4.17. When this effect is included, the local axis z-component of velocity at the horizontal stabiliser centre of pressure is given by:-

$$w_{hsif} = w_{hswd} + w_{ifhs}$$

where the induced upwash component, w_{ihs} , is obtained from wind-tunnel testing and the z-component of velocity of the horizontal stabiliser centre of pressure, w_{hswd} , is defined at the end of this section.

In sideslipping flight the horizontal stabiliser experiences a reduction in rotor induced upwash to that encountered in the corresponding longitudinal case, also, an asymmetric upwash distribution is now evident across the span. The combined effect is therefore the generation of pitch up and rolling moments about the vehicle C.G. The asymmetry of the wake impingement further influences the moments generated by the empennage through the response of the vertical fins. In helicopter mode the rotor wake was found to have a destabilising effect at yaw angles of less than 12 degrees, however, at higher incidences the wake was found to increase the fin effectiveness and thus increases the yaw stability. Assymmetric wake impingement is not however currently modelled in GTILT and it is felt that this should form an item of future work.

The horizontal stabiliser experiences a further downwash component due to the wake deflection generated by the wing and nacelles. Wind-tunnel testing can again be utilised to obtain data which describes this effect (Harendra et al 1973). This data is generally presented in the form of a downwash angle through which the freestream velocity at the horizontal stabiliser should be rotated in order to include the effect of wing/nacelle wake deflection. Thus, the following rotation of the freestream velocity is required to model the effect of wing/nacelle downwash on the horizontal stabiliser:-

$$\begin{bmatrix} u_{hswd} \\ v_{hswd} \\ w_{hswd} \end{bmatrix} = \begin{bmatrix} \cos\epsilon_w & 0 & \sin\epsilon_w \\ 0 & 1 & 0 \\ -\sin\epsilon_w & 0 & \cos\epsilon_w \end{bmatrix} \begin{bmatrix} u_{hsfs} \\ v_{hsfs} \\ w_{hsfs} \end{bmatrix}$$

where the freestream velocity vector is given by the methodology described in Appendix 3 and the downwash angle ϵ_w , obtained from wind tunnel testing, is provided in Table A4.16 of Appendix 4.

2.2.2 Modelling of Rotor/Wing Interaction

In the tilt-rotor configuration the wing and rotors operate in close proximity and this produces levels of mutual interaction which can influence the performance of both these components. When operating at low speeds in helicopter mode the velocity of the rotor induced flow is at its maximum, as the nacelles are tilted forward the vehicle accelerates and the velocity of the induced flow diminishes. Consequently, the level of rotor/wing interaction is at its most severe during low speed flight in helicopter mode. This is

substantiated by McVeigh et al (1988) who demonstrate that the wing experiences a maximum download in hovering flight and that rotor performance is also compromised in this phase due to reingestion of the the rotor wake and the ground effect presented by the wing. The analytic models of Clark (1985) and Lesching and Wagner (1990) address the problem of rotor/wing interactions in the tilt-rotor configuration but, as stated previously, these are unsuitable for inclusion in a flight mechanics model.

Mil et al (1966) provide analytic expressions which describe the effects of rotor/wing interaction on a compound helicopter with side-by-side rotors. This work may be of use when modelling the effects of rotor/wing interactions which take place on the tilt-rotor configuration when flying in helicopter mode. However, McVeigh et al (1988) illustrate that the mechanism by which rotor/wing interactions occur is strongly dependent on nacelle incidence, consequently , the validity of the expressions quoted by Mil et al (1966) is, at best, limited to helicopter mode flight states.

Rotor wake impingement on the wing has been included in GTILT by superimposing the uniform component of induced flow onto the freestream velocity with the path of the downwash component being assumed as parallel to the rotor shaft. No account is taken of vehicle velocity when evaluating the path of the induced flow and therefore the induced flow is considered to travel parallel to the rotor shaft in all flight states. The area of the wing immersed in the wake is assumed equal to the circular arc directly below the rotor when the vehicle is in helicopter mode and is shown in Figure 1.1. Hence, it can be seen that the modelling of the wake impingement is most accurate in low speed helicopter mode flight where, as previously described, the influence of the rotor flowfield acting on the wing is most severe. For the wing panel influenced by the rotor wake the velocity at its centre of pressure is given by:-

$$\begin{bmatrix} u_{wif} \\ v_{wif} \\ w_{wif} \end{bmatrix} = \begin{bmatrix} u_{wfs} \\ v_{wfs} \\ w_{wfs} \end{bmatrix} + \begin{bmatrix} \cos\gamma & 0 & -\sin\gamma \\ 0 & 1 & 0 \\ \sin\gamma & 0 & \cos\gamma \end{bmatrix} \begin{bmatrix} 0 \\ 0 \\ -w_{if} \end{bmatrix}$$

where the freestream velocity vector is evaluated by the methodology described in Appendix 3 and the uniform induced flow component, w_{if} , is given in section 2.1.10.

From the work done by Lesching and Wagner (1990) and McVeigh et al (1988) it is evident that the influence of the wing on rotor performance is negligible in aeroplane mode but assumes progressively more importance as the nacelles are *rotated* towards helicopter mode. However, both papers estimate that the rotor thrust is only reduced by approximately 1.2% due to the presence of the wing in

hovering flight. It was therefore decided to neglect the influence of the wing on rotor performance.

2.3 Control Authority

On the tilt-rotor configuration control authority is exerted through a combination of rotor blade pitch deflections and aerodynamic control surface displacements. In low speed helicopter mode flight, authority is primarily applied through blade root pitch deflections with the aerodynamic surfaces exerting progressively more influence as the nacelles are *rotated* to aeroplane mode. The manner in which this control methodology has been incorporated into the GTILT model will now be discussed.

2.3.1 Rotor Control

Rotor control authority is provided by applying blade pitch deflections to the two side-by-side contra-rotating rotors, this yields the following five control states:-

1. Combined Collective, θ_{0c}
2. Differential Collective, θ_{0d}
3. Combined Longitudinal Cyclic, θ_{1sc}
4. Differential Longitudinal Cyclic, θ_{1sd}
5. Combined Lateral Cyclic, θ_{1cc}

An additional state, differential lateral cyclic, is possible but was considered to offer no practical benefit and was neglected.

In helicopter mode the above control states provide control authority as given in Table 2.1:-

Axis	Control
Pitch	Combined Longitudinal Cyclic
Roll	Differential Collective + Combined Lateral Cyclic
Yaw	Differential Longitudinal Cyclic
Heave	Combined Collective

Table 2.1 GTILT Control States and their Authority in Helicopter Mode

These control states are converted into blade pitch control by the following expressions:-

$$\theta_{0l} = \frac{\theta_{0c} + \theta_{0d}}{2}, \quad \theta_{0r} = \frac{\theta_{0c} - \theta_{0d}}{2}$$

$$\theta_{1sl} = \frac{\theta_{1sc} + \theta_{1sd}}{2}, \quad \theta_{1sr} = \frac{-\theta_{1sc} + \theta_{1sd}}{2}$$

$$\theta_{1cl} = \frac{\theta_{1cc}}{2}, \quad \theta_{1cr} = \frac{-\theta_{1cc}}{2}$$

As can be seen a positive input of differential collective decreases the collective of the right rotor relative to the left, thus, a positive displacement of this control will tend to generate a roll in the positive direction about the body axis set. Additionally, due to the fact that the rotors are rotating in opposite directions, an increase in collective of the left rotor relative to the right will generate an unbalanced reaction torque about the vehicle C.G. In this case a negative yawing moment is produced about the body axis set and the vehicle will tend to yaw to the left for a positive input of differential collective.

A positive input of combined longitudinal cyclic will incline both rotor discs forward, therefore, a positive displacement of this control will cause a pitch down of the vehicle about the body axis set. A positive input of differential longitudinal cyclic inclines the right rotor surface aft relative to the left and this will produce a positive yaw about the body axis set.

A positive input of combined lateral cyclic inclines the plane of both rotors to the right and thus, will generate a force to the right and a roll to the right. Inputs to combined lateral cyclic and differential collective can be used in unison to control the vehicle bank attitude when in helicopter mode. This is the Lateral Translation Mode (LTM) and is described in the Bell-Boeing Tilt-Rotor Handling Qualities Short Course Notes.

As stated previously, the rotor control states are washed out as the nacelles are *rotated* towards aeroplane mode, these states are therefore related to piloted stick deflections according to the following:-

$$\theta_{0d} = \frac{d\theta_{0d}}{dX_{lat}} (X_{lat} - X_{lat_n}) + \theta_{0d_n}$$

$$\theta_{1sc} = \frac{d\theta_{1sc}}{dX_{long}} (X_{long} - X_{long_n}) + \theta_{1sc_n}$$

$$\theta_{1sd} = \frac{d\theta_{1sd}}{dX_{pedal}} (X_{pedal} - X_{pedal_n}) + \theta_{1sd_n}$$

$$\theta_{1cc} = \frac{d\theta_{1cc}}{dX_{clc}} (X_{clc} - X_{clc_n}) + \theta_{1cc_n}$$

where the subscript, n, denotes the neutral position.

The rotor control gears are all functions of nacelle incidence and are defined by means of "look-up" tables. The combined collective input, θ_{0c} , is measured in terms of blade root pitch and is not geared to a control inceptor.

2.3.2 Aerodynamic Control Surfaces

Displacements of the following four aerodynamic surfaces are available to the pilot:-

1. Ailerons
2. Flaps
3. Elevators
4. Rudder

The influence of the flaps, elevators and rudders have been included through the aerodynamic force and moment coefficients which are quoted for a range of flap settings and empennage control surface displacements. The authority of the ailerons has been included by means of an effectiveness coefficient which is used to evaluate a rolling moment that is input to the overall vehicle equations of motion.

Deflection of the ailerons and empennage control surfaces are related to piloted stick displacements by the following:-

$$\delta_a = \frac{d\delta_a}{dX_{lat}} (X_{lat} - X_{lat_n}) + \delta_{a_n}$$

$$\delta_e = \frac{d\delta_e}{dX_{long}} (X_{long} - X_{long_n}) + \delta_{e_n}$$

$$\delta_r = \frac{d\delta_r}{dX_{pedal}} (X_{pedal} - X_{pedal_n}) + \delta_{r_n}$$

On the XV-15 proof-of-concept tilt-rotor vehicle the gearing between stick displacement and control surface deflection is fixed throughout the flight envelope with the authority of the aerodynamic control surfaces being dependent on the local dynamic pressure. The V-22 utilises a more complex fly-by-wire control system in which the software "shapes" the gearing between control stick and aerodynamic surface

according to nacelle incidence and freestream velocity. This is facilitated in the GTILT model by the inclusion of a "look-up" table which defines the gearing between control inceptor and aerodynamic surface.

The overall control vector for the tilt-rotor is therefore given by:-

$$\mathbf{c} = \begin{bmatrix} \theta_{0c} \\ X_{lat} \\ X_{long} \\ X_{pedal} \\ X_{clc} \end{bmatrix}$$

2.4 Locating the Vehicle Centre of Gravity

A significant proportion of the tilt-rotor's mass (approximately one third in the case of the XV-15) is associated with the engines and transmission and therefore large shifts occur in the location of the vehicle centre of gravity during transitional flight. This must be considered if the vehicle behaviour is to be accurately predicted. In GTILT, the location of the vehicle centre of gravity is given by the following expressions:-

$$\left. \begin{aligned} X_{cg} &= X_{cgdat} + \left(\frac{m_{nac}}{m_v} \right) \delta X_{cg} \\ Z_{cg} &= Z_{cgdat} + \left(\frac{m_{nac}}{m_v} \right) \delta Z_{cg} \end{aligned} \right\} \quad (\text{eqns 2.29})$$

where:-

X_{cgdat} and Z_{cgdat} are datum centre of gravity positions, in GTILT these are taken to correspond with the location of the centre of gravity in helicopter mode.

$\left(\frac{m_{nac}}{m_v} \right)$ is the ratio of the combined mass of the nacelles to the overall vehicle mass.

The horizontal and vertical displacements of the nacelle centre of gravity from the datum position, δX_{cg} and δZ_{cg} , are given by:-

$$\delta X_{cg} = X_{cgnac} (\cos\gamma - 1) - Z_{cgnac} \sin\gamma$$

$$\delta Z_{cg} = Z_{cgnac} (\cos\gamma - 1) + X_{cgnac} \sin\gamma$$

Where X_{cgnac} and Z_{cgnac} are the horizontal and vertical co-ordinates of the nacelle centre of gravity in helicopter mode and are expressed in the body axis set.

When evaluating the moments acting on the centre of gravity it is most convenient to refer the location of the various components through a fixed point on the airframe. In GTILT the reference point is taken to lie on the vehicle centreline with the longitudinal and vertical coordinates being given by the corresponding parameters defining the locations of the rotor shaft pivots.

The model derived in this chapter has been configured using XV-15 data and, in Chapter 5, its capability for accurately modelling the tilt-rotor configuration is demonstrated in the quality of its prediction of vehicle trim and dynamic response throughout the flight envelope.

Chapter 3

PARTIAL PERIODIC TRIM ALGORITHM

Existing rotorcraft models commonly utilise quasi-steady disc models to describe the behaviour of the rotor (Thomson 1992, Padfield 1981 and Harendra et al 1973). For a fixed flight state this leads to the prediction of constant rotor forces and moments, also, since the solution is carried out in multi-blade coordinates, the trimmed blade flap is described by non-time varying parameters. As none of the driving influences are oscillatory, a trim state can be said to have occurred when the vehicle adopts a constant flight state or, more directly, when the equations of motion yield zero rates of change in the flight states. Therefore, in order to obtain the required controls to produce a given trimmed flight state the acceleration terms in the equations of motion are set to zero and an iteration in the control displacements performed until the flight state converges to the specified condition.

GTILT is driven by a more sophisticated rotor model, as derived in Chapter 2, in which the equations are nonlinear and the trimmed solutions periodic. As the equations of motion reflect any periodicity in the rotor forces and moments the vehicle will adopt a periodic rather than constant flight state when in the trim. Also, blade flapping behaviour is now modelled using individual blade coordinates, hence, trimmed blade flap is described by periodic parameters. This periodicity in trimmed flight state and trimmed blade flap leads to a relatively complex enigma when seeking the correct control input to produce a given trim state. Now it is necessary to solve two interlinked problems simultaneously; the required control input to achieve the desired mean flight state must be ascertained whilst concurrently calculating the correct initial conditions to ensure periodicity in that flight state.

The trimming algorithm used in previous rotorcraft models which incorporate rotor disc representations is therefore inadequate and an alternative method is now required.

Given dynamic stability and a fixed control input, the most straightforward way to establish the corresponding trim state would be to integrate the equations of motion until the vehicle adopted a periodic flight state. This could be used as a basis for an iteration scheme to obtain the control input required to trim the vehicle to a given flight state (Houston 1992), however, this method faces two major problems. Firstly,

the point at which the trim had been achieved would be unclear; ascertaining when the transients had decayed to zero and the remaining oscillations were purely due to the periodic trim could introduce errors which affect the performance of the iteration. Secondly, for each iteration a finite length of time would elapse before the flight state settled to its trim condition, thus, if the system were lightly damped, the computing time for convergence could be prohibitively long. In the worst case an initial guess near a stability boundary could produce divergent transients and the scheme would fail to converge. Hence it was concluded that this method was also unsuitable and that a more reliable alternative should be sought.

One method of obtaining the control displacements and initial conditions necessary to produce a given trimmed periodic flight state is that of Periodic-Shooting/Newton-Raphson Iteration. An algorithm using this technique has been developed and incorporated into GTILT. The most appropriate starting point for the development of this algorithm is to clarify the definition of periodic trim with regard to rotorcraft simulation.

3.1 Definition of Periodic Trim

The periodicity of the rotor model equations is a consequence of two factors influencing the behaviour of a rotor blade as it advances round the azimuth. Firstly, if a constant cyclic pitch is input then the blade angle of attack will vary periodically as it advances round the azimuth. Secondly if the vehicle has a constant non-zero velocity then the blade will experience a sinusoidal variation in the aerodynamic velocity as it rotates round the disc. Both these effects cause the rotating blade to generate periodic forces and moments in trimmed flight.

The period of oscillation for the trimmed rotor forces and moments is dependent upon the number of blades in the rotor. This is because each azimuthal position has its own associated blade pitch and aerodynamic velocity, thus for identical blades, each blade will generate the same contribution to the rotor forces and moments as it passes through that position. Thus, an n bladed rotor has to rotate through $2\pi/n$ radians to have had, instantaneously, a blade in all azimuthal positions; therefore the full period of trimmed rotor forces and moments is described in $2\pi/n$ radians of revolution. When seeking a trim state for a given set of controls one is interested in the effect the forces and moments have on the vehicle's flight state. In this case it is most convenient to consider body axis states because the parameters defining the vehicle's flight state are then directly related to the forces and moments through the equations of motion. It follows that the period of oscillation for the vehicle's body axis flight states are the same as that of the driving rotor forces and moments, hence, the period of

oscillation for the vehicle flight states will be described in $2\pi/n$ radians of rotor revolution. It can therefore be seen that the vehicle has achieved a trimmed flight state when Equation 3.1 is satisfied.

$$\begin{bmatrix} u_a \\ v_a \\ w_a \\ p \\ q \\ r \\ \theta_f \\ \phi_f \end{bmatrix}_{\psi_r=0} = \begin{bmatrix} u_a \\ v_a \\ w_a \\ p \\ q \\ r \\ \theta_f \\ \phi_f \end{bmatrix}_{\psi_r=\frac{2\pi}{n}} \quad (\text{eqn 3.1})$$

Direct inclusion of the rotor induced flow states in the partial periodic trim algorithm is dependent on the induced flow model being used. When the Glauert model is employed the initial induced flow states are evaluated by means of the iteration scheme portrayed in Figure 2.9. Consequently, the trimmed induced flow states corresponding to a set of trimmed initial rotor and body axis states can be ascertained without direct inclusion in the partial periodic trim algorithm. The Peters-HaQuang representation utilises a first order differential equation, Equation 2.26, to model the rotor induced flow and it is necessary to ascertain the trimmed initial states of this equation by direct inclusion to the partial periodic trim algorithm. The subsequent derivation assumes the use of Peters-HaQuang modelling to represent the induced flow, if Glauert modelling is to be used then the induced flow states should be removed from the overall state vector.

From Equation 2.26 it can be seen that the induced flow generated by the rotor is closely related to the rotor thrust, pitching and rolling moments. Therefore, the periodicity of the induced flow states will also be described in $2\pi/n$ radians of rotor revolution. If the rotor is in trim then the induced flow will satisfy Equation 3.2 given below:-

$$\begin{bmatrix} w_{ifr} \\ p_{ifr} \\ q_{ifr} \\ w_{ifl} \\ p_{ifl} \\ q_{ifl} \end{bmatrix}_{\psi_r=0} = \begin{bmatrix} w_{ifr} \\ p_{ifr} \\ q_{ifr} \\ w_{ifl} \\ p_{ifl} \\ q_{ifl} \end{bmatrix}_{\psi_r=\frac{2\pi}{n}} \quad (\text{eqn 3.2})$$

As the rotor must rotate through 2π radians for each blade to have passed through all azimuthal locations then the full period of the trimmed blade states is

described in one complete revolution of the rotor. The period of these states is therefore independent of the number of blades in the rotor. Thus, for an n bladed model including two flapping states per blade Equation 3.3 will be satisfied if the rotor is in trim.

$$\begin{bmatrix} \beta_1 \\ \dot{\beta}_1 \\ \beta_2 \\ \dot{\beta}_2 \\ \vdots \\ \vdots \\ \beta_n \\ \dot{\beta}_n \end{bmatrix}_{\psi_r=0} = \begin{bmatrix} \beta_1 \\ \dot{\beta}_1 \\ \beta_2 \\ \dot{\beta}_2 \\ \vdots \\ \vdots \\ \beta_n \\ \dot{\beta}_n \end{bmatrix}_{\psi_r=2\pi} \quad (\text{eqn 3.3})$$

It is desirable to minimise the number of computations required to ascertain periodicity because this will reduce the convergence time of the following iteration scheme. From Equations 3.1, 3.2 and 3.3 it is evident that one revolution of the rotor is required to check for periodicity in the blade states whereas the rotor need only rotate through $2\pi/n$ radians to check for periodicity in the induced flow and vehicle flight states. However, a trimmed rotor describes a surface which is constant in form and fixed in orientation and this characteristic can be exploited to ascertain blade periodicity in $2\pi/n$ radians of revolution. In order to produce this constant surface all the blades must follow the same trajectory as they advance round the rotor disc and, as each blade starts rotating from a different azimuthal position, there is a shift in phase of $2\pi/n$ radians between the path of each blade. A set of initial trimmed blade states therefore provides a description of the blade trajectory at discrete points round the rotor disc. Thus for a rotor in trim, the states of an arbitrary blade, m, at $\psi_r=2\pi/n$ radians will map onto the initial states of identical blade m+1 when $\psi_r=0$. This characteristic can be used as a criterion to ascertain rotor trim in $2\pi/n$ radians of revolution and reduces the number of computations required per iteration by a factor proportional to $1/n$. This forms the basis of the definition for a rotor in trim and Equation 3.4 expresses this in vector form.

$$\begin{bmatrix} \beta_1 \\ \dot{\beta}_1 \\ \beta_2 \\ \dot{\beta}_2 \\ \vdots \\ \beta_{n-1} \\ \dot{\beta}_{n-1} \\ \beta_n \\ \dot{\beta}_n \end{bmatrix}_{\psi_r = \frac{2\pi}{n}} = \begin{bmatrix} \beta_2 \\ \dot{\beta}_2 \\ \beta_3 \\ \dot{\beta}_3 \\ \vdots \\ \beta_n \\ \dot{\beta}_n \\ \beta_1 \\ \dot{\beta}_1 \end{bmatrix}_{\psi_r = 0} \quad (\text{eqn 3.4})$$

In Equation 3.4 the required mapping is achieved by shifting the order of elements in the state vector, however, this is rather cumbersome. It is more convenient if the states are mapped by the inclusion of a permutation matrix and this is now shown in Equation 3.5.

$$\begin{bmatrix} \beta_1 \\ \dot{\beta}_1 \\ \beta_2 \\ \dot{\beta}_2 \\ \vdots \\ \beta_{n-1} \\ \dot{\beta}_{n-1} \\ \beta_n \\ \dot{\beta}_n \end{bmatrix}_{\psi_r = \frac{2\pi}{n}} = \begin{bmatrix} 0 & 0 & 1 & 0 & 0 & 0 & \dots & 0 & 0 \\ 0 & 0 & 0 & 1 & 0 & 0 & \dots & 0 & 0 \\ 0 & 0 & 0 & 0 & 1 & 0 & \dots & 0 & 0 \\ 0 & 0 & 0 & 0 & 0 & 1 & \dots & 0 & 0 \\ \dots & \dots \\ \dots & \dots \\ 0 & 0 & 0 & 0 & 0 & 0 & \dots & 1 & 0 \\ 0 & 0 & 0 & 0 & 0 & 0 & \dots & 0 & 1 \\ 1 & 0 & 0 & 0 & 0 & 0 & \dots & 0 & 0 \\ 0 & 1 & 0 & 0 & 0 & 0 & \dots & 0 & 0 \end{bmatrix} \begin{bmatrix} \beta_1 \\ \dot{\beta}_1 \\ \beta_2 \\ \dot{\beta}_2 \\ \vdots \\ \beta_{n-1} \\ \dot{\beta}_{n-1} \\ \beta_n \\ \dot{\beta}_n \end{bmatrix}_{\psi_r = 0} \quad (\text{eqn 3.5})$$

As can be seen the permutation matrix is the identity matrix with the non-zero elements shifted to the right an amount corresponding to the number of states per blade. The versatility of this definition is reflected by the ease in which more states per blade can be added, for example, two lag states could be included in this definition by simply shifting the non-zero permutation elements a further two locations to the right.

The expressions given in Equations 3.5, 3.1 and 3.2 can be combined to define the overall vehicle trim. For a vehicle with two three bladed rotors, two flapping states per blade and three inflow states per rotor the overall definition of trim becomes:-

$$\mathbf{s}_{(\psi_r = 2\pi/n)} = \mathbf{P}_v \mathbf{s}_{(\psi_r = 0)} \quad (\text{eqn 3.6})$$

where:-

$$\mathbf{s} = \begin{bmatrix} s_{rr} \\ s_{rl} \\ s_{if} \\ s_{fs} \end{bmatrix}$$

$$\mathbf{P}_v = \begin{bmatrix} \mathbf{P}_6 & \mathbf{0} & \mathbf{0} & \mathbf{0} \\ \mathbf{0} & \mathbf{P}_6 & \mathbf{0} & \mathbf{0} \\ \mathbf{0} & \mathbf{0} & \mathbf{I}_6 & \mathbf{0} \\ \mathbf{0} & \mathbf{0} & \mathbf{0} & \mathbf{I}_8 \end{bmatrix}$$

and introducing the following notation for future convenience:-

$$s_{rr} = \begin{bmatrix} \beta_{1r} \\ \dot{\beta}_{1r} \\ \beta_{2r} \\ \dot{\beta}_{2r} \\ \beta_{3r} \\ \dot{\beta}_{3r} \end{bmatrix} = \begin{bmatrix} s_1 \\ s_2 \\ s_3 \\ s_4 \\ s_5 \\ s_6 \end{bmatrix}, \quad s_{rr} = \begin{bmatrix} \beta_{1l} \\ \dot{\beta}_{1l} \\ \beta_{2l} \\ \dot{\beta}_{2l} \\ \beta_{3l} \\ \dot{\beta}_{3l} \end{bmatrix} = \begin{bmatrix} s_7 \\ s_8 \\ s_9 \\ s_{10} \\ s_{11} \\ s_{12} \end{bmatrix}$$

$$s_{if} = \begin{bmatrix} w_{ifr} \\ p_{ifr} \\ q_{ifr} \\ w_{ifl} \\ p_{ifl} \\ q_{ifl} \end{bmatrix} = \begin{bmatrix} s_{13} \\ s_{14} \\ s_{15} \\ s_{16} \\ s_{17} \\ s_{18} \end{bmatrix}, \quad s_{fs} = \begin{bmatrix} u_a \\ v_a \\ w_a \\ p \\ q \\ r \\ \theta \\ \phi \end{bmatrix} = \begin{bmatrix} s_{19} \\ s_{20} \\ s_{21} \\ s_{22} \\ s_{23} \\ s_{24} \\ s_{25} \\ s_{26} \end{bmatrix}$$

and:-

\mathbf{P}_6 is a 6 x 6 permutation matrix of the form given in Equation 3.5

$\mathbf{0}$ are zero matrices of a suitable order

\mathbf{I}_m is the m x m identity matrix

If the above mapping were to be carried out over 2π radians of rotor revolution, e.g. for a single bladed rotor, then the permutation matrix would become the identity matrix and the definition becomes an extension of that quoted by Peters and Izadpanah.

The definition of trim given in Equation 3.6 could be used as part of an iteration scheme to establish the initial conditions which ensure a trimmed periodic

flight state for a given control input. This would only be of great benefit if the control displacements necessary to produce a given trim state were known. This definition has therefore been incorporated into a more complex scheme which determines both the necessary controls and initial conditions to produce a specified trimmed flight state. The derivation of this iteration scheme is now discussed.

3.2 Specification and Convergence of Periodic Tilt-Rotor Trim

Helicopters have four control states available to the pilot and thus four flight states can be directly controlled. Generally, trim algorithms reflect this degree of authority by allowing four trajectory axis flight states to be specified explicitly; the required control inputs are then ascertained by an iterative process during which the body attitudes are also found. A tilt-rotor has five control states available to the pilot and, as discussed in Chapter 2, the additional state is used to control bank angle, therefore, bank angle can now be specified as part of a requested trim state.

Rotorcraft models which use quasi-steady rotor map/disc algorithms yield constant trimmed flight states, thus the trimming iteration can be said to have converged when the current control input produces flight states satisfying the specified conditions. The closest periodic equivalent to the quasi-steady convergence criteria is to consider the required trim to have been achieved when the time averaged integrals of the specified states converge to yield the required values. Thus for an individually bladed tilt-rotor model in helicopter mode the trim convergence criterion is as given in Equation 3.7.

$$\mathbf{x}_{fsCT} = \frac{1}{t_p} \int_0^{t_p} \mathbf{x}_{fsCFS} = \mathbf{x}_{fsST} \quad (\text{eqn 3.7})$$

where:-

$$\mathbf{x}_{fs} = \begin{bmatrix} V_f \\ \beta_f \\ \gamma_f \\ \Omega_f \\ \phi_f \end{bmatrix}$$

and:-

V_f = vehicle total velocity
 β_f = fuselage side-slip angle
 γ_f = fuselage angle of climb

Ω_f = turn rate

ϕ_f = fuselage angle of bank

t_p = time for rotor to rotate through $2\pi/n$ radians

Subscripts CT, CFS and ST indicate current mean trim, current flight state and specified mean trim respectively.

As stated previously one must solve two problems simultaneously when determining the necessary control displacements to achieve a specified periodic trimmed flight condition. It can be seen that one must obtain the necessary control displacements to satisfy Equation 3.7 whilst concurrently ascertaining the correct initial conditions to ensure periodic trim by satisfying Equation 3.6. If one performs a first order Taylor expansion of these expressions then this problem can be rewritten in a form suitable for solution by Newton-Raphson iteration.

Thus, for a tilt-rotor with 3 blades per rotor, 2 states per blade, 3 induced flow states per rotor and the five control states previously discussed, the Taylor expansion for a general vehicle state, s_i (for $i \leq 12$), is given in Equation 3.8:-

$$\begin{aligned}
 s_i(2\pi/n) = & s_{jt}(0) + \frac{\partial s_i(2\pi/n)}{\partial s_1(0)} (s_1(0) - s_{1t}(0)) + \frac{\partial s_i(2\pi/n)}{\partial s_2(0)} (s_2(0) - s_{2t}(0)) + \\
 & \dots\dots + \frac{\partial s_i(2\pi/n)}{\partial s_{26}(0)} (s_{26}(0) - s_{26t}(0)) + \frac{\partial s_i(2\pi/n)}{\partial \theta_{0c}(0)} (\theta_{0c} - \theta_{0ct}) + \\
 & \dots\dots + \frac{\partial s_i(2\pi/n)}{\partial \theta_{1cc}(0)} (\theta_{1cc} - \theta_{1cct}) \qquad \qquad \qquad \text{(eqn 3.8)}
 \end{aligned}$$

In order to map the blade states correctly, as defined previously by the permutation matrix, then the indices i and j are related by the following:-

If $1 \leq i \leq 4$ or if $7 \leq i \leq 10$ then $j=i+2$

If $i=5$ then $j=1$, if $i=6$ then $j=2$

If $i=11$ then $j=7$, if $i=12$ then $j=8$

and the Taylor expansion for a general vehicle state, s_i (for $i > 12$), is now given in Equation 3.9:-

$$\begin{aligned}
s_i(2\pi/n) = & s_{i1}(0) + \frac{\partial s_i(2\pi/n)}{\partial s_1(0)} (s_1(0) - s_{1t}(0)) + \frac{\partial s_i(2\pi/n)}{\partial s_2(0)} (s_2(0) - s_{2t}(0)) + \\
& \dots + \frac{\partial s_i(2\pi/n)}{\partial s_{26}(0)} (s_{26}(0) - s_{26t}(0)) + \frac{\partial s_i(2\pi/n)}{\partial \theta_{0c}} (\theta_{0c} - \theta_{0ct}) + \\
& \dots + \frac{\partial s_i(2\pi/n)}{\partial X_{clc}} (X_{clc} - X_{clct}) \quad \text{(eqn 3.9)}
\end{aligned}$$

The corresponding Taylor expansion for a general flight state, x_{ifs} , is as given below in Equation 3.10.

$$\begin{aligned}
x_{ifsCT}(2\pi/n) = & x_{ifsST} + \frac{\partial x_{ifsST}}{\partial s_1(0)} (s_1(0) - s_{1t}(0)) + \frac{\partial x_{ifsST}}{\partial s_2(0)} (s_2(0) - s_{2t}(0)) + \\
& \dots + \frac{\partial x_{ifsST}}{\partial s_{26}(0)} (s_{26}(0) - s_{26t}(0)) + \frac{\partial x_{ifsST}}{\partial \theta_{0c}} (\theta_{0c} - \theta_{0ct}) + \\
& \dots + \frac{\partial x_{ifsST}}{\partial X_{clc}} (X_{clc} - X_{clct}) \quad \text{(eqn 3.10)}
\end{aligned}$$

These expressions can now be rewritten in the following form:-

$$s(2\pi/n) = P_v \zeta + J_{11} (s(0) - \zeta) + J_{12} (c - c_t) \quad \text{(eqn 3.11)}$$

$$x_{fsCT} = x_{fsST} + J_{21} (s(0) - \zeta) + J_{22} (c - c_t) \quad \text{(eqn 3.12)}$$

where:-

$$s = \text{Vehicle state vector} = \begin{bmatrix} s_{rr} \\ s_{rl} \\ s_{if} \\ s_{fs} \end{bmatrix}$$

$$\zeta = \text{Trimmed initial vehicle state vector} = \begin{bmatrix} s_{rrt}(0) \\ s_{rlt}(0) \\ s_{ift}(0) \\ s_{fst}(0) \end{bmatrix}$$

P_v = Permutation matrix

$$\mathbf{c} = \text{Control vector} = \begin{bmatrix} \theta_{0c} \\ X_{lat} \\ X_{long} \\ X_{pedal} \\ X_{clc} \end{bmatrix}$$

and suffix, t, denotes trimmed state or trimmed state vector.

Also \mathbf{J}_{11} , \mathbf{J}_{12} , \mathbf{J}_{21} , \mathbf{J}_{22} are elements of the Jacobian matrix such that:-

$$\mathbf{J}_{11} = \begin{bmatrix} \frac{\partial s_1(2\pi/n)}{\partial s_1(0)} & \frac{\partial s_1(2\pi/n)}{\partial s_2(0)} & \cdots & \cdots & \frac{\partial s_1(2\pi/n)}{\partial s_{25}(0)} & \frac{\partial s_1(2\pi/n)}{\partial s_{26}(0)} \\ \frac{\partial s_2(2\pi/n)}{\partial s_1(0)} & \frac{\partial s_2(2\pi/n)}{\partial s_2(0)} & \cdots & \cdots & \frac{\partial s_2(2\pi/n)}{\partial s_{25}(0)} & \frac{\partial s_2(2\pi/n)}{\partial s_{26}(0)} \\ \cdots & \cdots & \cdots & \cdots & \cdots & \cdots \\ \frac{\partial \ddot{s}_{25}(2\pi/n)}{\partial s_1(0)} & \frac{\partial \ddot{s}_{25}(2\pi/n)}{\partial s_2(0)} & \cdots & \cdots & \frac{\partial \ddot{s}_{25}(2\pi/n)}{\partial s_{25}(0)} & \frac{\partial \ddot{s}_{25}(2\pi/n)}{\partial s_{26}(0)} \\ \frac{\partial \ddot{s}_{26}(2\pi/n)}{\partial s_1(0)} & \frac{\partial \ddot{s}_{26}(2\pi/n)}{\partial s_2(0)} & \cdots & \cdots & \frac{\partial \ddot{s}_{26}(2\pi/n)}{\partial s_{25}(0)} & \frac{\partial \ddot{s}_{26}(2\pi/n)}{\partial s_{26}(0)} \end{bmatrix}$$

$$\mathbf{J}_{12} = \begin{bmatrix} \frac{\partial s_1(2\pi/n)}{\partial \theta_{0c}} & \frac{\partial s_1(2\pi/n)}{\partial X_{lat}} & \frac{\partial s_1(2\pi/n)}{\partial X_{long}} & \frac{\partial s_1(2\pi/n)}{\partial X_{pedal}} & \frac{\partial s_1(2\pi/n)}{\partial X_{clc}} \\ \frac{\partial s_2(2\pi/n)}{\partial \theta_{0c}} & \frac{\partial s_2(2\pi/n)}{\partial X_{lat}} & \frac{\partial s_2(2\pi/n)}{\partial X_{long}} & \frac{\partial s_2(2\pi/n)}{\partial X_{pedal}} & \frac{\partial s_2(2\pi/n)}{\partial X_{clc}} \\ \cdots & \cdots & \cdots & \cdots & \cdots \\ \frac{\partial \ddot{s}_{25}(2\pi/n)}{\partial \theta_{0c}} & \frac{\partial \ddot{s}_{25}(2\pi/n)}{\partial X_{lat}} & \frac{\partial \ddot{s}_{25}(2\pi/n)}{\partial X_{long}} & \frac{\partial \ddot{s}_{25}(2\pi/n)}{\partial X_{pedal}} & \frac{\partial \ddot{s}_{25}(2\pi/n)}{\partial X_{clc}} \\ \frac{\partial \ddot{s}_{26}(2\pi/n)}{\partial \theta_{0c}} & \frac{\partial \ddot{s}_{26}(2\pi/n)}{\partial X_{lat}} & \frac{\partial \ddot{s}_{26}(2\pi/n)}{\partial X_{long}} & \frac{\partial \ddot{s}_{26}(2\pi/n)}{\partial X_{pedal}} & \frac{\partial \ddot{s}_{26}(2\pi/n)}{\partial X_{clc}} \end{bmatrix}$$

$$\mathbf{J}_{21} = \begin{bmatrix} \frac{\partial V_f}{\partial s_1(0)} & \frac{\partial V_f}{\partial s_2(0)} & \cdots & \cdots & \frac{\partial V_f}{\partial s_{25}(0)} & \frac{\partial V_f}{\partial s_{26}(0)} \\ \frac{\partial \beta_f}{\partial s_1(0)} & \frac{\partial \beta_f}{\partial s_2(0)} & \cdots & \cdots & \frac{\partial \beta_f}{\partial s_{25}(0)} & \frac{\partial \beta_f}{\partial s_{26}(0)} \\ \frac{\partial \gamma_f}{\partial s_1(0)} & \frac{\partial \gamma_f}{\partial s_2(0)} & \cdots & \cdots & \frac{\partial \gamma_f}{\partial s_{25}(0)} & \frac{\partial \gamma_f}{\partial s_{26}(0)} \\ \frac{\partial \Omega_f}{\partial s_1(0)} & \frac{\partial \Omega_f}{\partial s_2(0)} & \cdots & \cdots & \frac{\partial \Omega_f}{\partial s_{25}(0)} & \frac{\partial \Omega_f}{\partial s_{26}(0)} \\ \frac{\partial \phi_f}{\partial s_1(0)} & \frac{\partial \phi_f}{\partial s_2(0)} & \cdots & \cdots & \frac{\partial \phi_f}{\partial s_{25}(0)} & \frac{\partial \phi_f}{\partial s_{26}(0)} \end{bmatrix}$$

$$J_{22} = \begin{bmatrix} \frac{\partial V_f}{\partial \theta_{0cc}} & \frac{\partial V_f}{\partial X_{lat}} & \frac{\partial V_f}{\partial X_{long}} & \frac{\partial V_f}{\partial X_{pedal}} & \frac{\partial V_f}{\partial X_{clc}} \\ \frac{\partial \beta_f}{\partial \theta_{0cc}} & \frac{\partial \beta_f}{\partial X_{lat}} & \frac{\partial \beta_f}{\partial X_{long}} & \frac{\partial \beta_f}{\partial X_{pedal}} & \frac{\partial \beta_f}{\partial X_{clc}} \\ \frac{\partial \gamma_f}{\partial \theta_{0cc}} & \frac{\partial \gamma_f}{\partial X_{lat}} & \frac{\partial \gamma_f}{\partial X_{long}} & \frac{\partial \gamma_f}{\partial X_{pedal}} & \frac{\partial \gamma_f}{\partial X_{clc}} \\ \frac{\partial \Omega_f}{\partial \theta_{0cc}} & \frac{\partial \Omega_f}{\partial X_{lat}} & \frac{\partial \Omega_f}{\partial X_{long}} & \frac{\partial \Omega_f}{\partial X_{pedal}} & \frac{\partial \Omega_f}{\partial X_{clc}} \\ \frac{\partial \phi_f}{\partial \theta_{0cc}} & \frac{\partial \phi_f}{\partial X_{lat}} & \frac{\partial \phi_f}{\partial X_{long}} & \frac{\partial \phi_f}{\partial X_{pedal}} & \frac{\partial \phi_f}{\partial X_{clc}} \end{bmatrix}$$

Equations 3.11 and 3.12 can now be combined and re-arranged to give the iteration scheme:-

$$\begin{bmatrix} s(0) \\ c \end{bmatrix}_{i+1} = \begin{bmatrix} s(0) \\ c \end{bmatrix}_i - \begin{bmatrix} J_{11} - P_v & J_{12} \\ J_{21} & J_{22} \end{bmatrix}^{-1} \begin{bmatrix} s(2\pi/n) - P_v s(0) \\ x_{fsCT} - x_{fsST} \end{bmatrix}$$

The scheme derived above can now be used to concurrently evaluate the necessary controls and initial conditions required to achieve a specified periodic trim state. In Chapter 5, this scheme is shown to be robust and capable of rapidly evaluating the required blend of initial conditions and control inputs necessary to produce a wide range of specified periodic trim states.

Chapter 4

PARALLEL IMPLEMENTATION

GTILT is driven by the individual blade model derived in Chapter 2, this model allows the definition of representative blade geometries and aerodynamic characteristics but requires the use of numerical techniques in its solution. The computational effort necessary to perform this numerical solution creates the requirement for an advanced computing system or supercomputer if prohibitively long run-times are to be avoided. It is possible to reduce computational time by structuring the model as a set of sequential programs which can run independently of each other and only interact to exchange information. These programs can therefore be executed simultaneously in parallel on separate processors, hence, this method is known as parallel processing. As the model has now been divided into concurrently running sections then major savings in run-time are possible. In order to implement this parallelised model a multiprocessor machine is required, an example of which is available at the University of Glasgow in the form of a Meiko Computing Surface which is described in Section 4.1. The GTILT model has been parallelised and implemented on this computing surface and this will now be discussed.

4.1 The Meiko Computing Surface

The Meiko computing surface at the University of Glasgow contains 40 T800 transputers. Each transputer is capable of loading and running its own piece of sequential code autonomously from the other transputers on the surface and has four pairs of hard links available for use in the assembly of user defined topographies. Once connected, these links are employed as communication paths between the transputers in the network. Communication between computing surface and host terminal is achieved via the local host board which is connected to one transputer in the network through a pair of hard links. Soft links connect the network to various internal libraries which perform functions such as connecting transputers to the internal filing system, converting between message passing protocols and the routing of debugging messages back to the user terminal. The characteristics mentioned above are highlighted by the example topography shown in Figure 4.1 and this will now be described.

In this example four transputers, a master and three slaves, are connected together to form a ring topography with information being passed clockwise around the ring through the hard links, 'ring[0]' to 'ring[3]'.

The master process is connected to the user terminal through the local host and the internal library procedures 'fileSysMux' and 'fsysKeyScreen.' The procedure 'fileSysMux' is required to multiplex messages to and from the internal filing system, the keyboard and the screen onto the single pair of hard links 'toHost' and 'fromHost'. 'fileSysMux' transmits and receives data in filing system protocol but the soft links 'keyboard' and 'screen' convey data in streams protocol, hence, the internal library procedure 'fsysKeyScreen' is required to convert between these two protocols. Thus, for information to be transmitted from the master process to the user's screen it first travels along the soft link 'screen' to the library procedure 'fsysKeyScreen'. Here it is converted to filing system protocol before being transmitted along the soft link 'toFileSys[0]'. On reaching the library procedure 'fileSysMux' the information is multiplexed onto the hard link 'toHost', this transmits to the host board from which the information is interfaced to the user terminal. Data entered at the user's keyboard reaches the master process by the equivalent reverse route.

The master process can also read and write to file; in this example access to files is achieved through the channel pair 'fromFileSys[1]' and 'toFileSys[1]'. The library procedure 'fileSysMux' multiplexes these soft links onto the hard links 'toHost' and 'fromHost' which transmit to the local host board where the data is interfaced to the user terminal.

The library procedure 'fsysKeyScreen' accesses a further link to those mentioned above. A soft link, in this example 'debug', can be used to convey information to the supervisor bus. The supervisor bus acts as a control and monitoring system which connects all elements in the computing surface together, hence, it can be used to relay information from the transputers to the local host and from there to the user terminal. However, due to an incompatibility in message passing protocols, 'debug' cannot be connected directly to the supervisor bus, instead connection must be made through two internal library procedures. The supervisor bus is connected to the library procedure 'MK04xsystem' which receives data in streams protocol and transmits in supervisor protocol, hence, the library routine Superstreams is required to act as a filter to convert between these two message passing etiquettes. The capability of passing information via the supervisor bus is useful because it provides an alternative lower level route to the user terminal. Now debugging messages can still be sent to the user's terminal should communication fail through the normal route. Additionally, screen channels from the slave

processes can be connected to the supervisor bus in a similar way, hence, debugging messages can be passed from the slaves to the user terminal without first having to pass through the master.

The programming language native to the transputer is OCCAM and at the lowest level transputer topographies are formed using OCCAM harnesses. When necessary, code written in higher level languages such as FORTRAN can be compiled and linked to library files before being loaded onto the network by the OCCAM harness. Two major problems arise when using this method, firstly, all the hard the soft links necessary to produce the required topography must be specified explicitly in the OCCAM harness. Secondly, when passing a data stream from an originating process to its destination the information must be specifically received and transmitted at each intermediate stage. Unless the topography is relatively simple it can be seen that prohibitive difficulties will arise when establishing the necessary links to create a given architecture. The scheduling of communications between processes would also be a very difficult task in all but the simplest of transputer architectures.

Due to these problems it is preferable to generate transputer architectures and communicate between processes using a higher level method which does not require the OCCAM harness. It is possible to achieve this by using a software package written and marketed by the Meiko Group of Companies (Meiko Limited, 1990, Meiko Limited 1991). This package is called CS - Communicating Sequential - Tools and is a background process that makes the transputer hardware accessible to programs written in higher level languages such as FORTRAN. The two major aspects of CS Tools which have been utilised in the parallelisation of GTILT are its communication services and configuration tools.

4.1.1 CS Tools Configuration Tools

When using CS Tools the configuration of the transputer network is specified by an OCCAM PAR loader file in which the user can define a customised transputer topography or select an 'off the shelf' architecture from a library. Programs written in high level languages such as FORTRAN can be compiled and linked to object files before being loaded onto the network, the distribution of these processes is also specified in the PAR loader file. At run-time the CS tools software generates the hard and soft links and loads the processes onto the network according to the information in the PAR loader file. The characteristics of the PAR file are highlighted by the example shown in Figure 4.2 where a pentangle topography is created.

As can be seen the PAR file firstly defines the process distribution before stating the manner in which the topography is to be formed, in this case the network is userdefined so the architecture is created by the 'closeto' statements which install hard links between the specified processes. The links to and from the host need not be defined because they are connected to processor zero by default. it is therefore most convenient to load the master process onto processor 0 as this is closest to the local host.

4.1.2 CS Tools Communication Services

The communication services enable inter-processor communications to be established through a facility called the Computing Surface Network or CSN which is a background OCCAM process that runs on all transputers in the network. The CSN routes data transmission between processes and thus makes the topology of the network invisible so that all communications appear to be point-to-point. Higher level processes are connected to the CSN via transports through which data can be both transmitted and received. When a transport is opened it is assigned its own unique address on the CSN, this is called the NET ID, for data to be passed between processes the sender must firstly determine the NET ID of the recipient transport. The NET ID of a transport is made available by 'registering' the process name and corresponding transport NET ID, other processes can then 'look-up' the NET ID of the recipient transport before transmitting data. Inter processor communication can now be carried out by transmitting data down the sender's transport to the CSN, here the underlying software optimally routes the data to the specified transport. This receives the transmission and conveys it to the destination high level process. All interactions made between high level processes via the CSN are carried out through CS tools library functions, the above characteristics and their corresponding function calls are demonstrated by the example now discussed.

The master and third slave from the pentangle topography described above are shown connected to the CSN in Figure 4.3. The function calls required to connect the processes to the CSN and perform subsequent communications are also included in the figure. In all function calls the integer returned to the parameter 'returncode' indicates whether the function has been successfully completed or, if not, provides some information on the nature of the error.

The function `csnOpen` opens the transport to the CSN and returns the NET ID to the second argument in the function parameter list. The first argument can be used to specify a particular transport with which communication is to be carried out, in this case the transports are free to communicate with any other on the network and the

parameter CSN NULL ID is used to indicate this. The slave now registers its process name and transport NET ID using the function `csnRegname`. At the same stage the master looks up the NET ID of the recipient transport by calling the function `csnLookupName`. In this case `csnLookupName` provides the NET ID of the transport registered to the process 'slave3' and returns it to the parameter 'slave3Id'. The final argument in the `csnLookupName` parameter list is used to force the function to wait until the recipient transport has been registered. If this flag is not set then errors could occur should the sender attempt to find the NET ID of a transport which has not yet been registered on the CSN.

Information can now be transmitted from the master and received by the slave using the functions `csn tx` and `csn rx` respectively.

To transmit data using `csn tx` certain important parameters must be specified. The source transport NET ID, or the route from source high level process to CSN, must be indicated, in this example the previously registered 'outMaster' is used to convey data from the master process to the CSN. The destination transport must be specified, in this case the transport 'Slave3in' which was previously 'looked up' is used to carry information from CSN to the process 'slave 3'. Communication between processes using the CSN can be either synchronous or asynchronous, generally it is safer to use synchronous transfers because then it is easier to ensure that the data is received correctly. The parameter which flags synchronous or asynchronous communication is the second element of the `csn tx` function parameter list, in this case the communication is synchronous so the flag is set at zero - for asynchronous communication the flag should be set to one. Finally, the variable name of the data string to be transmitted and the number of bytes it contains must be specified, in this example the data is stored under the name 'variable', and the number of bytes to be transmitted is 'nBytes'.

The corresponding function which receives the transmission to the slave is `csn rx`. The parameter list of this function contains the NET ID of the local transport, the variable name into which the data is to be stored and the number of bytes of data to be received. In this example the local transport is free to communicate with any other process on the network, therefore, `csn rx` cannot be used to receive data from a specific source transport. However, on completion of communication the second element of the parameter list can be used to indicate the address of the source transport, in this case this facility is of little use and the parameter is set to CSN NULL ID.

When this communication is transmitted from the master to slave 3 the CSN establishes the best route, for example, if one particular path is busy then the CSN will

elect the best alternative at that particular time. This implies that the routing of messages is flexible and that the chosen optimal communication path between two given processes will vary at different instances in time. If communications had to be specifically routed at each intermediate stage then these processes would be slowed by the continual receipt and transmission of information destined for other sites. Also the synchronising and optimisation of data transfer would be exceedingly complex in all but the most simple of topographies.

This technique of communication is analogous to a telephone network where a high level process is represented by a telephone subscriber, a transport is represented by a telephone line and the CSN is represented by the exchange. Each subscriber's telephone line allows that subscriber to communicate with any other in the network; however in order to do so the recipient's telephone number must first be determined. The sender can then dial the recipient and transmit a message which is routed by the telephone exchange.

4.2 Topography Used in the Parallelisation of GTILT

As the rotor model derived in Chapter 2 is generic in nature it was developed to be valid for a range of rotors irrespective of the number of blades they contain. When the model is parallelised it is designed to portray the behaviour of each blade using code running on a dedicated transputer. To allow a reasonable degree of flexibility a single topography should be capable of supporting simulations of a range of vehicles each with a different number of rotor blades. Existing tilt-rotors and proposed future designs (Bell-Boeing Study Team 1987) all have three blades per rotor and few rotorcraft have more than five blades per rotor, hence, it was felt that a topography which could support simulations of vehicles with between two and five blades per rotor would provide adequate scope for future development. The tilt-rotor simulation model GTILT has been parallelised and implemented on the transputer topography shown in Figure 4.4. The formation of this topography and all interprocessor communications are carried out using the CS Tools package described previously in sections 4.1.1 and 4.1.2.

With reference to Figure 4.4 it can be seen that the transputer topography reflects the physical geometry of the vehicle being modelled. The left and right groups of slaves are used to describe the effects of the corresponding rotor with each slave representing an individual blade. The processor which links the two 'rotors' together is the 'master' which models the vehicle aerodynamics and contains the solver for the fuselage equations of motion. All interactions with the user are carried out by the 'master', hence, it is run on processor zero which is most closely linked to the user

terminal. The communication paths have been established to minimise the distance between processes which most frequently interact. The 'topslave' controls all the slaves in its rotor and consequently it requires to communicate with them regularly, therefore, good communication links should exist between 'topslave' and its 'slaves'. Additionally, most communications between 'master' and 'slaves' must first be processed by the 'topslave' (e.g. the conversion of body axis c.g. velocities and accelerations to the corresponding parameters in shaft axis for the rotor hubs), hence, the 'topslave' also requires to be close to the 'master'. It would therefore be advantageous if the 'topslave' could be directly connected to all its 'slaves' and the 'master'; however, only four link pairs are available so this level of networking is not possible. As a result the 'topslave' is not directly connected to 'slave 3'; consequently, for data to be transferred between these two processes it must first pass through one intermediate stage. It can be seen that 'slave 3' is the most distant slave from the 'master' and should only be used if five bladed rotors are to be modelled.

A large number of links exist between the slaves which form each 'rotor' and these links are used to provide alternative communication paths should one route be busy. For example, if the 'topslave' wished to communicate with 'slave 3' then the Computing Surface Network (CSN) can transmit the data along three alternative routes all of which are the same length. Therefore, these additional paths prevent a delay in communication should one route be blocked.

4.3 Parallel Implementation of GTILT

As stated above the transputers are organised in an hierarchical order with each processor running a section of sequential FORTRAN code which models the behaviour of one component of the vehicle. The functions carried out by each process can be summarised as follows:-

1. The master process is responsible for:-
 - a) Performing all interactions with the user.
 - b) Governing the actions of the 'topslave' and 'slave' processes.
 - c) Calculating the aerodynamic forces and moments acting on the vehicle.
 - d) Solving the equations of motion to calculate the vehicle rates and accelerations for the subsequent time step.

2. The topslave process is responsible for:-
 - a) Governing the actions of the 'slaves' under it's command.
 - b) Calculating the flap, thrust, forces and moments of blade 1.

- c) Calculating the rotor inflow at each time step.
- d) Summing the individual blade contributions to calculate the overall rotor forces and moments in body axis.

3. The slave process is responsible for:-

- a) Calculating the flap, thrust, forces and moments of its blade.

Flowcharts showing the sequence of operations carried out by the 'master', 'topslave' and 'slave' processes when using Glauert inflow modelling are given in Figures 4.5 to 4.11. The parallel scheduling of operations for one time step of a simulation using Glauert inflow modelling for a vehicle with three blades per rotor is shown in Figure 4.12

4.4 Synchronisation of Communications

As stated in Section 4.1, each process receives information from the CSN through a single transport, therefore, communications from all other members of the network must be routed through that transport. This means that the receiving process cannot selectively accept transmissions from processes in a pre-determined order but instead receives in the order that the transmissions are made. As all individual processes run sequentially then the order of message transmission from each process is fixed, however, as the processes run concurrently then the sequencing of transmissions from different sources may vary. In order to prevent processes receiving communications out of phase with the sequence of appropriate recipient function (CSN RX) calls some form of flagging is required. This method of message synchronisation is exemplified by the interchange carried out between 'master' and 'topslaves' at the beginning of each time step. Here the 'master' flags the 'topslaves' to indicate that it has finished passing the body axis C.G. velocities and accelerations to the 'slaves'. The 'topslaves' are now free to transmit their shaft axis rotor hub velocities and accelerations to the 'slave' processes. This exchange is necessary to prevent the communications to the 'slaves' becoming out of phase with the corresponding CSN RX calls, in which case the 'slaves' would confuse the communication from the 'topslave' as being the C. G. body axis velocity and accelerations transmission from the 'master'. This kind of error is difficult to trace because the inclusion of debugging statements alters the execution speeds of the sequential processes and hence changes the phasing of message transmissions.

Flagging is best used when a series of communications which vary in size or concern information widely differing in nature is expected because this creates the need for a sequence of dedicated CSN RX calls in the recipient process. One drawback

of this method occurs when a process runs slower than expected and is consequently late in transmitting which causes subsequent transmissions to block until the tardy communication has completed. When a process is receiving groups of similar data from separate processes, for example, when the 'topslave' receives the individual blade flapping states from the 'slaves', then the time for communication can be reduced if the destination process receives the information using a 'generic' function call. Now data can be communicated in the order that the source processes are ready to transmit. When necessary, the communication's source can be marked by transmitting a one dimensional array of information, the first element of which contains an integer identifying the source process with subsequent elements containing the relevant information.

4.5 Run Time Performance of the GTILT Model

When running from within the CS tools environment it is not possible to access the internal transputer clock and this makes it very difficult to calibrate the performance of GTILT. It was however recognised that some assessment of the model's performance was required and this was achieved by recording the elapsed time between the displaying of consecutive messages to the screen. When using a 6mS frame time to model the XV-15, it was ascertained that a typical trim of 5 iterations required, on average, 245 (+/-5) seconds of run time to complete and the evaluation of a 5 second time response required approximately 200 (+/- 5) seconds of run time. This performance compares favourably with that of Helistab (Padfield 1981) which, when running sequentially on a MicroVax, was found to take approximately 180 seconds to perform a similar 5 second (6mS frame time) simulation of a Westland Lynx Helicopter. Helistab is a model of established merit in the field of rotorcraft design, consequently, this comparison shows that the performance of GTILT is acceptable when used as a design tool.

The current software implementation of GTILT is structured in an inefficient form with some calculations being repeated on several occasions during each frame. (For example, the evaluation of the blade element velocity components u_p and u_t and blade incidence, α , is repeated three times at each time step). If necessary, significant improvements in performance could therefore be obtained by restructuring the existing software in a more efficient manner.

In order to obtain real time performance it would be necessary to reduce run times by at least a factor of 40 from their present levels. To achieve this reduction, it is envisaged that the best approach would be to access the internal clock or, if this were not possible, write a timer in OCCAM. This device could then be used to ascertain

periods where processors were lying idle and also highlight sections of code which were particularly inefficient. Suitable improvements could then be made to the software and the new levels of performance appraised. If further improvements in performance were required then strategic sections of code could be written in OCCAM or some modelling fidelity could be sacrificed (eg less blade elements could be included or a longer frame time utilised).

From the preceding discussion it is evident that the current performance of GTILT is acceptable in the capacity of a design tool. It is envisaged that GTILT could also be used to support real time simulations if some restructuring were carried out on the existing code.

Chapter 5

RESULTS

The GTILT model has been configured using XV-15 data quoted by Harendra et al 1973 (these are given in Appendix 4) and this has enabled a realistic investigation into the robustness of the periodic trim algorithm derived in Chapter 3 to be carried out. This trimming algorithm has been used to satisfactorily predict the required combination of control displacements and initial conditions necessary to produce trimmed flight throughout the vehicle flight envelope. A detailed discussion describing the convergence histories for some specimen flight states is provided in Section 5.1.

It is recognised that the validity of GTILT must be established and, ideally, this would be performed through a comparison of predicted model behaviour and flight test data obtained from the real aircraft. This comparison would normally fall into two distinct categories, firstly, the trim states adopted by the model would be verified with those of the actual vehicle for a range of airspeeds and nacelle incidences. Secondly, the vehicle response to a range of standard test inputs (steps, ramps or doublets) would be compared with that of the model in order to ascertain the fidelity of GTILT throughout the flight envelope. However, tilt-rotor flight test data is not currently available in the United Kingdom and some meaningful validation of the GTILT model must therefore be obtained by other means. An existing rotorcraft model, the Bell C81 (Van Gaasbeek 1981), is of established validity when predicting the behaviour of the tilt-rotor configuration (Schillings et al 1990) and therefore good correlation with this model would be encouraging. The Bell C81 model has been used to predict the longitudinal trim states adopted by the XV-15 for a range of airspeeds and nacelle incidences and the results produced are quoted by Harendra et al (1973). It has therefore been possible to verify the predicted longitudinal trim states of GTILT against those of the similarly configured Bell C81 model and a quantitative comparison is provided in Section 5.2.

Unfortunately, it has not been possible to obtain similar C81 data depicting the dynamic response of the XV-15 configuration to the range of control inputs previously described. However, the response predicted by the GTILT model has been investigated throughout the flight envelope and the results of this exercise are discussed qualitatively in Section 5.3.

5.1 Convergence of Partial Periodic Trimmer

Flight path and control iteration histories for a 240 Knot level flight trim in aeroplane mode are depicted in Figures 5.1 and 5.2 respectively. As can be seen convergence is achieved in six iterations with the solution being closely approximated after only three iterations despite the fact that a fairly poor initial guess was made. The robustness of the trimming method is highlighted by the iteration history for the climb angle, γ , where a large angle of climb (greater than 40°) is produced at the first iteration. Such a climb angle produces vehicle angles of attack at the extreme limit of the component look-up tables. Despite this, the iteration continues rapidly to convergence thus demonstrating the reliability of the trimming algorithm.

Similar iteration histories for a 10 Knot forward flight case with 4° bank angle in helicopter mode are given in Figures 5.3 and 5.4. Again it can be seen that convergence is rapid with the required trimmed flight state being obtained in 4 iterations. With reference to Figure 5.4 it is evident that displacements in all 5 controls are required to produce this trim. The input of combined collective generates the necessary thrust to balance the aerodynamic and gravitational forces acting on the vehicle with the longitudinal stick displacement being required to balance the pitching moment acting on the vehicle CG at the trimmed incidence and speed. The input of combined lateral cyclic, in this case about 4° per rotor, orientates the rotor thrust vectors to the vertical whilst the vehicle flies with 4° degrees angle of bank. This control displacement also generates an unwanted rolling moment which would tend to produce a roll to the left, hence, the input of lateral stick is required to offset this. In helicopter mode, the lateral stick displacement generates a rolling moment by increasing the collective of one rotor relative to the other, this also produces a yawing moment which, in this case, would tend to yaw the vehicle to the left. In order to balance the unwanted yawing moment an input of right pedal is required and the zero sideslip flight path maintained. The combination of controls described above is qualitatively valid as it forms a recognised strategy for maintaining a prescribed bank angle and is described in the Bell-Boeing Tilt-Rotor Handling Qualities Short Course Notes as the Lateral Translation Mode (LTM). The most practical uses of the LTM can be summarised as follows:-

1. To produce pure (wings level) translational flight, for example across a the deck of a ship.
2. To hover wings level in a crosswind.
3. To achieve a desired bank angle in the hover, for example parallel to a slope prior to landing.

However, the combined lateral cyclic also provides the pilot with the ability to control the vehicle bank angle during turning flight. By resolving the forces acting on the vehicle Etkin (1971) shows that the angle of bank produced in a co-ordinated turn can be approximated by:-

$$\phi = \tan^{-1}\left(\frac{\Omega_f V_f}{g}\right) \quad (\text{eqn 5.1})$$

With reference to data provided in Appendix 4 it can be seen that $\pm 4^\circ$ (± 0.0698 radians) of combined lateral cyclic may be applied in helicopter mode, therefore, in this regime the pilot can establish co-ordinated turns with angles of bank in the range:-

$$\phi = \tan^{-1}\left(\frac{\Omega_f V_f}{g}\right) \pm 0.0698 \text{ radians} \quad (\text{eqn 5.2})$$

From Appendix 4 it is also evident that the combined lateral cyclic is linearly washed out as the nacelles are tilted from $\gamma = 10^\circ$ to $\gamma = 15^\circ$ and therefore the pilot has decreasing control over the vehicle bank angle during this phase. Hence, a "corridor" of bank attitudes exists in which the pilot can achieve a co-ordinated turn at a specified airspeed and turn rate. The gearing between piloted stick displacements and θ_{1cc} is such that this "corridor" is 8° wide at nacelle angles between 0° and 10° . A linear narrowing of the "corridor" then occurs until, at a nacelle angle of 15° , the pilot no longer has direct control over the vehicle bank attitude. Thus, care must be taken when specifying vehicle bank attitude as part of a requested turning trim state because a poorly selected value would require an input of combined lateral cyclic outwith the control limits and thus lead to the failure of the iteration scheme.

The robustness of the trim algorithm is highlighted by its ability to produce specified trim states in turning flight (within the bank angle "corridor") at nacelle angles close to 15° . This is demonstrated in Figures 5.5 and 5.6 where a 10° per second turn rate at 80 Knots is obtained with a 36° angle of bank (as specified by Equation 5.1) being commanded. In this example a nacelle angle of 14.9° was selected therefore, according to the scheduling of the control gearing, the maximum authority of the combined lateral cyclic is $\pm 0.08^\circ$. As the combined lateral cyclic is exerting negligible authority it may be expected that the Jacobian matrix would become subject to numerical instabilities. However, despite this, the trim algorithm is still capable of obtaining a converged solution in six iterations from a relatively poor initial guess.

With reference to Figure 5.5 it can be seen that the specified turning flight trim state is obtained using approximately 45° blade root pitch to balance the

aerodynamic and gravitational forces acting on the vehicle airframe. At nacelle angles close to helicopter mode the fuselage must be pitched down in order to achieve forward flight and therefore the forward longitudinal stick displacement is necessary to balance the pitching moments acting on the vehicle CG at this nacelle incidence and airspeed. The bank angle adopted for this turn rate and airspeed was closely predicted by Equation 5.1 therefore only a small input of combined lateral cyclic is required to produce the specified 36° of bank. This input of combined lateral cyclic generates a negligible rolling moment on the vehicle CG and therefore the witnessed neutral, or 50%, lateral stick input is required to produce the trim. The yaw rate generated in turning flight causes the rotor towards the outside of the turn to experience a larger X_{body} component of velocity than its counterpart towards the centre of the turn. (In this case the yaw rate is 0.14 rads^{-1} and this produces a X_{body} velocity differential between the rotor hubs of 1.4 ms^{-1}). At nacelle angles close to helicopter mode, this velocity differential causes an increase in the dynamic pressure acting on the advancing blades towards the outside of the turn relative to those towards the inside of the turn. This tends to produce greater longitudinal flapping on the outboard rotor and therefore can be considered as an uncommanded input of differential longitudinal cyclic which would yaw the vehicle out of the turn. In this case the uncommanded input of longitudinal cyclic would tend to generate a yaw to the left and, in order to oppose this, the witnessed 55% right pedal input is necessary.

5.2 Verification of GTILT

Adequate verification of GTILT has proved problematical due to the lack of available flight test data. However, it has been possible to compare predicted longitudinal XV-15 trim states with those of the Bell C-81 model using data published by Harendra et al 1973 and the results of this exercise will now be discussed. When reading this section it should be noted that the Bell data has been measured from poorly reproduced graphs, consequently, there may be sizeable errors associated with this data ($\pm 0.75^\circ$ in fuselage pitch attitude, $\pm 1.3^\circ$ in blade root pitch and 0.75% in longitudinal stick).

5.2.1a Verification of Longitudinal Trim States Adopted by the Vehicle in Helicopter Mode

Figure 5.7 shows a comparison of the predicted longitudinal trim states for the vehicle in helicopter mode across a range of forward flight speeds.

With reference to this figure it can be seen that the predicted blade root pitch shows good agreement for trim speeds up to 40 Knots. Between 40 Knots and 80 Knots GTILT estimates that progressively more collective is required to produce the

trim than does the Bell C81 with a maximum difference of 1.5 degrees occurring at 80 Knots (It should be noted that a possible error of +/- 1.3° is associated with the Bell data and this could improve agreement to 0.2°). At trim speeds above 80 Knots correlation between the models improves with GTILT estimating the requirement of 0.5 degrees more collective to produce 140 knots trimmed flight. It is most probable that the disparities in predicted blade pitch are attributable to the modelling of the rotor wake impingement on the wing. For all flight speeds and configurations, GTILT assumes that the area of wing immersed in the wake is equal to the circular arc directly below the rotor when the vehicle is in helicopter mode. This approximation is valid when the velocity of the vehicle is negligible relative to the velocity of the induced flow, however, at higher flight speeds the rotor wake will be washed backwards and will impinge on a smaller wing area. This leads to a decreased induced download and consequently the amount of combined collective required to produce the trim is over predicted by GTILT. At high forward speeds the velocity of the rotor wake decreases to such an extent that the induced downforce is negligible and the approximation made in GTILT becomes less significant and correlation improves. In order to investigate this, the impinged wing area in the GTILT model has been reduced to zero and the 80 Knot trim state re-evaluated. In this case the blade pitch required to produce trimmed flight reduced to 42.2° which is within 0.5° of the measured C81 value. Therefore, the 1.5° disparity at 80 Knots can be attributed to the modelling of rotor wake impingement in GTILT and errors in the measurement of the Bell data.

The longitudinal stick displacements required to produce trimmed flight show good agreement throughout the quoted speed range. Both models exhibit the same general trend of increasing forward longitudinal stick with trimmed airspeed and show a stick reversal occurring at the lower end of the quoted speed range. This reversal is generated as a result of the rotor upwash striking the horizontal stabiliser which has the net effect of generating a pitch down moment that has to be offset by a more aft input of longitudinal stick. At higher airspeeds the wing downwash on the horizontal stabiliser becomes more effective providing a stable stick gradient with increasing airspeed. GTILT and the Bell C81 use different wind tunnel data to model the rotor wake impingement on the horizontal stabiliser, therefore, impingement on this component is predicted to occur at different airspeeds. Consequently, the stick reversal occurs at higher airspeed in GTILT than in the Bell C81.

In both models the vehicle pitch attitude becomes increasingly nose down as the trimmed forward speed increases, however, a small disparity exists between the models across the speed range. It is suspected that this is due to minor differences in

the evaluation of the overall pitching moment which forces the vehicle to adopt a slightly different pitch attitude in order to achieve a moment balance.

5.2.1b Verification of Longitudinal Trim States Adopted by the Vehicle in Transitional Flight

Figure 5.8 and Figure 5.9 show a comparison of the predicted longitudinal trim states for the vehicle flying with 15° and 30° nacelle angle respectively.

With reference to Figure 5.8 it can be seen that good correlation exists for the vehicle flying with 15° nacelle angle. The only significant difference is evident in the blade root pitch required to produce trimmed flight between 40 and 100 Knots. The additional inputs of collective required by GTILT to produce trimmed flight in this speed range are attributable to the modelling of the induced download on the wing and this is described previously in Section 5.2.1a where the helicopter mode results are discussed.

At 30° nacelle angle the comparison of predicted longitudinal stick displacements generally shows good agreement with a maximum difference of approximately 8% occurring at 100 Knots. Both models exhibit a change in longitudinal stick gradient at the lower end of the quoted speed range, however, the Bell model predicts this occurrence at 80 Knots whereas GTILT predicts it at 40 Knots. This change in longitudinal stick gradient is essentially similar to the helicopter mode stick reversal and is thus attributable to the rotor wake impinging on the horizontal stabiliser. For reasons discussed previously in Section 5.2.1a, the Bell model and GTILT predict that this effect occurs at different airspeeds and therefore the change in longitudinal stick gradient is shown to occur at a lower airspeed by GTILT than the C81.

The adopted fuselage pitch attitudes show good agreement throughout the range of quoted airspeeds with a maximum disparity of approximately 2° occurring at an airspeed of 40 Knots.

The comparison of predicted longitudinal trim states for the vehicle flying with 60° nacelle angle is given in Figure 5.10. With reference to this figure it is evident that excellent agreement exists between the two models for the fuselage pitch attitudes and longitudinal stick positions necessary to produce trimmed flight throughout the quoted range of airspeeds. Good agreement can also be seen in the blade root pitch required to produce the trim with a maximum disparity of about 2.5° (or 4%) being evident at 180 Knots.

5.2.1c Verification of Longitudinal Trim States Adopted by the Vehicle in Aeroplane Mode

Figure 5.11 shows a comparison of the predicted longitudinal trim states for the vehicle in aeroplane mode across a range of flight speeds.

It can be seen that good correlation exists between the two models for the predicted blade root pitch across the quoted range of trim speeds. However, the relationship between trim speed and required blade pitch is predicted as being non-linear by GTILT whereas the Bell model shows this as being linear. It is suspected that the difference is attributable to the evaluation of the rotor thrust. GTILT includes the normal component of velocity, u_p , when calculating the blade element dynamic pressure, consequently, rotor thrust is a function of $(u_p^2 + u_t^2)$. This is reflected in the collective input required to produce trimmed flight by a non-linear variation with increasing u_p . The C81 model applies a linear correction factor onto the rotor thrust to include the effect of increasing u_p and this is reflected by the linear relationship between collective input and trimmed airspeed.

It is of interest to note that a larger input of collective is required to produce 140 knot trimmed flight in aeroplane mode than helicopter mode despite the fact that the rotors are producing considerably more thrust in the latter case. This is mainly because the significantly higher normal velocity component in aeroplane mode generates a reduction in the blade angle of attack which has to be offset by a larger collective input.

Excellent agreement is obtained for the predicted longitudinal stick displacement and vehicle pitch attitude required to produce trimmed flight. The difference in longitudinal stick displacement does not exceed 1% and the pitch attitude is predicted to within 1 degree throughout the quoted range.

It can be seen that the characteristics of the longitudinal trim states adopted by the vehicle alter as the nacelle angle is advanced from 30° to 60° and this will now be discussed.

At nacelle angles less than 60° the vehicle is controlled in a similar manner to a conventional helicopter and therefore increased airspeed is obtained by orientating the rotor thrust vectors forwards. This is achieved by a forward input of combined longitudinal cyclic as shown in Figures 5.7, 5.8 and 5.9. where greater forward longitudinal stick displacements are generated as airspeed increases. The forward input of longitudinal cyclic has a secondary effect of generating a nose down pitching moment, hence, the vehicle pitch attitude becomes more nose down with increasing

airspeed and this is again shown in Figures 5.7, 5.8 and 5.9. When the thrust vectors are orientated forwards their vertical components decrease and consequently more power is required to balance the vehicle weight. Additional power is also required to offset the greater aerodynamic drag which occurs as the trimmed airspeed increases. Figures 5.7, 5.8 and 5.9 reflect this trend of increasing power by showing the requirement for larger inputs of combined collective as airspeed advances above 80 Knots. At lower airspeeds the combined collective required to produce trimmed flight is seen to dip as airspeed increases from the hover. This is because the rotor efficiency improves as the vehicle moves out of the hover (Johnson 1980b), therefore, less combined collective is input to produce the necessary thrust.

As the nacelle angle increases beyond 60° the vehicle behaves in a similar manner to a conventional fixed wing turbo-prop. In this regime most of the vehicle weight is balanced by the wing lift with the majority of the rotor thrust being used to oppose the aerodynamic drag. At lower airspeeds the dynamic pressure acting on the wing is reduced, consequently, the vehicle must adopt a greater nose up attitude so that the wing generates sufficient lift to balance the vehicle weight. At higher airspeeds the dynamic pressure increases and the wing is able to produce the required lift at lower angles of attack, therefore, the vehicle pitch attitude decreases. The longitudinal stick inputs necessary to produce trimmed flight reflect this by showing progressively greater forward displacements as airspeed increases. Increasing blade pitch is necessary to produce trimmed flight as airspeed increases and this is due to two effects. Firstly, greater rotor thrust is required to oppose the larger aerodynamic drag generated as airspeed increases. Secondly, the normal component of velocity, u_p , experienced by the rotors increases with airspeed consequently larger blade root pitch inputs are required to maintain the necessary rotor blade angles of attack.

5.2.2 Verification of Trim States Adopted in Turning Flight

Unfortunately, a quantitative verification of the turning flight trim states predicted by the GTILT model could not be carried out as no comparable Bell C81 data were available. In an attempt to ascertain the validity of the trim states adopted by GTILT in turning flight a qualitative investigation was performed and examples of this will now be discussed.

The first example is shown in Figure 5.12 and investigates the trim states adopted by the vehicle at nacelle angles where the combined lateral cyclic control is active, that is, for nacelle angles in the range 0 to 15 degrees. In this example a 10 degree per second turn rate was specified at an airspeed of 80 Knots with a bank angle of 38 degrees being commanded. According to Equation 5.1 the bank angle for this

turn rate and airspeed is 36 degrees, therefore, a combined lateral cyclic input is required to generate the additional 2° of bank.

As can be seen the blade root pitch required to produce this trimmed flight state decreases linearly from approximately 45° root pitch in helicopter mode to 43.75° root pitch at 12.5° nacelle angle. It is suspected that this is attributable to a reduction in aerodynamic drag acting on the vehicle airframe as the nacelles are *rotated*. Less thrust (or less collective) is therefore required from the rotors in order to produce the trim as the nacelle angle, γ , increases. The longitudinal stick displacements required to produce the specified trim also demonstrate a linear variation with nacelle incidence. This is because the rotors generate an increasing pitch down moment as the nacelles are *rotated* and hence progressively larger inputs of aft longitudinal stick are required to produce the specified trim as γ increases.

With reference to the plots depicting the pedal and lateral stick inputs necessary to produce the trim it can be seen that relatively constant displacements of these controls (<1% variation) are necessary throughout the range of quoted nacelle angles. As the nacelles are tilted through 8° it can be seen that a trend of increasing lateral stick and pedal displacements is initiated. This trend is generated as the rotor control states are washed out and therefore larger deflections of the aerodynamic surfaces are necessary to produce the required control forces. As the gearings between piloted stick displacements and aerodynamic control surface deflections are fixed, the requirement for increasing deflections of these surfaces is manifest in the generation of larger stick and pedal displacements.

It can be seen that the inputs of combined lateral cyclic remain fairly constant at approximately 27% stick for nacelle incidences between 0° and 10°. With reference to Appendix 4 it is evident that the gearing between piloted stick displacements and θ_{1cc} remains constant for this range of nacelle incidences and, in this regime, the range of authority for the combined lateral cyclic is +/-4°. Therefore the 27% stick displacement corresponds to a 2° input of left combined lateral cyclic and this is consistent with maintaining the required orientation of the rotor thrust vectors whilst the vehicle flies with the additional 2° of bank. As γ increases between 10° and 15° the combined lateral cyclic is progressively washed out, therefore, increasing stick displacements are necessary to generate the required 2° input of this control. At a nacelle angle of approximately 12.5° the gearing between piloted stick displacement and θ_{1cc} is such that the stick input reaches its left control limit, hence, the specified trim state could not be achieved at nacelle angles of greater than 12.5°.

The second example of turning flight is shown in Figure 5.13 and depicts the trim states adopted when performing a 200 Knot, zero sideslip turn. The results are quoted for a range of turn rates from 0 to 19 degrees per second whilst the vehicle is configured in aeroplane mode. In this mode of flight the combined lateral cyclic control is inactive and bank angle can therefore no longer be directly controlled, consequently, the vehicle adopts the bank angle specified by Equation 5.1. With reference to Figure 5.13 it can be seen that increasing amounts of combined collective, aft longitudinal stick and vehicle pitch attitude are required as turn rate increases. Such a trend is quantitatively valid and is described by Etkin (1972) as resulting from the necessity for additional lift as turn rate increases. From Figure 5.13 it can be seen that an input of right pedal is necessary to produce the specified zero sideslip turn. In this regime the rotor towards the outside of the turn experiences a larger normal velocity component, u_p , than the inboard rotor and, as a result, the angle of attack experienced by the outboard rotor is reduced. Hence, for a fixed combined collective input, this rotor generates less thrust than its counterpart on the inside of the turn. This asymmetry generates a yawing moment out of the turn (2240Nm in the case of the 19 degree per second turn rate) which has to be offset by the right pedal input in order to produce the specified flight state.

5.3 Response of Vehicle to a Range of Control Inputs

In order to qualitatively validate the dynamic behaviour of the model, doublets were individually applied to all the control states and the predicted dynamic response investigated. In all cases, a 10% stick displacement was applied from trim and held for 1 second the input was then reversed and held again for 1 second before being returned to the original trimmed position. For the longitudinal controls the inputs were applied in a forward then aft sequence and for the lateral controls the inputs were applied to the right then the left. The doublet to combined collective was injected by increasing the blade pitch by 2° from trim and then reducing it by 2° from trim. This was repeated for a range of nacelle angles and the results produced in helicopter mode, transitional flight (at 45 degree nacelle angle) and aeroplane mode will now be discussed.

5.3.1a Helicopter Mode - Doublet in Combined Collective

The response of the vehicle to a 1 second doublet of +/- 2° combined collective is shown in Figures 5.14 and 5.15 where the body axis flight states and Euler attitudes are shown respectively. With reference to Figure 5.14 it can be seen that only the longitudinal flight states are excited by this sequence of control displacements and, due to the symmetry of the vehicle, there is no coupling with the lateral states. As the rotors are positioned forwards of the vehicle CG then an input of combined collective

generates both a force in the Z_{body} direction and also a pitching moment about the C. G. This is evident from Figure 5.14 where the w_a component of velocity is seen to increase by approximately 0.5 ms^{-1} in response to the initial input of combined collective. This input also generates a pitch up moment and this is shown in the plots of pitch rate, q , and pitch attitude, θ , where a maximum pitch rate of 0.05 radians per second and a maximum displacement from trimmed pitch angle of 2.5 degrees are evident. The sequence of control displacements is closely followed by the initial response of the Z_{body} component of velocity, w_a , pitch rate, q , and can also be seen in the initial response of the fuselage pitch angle θ . This initial response is heavily damped and has a period of approximately 4 seconds, therefore, this motion takes the form of the short period mode as described by Etkin (1972). The plots of X_{body} velocity component, u_a , and pitch attitude, θ , show that a more lightly damped mode is adopted, after the doublet is injected, 5 seconds into the simulation. This mode has a period of approximately 30 seconds and involves an interaction between airspeed and fuselage pitch angle. From $t=5$ seconds to $t=12$ seconds the vehicle pitches down and accelerates then a pitch up motion combined with deceleration is observed. This motion is described by Prouty (1990) and Reichart (1973) as the phugoid mode and, at low nacelle angles, the phugoid is driven by the following characteristic behaviour of the rotors:-

1. As the vehicle accelerates the advancing blades experience an increase in dynamic pressure, this tends to produce an increase in longitudinal flapping which orientates the thrust vectors aft, therefore, the vehicle pitches up and decelerates.
2. The deceleration tends to reduce the dynamic pressure acting on the advancing blades and this reduces the longitudinal flapping. The thrust vectors are now orientated forwards causing the vehicle to pitch down and accelerate.

Figure 5.16 shows time histories of the the average rotor forces in the F_x , F_z respectively directions and also the pitching moment produced by the rotors, M_y , during this simulation. Between $t=1$ second and $t=3$ seconds the immediate influence of the collective doublet can be seen with the most significant response being in F_z where an oscillation of approximately 15000N is witnessed. From Figure 5.7 it can be seen that some longitudinal cyclic is input ($\approx 66\%$ forward) and this orientates the rotor thrust vectors slightly forwards, thus, the doublet of combined collective also produces the immediate oscillation of $\pm 1000\text{N}$ in F_x . As stated previously, the rotors are positioned forward of the vehicle CG and hence the doublet of combined collective has a direct effect on the vehicle pitching moment, this can be seen in Figure 5.16 where the

doublet causes an oscillation of +/- 3000 Nm in M_y . The rotor characteristic which drives the phugoid mode is also evident in this figure - approximately 5 seconds into the simulation oscillations of roughly +/- 100N are evident in the time histories of F_x and F_z . These oscillations are produced as the rotor thrust vectors are tilted fore and aft as airspeed fluctuates. Oscillations of approximately 400Nm are also evident in the time history of M_y and these pitching moment fluctuations are again generated as the rotor tip path plane tilts fore and aft as the airspeed varies. As previously stated, it is this fluctuation in rotor pitching moment with airspeed which drives the phugoid mode.

Bramwell (1990) shows that this motion can be unstable for helicopters, however, the horizontal stabiliser on the tilt-rotor does provide damping and with reference to Figure 5.45 it can be seen that such oscillations, though lightly damped, would decay to zero after approximately 140 seconds.

It can therefore be seen that a doublet of combined collective in helicopter mode excites both the short period and phugoid modes with no coupling to the lateral states. The short period mode is heavily damped and decays rapidly after the doublet is injected, however, the phugoid is more lightly damped and is still evident at the completion of the simulation. These observations are consistent with discussions in Prouty (1990) and Bramwell (1990).

5.3.1b Helicopter Mode - Doublet in Lateral Stick

The plots showing the response of the vehicle to a 1 second, 10% doublet in lateral stick are shown in Figures 5.17 and 5.18. With reference to these figures it can be seen that coupling exists between the longitudinal and lateral flight states in response to this control input. From Figure 5.17 it is evident that roll rate responds instantly to the doublet in lateral stick with a maximum roll rate of approximately 0.22 radians per second being achieved. In helicopter mode, roll authority is exerted by increasing the collective of one rotor relative to the other and this generates an unbalanced torque which excites the witnessed yawing motion. It can be seen that this yawing motion is lightly damped and it is suspected that, once initiated, the motion is driven by uncommanded inputs of differential longitudinal cyclic as described in Section 5.1 of this Chapter.

The Y_{body} velocity component, v_a , is seen to follow the vehicle bank angle, ϕ_f , this is because the gravitational force component, $g \cos\theta_f \sin\phi_f$, exerts a greater influence in the Y_{body} body direction as bank angle increases. This force generates an acceleration in the Y_{body} direction and hence the witnessed variation in the lateral velocity component v_a is produced.

The average rotor forces and moments produced during this simulation are shown in Figure 5.19 and from this it can clearly be seen that the doublet of lateral stick has an immediate effect on F_y , M_x , and M_z . From the plot of M_x it is evident that the doublet produces a peak to peak oscillation of $\pm 30000\text{Nm}$ in rolling moment due to the differential thrust, a similar oscillation of $\pm 3000\text{Nm}$ is witnessed in M_z due to the differential torque as previously described. It can also be seen that the F_y force initially follows the roll rate, p , this is because the v_{hb} component of hub velocity is dependent upon the the sum of the following two products $-p z_{cg} + l_s p \cos \gamma$ (as given by Equation 2.6). Thus, as the vehicle rolls to the right in helicopter mode, the v_{hb} velocity component increases and this promotes lateral flapping in a similar manner to the mechanism previously described in the longitudinal case. This lateral flap tends to orientate the rotor tip path plane to the left as the vehicle rolls to the right (and vice versa) and hence produces the initial response in F_y . After the initial response decays, oscillations of approximately 7 seconds period remain in the plot of F_y ; these are generated as a result of the witnessed oscillations in the lateral velocity component v_a by a similar mechanism to that previously described in the longitudinal case.

The coupling to the longitudinal states is triggered by the immediate response of the rotor pitching moment to the control input. From Figure 5.19 it can be seen that the doublet produces an immediate oscillation of $\pm 100\text{Nm}$ in the rotor pitching moment and this is sufficient to excite the phugoid mode. Hence, the witnessed oscillations in longitudinal rotor forces and moments with vehicle airspeed and pitch angle are produced in a similar manner to that described in Section 5.3.1. It should however be noted that the peak to peak oscillations of these longitudinal states are considerably reduced over those obtained when the combined collective or longitudinal stick controls were perturbed.

The plots shown in Figure 5.18 of vehicle bank angle, ϕ_f , and heading angle, ψ_f , show that the vehicle enters a turn to the right when the doublet is initiated and this is consistent with the initial right input of lateral stick. The vehicle does not, however, roll wings level once the sequence of control inputs has been completed and 0.2° of bank is evident on completion of the simulation - this bank angle produces the linearly increasing heading angle which is witnessed from $t=15$ seconds until the completion of the simulation. This behaviour suggests that the vehicle has some instabilities within its flight envelope.

5.3.1c Helicopter Mode - Doublet in Longitudinal Stick

With reference to Figure 5.20 it can be seen that the vehicle demonstrates a similar response to the doublet of longitudinal stick as that exhibited to a doublet of combined

collective. In both cases only the longitudinal states are excited with no coupling to the lateral states being present. From the plots of the longitudinal states it can be seen that both the short period and phugoid modes are excited. The short period mode shows a pitch down and acceleration in response to the forward stick displacement; this is followed by a pitch up and deceleration as the input is reversed. After the short period mode decays, the phugoid is evident in the responses of vehicle pitch attitude, θ , and X_{body} velocity component, u_a ; this motion is driven by the same mechanism as described in Section 5.3.1. As there is no coupling to the lateral states the vehicle heading angle, ψ_f , and bank angle, ϕ_f , remain constant throughout the simulation.

5.3.1d Helicopter Mode - Doublet in Pedal

The response of the vehicle to a 10% doublet in pedal is given in Figures 5.22 and 5.23. With reference to these figures it can be seen that similar coupling exists between the lateral and longitudinal states as was experienced when the doublet of lateral stick was applied. From Figure 5.22 it is evident that the primary response of the vehicle to the input of right pedal is a yaw rate of 0.05 radians per second to the right and when the input is reversed the vehicle achieves a yaw rate of similar magnitude in the opposite direction. This disturbance subsequently excites a similar yawing motion to that witnessed in Section 5.3.1b and it is suspected that this is again attributable to the previously described uncommanded inputs of differential longitudinal cyclic. A significant adverse roll (maximum of +/-0.04 radians per second) is evident throughout the simulation and this response is again attributable to the uncommanded input of differential longitudinal cyclic. As described in Section 5.1, this effect causes greater longitudinal flapping on the rotor towards the outside of the turn than that experienced by the rotor towards the centre of the turn. The outboard thrust vector is therefore orientated further aft than that of the inboard rotor and hence a smaller F_z force is generated by the outboard rotor; this generates the adverse rolling moment. In this example the right rotor produces a F_z component of -29093N at $t=2$ seconds compared to -28112N generated by the left rotor at the same instant. Consequently, an adverse rolling moment of -4931Nm is produced and the vehicle rolls to the left (at 0.030 radians per second) whilst yawing to the right. When the pedal displacement is reversed then the vehicle is seen to roll to the right by a similar amount (0.045 radians per second) whilst yawing to the left. This motion is lightly damped and is seen to continue for the remainder of the simulation with progressively decreasing amplitude. Such coupling between roll and yaw is also experienced when a doublet in lateral stick is applied but is less obvious in Figure 5.17 due to the axis scaling utilised on the graph depicting roll response.

From Figures 5.22 and 5.23 it can be seen that the phugoid mode is excited by the pedal input and, as in the lateral stick case discussed in Section 5.3.2, this is attributable to a disturbance in the pitching moment produced by the rotors as the control input is injected. A slight instability in vehicle bank angle and heading angle is evident towards the end of the simulation and this effect is also discussed in Section 5.3.1b.

5.3.1e Helicopter Mode - Doublet in Combined Lateral Stick

The response of the vehicle to a doublet in combined lateral cyclic is shown in Figures 5.24 and 5.25 and from these figures it can be seen that the vehicle's primary response to this control input is demonstrated in the lateral states. A roll to the right of approximately 0.025 radians per second and a lateral velocity component, v_a , of 0.1 ms^{-1} , also to the right, are produced as the initial displacement of combined collective is input. On reversal of this control, the vehicle tends to roll and sideslip to the left and this behaviour is consistent with the sequence of applied control inputs. After the doublet is injected, oscillations in lateral velocity and roll are produced (the peak to peak amplitude in roll is small relative to the response during the period when the controls are input and is therefore not visible on the plot) and the period of these oscillations is approximately 7 seconds. Such a characteristic mode was evident in the response of the vehicle to a doublet in lateral stick and this behaviour is discussed in Section 5.3.1b. From Figure 5.24 it is evident that a small yaw rate (peak of 0.007 radians per second) is produced during the simulation and that this response follows the lateral velocity component v_a . This yawing behaviour is generated as a result of the rotor flapping motion produced in response to the lateral velocity component, v_a . As stated in Section 5.3.1b the main effect of this behaviour is to produce an increase in lateral flapping (which generates the oscillations in roll rate). However, as the rotors are acting as second order systems operating out of resonance (Prouty 1990, Bramwell 1986) the lag between applied force and maximum blade flap is less than 90° . Consequently, some secondary longitudinal flapping motion is also generated and, as the rotors are rotating in opposite directions, this produces aft flap on the right rotor and forward flap on the left rotor for a sideslip to the right. Hence, a small (positive) uncommanded input of differential longitudinal cyclic is generated with positive lateral velocity (and vice versa) and this drives the witnessed yawing motion.

It can be seen that there is coupling to the longitudinal states from this control input and this is again attributable to a pulse in the F_z rotor forces and this is described in Sections 5.3.1b and 5.3.1d. The level of coupling produced in this case is smaller than that generated by the lateral stick and pedal doublets and therefore the peak

to peak oscillations in the longitudinal states is reduced. Consequently, the scaling of the longitudinal plots is such that the periodic, n per rev, oscillations in the Z_{body} velocity component, w_a , and pitch rate can be seen; these oscillations are driven by the periodic rotor forces and moments. It should be noted that only 1 in 50 data points have been plotted when producing these graphs in order to reduce the amount of output data to a manageable level. Consequently, some data has been sacrificed and this leads to the apparent 'strobing' in the amplitude of the witnessed oscillations in w_a and pitch rate.

Time histories of the vehicle attitudes are shown in Figure 5.25 where the slight instability in bank angle is again evident. The roll to the right, increase in heading to the right and pitch response are all consistent with the previous discussion of the time histories for the body axis states.

5.3.2a Transitional Flight at 45° Nacelle - Doublet in Combined Collective

The vehicle response to a 1 second doublet in combined collective whilst flying at 45° nacelle angle is shown in Figures 5.26 and 5.27. With reference to these figures it is apparent that the response produced is similar to that described in Section 5.3.1a where the vehicle was flying in helicopter mode and the same control sequence applied. However, some subtle differences do exist between the two cases mainly because the rotor thrust vectors have a larger X_{body} component at 45° nacelle angle than in helicopter mode. This forward orientation of the thrust vectors produces a negative pitching moment on the vehicle centre of gravity which would tend to cause the vehicle to pitch down. An aft input of longitudinal stick, 12%, and large pitch attitude, 20°, are both required to offset this tendency and produce the 80 Knot trimmed level flight. Another manifestation of the more forward orientation of the thrust vectors is that the combined collective now exerts a more direct influence on the X_{body} velocity component, u_a . This is evident from Figure 5.26 where the doublet is seen to have an immediate effect on this parameter with an oscillation of $\pm 0.75\text{ms}^{-1}$ being produced in u_a as a direct consequence to the sequence of applied control displacements.

The velocity component acting in the Z_{body} direction, w_a , pitch rate, q , and pitch angle, θ , are also seen to respond immediately to the doublet in combined collective and the oscillations produced in these parameters form the short period mode as described in Section 5.3.1a. Five seconds into the simulation the short period oscillations decay to zero and the phugoid is once again apparent.

As described in Section 5.3.1a, there is no coupling to the lateral states and therefore the lateral velocity, angular velocities and attitudes remain consistently zero throughout the simulation.

5.3.2b Transitional Flight at 45° Nacelle - Doublet in Lateral Stick

Time histories showing the vehicle's response to a 2 second doublet in lateral stick whilst in transitional flight is given in Figures 5.28 and 5.29.

From Figure 5.28 it can be seen that the roll rate, p , and yaw rate, r , both respond instantly to the sequence of control displacements. The initial roll response is similar in magnitude to that experienced in helicopter mode (as discussed in Section 5.3.1b), however, the initial response in yaw is larger in amplitude and 180° out of phase to that previously observed in helicopter mode and this will now be discussed. In transitional flight, control authority is exerted by a blend of aerodynamic control surface displacements and rotor blade pitch deflections; as described in Section 2.3.1 of Chapter 2. From the description given in Sections 2.3.1 and 2.3.2 it can be seen that a lateral stick displacement generates control forces and moments by means of an aileron deflection and differential collective input. During transitional flight the primary authority of the differential collective shifts from roll to yaw as the nacelles are tilted forwards, therefore, lateral stick deflections produce variations in both rolling and yawing moments in this regime. Consequently, the yawing motion produced by the doublet in lateral stick is more significant in this transitional case than that experienced when the same doublet was applied to the vehicle in helicopter mode. The mechanism by which the input of differential collective produces this yawing motion also changes as the nacelles are transitioned from helicopter mode. At low nacelle angles the yawing motion is produced as a result of an asymmetry between the right and left in rotor torques, whereas, at higher nacelle angles the yaw is generated by an asymmetry in the magnitude of the rotor thrust vectors. The initial response in yaw rate is therefore 180° out of phase to that produced in helicopter mode because the yawing moment produced by the rotors is generated by a different mechanism.

As in the comparable helicopter mode case, described in Section 5.3.1b, the doublet in lateral stick again produces oscillations in the lateral velocity component, v_a , however, in this example the response of v_a does not initially follow the vehicle bank angle, ϕ as occurred in helicopter mode. This is because the dominant term in the relevant equation of motion, quoted at the beginning of Chapter 2, is now the inertial term, $-(ru_a - pw_a)$, instead of the gravitational term, $g\cos\theta\sin\phi$, as in the helicopter mode case. Therefore the initial lateral velocity response of the vehicle differs between the two cases. As the simulation continues beyond $t=7$ seconds the magnitude of the

roll and yaw rates decreases and the gravitational term becomes dominant, therefore, the lateral velocity component tends to follow the vehicle bank angle towards the end of the simulation.

From Figures 5.28 and 5.29 it can be seen that coupling exists to the longitudinal states and the phugoid is excited, the mechanism by which this occurs is described in Section 5.3.1b.

The time histories of the vehicle Euler attitudes are shown in Figure 5.29, from this it can be seen that the doublet generates a roll and increase in heading to the right and this is consistent with the response of the body axis states.

5.3.2c Transitional Flight at 45° Nacelle - Doublet in Longitudinal Stick

The response of the vehicle to a 1 second doublet in longitudinal stick is shown in Figures 5.30 and 5.31. From these plots it can be seen that the response produced is similar to that demonstrated in helicopter mode when the same sequence of control inputs was applied. In both cases only the longitudinal states are excited with no coupling to the lateral states being present. The heavily damped short period mode is again excited in immediate response to the control input with oscillations attributable to the phugoid being visible during the final 25 seconds of the simulation. These characteristics were evident in the helicopter mode case and are discussed in Section 5.3.1c.

5.3.2d Transitional Flight at 45° Nacelle - Doublet in Pedal

Time histories depicting the vehicle motion excited by a doublet in pedal are shown in Figures 5.32 and 5.33.

From these figures it can be seen that the primary response of the vehicle is demonstrated in the lateral states with a roll rate of -0.04 radians per second and a yaw rate of 0.025 radians per second being generated as the initial pedal displacement is made. This strong coupling between roll and yaw is attributable to the fact that control authority from a pedal input is exerted by a blend of rudder deflection and differential longitudinal cyclic blade displacements as described in Chapter 2, Sections 2.3.1 and 2.3.2. As described in Section 5.3.2b the axis round which rotor controls exert their influence alter as the nacelles are *rotated*. For the differential longitudinal cyclic input a yawing moment is generated in helicopter mode, however, in aeroplane mode a rolling moment is produced by the same control. Therefore, at 45° nacelle an input of right pedal generates a both a yaw to the right and a roll to the left and this effect is witnessed in the response of these parameters shown in Figure 5.32. From this figure

it can be seen that the vehicle yaws to the left and rolls to the right on reversal of the pedal input and this is consistent with an input of left pedal.

Small oscillations, (maximum of $\pm 0.5\text{ms}^{-1}$) are produced in the lateral velocity component, v_a , and it is suspected that these are attributable to inertial forces, $-(ru_a - pw_a)$, rather than gravitational effects ($g\cos\theta\sin\phi$) because only small bank angles are produced.

With reference to the time histories of the longitudinal states it can be seen that the phugoid mode is once again excited by the pedal doublet. As in Section 5.3.1e the n per rev oscillations in pitch rate, q , can be seen in the time history of this parameter.

From the graphs depicting the response of the vehicle attitudes it can be seen that a bank to the left and increase in heading to the right are produced by the right pedal input, on reversal of this control, the bank angle tends to the right and the heading angle tends to the left. This is consistent with the preceding discussion on the body axis states.

5.3.3a Aeroplane Mode - Doublet in Combined Collective

The motion generated by a doublet in combined collective, whilst the vehicle is configured in aeroplane mode, is shown in Figures 5.34 and 5.35.

From Figure 5.34 it can be seen that the 4° increase in blade root pitch produces a rapid acceleration in the X_{body} velocity component, u_a , of approximately 2ms^{-1} . This immediate response is generated because the rotor thrust vectors are now orientated closely parallel to the X_{body} axis and therefore the combined collective control strongly influences the rotor force component acting in this direction. As the rotor hubs are positioned above the vehicle centre of gravity, the increased thrust produced by the initial control displacement causes the vehicle to pitch down at approximately 0.075 radians per second, this motion causes the vehicle pitch attitude to move from 2.5° nose up to 1° nose down and this shift in orientation leads to the reduction in the longitudinal velocity component, w_a . On reversal of the combined collective input a deceleration in u_a is witnessed whilst the vehicle pitches up and accelerates in w_a . This motion excites the short period mode which is seen to decay to zero approximately 3 seconds after the doublet is injected. In this case oscillations due the phugoid mode are less significant than in the previous examples because the orientation of the nacelles is such that the interaction between longitudinal flapping motion and velocity, described in Section 5.3.1a, no longer occurs. The phugoid mode

is therefore heavily damped and the vehicle returns to its original trim state approximately 15 seconds into the simulation.

As in the helicopter and transitional examples there is no coupling to the lateral states when an input of combined collective is applied.

5.3.3b Aeroplane Mode - Doublet in Lateral Stick

The response of the vehicle to a 10% doublet in lateral stick is shown in Figures 5.36 and 5.37, from these figures it can be seen that the primary response of the vehicle is demonstrated in the lateral states.

As the right input is applied the vehicle rolls to the right at 0.25 radians per second and also yaws to the right at 0.02 radians per second. This coupling between roll and yaw is created because the roll rate effectively increases the rotational velocity of one rotor relative to the other, as shown by Equation 2.8. Hence, the rotors tend to produce differential thrust (in this case F_x for the right rotor is 1880N and for the left is 2641N at $t=2$ seconds), which generates a yawing moment (3708Nm in this case) into the turn. This effect can be thought of as an uncommanded input of differential collective and is documented in the Bell-Boeing Tilt-Rotor Handling Qualities Short Course Notes. On reversal of the stick displacement the vehicle is seen to roll and yaw to the left by a similar mechanism.

The oscillations in lateral velocity component, v_a , are generated as a consequence of the previously described variations in the inertial and gravitational lateral force components.

5.3.3c Aeroplane Mode - Doublet in Longitudinal Stick

The response to a doublet in longitudinal stick is shown in Figures 5.38 and 5.39 and from these figures it can be seen that the motion excited is purely in the longitudinal states with no coupling to the lateral states being produced.

From the time histories of the longitudinal states it can be seen that the vehicle pitches down and accelerates as the forward stick displacement is applied, on reversal of the input, the vehicle pitches up and decelerates and this motion is consistent with the sequence of control displacements applied. Both the short period and phugoid modes are excited by this sequence of control displacements with a maximum pitch rate of 0.6 radians per second being produced as the doublet is injected. As described in Section 5.3.3a the phugoid is heavily damped in aeroplane mode and therefore the

vehicle nearly regains the original 200 Knot level flight trim on completion of the simulation.

5.3.3d Aeroplane Mode - Doublet in Pedal

The motion excited by a 10 percent, 2 second doublet in pedal is shown by the time histories given in Figures 5.40 and 5.41.

From these figures it can be seen that the primary response of the vehicle is demonstrated in roll and yaw. As the right pedal is applied the vehicle yaws and rolls to the right with the peak roll rate lagging the peak yaw rate by approximately 1.5 seconds. The rolling motion is generated as a result of differential lift produced by the wings as the yaw rate develops - the wing towards the outside of the yawing turn experiences a higher dynamic pressure than the wing towards the centre of this turn, differential lift is generated and a rolling moment therefore produced. On reversal of the pedal input the vehicle is seen to yaw and roll to the left by a similar mechanism. The oscillations produced are heavily damped and decay 15 seconds into the simulation.

The oscillations in lateral velocity component, v_a , are generated as a result of variations in the lateral gravitational and inertial forces - these effects are discussed in previous sections of this chapter.

The time histories of the longitudinal flight states show that short period and phugoid oscillations are produced during this simulation and it is suspected that this motion is excited by an acceleration in vehicle pitch attitude, θ . From the equations of motion given at the beginning of Chapter 2, it can be seen that an acceleration is produced in θ if the vehicle banks and yaws concurrently (as occurs in this simulation); the resulting increase in pitch attitude then triggers the motion witnessed in the longitudinal states. The resulting oscillations are however heavily damped and the vehicle is seen to have regained the initial 200 Knot level flight trim by the end of the simulation.

5.4 Transitional Time Histories

Tilt-rotor aircraft exhibit highly non-linear behaviour throughout their flight envelope, mainly due to non-linear aerodynamic characteristics and strong coupling between control states (Marr and Roderick, 1974), and this creates difficulties when attempting to force the vehicle to follow a prescribed flight path. One concept recognised to be of value when controlling the trajectory of vehicles with such non-linearities is the use of systems which incorporate model inversion in the feed forward path (Smith and Meyer,

1987). In this technique a fully non-linear simulation model of the vehicle is continually inverted in real time to determine the control inputs necessary to produce the demanded flight path. A methodology similar to this has been used to predict the control inputs necessary to obtain a specified flight path during full transitions to and from aeroplane mode.

Essentially, the trimming algorithm described in Chapter 3 performs a model inversion whereby a desired trajectory axis trim state is specified and the required controls ascertained. If a manoeuvre is divided into discrete intervals, then the trimming algorithm can be used to ascertain the necessary controls to recreate that manoeuvre at discrete points through its history. By linking this series of control inputs together a trim map which details the necessary scheduling of controls throughout the manoeuvre can be generated and subsequently used to drive the vehicle along the required flight path. This technique has been used to generate trim maps which predict the control inputs required for GTILT to follow a prescribed flight path during full transitions to and from aeroplane mode; these are given in Figures 5.42 and 5.44 respectively.

When generating these trim maps the transition was broken down into six equal segments with the trim algorithm establishing the control inputs necessary to produce the specified flight path at the end of each interval. For a transition from helicopter to aeroplane mode the flight path was defined as follows:-

1. The transition is initiated 5 seconds into the simulation and completed 15 seconds later.
2. Initial velocity of 80 Knots in helicopter mode with a linear acceleration to 120 Knots through the transition to aeroplane mode.
3. Zero angle of climb, turn rate, bank angle or sideslip specified throughout the manoeuvre.
4. A fifth order polynomial, $\gamma(t)$, was used to define the transitional profile of the nacelles with the coefficients being evaluated to satisfy suitable boundary conditions for γ , $\dot{\gamma}$ and $\ddot{\gamma}$.
5. Rotor speed and flap setting were maintained constant throughout the transition.

When transitioning from aeroplane to helicopter mode the above velocity and nacelle tilt profiles were reversed.

With reference to Figures 5.42 and 5.44 it can be seen that the profile of longitudinal stick displacements required to produce this flight path is highly

non-linear. This is attributable to the rotor wake and wing downwash modelling which causes the horizontal stabiliser to produce non-linear pitching moment variations with airspeed and nacelle incidence.

Flight path time histories for the transition from helicopter to aeroplane mode are given in Figure 5.43. From this figure it can be seen that the requested linear acceleration from 80 Knots to 120 Knots is achieved with only a small, heavily damped oscillation being present at the end of the transition. The specified zero angle of climb is not however maintained throughout the transition and a maximum climb angle of -15° is produced. It is suspected that this is because the trim map details the control inputs required to produce a series of steady state trims and consequently neglects the transitory vehicle dynamics generated when these states are linked together to form a flight path. The vehicle pitch attitude is unspecified when the trim map is constructed but can be seen to follow the sequence of longitudinal stick displacements.

Figure 5.43 also shows the accuracy by which the trim algorithm predicts the control displacements necessary to produce a specified trim. It can be seen that the specified trimmed aeroplane mode flight path is maintained for the duration of the simulation once the transition is completed.

With reference to Figure 5.45 it can be seen that the specified flight path is poorly replicated when transitioning from aeroplane to helicopter mode. It is evident that the phugoid mode is excited by the sequence on longitudinal stick displacements and this produces the oscillations in velocity, climb angle and pitch attitude. As described in Section 5.3.1a, the phugoid mode is lightly damped in helicopter mode and consequently the steady state trim is not obtained until approximately 140 seconds after the transition is completed.

From Figure 5.47 it can be seen that trim maps are more accurate when predicting the control displacements necessary to perform transitions carried out over a longer time period. In this case the transition is again to helicopter mode but is now carried out over 100 seconds and it is evident that the specified flight path is more closely replicated than in the 15 second transition. This is because the longitudinal stick displacements are input at a lower frequency and therefore do not excite the phugoid mode. Also, the vehicle accelerations are considerably reduced and consequently the manoeuvre more closely resembles the series of linked trim states on which the trim map was based.

It is felt that the results presented in this chapter demonstrate that GTILT contains no significant anomalies in its formulation. The novel periodic trimming

algorithm derived in Chapter 3 is shown to provide rapid convergence to a wide range of tilt-rotor trim states and the author recognises that this capability has greatly assisted in the development of GTILT to its current status. The dynamic responses produced by GTILT contain no anomalies and provide strong encouragement that the model has been formulated correctly and could therefore be used with confidence as a design tool.

The reader is directed towards the work of McVicar and Bradley (1990) where the rotor model derived in Chapter 2 was verified against an established rotorcraft simulation, HELISTAB (Padfield 1981). The levels of agreement obtained were extremely encouraging and promoted a high level of confidence in the formulation of the rotor model used in GTILT.

Chapter 6

CONCLUSIONS AND FUTURE WORK

6.1 Conclusions

The following achievements have been made during the course of this project:-

1. A mathematical simulation model, GTILT, has been developed in order to describe the behaviour of a generic tilt-rotor configuration. The main features of GTILT and the reasoning for their inclusion are given by the following:-

- a) The rotor forces and moments are generated by two contra-rotating rotors both of which are modelled by the individual blade algorithm derived in Chapter 2. This modelling technique allows the specification of representative blade geometries and aerodynamic characteristics and therefore produces a higher level of fidelity than would have been available from a disc model.
- b) The aerodynamic forces and moments acting on each of the main airframe components (wing, fuselage, horizontal stabilisers and vertical fins) have been considered separately and are modelled by means of look-up tables for aerodynamic force and moment co-efficients. This technique best facilitates the simulation of rotor wake impingement on the airframe and allows the user a large amount of freedom in specifying component geometries and aerodynamic properties.
- c) Rotor wake impingement of the wing and horizontal stabiliser has been included and this exerts a major influence on the overall performance of the vehicle. In particular, impingement of the rotor upwash on the horizontal stabiliser strongly effects the overall vehicle pitching moment and therefore has a direct bearing on the longitudinal stick position necessary to produce trimmed flight or to perform a specified manoeuvre. In the worst case this can lead to unacceptable adverse stick gradients which may have to be eliminated by means of augmented control or redesign of the vehicle configuration.

d) Control authority is applied through a blend of aerodynamic control surface displacements and blade root pitch deflections. The gearing between piloted stick displacement and control deflection is specified by means of a user defined look-up table. This blend of control states had to be included before GTILT would be of value in the design and formulation of tilt-rotor control laws.

2. In general, the forces and moments produced by a helicopter rotor are oscillatory in nature and, by modelling the behaviour of each blade individually, this oscillatory characteristic can be simulated. In the trim, the rotor forces and moments are periodic about a fixed mean and this is reflected in the trimmed flight state which is also periodic about a fixed mean. Therefore, the trimming algorithm associated with an individual blade model must be capable of producing a specified periodic trim state. An innovative trimming algorithm was developed to ascertain the correct initial conditions and control states necessary to produce a given specified periodic trim. This algorithm, derived in Chapter 3, was found to be robust and is capable of producing rapid convergence for most specified trim states.

3. The latest generation of rotor models, such as the individual blade model used in GTILT, can yield high levels of fidelity but are numerically intensive and consequently impractical when implemented on most computing facilities. However, the benefits offered by such models have become more accessible to rotorcraft simulationists with the advent of the new computational hardware. Parallel processing is one new technique which is recognised to be of value when applied to individual blade rotor modelling. GTILT was parallelised and implemented on a transputer architecture which was specially designed to support generic rotorcraft simulations. When simulating a rotorcraft with two three bladed rotors, GTILT was found to produce acceptable performance for use as a design tool. It is envisaged that the parallelised GTILT could be used to support real-time simulations, however, modifications to the existing software would be required in order produce the required levels of performance.

4. GTILT has been configured using XV-15 data and a series of predicted longitudinal trim states, evaluated at a range of nacelle incidences and airspeeds, were verified against those an established rotorcraft model. Generally correlation between the two models was found to be excellent with the slight disparities present being explicable and mainly attributed to differences in the modelling of the rotor wake impingement on the horizontal stabiliser and wing. Qualitative verification was also obtained for a range of lateral trim states, again at various nacelle incidences and

airspeeds, and no obvious inconsistencies were discovered with all witnessed trends being accountable.

5. GTILT was used to predict the dynamic response of the XV-15 to a range of control inputs whilst flying at various airspeeds and nacelle incidences. The results obtained were verified qualitatively and no inexplicable anomalies were discovered. It is appreciated that this by no means constitutes a comprehensive validation exercise and that good comparison with flight test data would have been significantly more conclusive. A large amount of effort was directed towards obtaining such data but regrettably none was forthcoming.

6. The trim algorithm derived in Chapter 3 can be used to generate trim maps which attempt to predict the sequence of control inputs necessary to force the vehicle to follow a prescribed flight path. Using this technique, trim maps were produced to force the vehicle to follow a specified trajectory during full transitions to and from helicopter mode.. When transitioning from helicopter mode, the trim map could accurately establish the sequence of control displacements necessary to force the vehicle to follow a prescribed flight path during a 15 second transition. However, when transitioning from aeroplane mode the manoeuvre must be carried out over a longer time period in order to avoid excitation of the phugoid mode which caused the vehicle to deviate from the specified trajectory.

From the above discussion it can be seen that GTILT is a representative tilt-rotor model capable of predicting quantitatively valid trim states and dynamic responses which appear to be qualitatively correct. Therefore, the basic aims of this project have been realised. However, it is recognised that further work is required before this model can be confidently used as a design tool

6.2 Suggestions for Future Research

The author highlights the following areas as requiring further work:-

1. It is felt that validation against flight test data should be the first stage in any future development of GTILT. Although quantitative verification of predicted longitudinal trim states has been obtained, the dynamic response and lateral trim states produced by the model still remain uncorroborated. A comparison with flight test data would illustrate any deficiencies in the existing model and associate an order of importance with the following items of remaining work.

2. In its present form the wake interaction between wing and rotor is modelled in a fairly rudimentary manner and this could be the source of inaccuracies.

The modelling of this interaction could be improved if the work of Mil et al (1966) were developed so that it was valid for the tilt-rotor configuration throughout the flight envelope. It should be noted that lifting line theory described by Kuethe and Chow (1986) represents one alternative technique by which the influence of wing proximity on the rotor performance could be ascertained

3. Asymmetric rotor wake impingement of the empennage influences the lateral moments acting on the vehicle Centre of Gravity, Marr and Sambell (1973), Marr and Roderick (1974) and Curtiss and Quackenbush (1989), and therefore effects the yaw and roll stability as described in Section 2.2.1. This effect is currently neglected in the GTILT model and should be included if the lateral flight states are to be quantitatively valid.

4. Current tilt-rotor aircraft (the V-22 and XV-15) utilise collective governing in order to control rotor speed (Bell-Boeing Short Course Notes); the pilot thrust lever is connected directly to the throttle with the governor adjusting collective pitch in order to maintain constant rotor speed. In GTILT piloted thrust lever displacements are interpreted as direct combined collective (θ_{cc}) blade pitch inputs with the rotor speed held to a constant specified value throughout the simulation. On the real vehicle, rotor speed will vary about a mean value as the pilot adjusts the thrust setting and this facet is not presently included in GTILT, therefore, modelling inaccuracies could occur. In helicopters such as the Lynx, rotor speed is rigidly governed and hence varies little with thrust variations. It is felt that rotor speed governing will be similarly rigid in this case and variations in rotor speed will not have a large effect on the behaviour of the vehicle. However, this assumption should be investigated.

5. If collective governing were included in GTILT then both rotors would no longer rotate with same angular velocity and the relationship between the periodicity of the trimmed blade states and the periodicity of the overall forces and moments would be influenced. It may be necessary to adapt the trim algorithm in order to cater for such an effect and this requires investigation.

6. The software implementation of the GTILT model is felt to be inefficient in its present form and restructuring would produce significant reductions in run time. It is recommended that the internal clock is accessed so that computational performance can be accurately ascertained and is of particular significance if real-time performance is sought. If it were not possible to access the internal clock then it is suggested that an OCCAM routine could be written as a timer.

7. The data describing the blade element aerodynamic lift and drag co-efficients is at present limited because constant values are assumed along the span. Tilt-rotor blades are designed to achieve an optimum compromise between propeller and rotor characteristics and therefore contain several aerodynamic sections along the span (Felker et al 1985). Consequently, the blade element lift and drag co-efficients will be functions of spanwise location, the facility to include such a feature is present in GTILT by means of a look-up table, however, at present the values are held constant due to lack of data. Attempts have been made to obtain lift and drag co-efficients for the blade sections on the XV-15 but have been unsuccessful, the behaviour of the blades would be more accurately represented if this data were obtained. Fidelity would be further enhanced if corrections for Mach number were also obtained because compressibility effects could then be modelled.

8. The area of the flight envelope in which simulations can be performed using GTILT is at present restricted because only limited aerodynamic data is available for the vehicle airframe. For example, the wing lift and drag coefficients are only defined for α in the range -90° to $+40^\circ$. It is suggested that the existing data is extended to cover the range -180° to $+180^\circ$ using a method similar to that quoted by Prouty (1990).

9. As stated in Chapter 1 it is hoped that GTILT will be used as a design tool in the formulation of tilt-rotor control laws. In order to fully realise this goal the model should be linearised because the user would then have more direct access to the stability and control characteristics of the vehicle. Techniques for linearising Level 1 models have long been established but the author is unaware of a corresponding methodology which is capable of dealing with the oscillatory nature of Level 2 models. This therefore represents the largest piece of work still to be carried out but is an important area of research because, if successful, the enhanced levels of fidelity offered by the latest generation of simulation models would become more readily available to control law designers.

Appendix One

The rotor inflow and blade flap states can be defined in terms of the time dependant functions F and G respectively:-

$$\frac{dv_{if}}{dt} = F(t, v_{if}, \beta)$$

$$\frac{d^2\beta}{dt^2} = G(t, v_{if}, \beta)$$

therefore, the following 4th order Runge-Kutta scheme can be used to integrate the blade flap and rotor inflow states:-

$$v_{if_{tstep+1}} = v_{if_{tstep}} + \frac{1}{6} \{K_1 + 2 K_2 + 2 K_3 + K_4\}$$

$$\beta_{tstep+1} = \beta_{tstep} + \frac{1}{6} \{L_1 + 2 L_2 + 2 L_3 + L_4\}$$

where:-

$$K_1 = h F(t, v_{if}, \beta) \quad , \quad L_1 = h G(t, v_{if}, \beta)$$

$$K_2 = h F\left(t + \frac{h}{2}, v_{if} + \frac{K_1}{2}, \beta + \frac{L_1}{2}\right) \quad , \quad L_2 = h G\left(t + \frac{h}{2}, v_{if} + \frac{K_1}{2}, \beta + \frac{L_1}{2}\right)$$

$$K_3 = h F\left(t + \frac{h}{2}, v_{if} + \frac{K_2}{2}, \beta + \frac{L_2}{2}\right) \quad , \quad L_3 = h G\left(t + \frac{h}{2}, v_{if} + \frac{K_2}{2}, \beta + \frac{L_2}{2}\right)$$

$$K_4 = h F\left(t + \frac{h}{2}, v_{if} + K_3, \beta + L_3\right) \quad , \quad L_4 = h G\left(t + \frac{h}{2}, v_{if} + K_3, \beta + L_3\right).$$

Appendix Two

The Peters-HaQuang model incorporated in GTILT takes the form:-

$$[M] \begin{bmatrix} \dot{w}_{ifh} \\ \dot{q}_{ifh} \\ \dot{p}_{ifh} \end{bmatrix} + [L]_{hnl}^{-1} \begin{bmatrix} w_{ifh} \\ q_{ifh} \\ p_{ifh} \end{bmatrix} = \begin{bmatrix} T_h \\ -L_h \\ -M_h \end{bmatrix}_{\text{aerodynamic}}$$

where:-

$$[L]_{hnl}^{-1} = [V] [T]^T [L]^{-1} [T]$$

$$[L]_{hnl}^{-1} = [V] [\tilde{L}]$$

The components of $[\tilde{L}]$ have been evaluated using the symbolic algebraic manipulation package, Mathematica, and are given by the following:-

$$\tilde{T}_{11} = \rho\pi R^2 \frac{d e}{b^2 e + 0.5 d e}$$

$$\tilde{T}_{12} = -\rho\pi R^2 \frac{b e \sin\psi_w}{b^2 e + 0.5 d e}$$

$$\tilde{T}_{13} = -\rho\pi R^2 \frac{b e \cos\psi_w}{b^2 e + 0.5 d e}$$

$$\tilde{T}_{21} = -\rho\pi R^3 \frac{b e \sin\psi_w}{b^2 e + 0.5 d e}$$

$$\tilde{T}_{22} = -\rho\pi R^3 \frac{((b^2 + 0.5d) \cos^2\psi_w + 0.5e \sin^2\psi_w)}{b^2 e + 0.5 d e}$$

$$\tilde{T}_{23} = -\rho\pi R^3 \frac{(b^2 + 0.5d - 0.5e) \sin 2\psi_w}{2(b^2 e + 0.5 d e)}$$

$$\tilde{T}_{31} = \rho\pi R^3 \frac{b e \cos\psi_w}{(b^2 e + 0.5 d e)}$$

$$\tilde{T}_{32} = -\rho\pi R^3 \frac{(b^2 + 0.5d - 0.5e) \sin 2\psi_w}{2(b^2 e + 0.5 d e)}$$

$$\tilde{T}_{33} = -\rho\pi R^3 \frac{0.5 (e \cos^2\psi_w + (2b^2 + d) \sin^2\psi_w)}{(b^2 e + 0.5 d e)}$$

where:-

$$b = \frac{15\pi}{64} \left(\frac{1 - \sin\chi}{1 + \sin\chi} \right)^{\frac{1}{2}}, \quad e = -\frac{4}{1 + \sin\chi}, \quad d = -\frac{4 \sin\chi}{(1 + \sin\chi)}$$

Appendix Three

If rotor wake and wing downwash effects are neglected then the lift and drag acting on a general airframe component, i , is given by:-

$$L_i = \frac{1}{2} \rho V_i^2 S_i C_{L_i}$$

$$D_i = \frac{1}{2} \rho V_i^2 S_i C_{D_i}$$

where C_{L_i} and C_{D_i} are functions of the component angle of attack and are specified, for the XV-15, in Appendix 4.

The velocity of the surface centre of pressure, V_i , is given by the following cross product:-

$$V_i = \begin{bmatrix} u_a \\ v_a \\ w_a \end{bmatrix} + \begin{vmatrix} \mathbf{i} & \mathbf{j} & \mathbf{k} \\ p & q & r \\ x_i & y_i & z_i \end{vmatrix}$$

where the co-ordinates of the component centre of pressure (x_i, y_i, z_i) are given in Appendix 4 by Table A4.10.

The orientation of the local axis set relative to the body axis set is shown in Figure A3.1, to convert the lift and drag from local to body axis components the following sequence of rotations is performed:-

$$\begin{bmatrix} \mathbf{i}_b \\ \mathbf{j}_b \\ \mathbf{k}_b \end{bmatrix} = \begin{bmatrix} \cos\alpha & 0 & -\sin\alpha \\ 0 & 1 & 0 \\ \sin\alpha & 0 & \cos\alpha \end{bmatrix} \begin{bmatrix} \cos\beta & -\sin\beta & 0 \\ \sin\beta & \cos\beta & 0 \\ 0 & 0 & 1 \end{bmatrix} \begin{bmatrix} \mathbf{i}_t \\ \mathbf{j}_t \\ \mathbf{k}_t \end{bmatrix}$$

The body axis moments acting on the vehicle C.G. generated as a result of the aerodynamic lift and drag forces acting on the surface are therefore given by:-

$$\begin{bmatrix} L \\ M \\ N \end{bmatrix} = \begin{vmatrix} \mathbf{i}_b & \mathbf{j}_b & \mathbf{k}_b \\ F_x & F_y & F_z \\ x_i & y_i & z_i \end{vmatrix}$$

Appendix Four

A 4.1. XV-15 Aerodynamic Data

The following XV-15 configurational data obtained from wind tunnel testing is quoted by Harendra et al (1973) as follows:-

α_{hs}	Elevator Deflection						
	-20°	-10°	-15°	0°	10°	15°	20°
-90.0°	0.0	0.0	0.0	0.0	0.0	0.0	0.0
-80.0°	-0.220	-0.285	-0.360	-0.425	-0.560	-0.580	-0.600
-70.0°	-0.380	-0.490	-0.600	-0.720	-0.865	-0.890	-0.920
-60.0°	-0.510	-0.640	-0.770	-0.900	-1.060	-1.090	-1.120
-50.0°	-0.600	-0.745	-0.890	-1.002	-1.175	-1.205	-1.240
-40.0°	-0.640	-0.800	-0.960	-1.050	-1.240	-1.260	-1.300
-36.0°	-0.600	-0.735	-0.930	-1.030	-1.230	-1.255	-1.290
-28.0°	-0.560	-0.680	-0.850	-1.010	-1.210	-1.240	-1.280
-24.0°	-0.500	-0.615	-0.780	-0.980	-1.185	-1.220	-1.260
-18.4°	-0.480	-0.540	-0.660	-0.920	-1.200	-1.210	-1.240
-17.5°	-0.450	-0.565	-0.710	-0.930	-1.260	-1.250	-1.250
-16.8°	-0.420	-0.550	-0.740	-0.990	-1.310	-1.290	-1.310
-16.0°	-0.380	-0.510	0.710	-1.120	-1.400	-1.330	-1.330
-15.6°	-0.350	-0.480	-0.700	-1.100	-1.440	-1.380	-1.350
-14.2°	-0.270	-0.400	-0.610	-1.010	-1.400	-1.550	-1.450
-12.5°	-0.150	-0.280	-0.480	-0.880	-1.310	-1.490	-1.600
-12.0°	-0.110	-0.240	-0.444	-0.852	-1.260	-1.464	-1.590
8.0°	1.330	1.180	0.976	0.568	0.160	-0.044	-0.180
12.0°	1.500	1.420	1.250	0.850	0.442	0.240	0.100
12.2°	1.480	1.430	1.270	0.860	0.450	0.260	0.120
13.0°	1.450	1.370	1.300	0.920	0.520	0.330	0.170
15.0°	1.360	1.270	1.200	1.000	0.650	0.450	0.290
16.0°	1.320	1.240	1.160	0.980	0.690	0.475	0.320
16.8°	1.320	1.200	1.150	0.940	0.700	0.490	0.340
18.0°	1.340	1.220	1.130	0.890	0.680	0.500	0.370
20.0°	1.380	1.280	1.180	0.880	0.600	0.465	0.380
24.0°	1.440	1.380	1.300	0.935	0.660	0.455	0.330
28.0°	1.500	1.440	1.370	1.000	0.730	0.500	0.380
32.0°	1.540	1.490	1.430	1.050	0.780	0.540	0.400
36.0°	1.570	1.535	1.470	1.080	0.820	0.560	0.410
40.0°	1.590	1.560	1.510	1.100	0.840	0.570	0.410

Table A4.1 - Horizontal Stabiliser Lift Co-efficient

α_{hs}	C_{dhs}
-90°	0.920
-80°	0.910
-70°	0.870
-60°	0.810
-50°	0.720
-40°	0.600
-36°	0.540
-32°	0.470
-28°	0.390
-24°	0.300
-20°	0.200
-16°	0.115
-12°	0.068
-8°	0.035
-4°	0.015
0°	0.009
4°	0.015
8°	0.035
12°	0.068
16°	0.115
20°	0.200
24°	0.340
28°	0.480
32°	0.610
36°	0.720
40°	0.800

Table A4.2 - Horizontal Stabiliser Drag Co-Efficient

β_{vt}	Rudder Deflection				
	-20°	-10°	0°	10°	20°
-90.0°	0.000	0.000	0.000	0.000	0.000
-40.0°	-1.110	-1.070	-1.000	-0.960	-0.920
-32.0°	-1.120	-1.020	-0.930	-0.840	-0.820
-28.0°	-1.090	-1.020	-0.940	-0.900	-0.870
-26.0°	-1.110	-1.070	-0.980	-0.930	-0.910
-24.0°	-1.150	-1.110	-1.030	-0.980	-0.920
-22.0°	-1.190	-1.140	-1.050	-0.980	-0.850
-20.0°	-1.220	-1.150	-1.050	-0.880	-0.740
-18.0°	-1.240	-1.140	-0.960	-0.770	-0.640
-16.0°	-1.180	-1.050	-0.860	-0.660	-0.520
-12.0°	-0.990	-0.840	-0.635	-0.450	-0.300
-8.0°	-0.76	-0.63	-0.425	-0.225	-0.090
8.0°	0.10	0.23	0.425	0.625	0.760
12.0°	0.31	0.44	0.635	0.840	0.990
16.0°	0.52	0.66	0.860	1.050	1.180
18.0°	0.64	0.77	0.960	1.140	1.240
20.0°	0.74	0.88	1.050	1.150	1.220
22.0°	0.85	0.98	1.050	1.140	1.190
24.0°	0.92	0.98	1.030	1.110	1.150
26.0°	0.91	0.93	0.980	1.070	1.110
28.0°	0.87	0.90	0.940	1.020	1.090
32.0°	0.82	0.84	0.930	1.020	1.120
40.0°	0.92	0.96	1.000	1.070	1.110
90.0°	0.00	0.00	0.000	0.000	0.000

Table A4.3.- Vertical Stabiliser Lift Co-efficient

α_{vs}	C_{dvs}
-90°	0.800
-40°	0.600
-32°	0.550
-28°	0.435
-24°	0.290
-20°	0.162
-16°	0.080
-12°	0.040
-8°	0.012
-4°	0.007
0°	0.004
4°	0.007
8°	0.012
12°	0.040
16°	0.080
20°	0.162
24°	0.290
28°	0.435
32°	0.550
40°	0.600
90°	0.800

Table A4.4. - Vertical Stabiliser Drag Co-efficient

α_f	Flaps(-28/-17.5)°		Flaps(40/25)°		Flaps(75/47)°	
	Aeroplane Mode	Helicopter Mode	Aeroplane Mode	Helicopter Mode	Aeroplane Mode	Helicopter Mode
-90.0°			0.0	0.0	0.0	0.0
-80.0°			-0.325	-0.245	-0.235	-0.190
-70.0°			-0.520	-0.400	-0.385	-0.305
-60.0°			-0.610	-0.480	-0.450	-0.333
-50.0°			-0.590	-0.420	-0.390	-0.220
-40.0°	-1.170	-0.960	-0.410	-0.265	-0.240	-0.105
-36.0°	-1.080	-0.830	-0.400	-0.250	-0.220	-0.090
-32.0°	-1.060	-0.805	-0.425	-0.260	-0.240	-0.095
-28.0°	-1.110	-0.850	-0.515	-0.300	-0.275	-0.120
-24.0°	-1.210	-0.945	-0.660	-0.380	-0.340	-0.160
-21.5°	-1.310	-1.030	-0.690	-0.440	-0.400	-0.210
-21.0°	-1.330	-1.060	-0.680	-0.440	-0.400	-0.210
-20.0°	-1.370	-1.100	-0.640	-0.395	-0.367	-0.188
-19.2°	-1.380	-1.120	-0.580	-0.360	-0.310	-0.140
-16.0°	-1.230	-0.950	-0.320	-0.165	-0.048	-0.040
-12.0°	-0.950	-0.730	0.000	0.063	0.272	0.268
-8.0°	-0.680	-0.502	0.320	0.291	0.591	0.496
-4.0°	-0.384	-0.275	0.640	0.581	0.910	0.714
0.0°	-0.064	-0.046	0.960	0.749	1.237	0.952
4.0°	0.256	0.182	1.240	0.975	1.460	1.170
8.0°	0.576	0.408	1.490	1.205	1.680	1.390
11.0°	0.770	0.590	1.680	1.380	1.800	1.500
12.0°	0.840	0.638	1.750	1.433	1.790	1.470
13.6°	0.950	0.730	1.800	1.500	1.710	1.390
16.0°	1.100	0.864	1.700	1.400	1.600	1.240
18.4°	1.200	0.950	1.560	1.260	1.490	1.160
20.0°	1.150	0.890	1.510	1.200	1.460	1.140
24.0°	0.930	0.680	1.480	1.150	1.460	1.160
28.0°	0.870	0.630	1.480	1.200	1.540	1.290
32.0°	0.910	0.680	1.690	1.320	1.690	1.380
36.0	1.050	0.800	1.760	1.410	1.780	1.440
40.0°	1.140	0.890	1.800	1.470	1.800	1.480

Table A4.5. - Wing and Nacelle Lift Co-efficient (Flaps Extended)

α_w	Flaps(0/0)°	
	Aeoplane Mode	Helicopter Mode
-40.0°	-0.930	-0.680
-36.0°	-0.840	-0.580
-32.0°	-0.840	-0.570
-28.0°	-0.890	-0.620
-24.0°	-1.000	-0.720
-20.0°	-1.150	-0.880
-19.5°	-1.150	-0.880
-16.0°	-0.950	-0.730
-15.5°	-0.910	-0.700
-13.0°	-0.750	-0.570
-12.0°	-0.670	-0.500
-11.0°	-0.600	-0.450
-8.0°	-0.383	-0.272
-4.0°	-0.063	-0.045
0.0°	0.257	0.183
4.0°	0.577	0.412
8.0°	0.880	0.640
11.0°	1.100	0.800
12.0°	1.190	0.870
13.0°	1.260	0.930
16.0°	1.480	1.095
17.0°	1.500	1.100
20.0°	1.380	0.980
24.0°	1.220	0.800
28.0°	1.200	0.780
32.0°	1.270	0.860
36.0	1.400	0.980
40.0°	1.460	1.060

Table A4.6. - Wing and Nacelle Lift Co-efficient (Wing Clean)

α_w	Flaps(-28/-17.5)°		Flaps(40/25)°		Flaps(75/47)°	
	Aeroplane Mode	Helicopter Mode	Aeroplane Mode	Helicopter Mode	Aeroplane Mode	Helicopter Mode
-90.0°			1.180	0.930	1.145	0.900
-80.0°			1.100	0.910	1.050	0.878
-70.0°			0.930	0.855	0.890	0.822
-60.0°			0.705	0.775	0.670	0.740
-50.0°			0.565	0.665	0.507	0.640
-40.0°	0.622	0.734	0.430	0.540	0.450	0.550
-36.0°	0.566	0.682	0.335	0.468	0.400	0.525
-32.0°	0.500	0.632	0.245	0.405	0.350	0.500
-28.0°	0.430	0.575	0.180	0.352	0.309	0.480
-24.0°	0.345	0.502	0.130	0.310	0.278	0.462
-20.0°	0.255	0.422	0.090	0.282	0.260	0.450
-16.0°	0.186	0.350	0.650	0.263	0.243	0.440
-20.0°	0.130	0.298	0.058	0.253	0.246	0.445
-12.0°	0.086	0.267	0.063	0.254	0.261	0.464
-8.0°	0.055	0.248	0.081	0.282	0.288	0.494
0.0°	0.047	0.239	0.109	0.313	0.328	0.536
4.0°	0.047	0.243	0.148	0.356	0.378	0.590
8.0°	0.065	0.258	0.200	0.410	0.444	0.658
12.0°	0.095	0.284	0.275	0.490	0.530	0.728
16.0°	0.138	0.332	0.380	0.566	0.642	0.789
20.0°	0.195	0.402	0.528	0.630	0.730	0.839
24.0°	0.287	0.476	0.630	0.690	0.790	0.880
28.0°	0.414	0.540	0.710	0.748	0.838	0.920
32.0°	0.510	0.600	0.764	0.800	0.883	0.955
36.0°	0.583	0.648	0.805	0.845	0.950	0.985
40.0°	0.640	0.695	0.865	0.888	1.025	1.015

Table A4.7. - Wing and Nacelle Drag Co-efficient (Flaps Extended)

α_w	Flaps(0/0)°	
	Aeroplane Mode	Helicopter Mode
-40.0°	0.575	0.685
-36.0°	0.505	0.635
-32.0°	0.425	0.580
-28.0°	0.327	0.522
-24.0°	0.230	0.450
-20.0°	0.150	0.370
-16.0°	0.089	0.295
-12.0°	0.042	0.246
-8.0°	0.025	0.219
-4.0°	0.017	0.212
0.0°	0.017	0.212
4.0°	0.035	0.231
8.0°	0.060	0.262
12.0°	0.100	0.300
16.0°	0.162	0.354
20.0°	0.247	0.436
24.0°	0.354	0.512
28.0°	0.493	0.580
32.0°	0.600	0.642
36.0°	0.660	0.698
40.0°	0.705	0.748

Table A4.7. - Wing and Nacelle Drag Co-efficient (Wing Clean)

The following expressions, again quoted from Harendra et al (1973), have been used to model the body axis aerodynamic forces and moments acting on the vehicle fuselage:-

For α_F and $\beta_F \leq 20^\circ$

$$L_{\text{fuse}} = q_f (L_0 + L_1 \alpha_F)$$

$$D_{\text{fuse}} = q_f (D_0 + D_1 \alpha_F + D_2 \alpha^2 + D_3 |\beta_F|)$$

$$M_{\text{fuse}} = q_f (M_{\alpha f}(\alpha_F) + M_2 |\beta_F|)$$

$$Y_{\text{fuse}} = q_f (Y_0 + Y_1 \beta_F + Y_2 \beta_F |\beta_F|)$$

$$I_{\text{fuse}} = q_f (I_0 + I_1 \beta_F)$$

$$N_{\text{fuse}} = q_f (N_0 + N_1 \beta_F)$$

For $|\alpha_F| > 20^\circ$ and $|\beta_F| < 70^\circ$

$$\left. \begin{array}{l} L_{\text{fuse}} = L_{\text{fuse}} \\ D_{\text{fuse}} = D_{\text{fuse}} \\ Y_{\text{fuse}} = Y_{\text{fuse}} \\ I_{\text{fuse}} = I_{\text{fuse}} \\ N_{\text{fuse}} = N_{\text{fuse}} \end{array} \right\} \text{ at } \alpha_f = \pm 20^\circ \text{ and } \beta_f = \pm 20^\circ$$

$$M_{\text{fuse}} = M_{\text{fuse}} \quad \text{at } \alpha_f = \pm 40^\circ \text{ and } \beta_f = \pm 20^\circ$$

For $|\alpha_F| > 20^\circ$ and $|\beta_F| < 70^\circ$

$$L_{\text{fuse}} = M_{\text{fuse}} = Y_{\text{fuse}} = I_{\text{fuse}} = N_{\text{fuse}} = 0$$

$$D_{\text{fuse}} = q_f D_4$$

where the necessary constants are given overleaf in Tables A4.8, and:-

$$q_f = \frac{1}{2} \rho V_f^2.$$

Equation	Constant	Value
L_{fuse}	L_0	$0.6717m^2$
	L_1	$4.817m^2/rad$
D_{fuse}	D_0	$0.1449m^2$
	D_1	0.0
	D_2	0.0
	D_3	$0.0122m^2/rad$
	D_4	$11.61m^2$
M_{fuse}	M_2	$15.413m^3/rad$
	M_α	(Table A4.9)
Y_{fuse}	Y_0	0.0
	Y_1	$-7.665m^2/rad$
	Y_2	0.0
I_{fuse}	I_0	0.0
	I_1	$-12.168m^3/rad$
N_{fuse}	N_0	0.0
	N_1	$-38.127m^3/rad$

α_f	M_α
-40°	$-7.985m^3$
-36°	$-7.985m^3$
-32°	$-7.985m^3$
-28°	$-7.985m^3$
-24°	$-7.985m^3$
-20°	$-7.985m^3$
-16°	$-7.985m^3$
-12°	$-9.060m^3$
-8°	$-8.120m^3$
-4°	$-6.140m^3$
0°	$-4.134m^3$
4°	$-2.124m^3$
8°	$-0.320m^3$
12°	$-1.600m^3$
16°	$-2.665m^3$
20°	$-3.200m^3$
24°	$-3.200m^3$
28°	$-2.930m^3$
32°	$-2.130m^3$
36°	$-2.130m^3$
40°	$-2.664m^3$

Tables A4.8. and A4.9. Constants Required by Equations Giving Aerodynamic Forces and Moments Acting on Fuselage

A4.2 XV-15 Configurational Data

As stated at the end of Chapter 2, it is most convenient to define the location of the vehicle's components relative to some fixed reference point and, in GTILT, this point is taken to lie on the vehicle centreline with the longitudinal and vertical components coinciding with the location of the rotor shaft pivots. The locations of the vehicle's main components are defined, relative to this reference point, according to the following table:-

Component	Chord (m)	Span (m)	Area (m ²)	X _i (m)	Y _i (m)	Z _i (m)
Wing/Pylon	1.5926	9.8054	16.8154	0.2243	+/- 2.6035	0.1054
Horizontal Stabiliser	1.1948	3.9106	4.6684	-6.6040	0.0	-0.0762
Vertical Stabiliser	2.3104	1.1354	2.3458	-6.8580	+/-1.9558	0.3985
Fuselage	-	-	-	0.1778	0.0	0.4064
Pivot	-	-	-	0.0	+/-4.9027	0.0
Pylon	-	-	-	0.2108	+/-4.9027	-0.4572
Centre of Gravity (Helicopter Mode)	-	-	-	0.0241 (+/-0.0622)	0.0	0.4661

Table A4.10. Location of Vehicle Components Relative to the Reference Point

The inertia of the vehicle is within the range:-

I _{xx} :	57465	to	57465	Kg m ²
I _{yy} :	19296	to	19460	Kg m ²
I _{zz} :	67066	to	67230	Kg m ²
I _{zx} :	4000	to	4000	Kg m ²

and the nacelle inertia, $I_{yy_{nac}}$, is given by:

$$I_{yy_{nac}} = 584.436 \text{ Kg m}^2.$$

When evaluating the location of the vehicle CG using Equations 2.29. the following values were taken to define the mass of the nacelles and the position of the nacelle CG in helicopter mode:-

$$m_{nac} = 1810 \text{ kg} \quad , \quad X_{cgnac} = 0.21082 \text{ m} \quad , \quad Z_{cgnac} = -0.4572 \text{ m}$$

When performing the validation exercise described in Chapter 6 the moments of inertia were taken to be:-

$$I_{xx} = 57465 \text{ Kg m}^2 \quad , \quad I_{yy} = 19460 \text{ Kg m}^2 \quad , \quad I_{zz} = 67066 \text{ Kg m}^2$$

and an aft CG of $X_{cg} = -0.0381\text{m}$ was assumed.

A4.3. Rotor Configurational Data

Harendra et al (1973) quote the following data to define the salient rotor parameters:-

Number of Blades Per Rotor (n)	-	3
Rotor Radius (R)	-	3.81 m
Shaft Length (l_s)	-	1.4225 m
Blade Flap Inertia (I_b)	-	140 kg m ²
Flapping Spring Rate (K_B)	-	17480 Nm rad ⁻¹
Rotor Angular Velocity (Ω)		
Helicopter Mode	-	59.17 rads ⁻¹
Transitional Mode	-	59.17 rads ⁻¹
Aeroplane Mode	-	47.96 rads ⁻¹
Lift Curve Slope (a_0)	-	5.88 rad ⁻¹
Profile Drag Co-efficient (δ)	-	0.002

with the blade twist and chord distributions being defined overleaf by table A4.11:-

r_b m	Ch(r_b) m	$\theta_{tw}(r_b)$ degrees
0.0	0.4728	40.900
0.381	0.4259	36.159
0.762	0.3789	30.596
1.143	0.3556	24.007
1.524	0.3556	17.750
1.905	0.3556	13.401
2.286	0.3556	10.199
2.667	0.3556	7.649
3.048	0.3556	5.157
3.429	0.3556	2.550
3.810	0.3556	0.000

Table A4.11. - Blade Chord and Twist Distributions

A4.4. Control Limits and Gearings

The limits for the control displacements are given as:-

$$\delta X_{long} = +/- 4.8 \text{ inches}$$

$$\delta X_{lat} = +/- 4.8 \text{ inches}$$

$$\delta X_{pedal} = +/- 2.5 \text{ inches}$$

$$\delta X_{clc} = +/- 1.5 \text{ inches}$$

The gearings between piloted stick input and aerodynamic control surface displacement at all airspeeds and nacelle incidences are given by:-

$$\frac{\delta e}{\delta X_{long}} = -4.16^\circ/\text{inch}$$

$$\frac{\delta r}{\delta X_{pedal}} = 8^\circ/\text{inch}$$

$$\frac{\delta a}{\delta X_{lat}} = -3.93^\circ/\text{inch}$$

The corresponding gearing for combined longitudinal cyclic is a function of nacelle incidence and is given by table A4.13:-

Nacelle Angle (Degrees)	$\frac{\delta\theta_{1sc}}{\delta X_{long}}$ (°/inch)
0	4.200
10	4.180
20	3.960
30	3.620
40	3.200
50	2.700
60	2.080
70	1.420
80	0.724
90	0.000

Table A4.13. - Gearing Beteen Longitudinal Stick and Combined Longitudinal Cyclic

The gearing between lateral stick X_{lat} and differential collective pitch is a function of both nacelle incidednce and airspeed according to the scheduling given by Table A4.14:-

Nacelle Angle (Degrees)	$\frac{\delta\theta_{1sd}}{\delta X_{pedal}}$ (°/inch)		
	0 - 60 Knots	80 Knots	100 Knots →
0	3.20	2.080	0.800
10	3.16	2.050	0.788
20	3.02	1.950	0.750
30	2.78	1.800	0.690
40	2.45	1.590	0.610
50	2.07	1.340	0.514
60	1.606	1.040	0.400
70	1.100	0.650	0.274
80	0.560	0.360	0.140
90	0.0	0.0	0.0

Table A4.14. - Gearing Between Pedal and Differential Longitudinal Cyclic

The gearing between lateral stick input and differential collective is purely a function of nacelle incidence and is given by Table A4.15.

Nacelle Angle (Degrees)	$\frac{\delta\theta_{0d}}{\delta X_{lat}}$ (°/inch)
0	1.25
10	1.212
20	1.150
30	1.082
40	1.000
50	0.876
60	0.730
70	0.586
80	0.418
90	0.242

Table A4.15. - Gearing Between Lateral Stick and Differential Collective

The gearing for the combined lateral cyclic control X_{clc} and the corresponding blade pitch deflection θ_{1cc} is a function of nacelle incidence given by the following:-

For:

$$\gamma < 10^\circ \quad \frac{\delta\theta_{1cc}}{\delta X_{clc}} = 5.334 \text{ °/inch}$$

$$10^\circ < \gamma < 15^\circ \quad \frac{\delta\theta_{1cc}}{\delta X_{clc}} \text{ linearly washed out to } 0 \text{ °/inch}$$

$$\gamma > 15^\circ \quad \frac{\delta\theta_{1cc}}{\delta X_{clc}} = 0$$

A4.4. Rotor Wake Impingement and Wing Downwash on Horizontal Stabiliser

Harenrdra et al (1973) quote the following for the wing wake deflection, ϵ_w , on the horizontal stabiliser according to Tables A4.16. given overleaf:-

Wing Wake Deflection, ϵ_w , in Aeroplane Mode				
α_w	Flaps(-28/-17.5)°	Flaps(0/0)°	Flaps(40/25)°	Flaps(75/47)°
-90.00°	0.00°	0.00°	0.00°	0.00°
-25.00°	0.00°	0.00°	0.00°	0.00°
-17.94°	0.00°	0.00°	0.00°	2.40°
-8.82°	0.00°	0.00°	2.00°	5.48°
-2.35°	0.00°	1.92°	4.38°	7.70°
0.00°	0.80°	2.52°	5.25°	8.50°
12.00°	4.88°	6.00°	9.90°	12.58°
13.80°	5.70°	6.50°	10.75°	12.80°
16.00°	6.24°	7.18°	11.40°	12.35°
16.50°	6.40°	7.40°	11.40°	12.10°
18.80°	6.80°	7.20°	10.60°	11.10°
20.00°	6.55°	6.70°	10.00°	10.40°
24.00°	4.00°	4.20°	6.00°	7.10°
28.00°	0.00°	0.00°	0.00°	0.00°
40.00°	0.00°	0.00°	0.00°	0.00°

Wing Wake Deflection, ϵ_w , in Helicopter Mode				
α_w	Flaps(-28/-17.5)°	Flaps(0/0)°	Flaps(40/25)°	Flaps(75/47)°
-90.00°	0.00°	0.00°	0.00°	0.00°
-28.65°	0.00°	0.00°	0.00°	0.00°
-22.15°	0.00°	0.00°	0.00°	0.00°
-17.80°	0.00°	0.00°	0.00°	0.00°
-15.50°	0.00°	0.00°	0.00°	0.00°
-12.41°	0.00°	0.00°	1.20°	2.00°
-7.60°	0.00°	0.00°	3.20°	3.75°
-2.94°	0.00°	2.00°	5.00°	5.40°
0.0°	1.00°	3.10°	6.15°	6.30°
8.00°	3.72°	6.30°	9.25°	9.20°
12.00°	5.08°	7.80°	11.00°	10.70°
13.00°	5.40°	8.30°	11.40°	11.00°
14.80°	6.00°	9.00°	11.95°	11.50°
16.00°	6.44°	9.60°	11.90°	11.40°
18.00°	7.00°	10.00°	11.20°	11.20°
20.00°	6.70°	9.30°	10.20°	10.20°
24.00°	4.20°	6.00°	6.80°	6.80°
28° - 40°	0.0°	0.0°	0.0°	0.0°

Tables A4.16. - Wing Wake Deflection on Horizontal Stabiliser

Marr and Sambell (1973) obtained the following data experimentally to describe the influence of the rotor upwash on the horizontal stabiliser:

Rotor Upwash Component, w_{if} (ms^{-1}), on Horizontal Stabiliser					
V_f (Knots)	$\gamma_s = 0^\circ$	$\gamma_s = 15^\circ$	$\gamma_s = 30^\circ$	$\gamma_s = 60^\circ$	$\gamma_s = 90^\circ$
0	0.0000	0.0000	0.0000	0.0000	0.0000
20	-1.0363	-1.2192	0.0000	0.0000	0.0000
40	-1.0973	-1.2192	0.0000	0.0000	0.0000
60	-1.8288	-1.2192	0.0000	0.0000	0.0000
80	-2.5603	-1.2192	-0.6401	0.0000	0.0000
100	-3.2918	-1.2192	-0.7620	-0.4672	0.0000
120	-3.2918	-1.2192	-0.7620	-0.2336	0.0000
140 →	-3.2918	-1.2192	-0.7620	0.0000	0.0000

Tables A4.17. - Rotor Upwash Component, w_{if} , on Horizontal Stabiliser

REFERENCES

1. Andres, J., Monti, G., "Eurofar - Status of the European Tilt-Rotor Project", Proceedings of the Fourteenth European Rotorcraft Forum, Milan, 1988
2. Bell-Boeing Study Team, "Civil Tilt-Rotor Missions and Applications: A Research Study", Summary Final Report NASA CR 177452, July 1987
3. Bell-Boeing, "Tilt-Rotor Handling Qualities Short Course Notes"
4. Bramwell, A. R. S., *Helicopter Dynamics*, (Edward Arnold (Publishers) Limited, London, 1976)
5. Brown, Col. B, M, et al , "Tilt - Rotor UAV: the Next Generation Unmanned System", Vertiflite, Volume 38, Number 3, May/June 1992
6. Chen, R. T. N., "A Survey of Nonuniform Models for Rotorcraft Flight Dynamics and Control Applications", Vertica, Volume 14, No. 2, 1990
7. Chen, R. T. N., Hindson, W. S., "Influence of Dynamic Inflow on the Helicopter Vertical Response", Vertica, Volume 11, No. 12, 1987
8. Churchill, G. B., Dugan, D. C., "Simulation of the XV-15 Tilt Rotor Research Aircraft", *NASA TM-84222*, March 1982
9. Clark, D. R., "Analysis of the Wing/Rotor and Rotor/Rotor Interactions Present in Tilt-Rotor Aircraft", The International Conference on Rotorcraft Basic Research, Army Research Office, Durham, North Carolina, February 1985
10. Clark, D. R., McVeigh, M. A., "Analysis of the Wake Dynamics of a Typical Tilt-Rotor Configuration in Transition Flight", Proceedings of the Eleventh European Rotorcraft Forum, London, 1985
11. Cooper, G., "Osprey is Back", *Aerospace*, Volume 19, Number 3, March 1992
12. Curtiss, H. C. Jr., Shupe, N. K., "Stability and Control Theory for Hingeless Rotors", Annual Forum of the American Helicopter Society, May 1971
13. Curtiss, H. C. Jr., Quackenbush, T. R., "The Influence of the Rotor Wake on Rotorcraft Stability and Control", Proceedings of the Rotorcraft Forum, Amsterdam, 1989

14. Du Val, R. W., "A Real Time Blade Element Helicopter Simulation for Handling Qualities Analysis", Proceedings of the Fifteenth European Rotorcraft Forum, Amsterdam, September 1989
15. Dunford, P., et al, "Testing the V-22 Osprey - a Significant Flight Test Challenge", Proceedings of the Sixteenth European Rotorcraft Forum, Glasgow, 1990
16. Edenborough, H., K., Gaffey, T., M., Weiberg, J. A., "Analyses and Tests to Confirm the Design of Proprotor Aircraft", AIAA Paper No. 72-803, August 1972
17. Etkin, B., *Dynamics of Atmospheric Flight*, (John Wiley and Sons Inc, New York, 1972)
18. Felker, F., F., et al, "Full Scale Tilt-Rotor Hover Performance", Annual Forum of the American Helicopter Society, May 1985
19. Gaonkar, G. H., Peters, D. A., "Review of Dynamic Inflow Modelling for Rotorcraft Flight Dynamics", *Vertica*, Volume 12, No. 3, 1988
20. Glauert, H., "A General Theory of the Autogyro", ARC R&M 1111, 1926
21. Harendra, P. B. et al, "A Mathematical Model for Real Time Flight Simulation of the Bell Model 301 Tilt Rotor Research Aircraft", *Bell Helicopter Company Report No. 301-099-001*, April 1973
22. Houston, S.S, "Rotorcraft Aeromechanics Simulation for Control Analysis - Mathematical Model Description", University of Glasgow, Department of Aerospace Engineering Report No 9123, 1991
23. Ishida, T., Nakatani, I., "TW-68 Tilt-Wing High Speed Commercial VTOL", *Vertiflite*, Volume 36, Number 1, January/February 1990
24. Johnson, W., "A Comprehensive Analytical Model of Rotorcraft Aerodynamics and Dynamics. Part 1: Analysis and Development", *NASA Technical Memorandum 81182*, June 1980a
25. Johnson, W., *Helicopter Theory*, (Princeton University Press, New Jersey, 1980b)
26. Kuethe, A. M., Chow, C., *Fundamentals of Aerodynamics*, (John Wiley and Sons, New York, 1986)

27. Lane, T., Alton, L., R., "The Civil Tilt-Rotor Aircraft's Potential in Developing Economies", *Vertiflite*, Volume 37, Number 1, January/February 1991
28. Lesching, A., Wagner, S., "Theoretical Model to Calculate Aerodynamic Interference Effects Between Rotor and Wing of Tilt-Rotors", *Proceedings of the Sixteenth European Rotorcraft Forum*, Glasgow, 1990
29. Mark, H., "Aircraft Without Airports the Tilt-Rotor Concept and VTOL Aviation", *Aerospace*, Volume 14, Number 3, March 1987
30. Marr, R. L., Roderick, W. E. B., "Handling Qualities Analysis of the XV-15 Tilt-Rotor Aircraft". 30th Annual Forum of the American Helicopter Society, May 1974
31. Marr, R. L., Sambell, K. W., "V/STOL Tilt-Rotor Study - Volume VI Hover, Low Speed and Conversion Tests of a Tilt-Rotor Aeroelastic Model", *NASA Contractor Report 114615*, May 1973
32. Martin, S., Ostlund, R., "V-22 Developmental Status", *Proceedings of the Fifteenth European Rotorcraft Forum*, Amsterdam, September 1989
33. McVeigh, M. A., et al, "Rotor/Airframe Interactions on Tilt-Rotor Aircraft", 44th Annual Forum of the American Helicopter Society, Washington D.C., 1988
34. McVicar, J. S. G., Bradley, R., "A Generic Rotor Algorithm for Application to Real-Time Tilt Rotor Simulation", *University of Glasgow, Department of Aerospace Engineering Report No. 9015*, September 1990
35. McVicar, J. S. G., Bradley, R., "A Generic Tilt-Rotor Simulation Model with Parallel Implementation and Partial Periodic Trim Algorithm", *Proceedings of the Eighteenth European Rotorcraft Forum*, Avignon, France 1992a
36. McVicar, J. S. G., Bradley, R., "A Partial Periodic Trim Algorithm for Application to Advanced Mathematical Models of Rotorcraft Vehicles", *Proceedings of the Kinematics and Dynamics Multi-Body Systems Seminar*, Institution of Mechanical Engineers Headquarters, London 1992b
37. McVicar, J. S. G., Bradley, R., "The Phase 1 GRTTRM - Parallel Implementation and Periodic Trim Algorithm", *University of Glasgow, Department of Aerospace Engineering Report No. 9111*, September 1991

38. Meerwijk, L., Brouwer, W., "A Real Time Helicopter Simulation Using the Blade Element Method", Proceedings of the Seventeenth European Rotorcraft Forum, Berlin, 1991
39. Meiko Limited, "CS Tools for SunOS" Volumes 1 and 2, 1990
40. Meiko Limited, "FORTRAN for CS Tools", 1991
41. Meriam, J. L., *Engineering Mechanics Volume 2, Dynamics*, (Wiley, New York, 1980)
42. Mil, M., L., et al "Helicopters Calculation and Design Volume 1. Aerodynamics" *NASA Technical Translation TT F-494*, September 1967
43. Nakatani, I., "Tilt-Wing Project Takes Cues From History", *Vertiflite*, Volume 37, Number 1, January/February 1991
44. Norwine, P., C., "The Coming Age of the Tilt-Rotor", *Vertiflite*, Volume 36, Numbers 1 and 3, January/February 1990 and March/April 1990
45. Padfield, G. D., "A Theoretical Model of Helicopter Flight Mechanics for Application to Piloted Simulation", *RAE Technical Report 81048*, April 1981
46. Padfield, G., D., "Theoretical Modelling for Helicopter Flight Dynamics: Development and Validation", Proceedings of the 16th ICAS Conference, London, 1988
47. Peters, D. A., HaQuang, N., "Dynamic Inflow for Practical Applications", *Journal of the American Helicopter Society*, Technical Note, October 1988
48. Peters, D. A., Izadpanah, A. P, "Helicopter Trim By Periodic Shooting with Newton-Raphson Iteration", Source Unknown
49. Pitt, D. M., Peters, D. A., "Theoretical Prediction of Dynamic Inflow Derivatives", *Vertica*, Volume 5, 1981
50. Prouty, R. W., *Helicopter Performance Stability and Control*, (Kreiger Publishing Company, Florida 1990)
51. Reichart, G, "Basic Dynamics of Rotors, Control and Stability of Rotary Wing Aircraft, Aerodynamics and Dynamics of Advanced Rotary-Wing Configurations". AGARD Conference Proceedings, LS-63, 1973

52. Rollet, P., Thibaudat, C., "Eurofar Simulation Trials on EPOPEE Simulator", Proceedings of the Eighteenth European Rotorcraft Forum, Avignon, September 1992
53. Schillings, J.,J., et al, "Maneuver Performance Comparison Between the XV-15 and an Advanced Tilt-Rotor Design", Journal of the American Helicopter Society, May 1990
54. Simpson, A., "A Plan For the DRA (B) Generic Aeroelastic Rotor Model", (Unpublished), February 1992
55. Smith, G. A., Meyer, G, "Aircraft Automatic Digital Flight Control System with Inversion of the Model in the Feed-Forward Path", Proceedings of the AIAA/IEE Digital Avionics Systems Conference, New York, 1985
56. Smith, G. A., Meyer, G, "Aircraft Flight Control System with Model Inversion", Journal of Guidance and Control, Volume 10, Number 3, May/June 1987
57. Thomason, T., H., "V-22 FSD Flight Test Status Report", Vertiflite, Volume 36, Number 6, November/December 1990
58. Thomson, D. G., Bradley, R., "An Investigation of Pilot Strategy in Helicopter Nap-of-Earth Manoeuvres by Comparison of Flight Data and Inverse Simulations", Proceedings of the Royal Aeronautical Society Conference: "Helicopter Handling Qualities and Control", London, November 1988
59. Thomson, D. G., Bradley, R., "The Development of Inverse Simulation for the Quantitative Assessment of Helicopter Handling Qualities", Proceedings of the AHS/NASA Conference: "Piloting Vertical Flight Aircraft: Flying Qualities and Human Factors", San Fransisco, January 1993
60. Thomson, D. G., "Development of a Generic Helicopter Mathematical Model for Application to Inverse Simulation", University of Glasgow, Department of Aerospace Engineering, Report No. 9216, June 1992
61. Van Gaasbeek, J., R., "Rotorcraft Flight Simulation Computer Program C81 with Data Map Interface", USAAVRADCOM TR-80-D-38A, October 1981

FIGURES

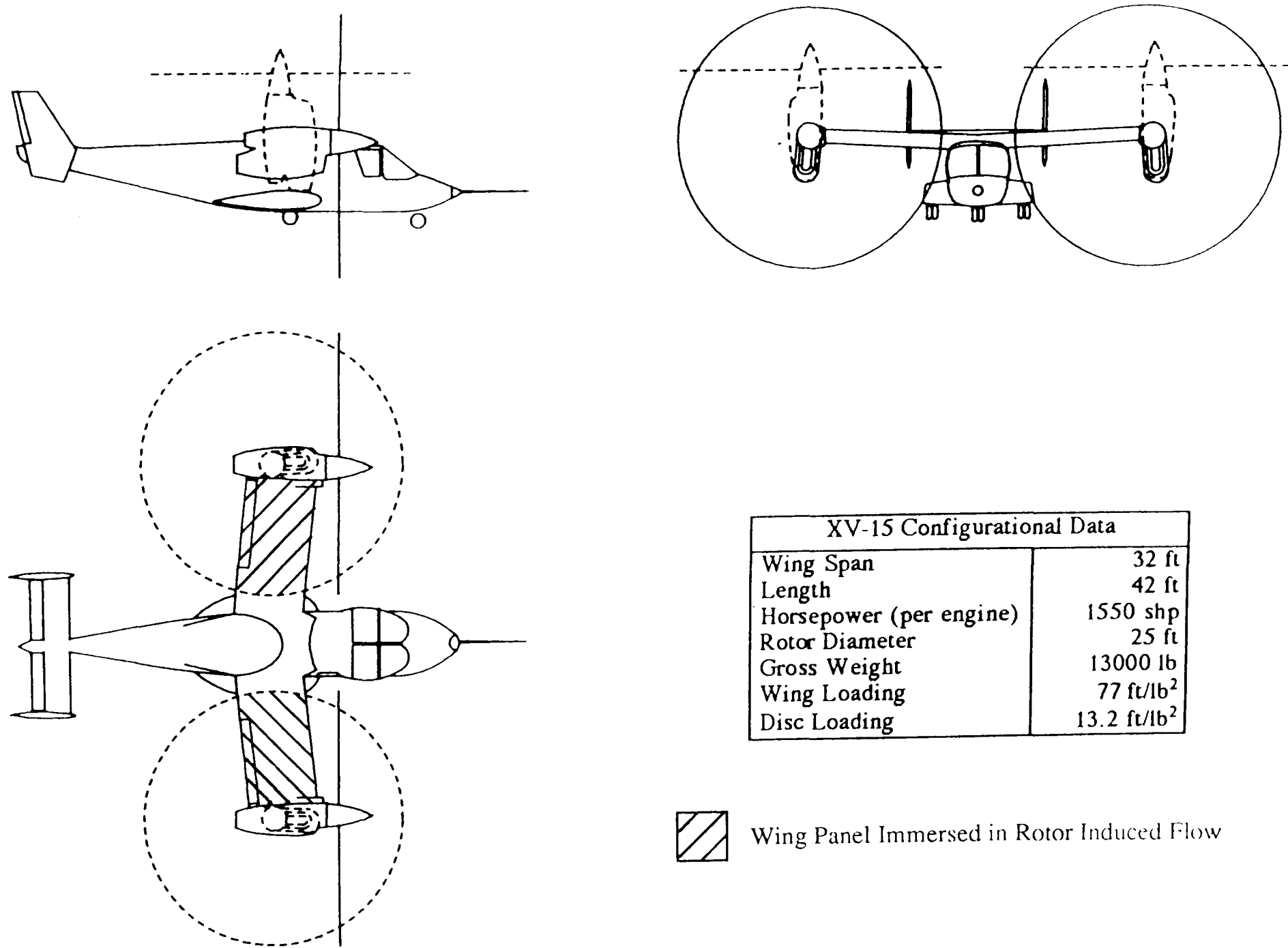


Figure 1.1 XV-15 Proof of Concept Tilt-Rotor Aircraft

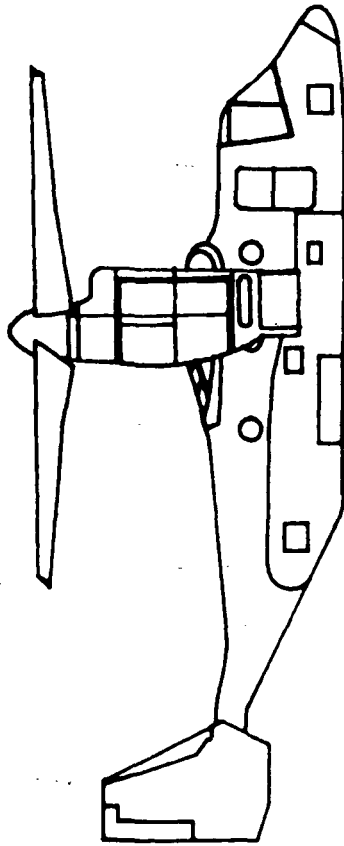
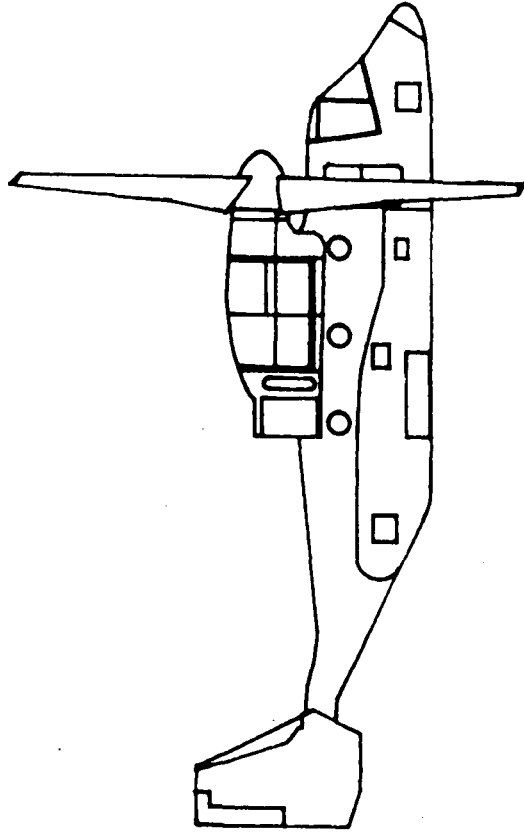


Figure 1.2 V-22 Tilt-Rotor Aircraft

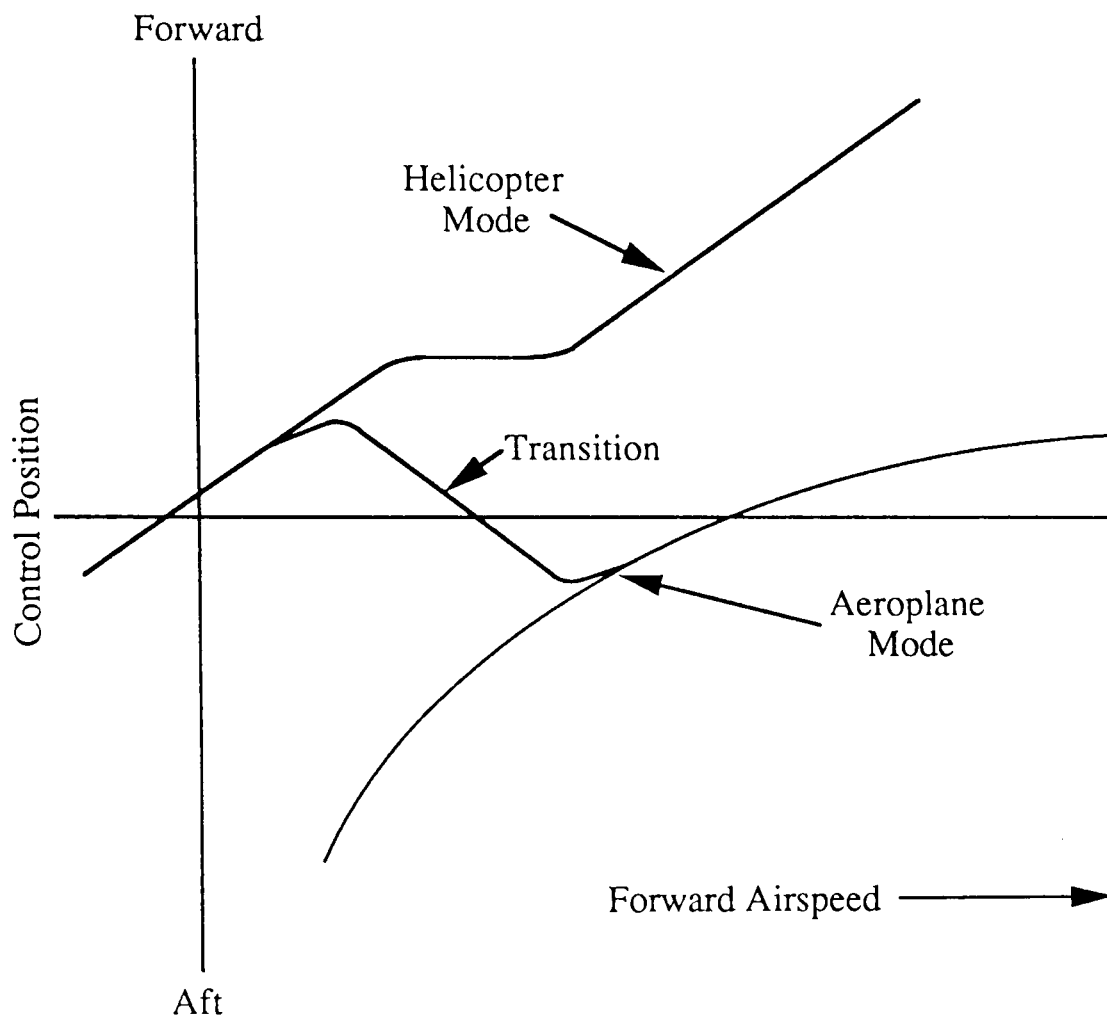


Figure 1.3 Tilt-Rotor Longitudinal Stick Position Against Trimmed Airspeed in Helicopter Mode and Aeroplane Mode (Adapted from Reichart 1973)

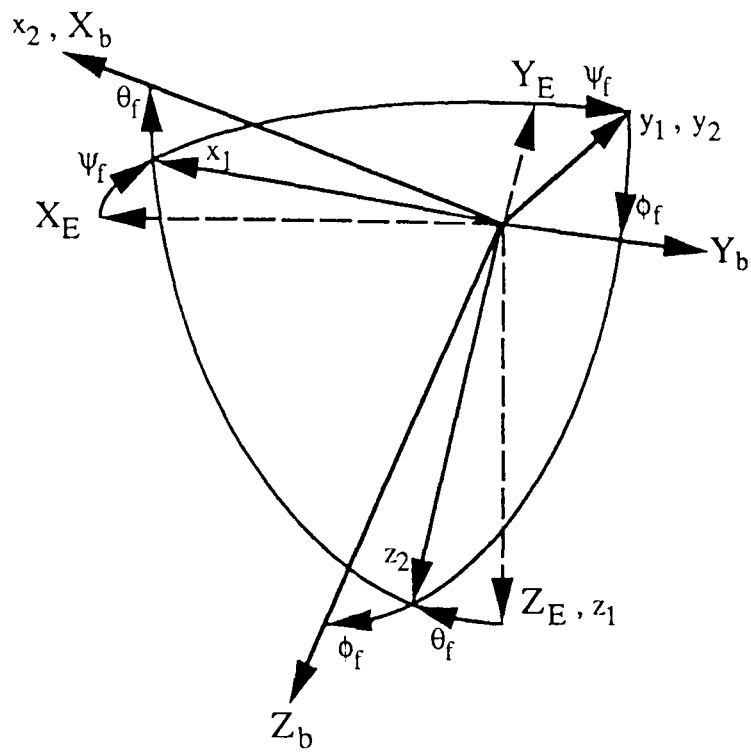


Figure 2.1 Euler Transformations Between Earth and Body Fixed Axis Sets

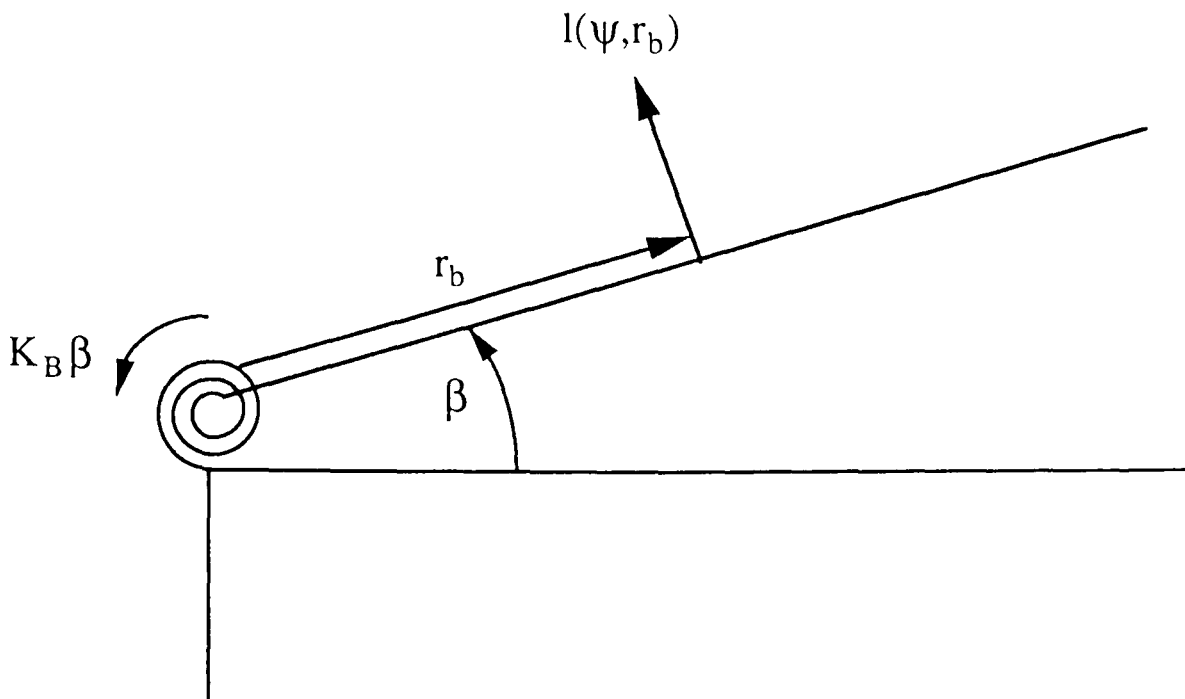


Figure 2.2 The Centre Spring Equivalent Model

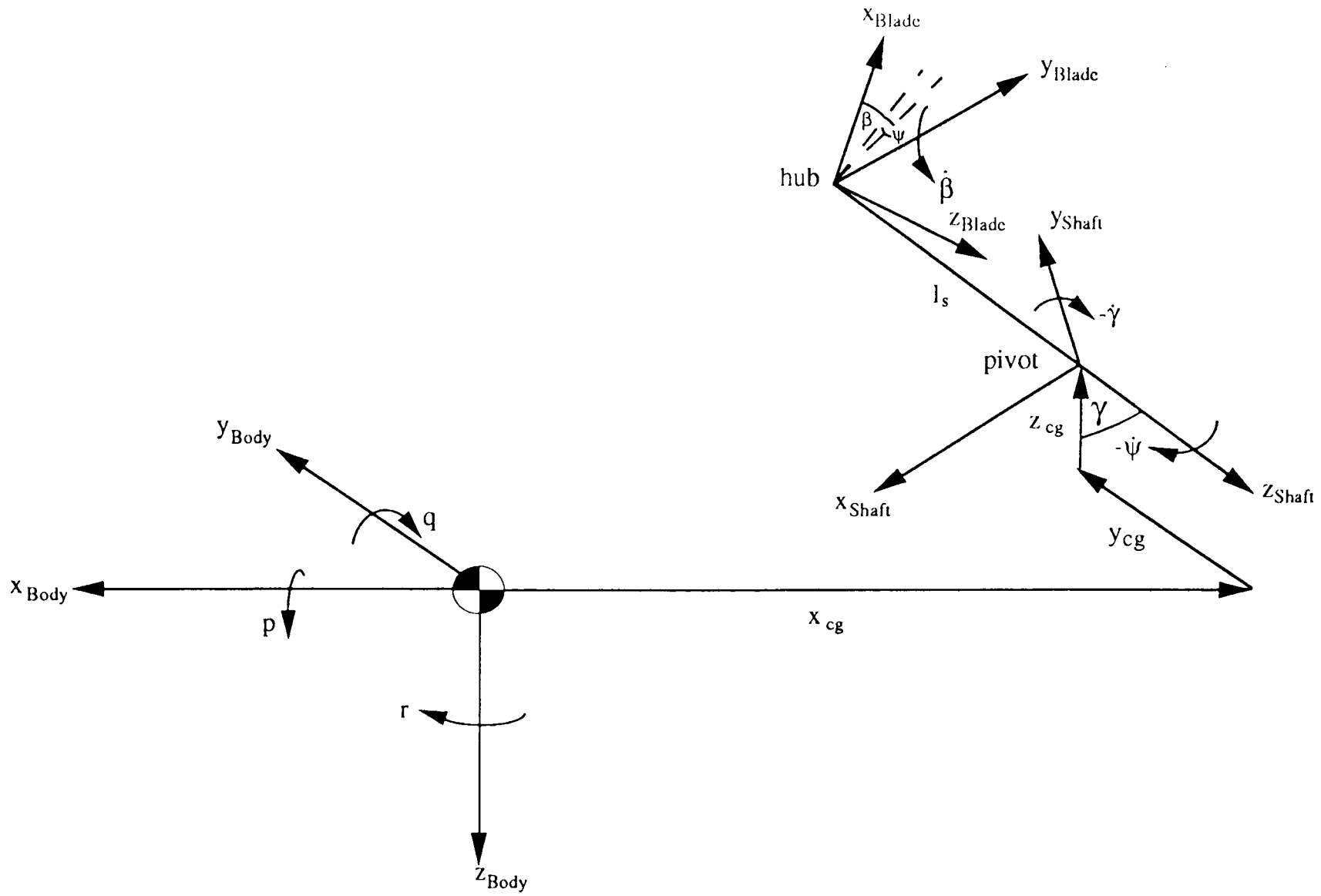


Figure 2.3 The Axis System Used In the Formulation of GTILT

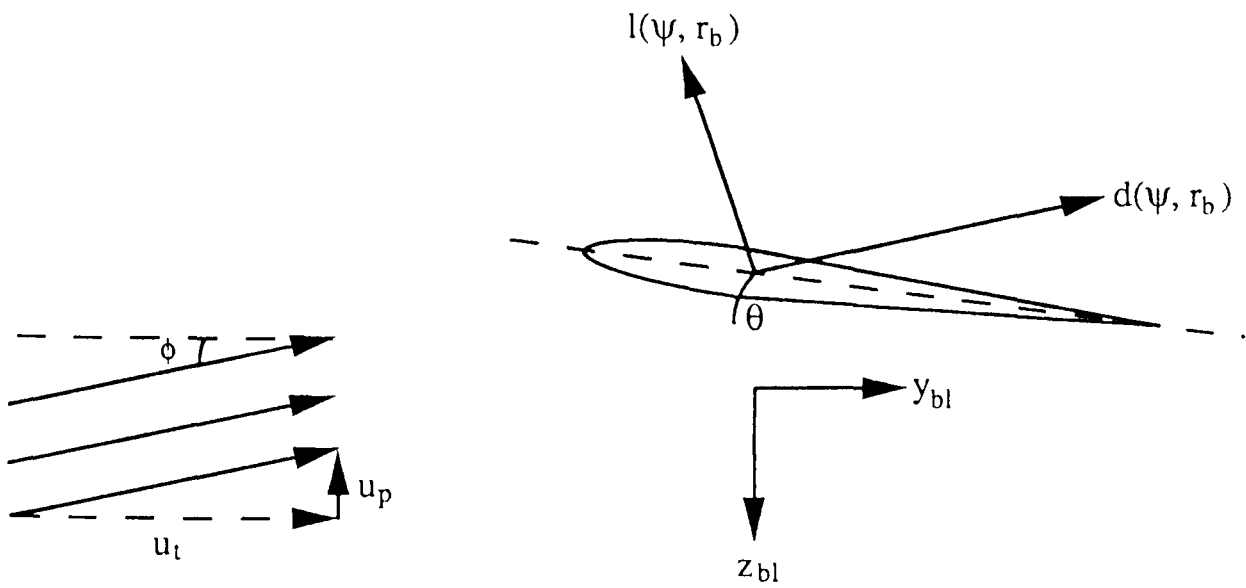
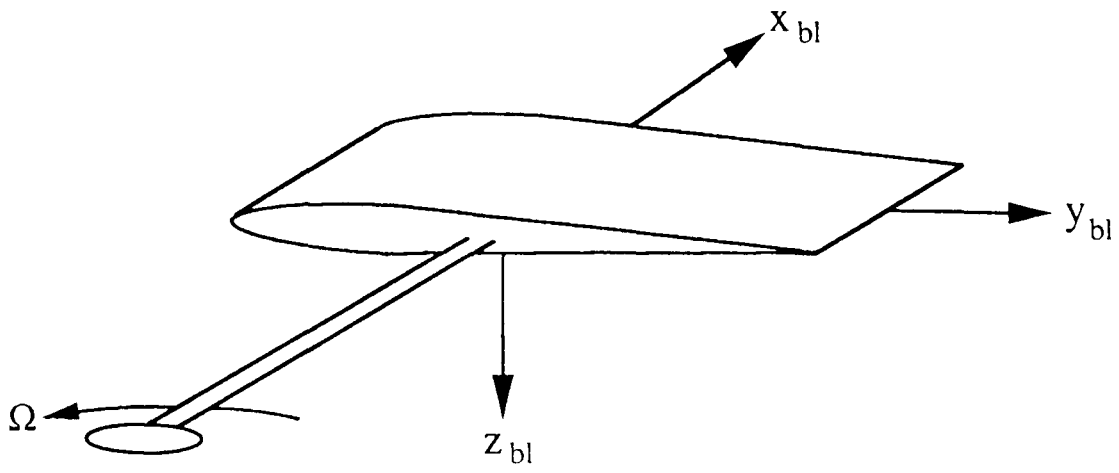


Figure 2.4 Aerodynamic Force and Velocity Components Acting on a Blade Element Rotating Anti-Clockwise when Viewed from Above

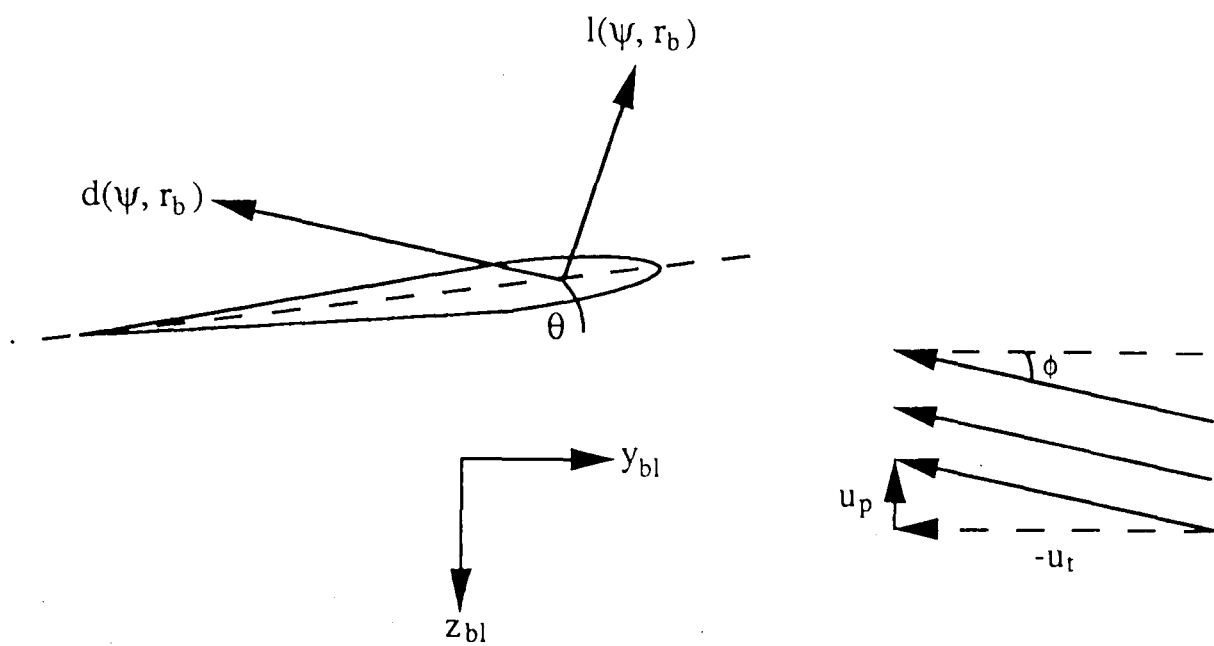
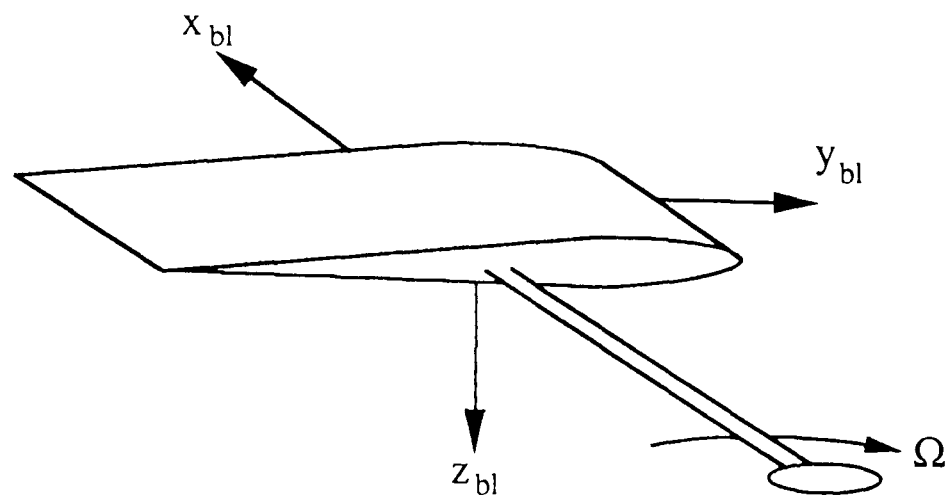


Figure 2.5 Aerodynamic Force and Velocity Components Acting on a Blade Element Rotating Clockwise when Viewed from Above

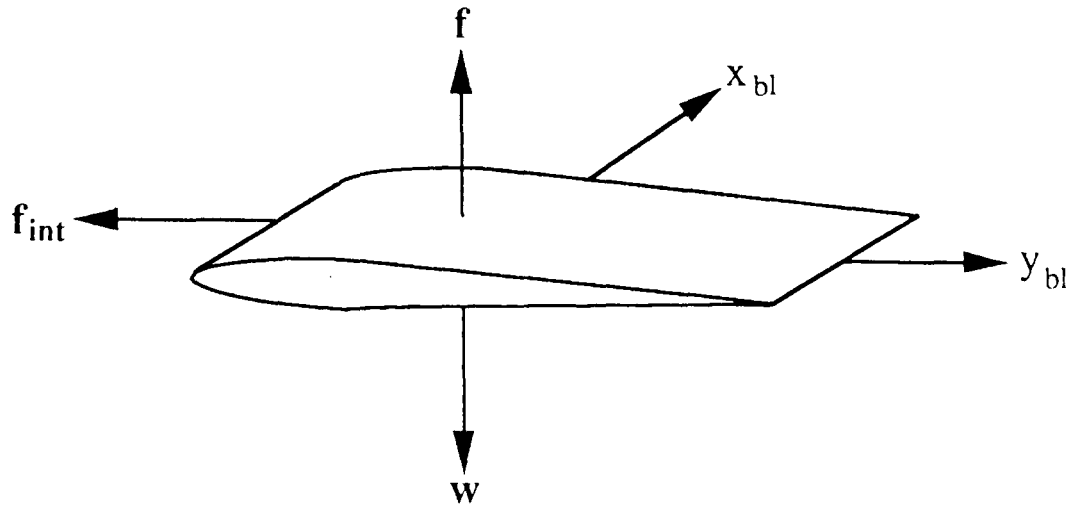


Figure 2.6 Aerodynamic and Internal Forces Acting on a Blade Element

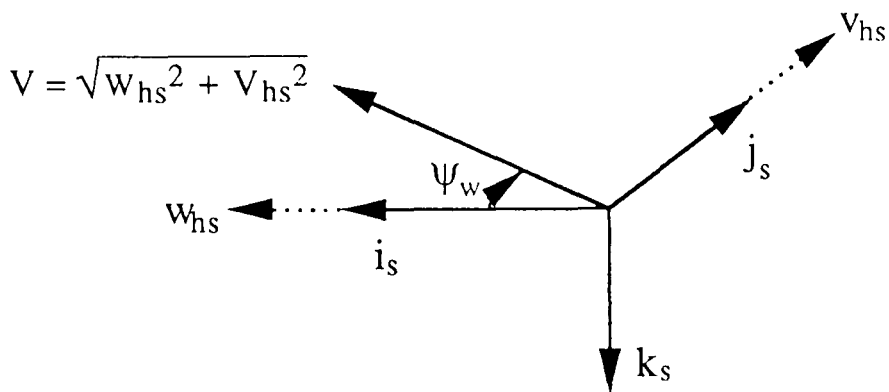


Figure 2.7 The Rotor Sideslip Angle

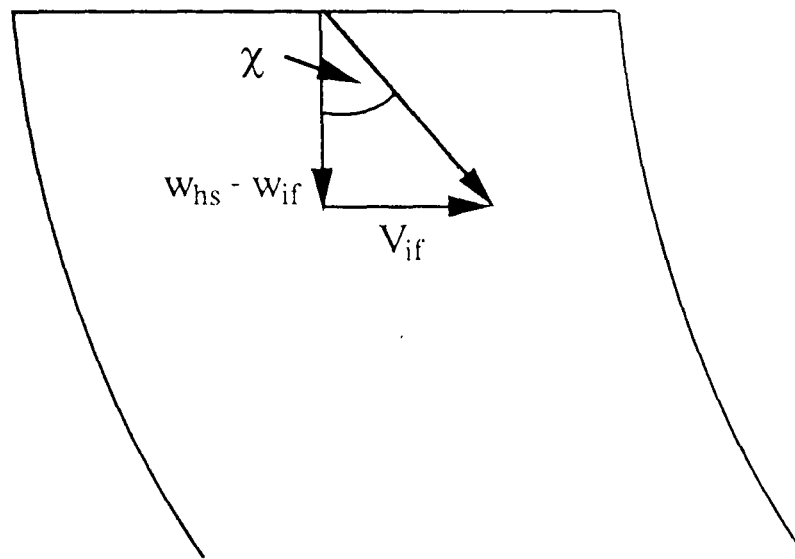


Figure 2.8 Rotor Wake Angle

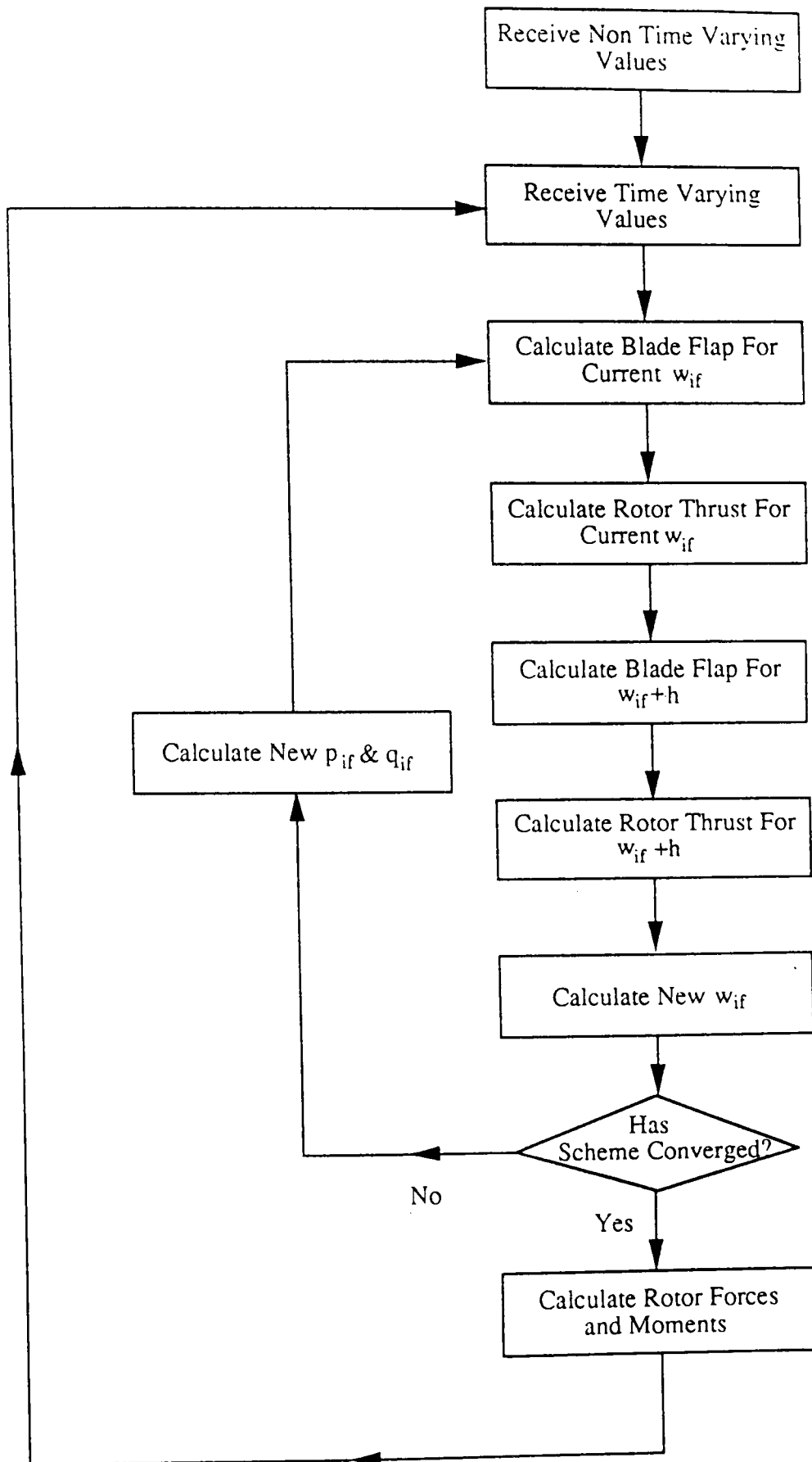


Figure 2.9 - The Glauert Solution Algorithm

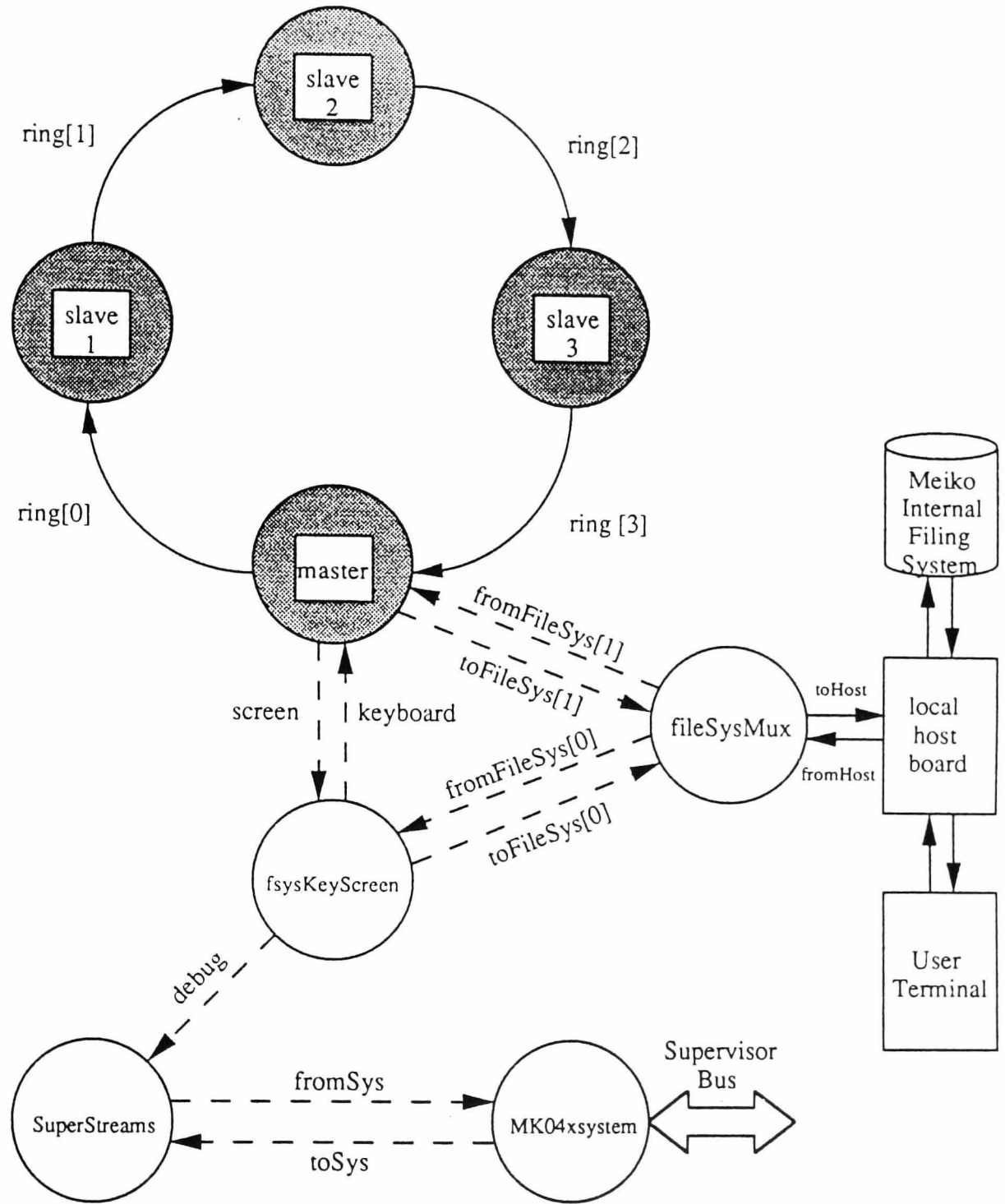


Figure 4.1 - An Example of a Simple Transputer Topography

```

par
processor 0 master
processor 1 toplave
processor 2 slave1
processor 3 slave2
processor 4 slave3
processor 5 slave4
networkis userdefined
closeto 0 1
closeto 2 1
closeto 3 1
closeto 5 1
closeto 4 3
closeto 5 4
closeto 2 5
closeto 2 4
closeto 5 3
end par

```

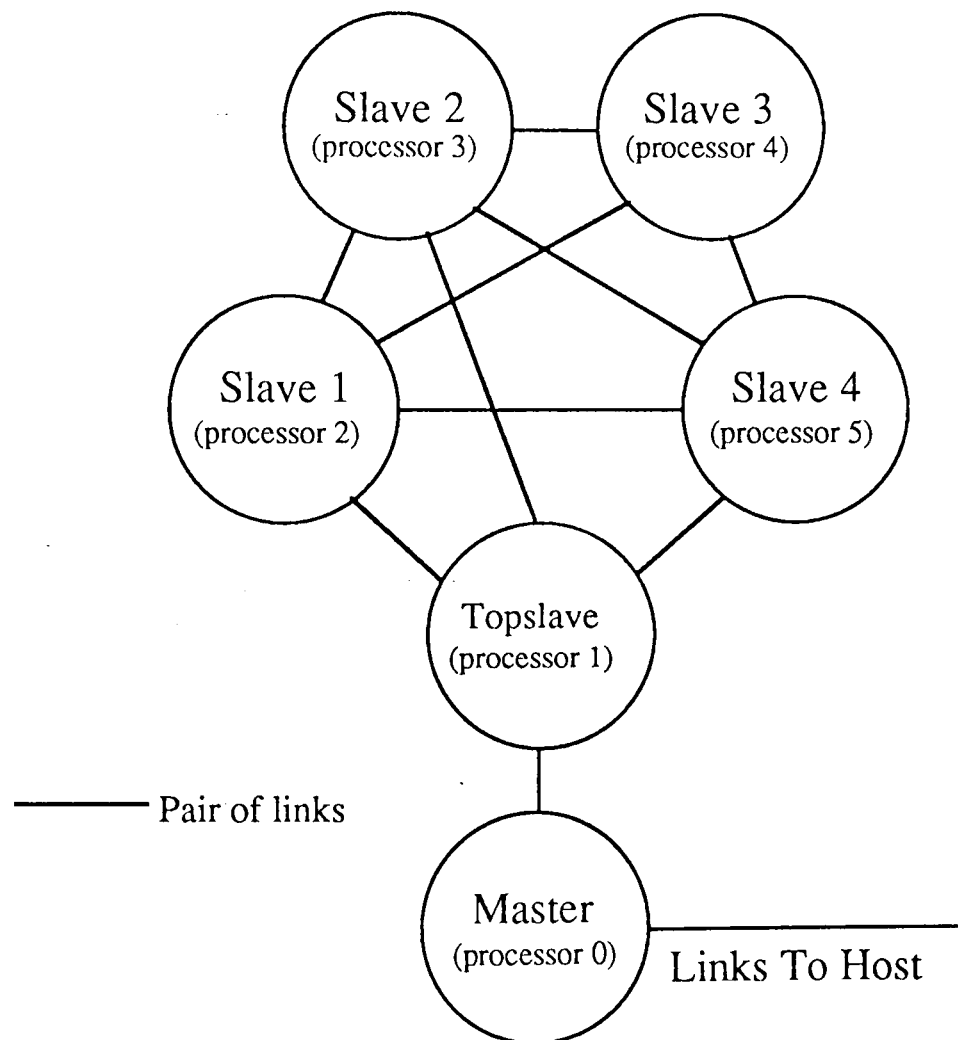
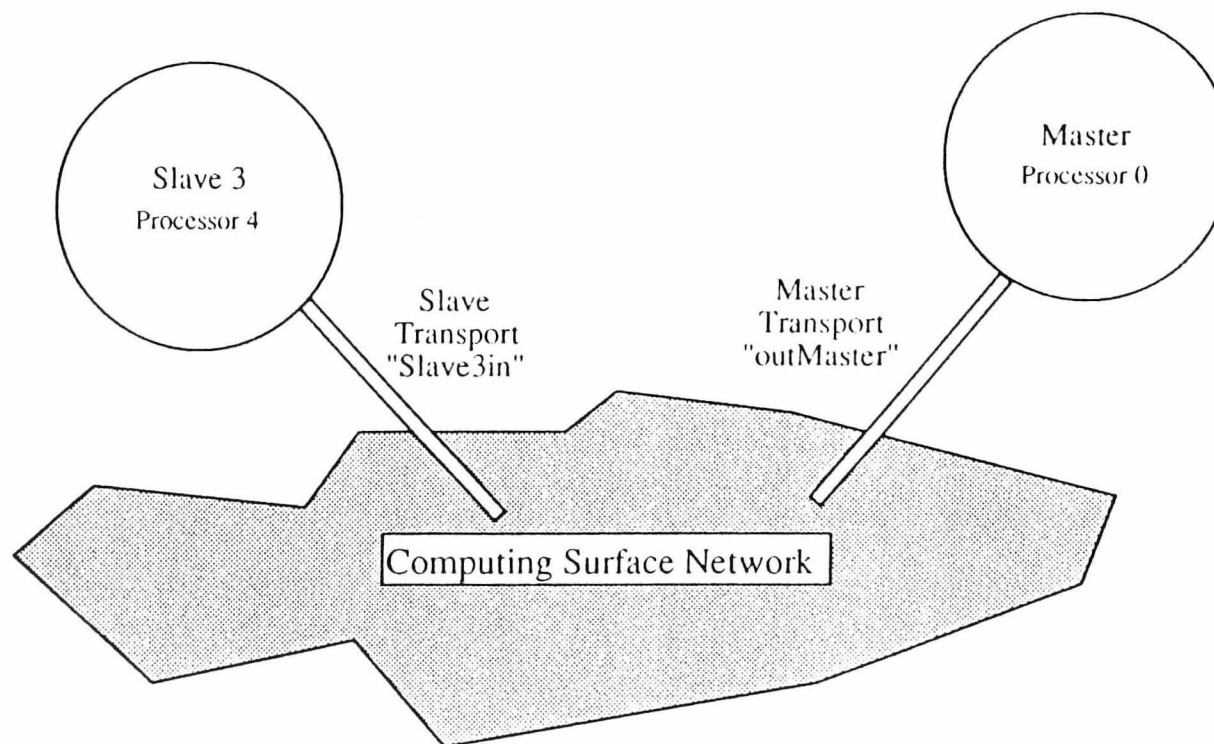


Figure 4.2: Pentangle Topography and Corresponding Par File



Master

```
returncode=csnOpen(CSN NULL ID, outMaster)
returncode=csnLookupName(slave3Id, 'slave3', 1)
returncode=csn tx(outMaster, 0, slave3Id,variable, nBytes)
```

Slave 3

```
returncode=csnOpen(CSN NULL ID,slave3In)
returncode=csnRegname(Slave3In, 'slave3')
returncode=csn rx(slave3In, CSN NULL ID, variable, nBytes)
```

Figure 4.3 Example of Communication Between High Level Processes Using the CSN

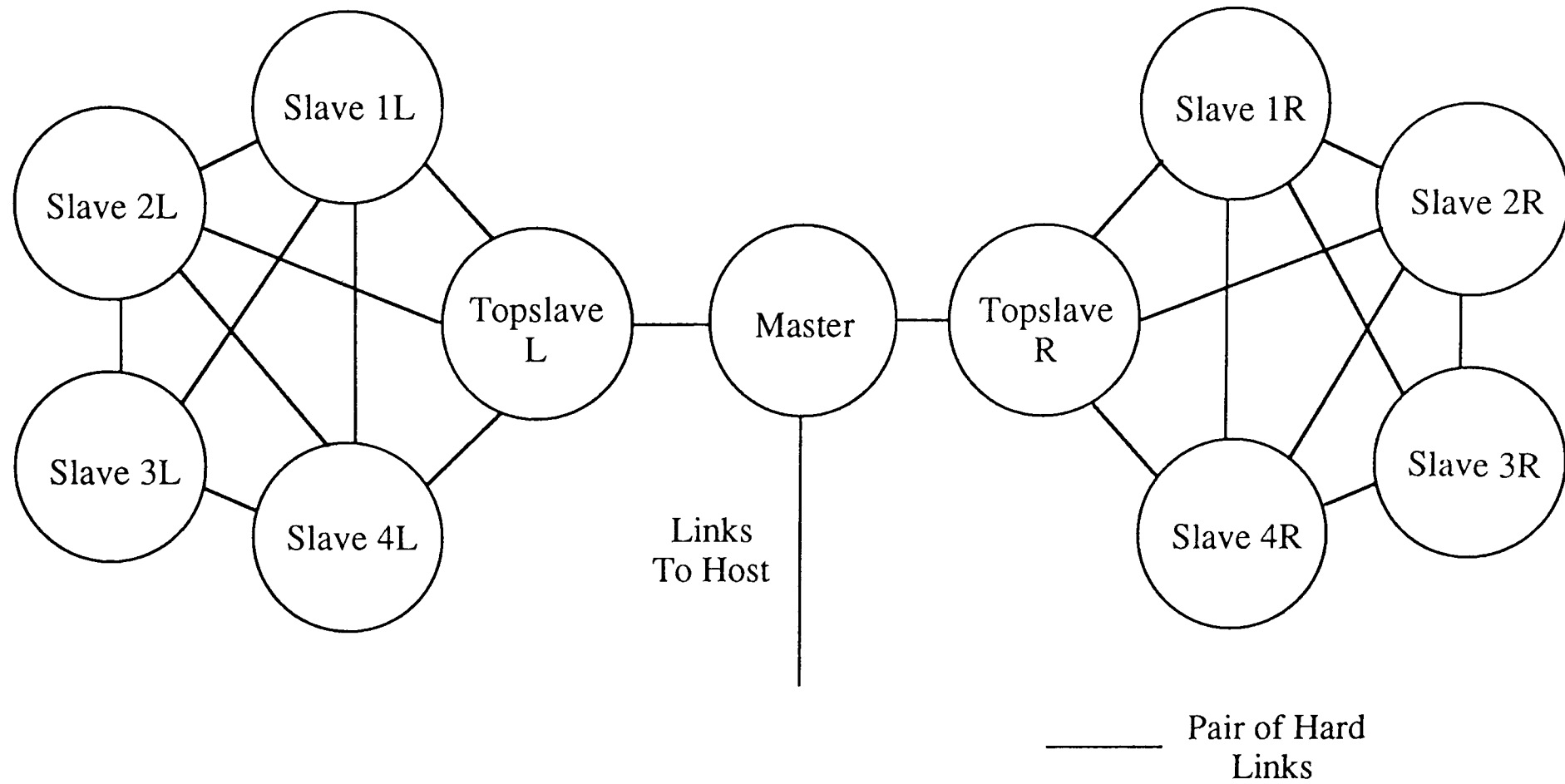


Figure 4.4 Transputer Topography Used in the Parallel Implementation of GTILT

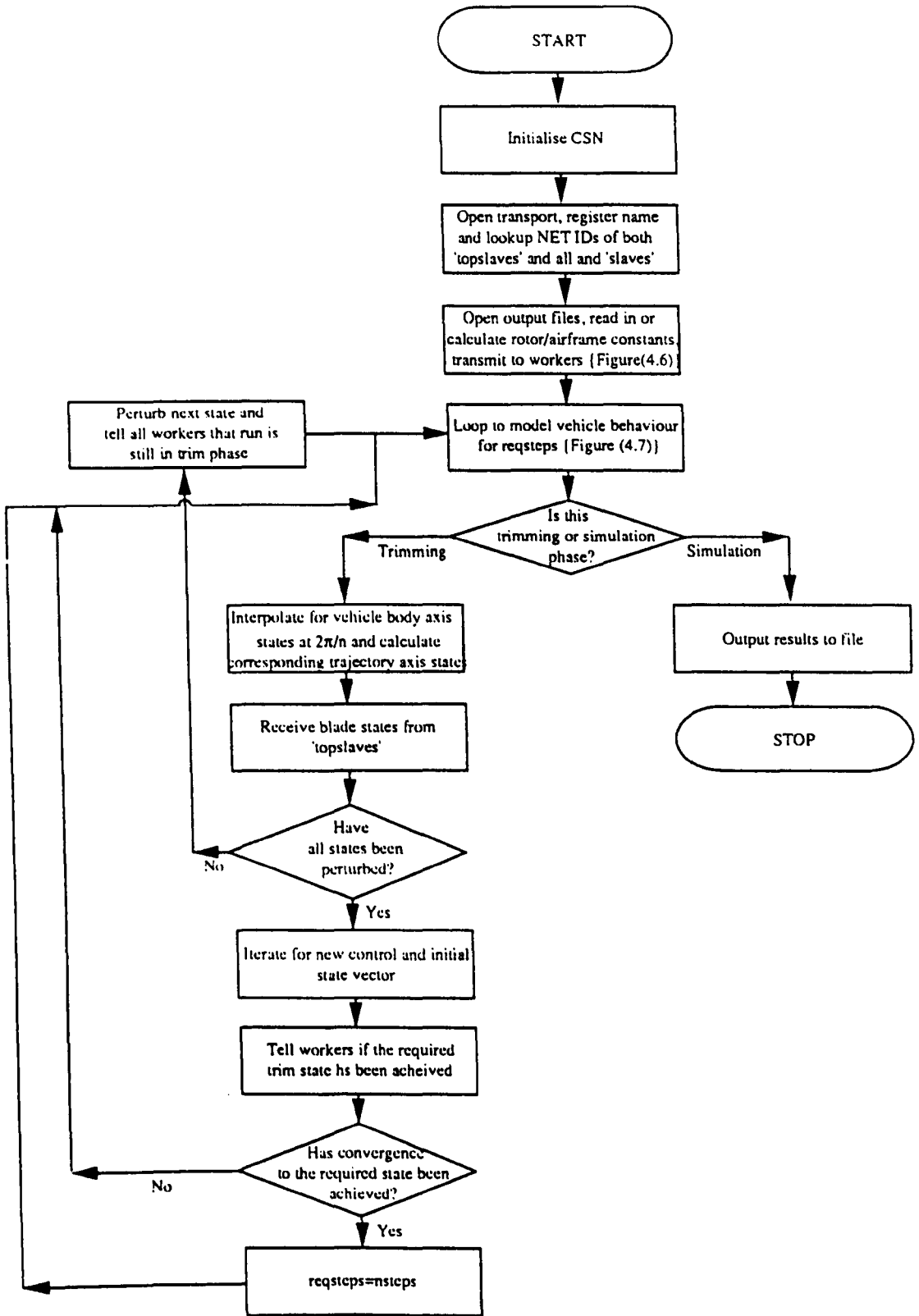


Figure 4.5 - 'Master' Process Flowchart

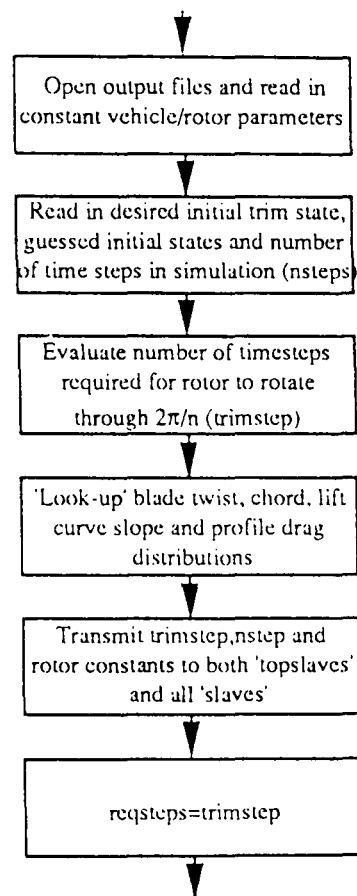


Figure 4.6 - Pre-Simulation Actions of 'Master' Process

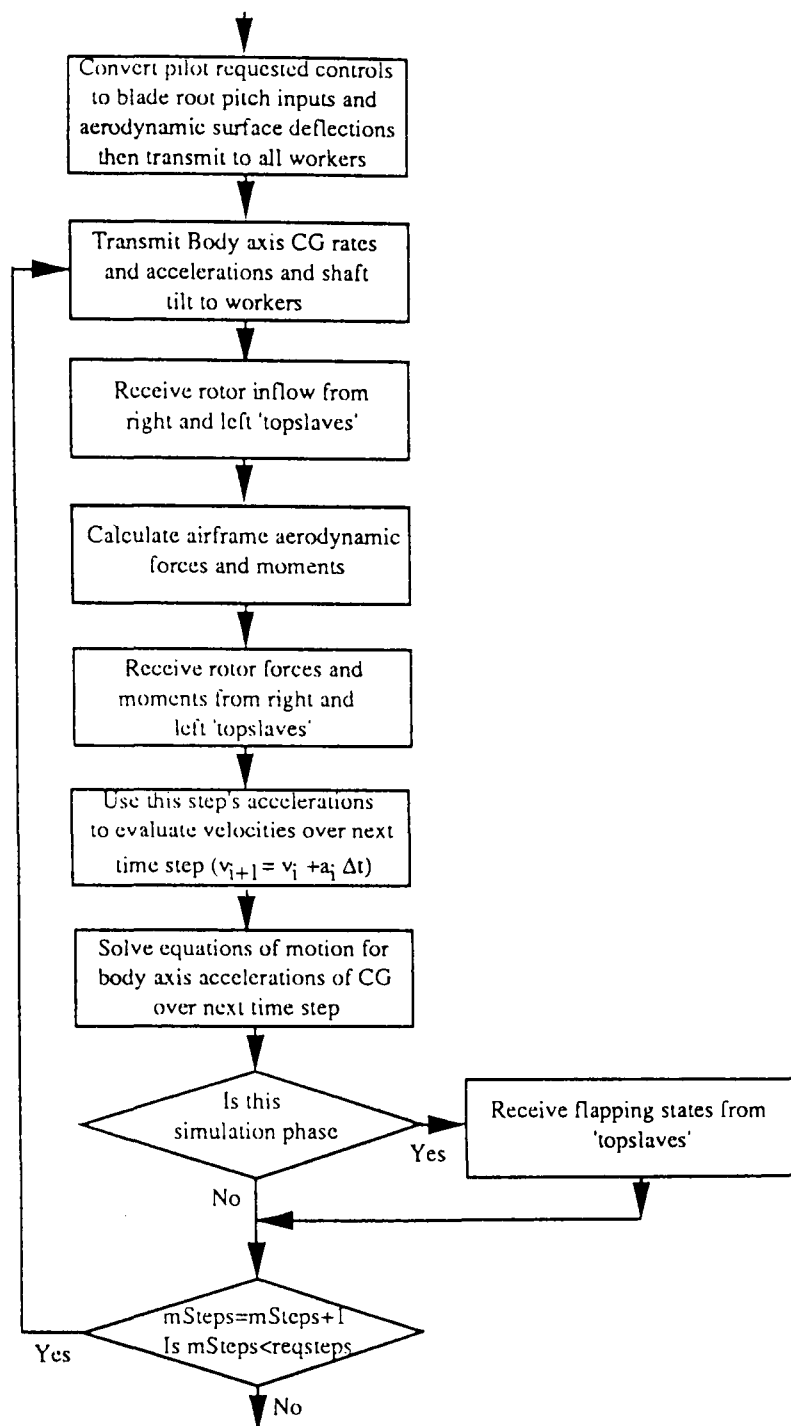


Figure 4.7 - Simulation Loop from 'Master' Process

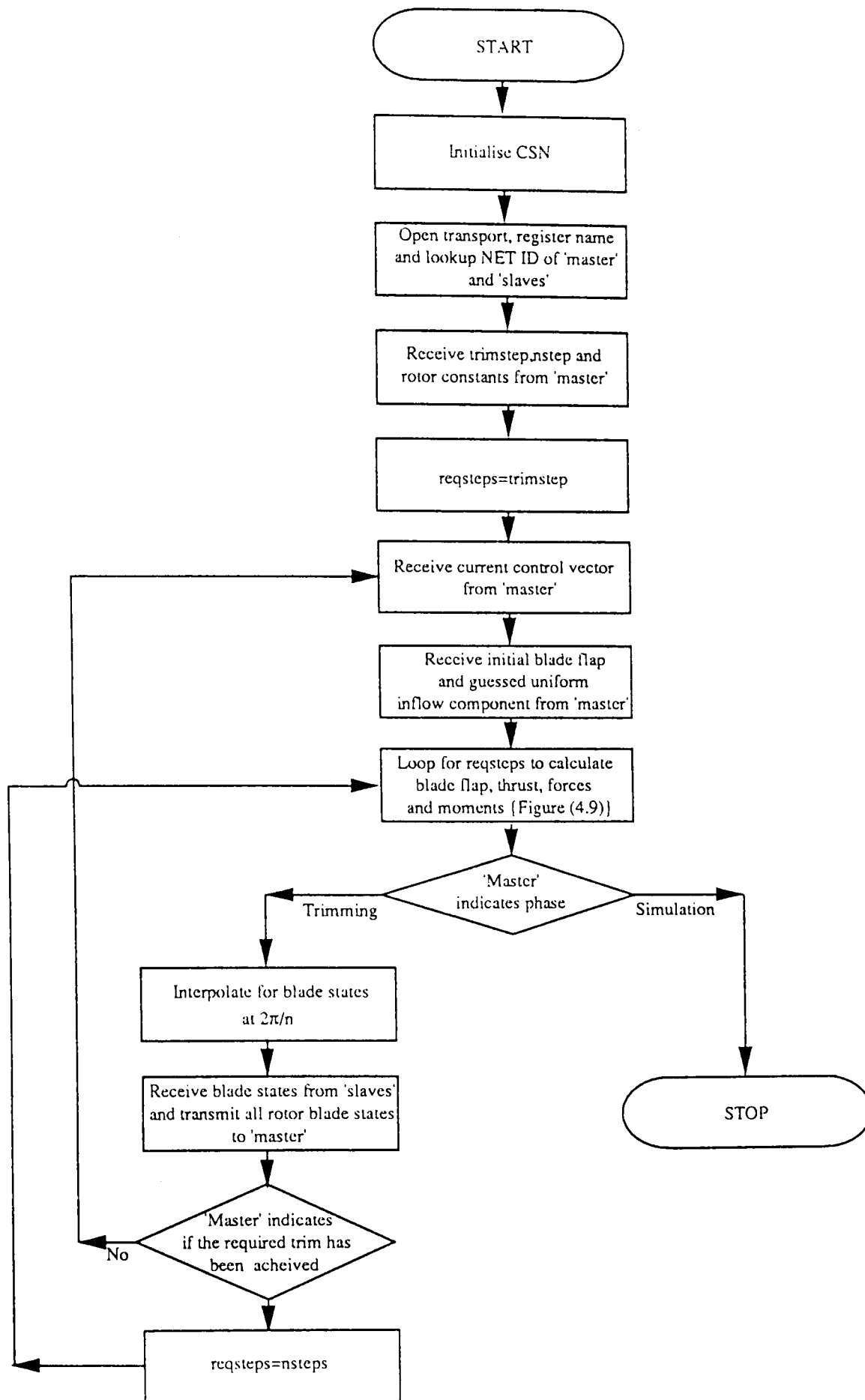


Figure - 4.8 'Topslave' Process Flowchart

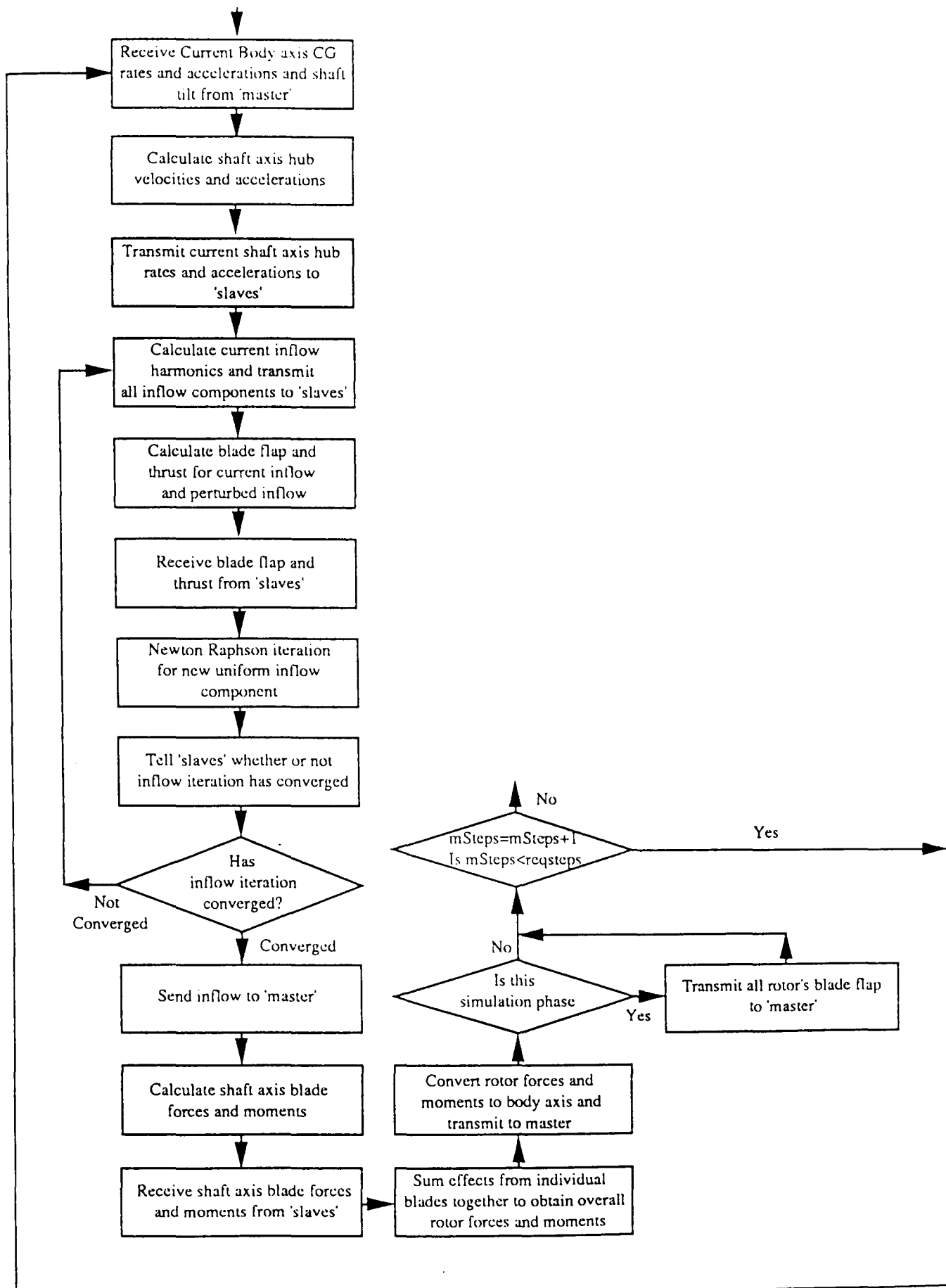


Figure 4.9 - Simulation Loop from 'Topslave' Process

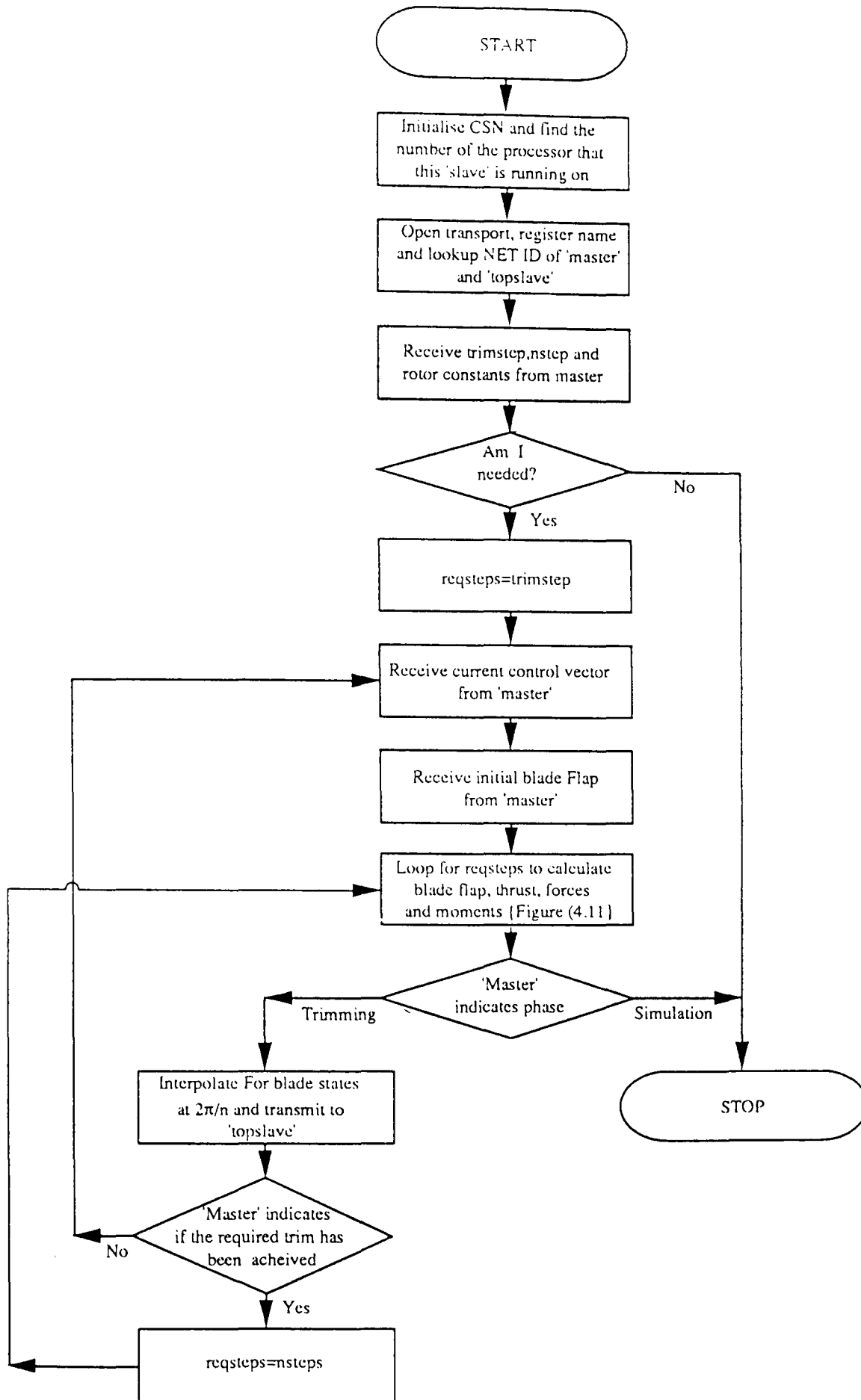


Figure 4.10 - 'Slave' Process Flowchart

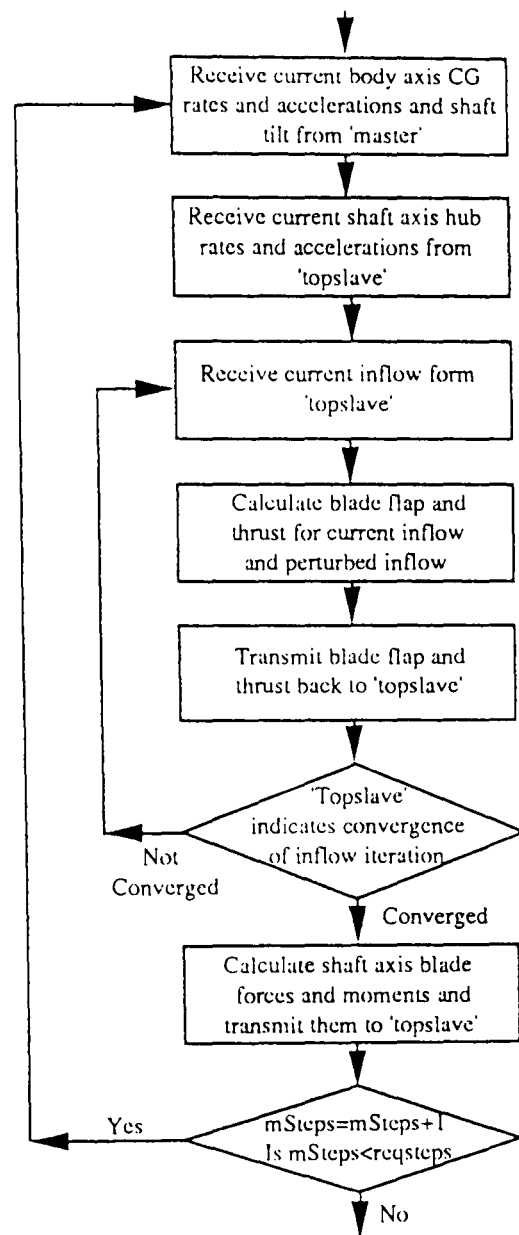


Figure 4.11 - Simulation Loop from 'Slave' Process

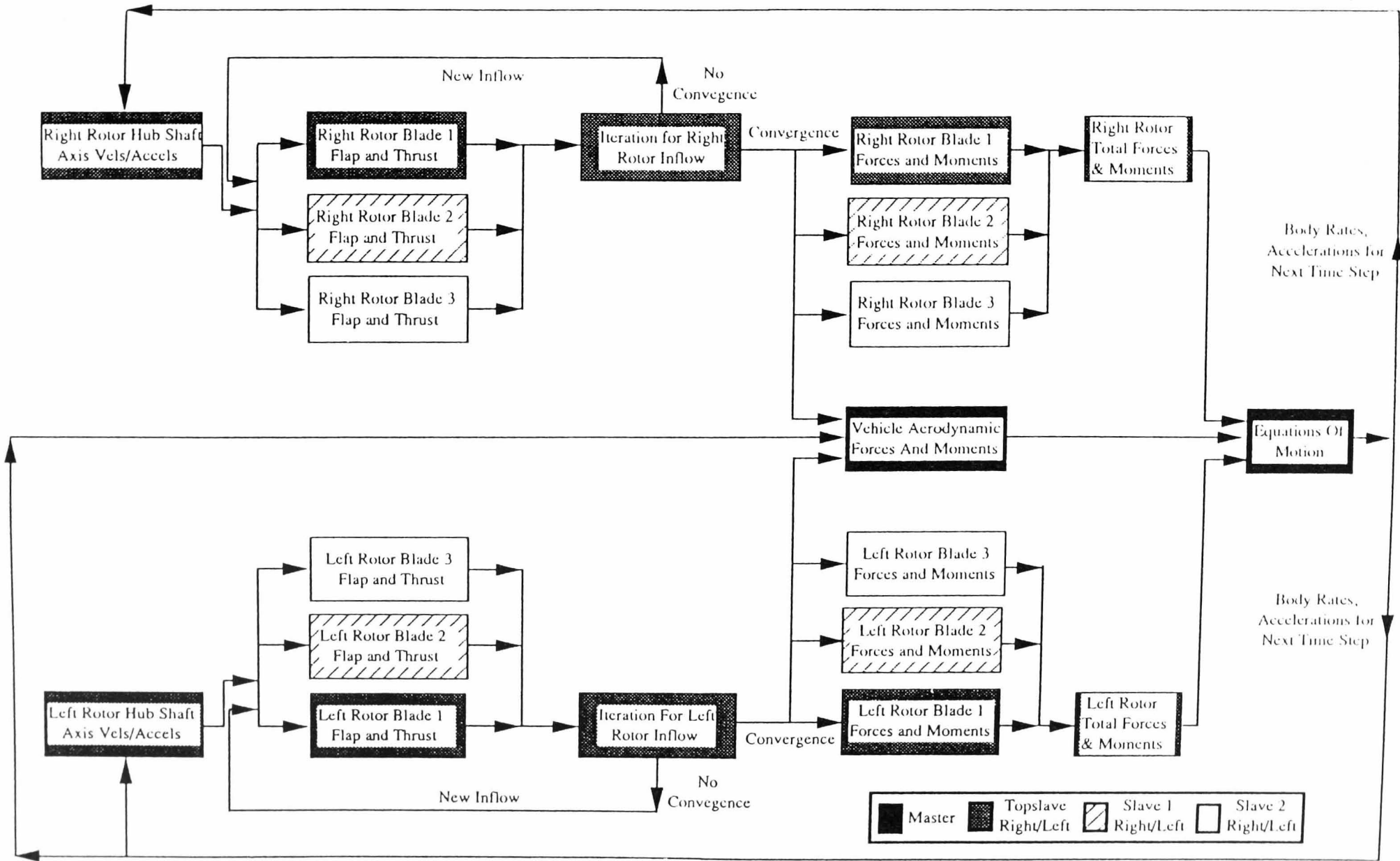


Figure 4.12 Scheduling of Processors in Parallelised GTILT

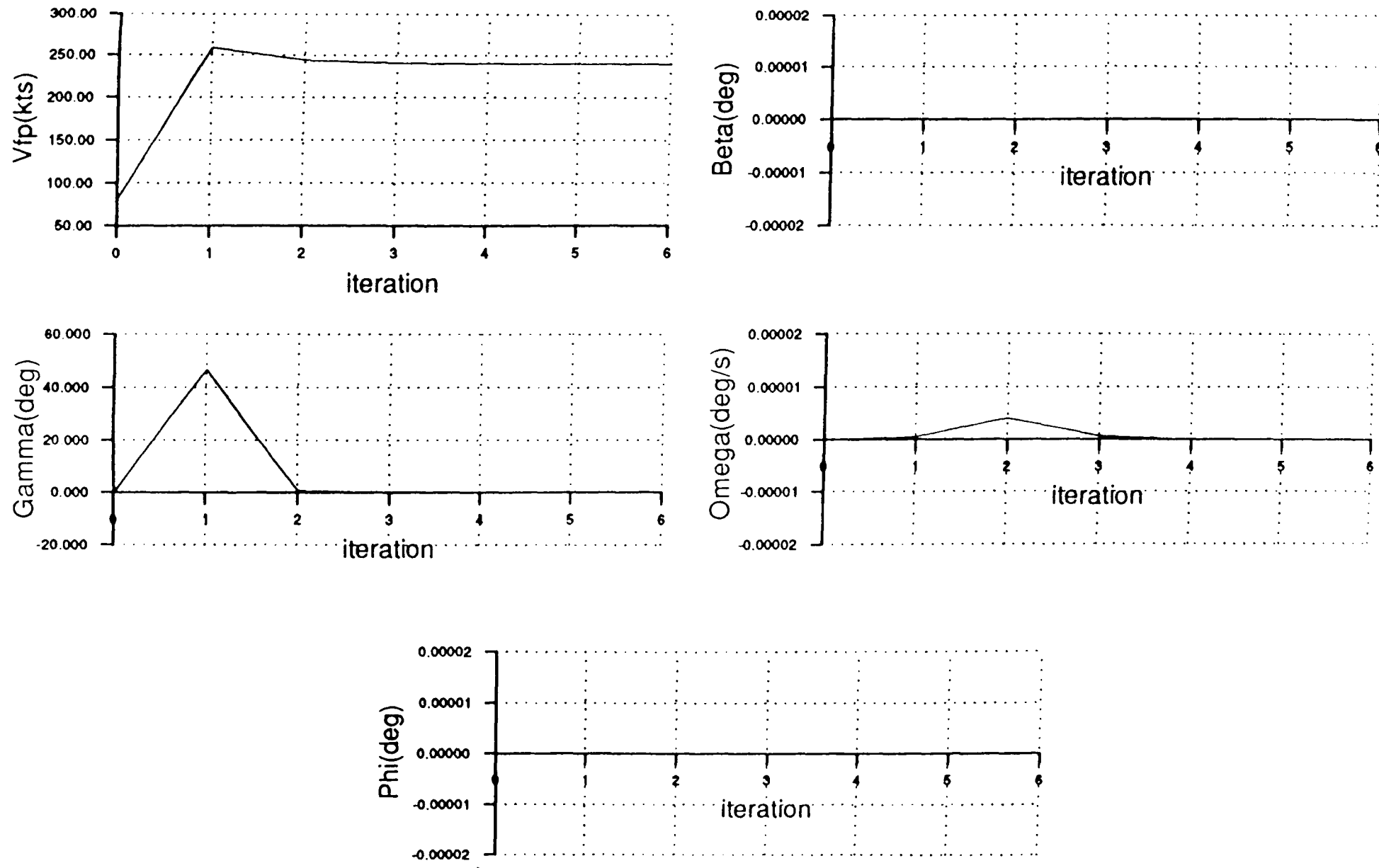


Figure 5.1 Flight Path Iteration History - 240 knots in Aeroplane Mode

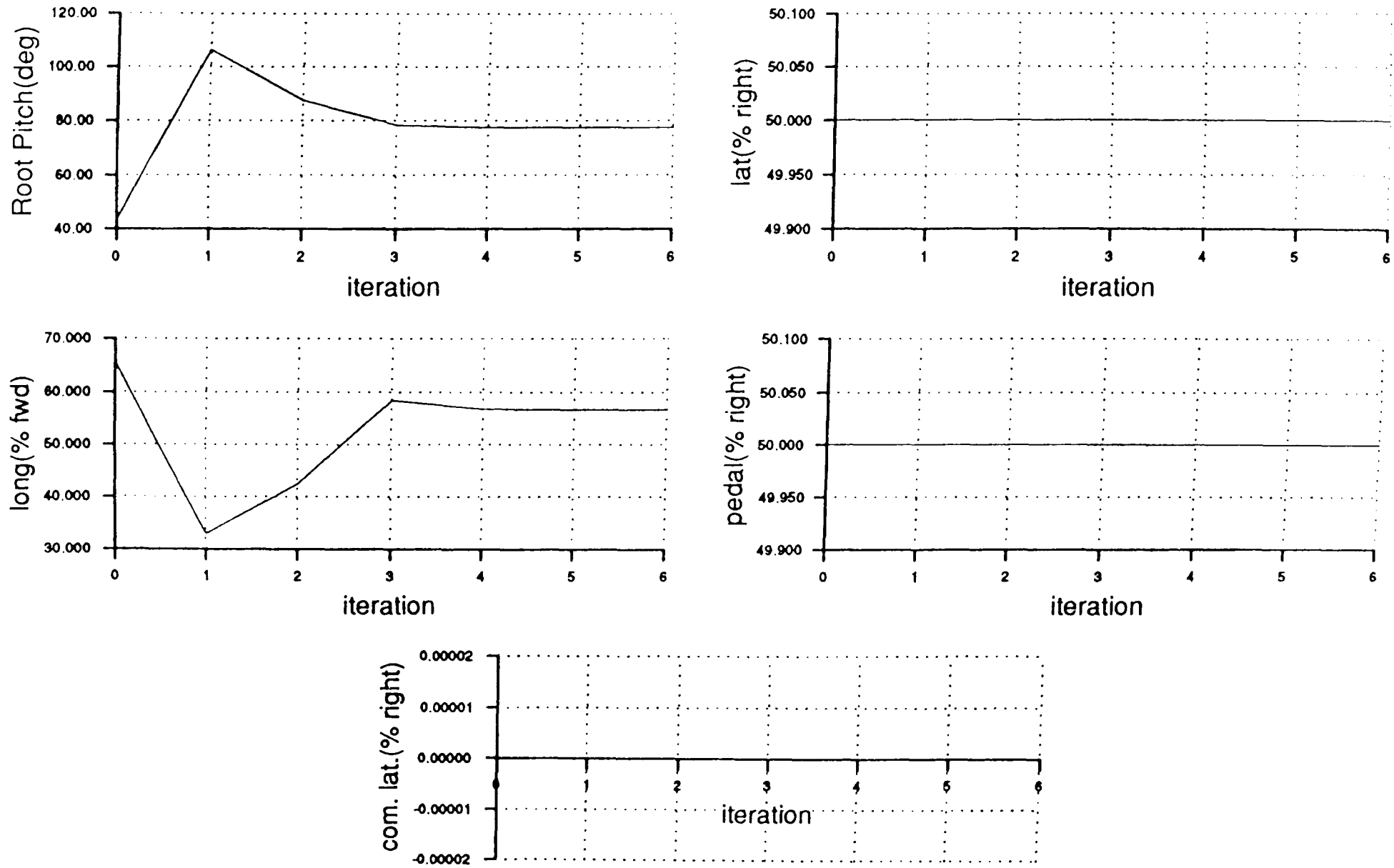


Figure 5.2 Control State Iteration History - 240 Knots in Aeroplane Mode

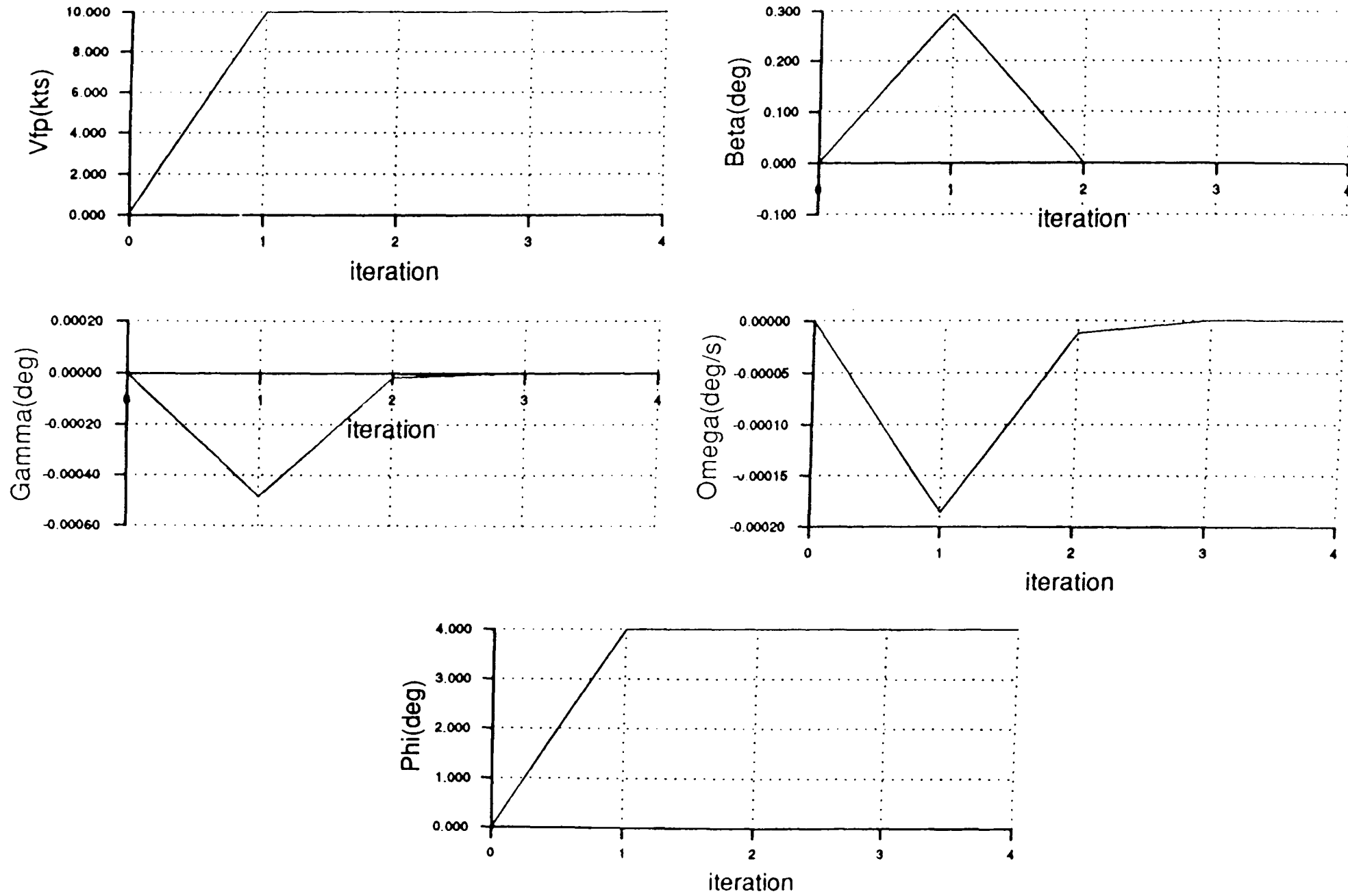


Figure 5.3 Flight Path Iteration History - 10 Knots 4 Degrees of Bank in Helicopter Mode

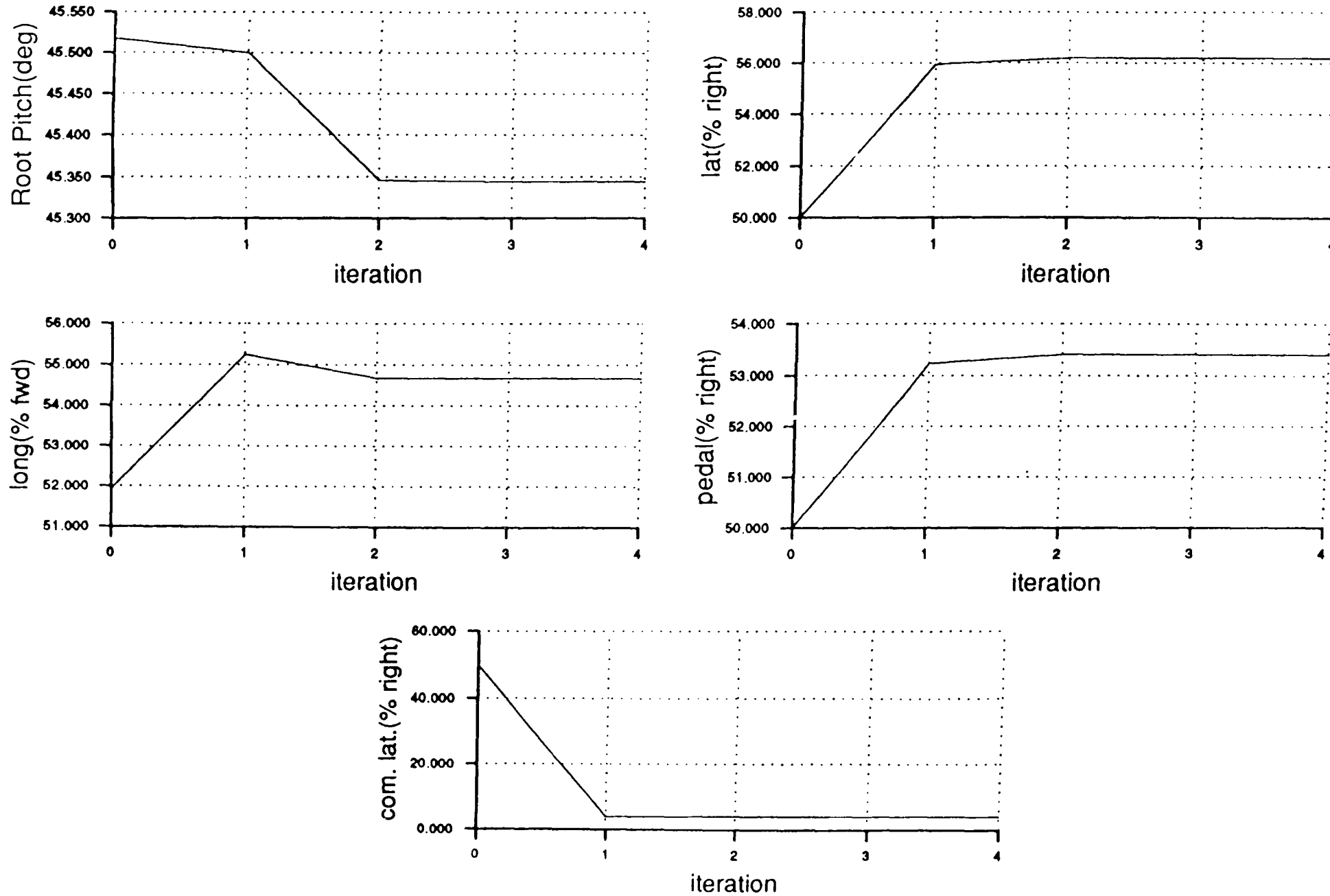


Figure 5.4 Control State Iteration History - 10 Knots 4 Degrees of Bank in Helicopter Mode

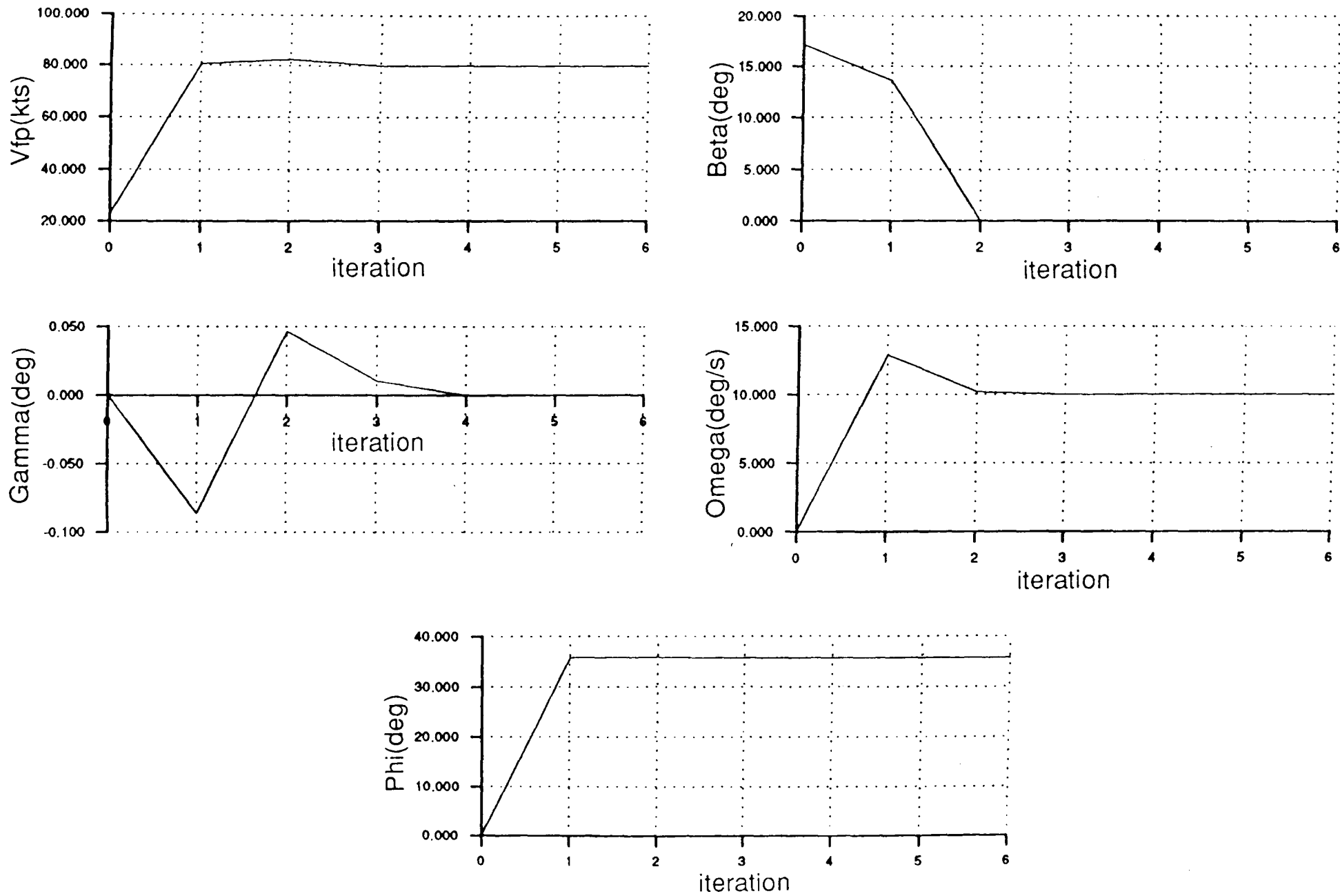


Figure 5.5 Flight Path Iteration History - 80 Knots, 10 Degree Per Second Turn Rate at 36 Degrees of Bank with 14.9 Degrees Nacelle Angle

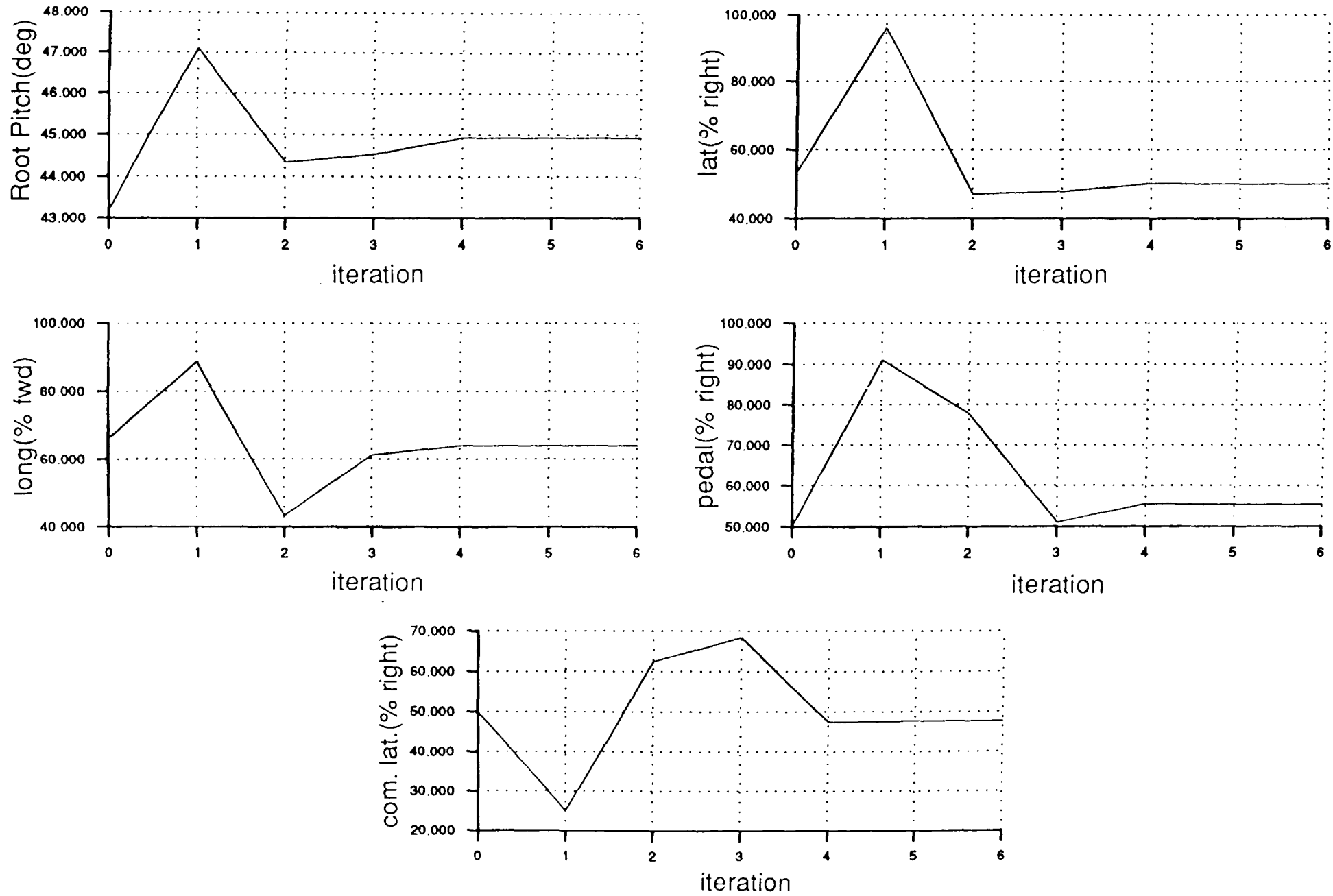


Figure 5.6 Control State Iteration History - 80 Knots, 10 Degree Per Second Turn Rate at 36 Degrees of Bank with 14.9 Degrees Nacelle Angle

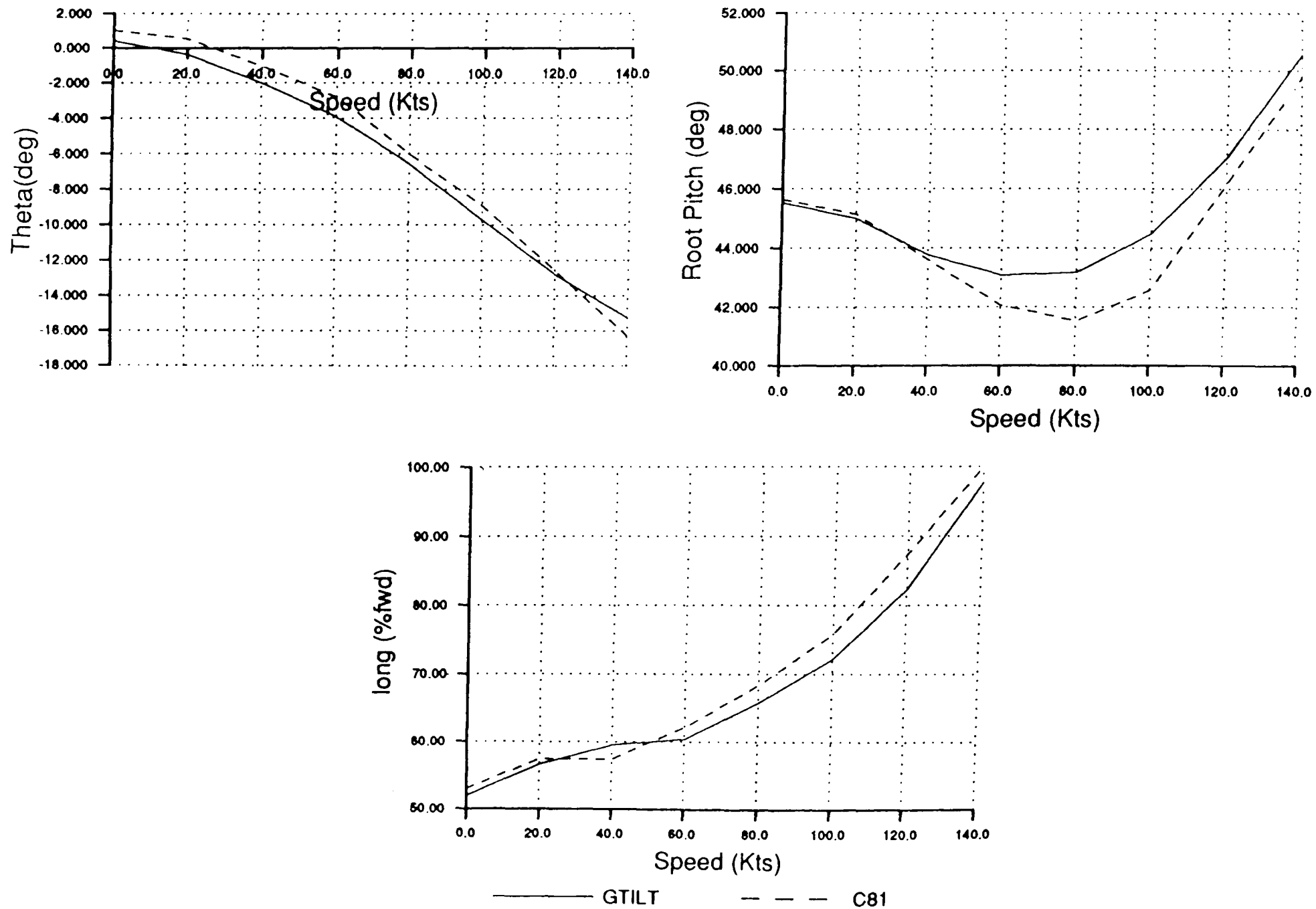


Figure 5.7 Comparison Between GTILT and Bell C81 - Longitudinal Trim in Helicopter Mode

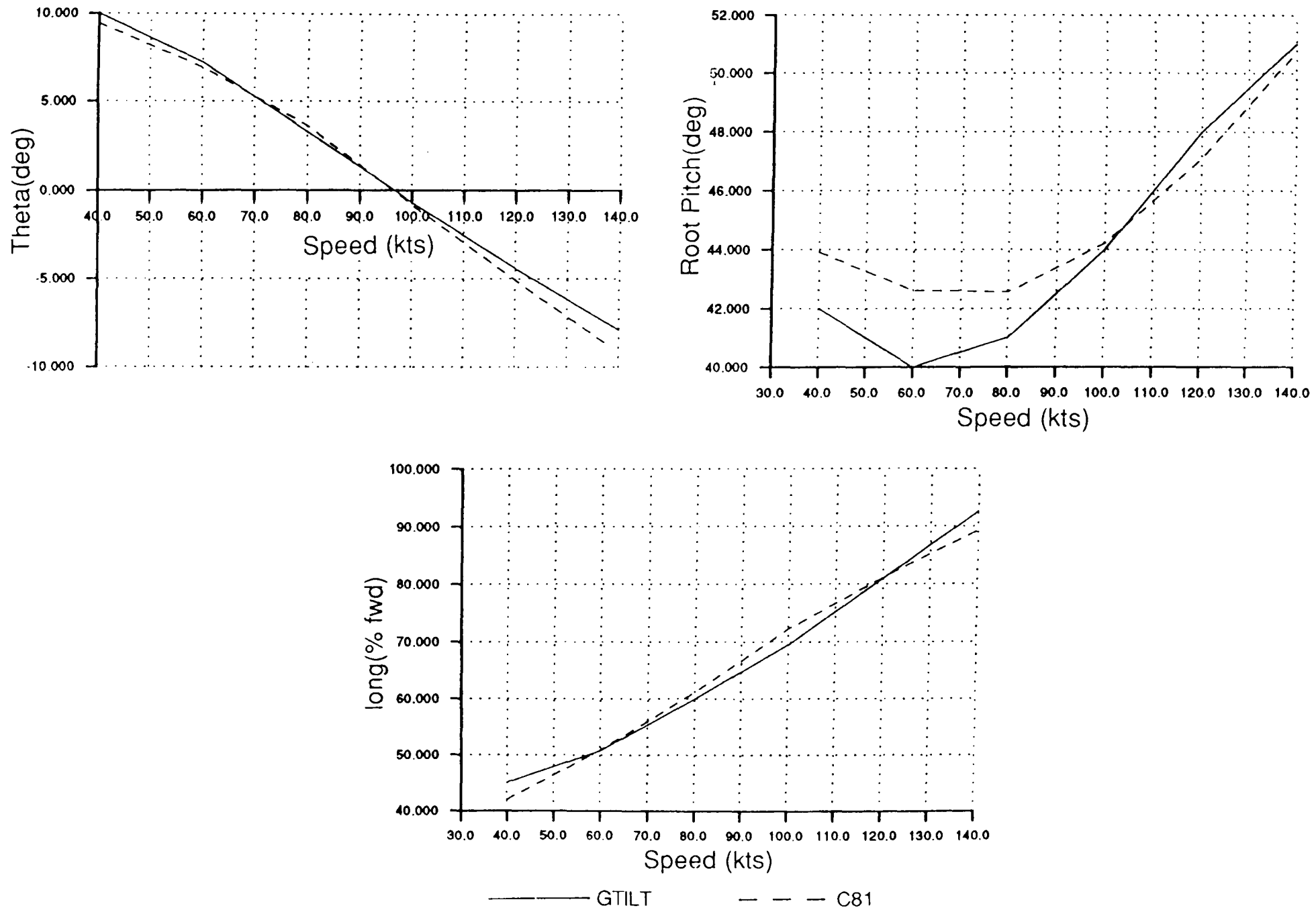


Figure 5.8 Comparison Between GTILT and Bell C81 - Longitudinal Trim at 15 Degrees Nacelle Angle

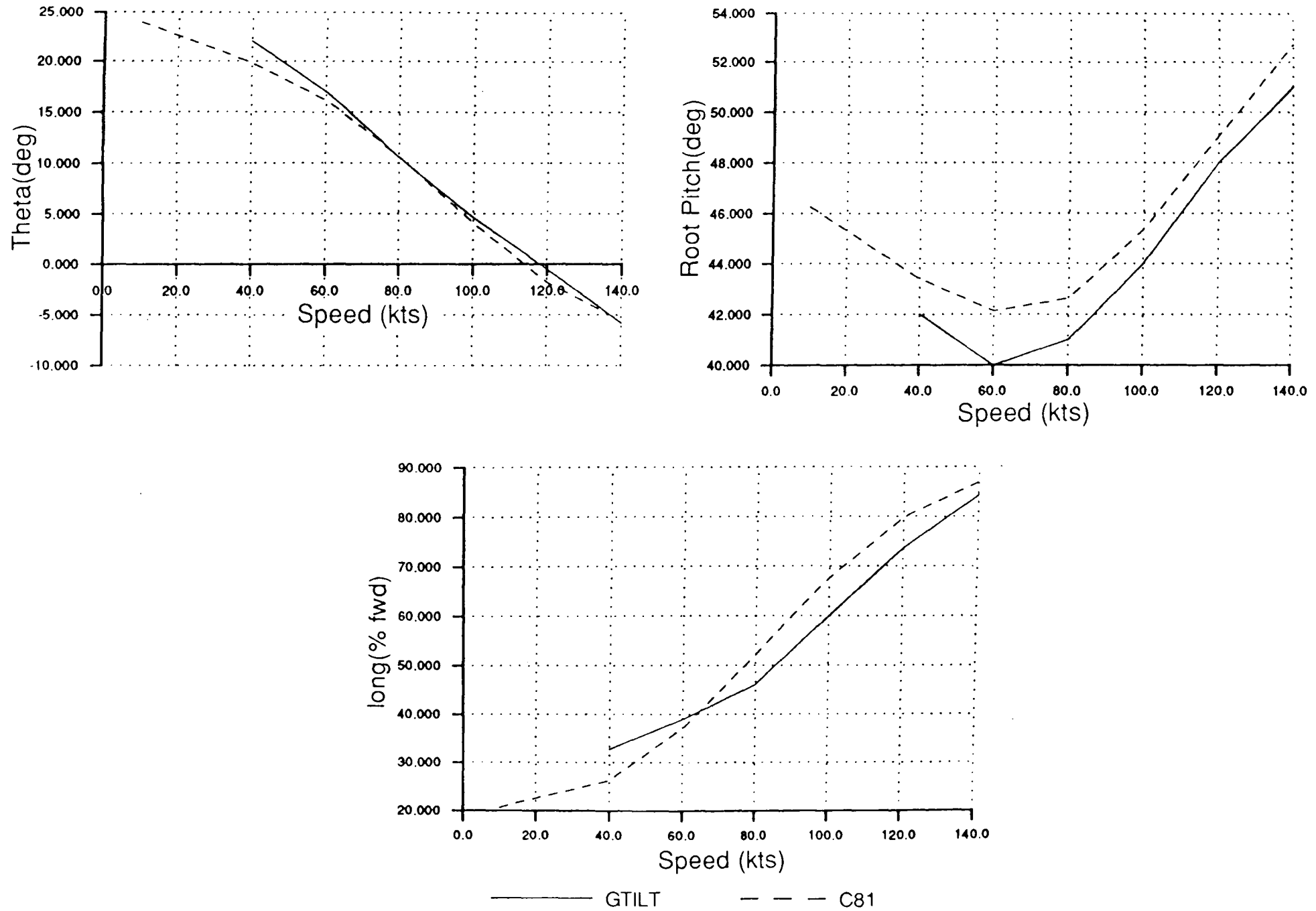


Figure 5.9 Comparison Between GTILT and Bell C81 - Longitudinal Trim at 30 Degrees Nacelle Angle

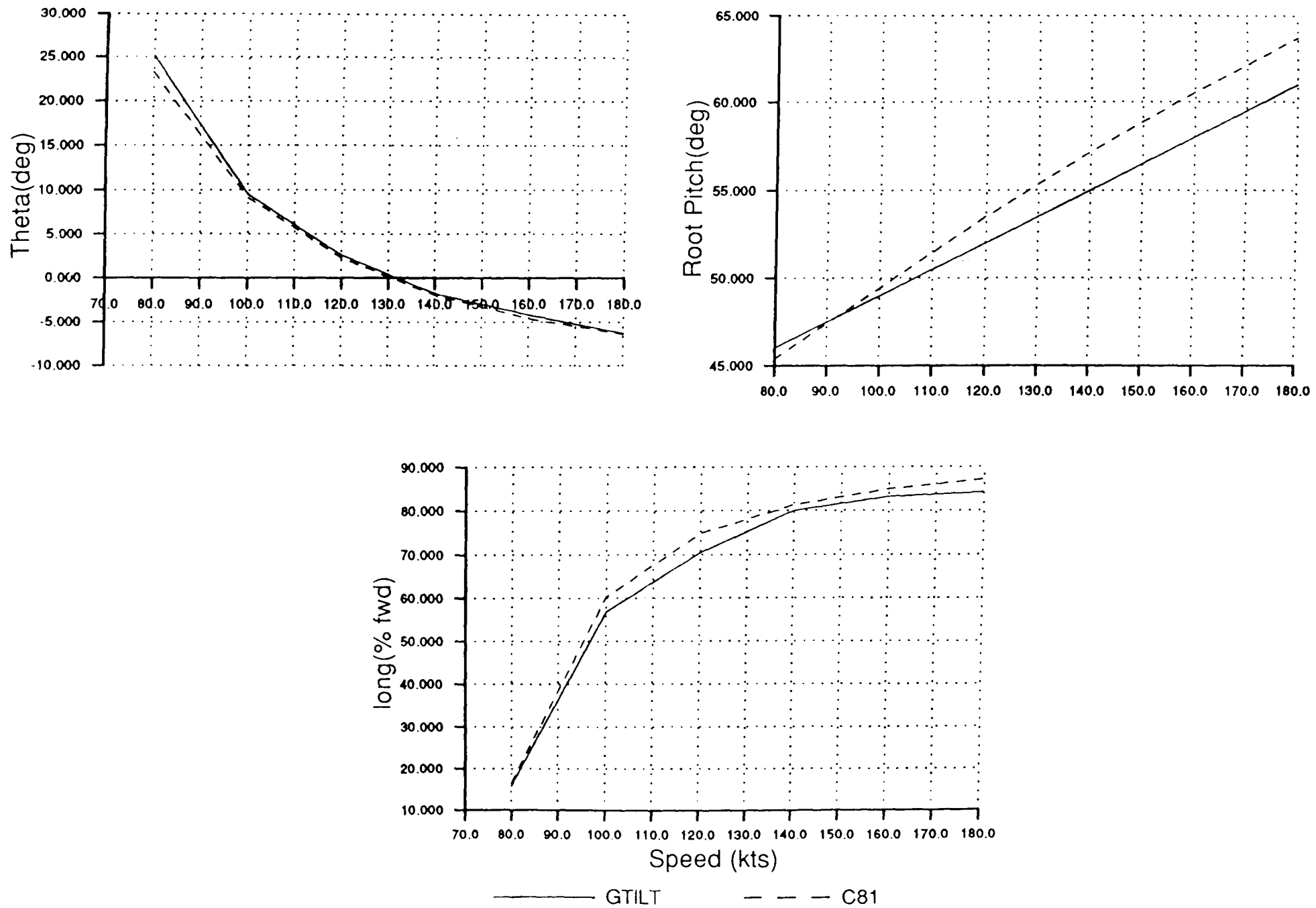


Figure 5.10 Comparison Between GTILT and Bell C81 - Longitudinal Trim at 60 Degrees Nacelle Angle

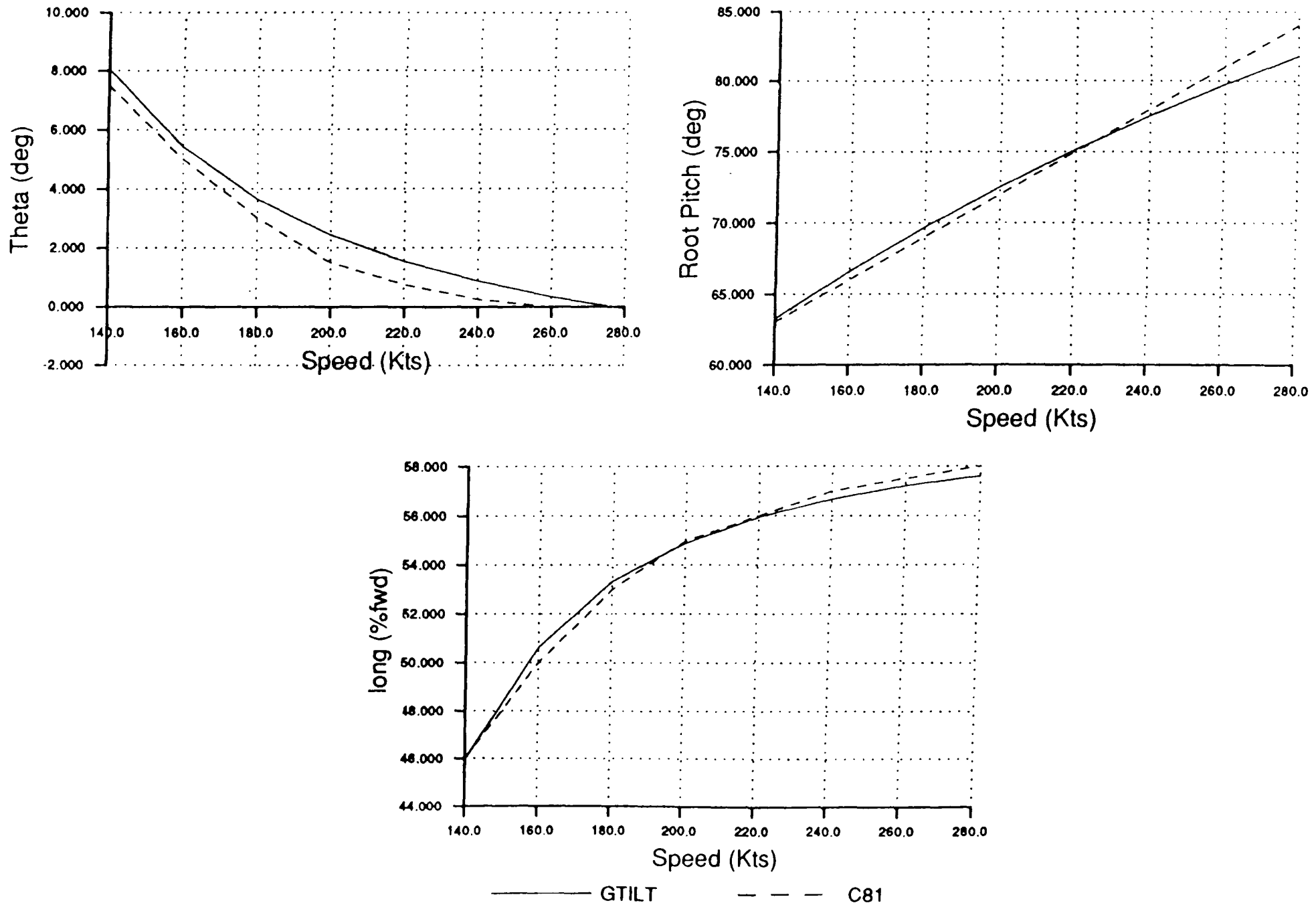


Figure 5.11 Comparison Between GTILT and Bell C81 - Longitudinal Trim in Aeroplane Mode

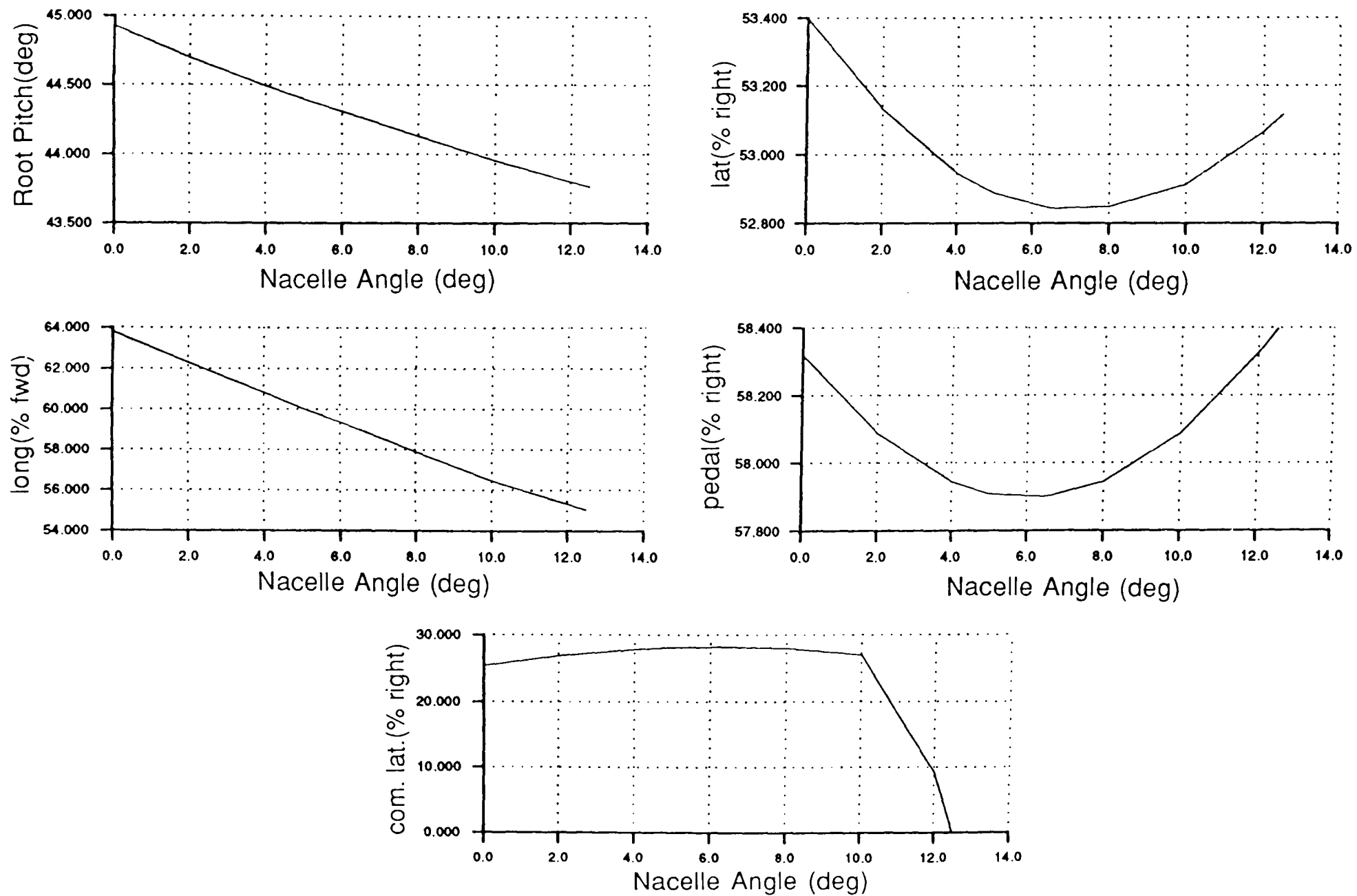


Figure 5.12 Controls Required To Produce 10 Degree Per Second Turn Rate at 38 degrees Bank
Nacelle Angles up to 15 Degrees

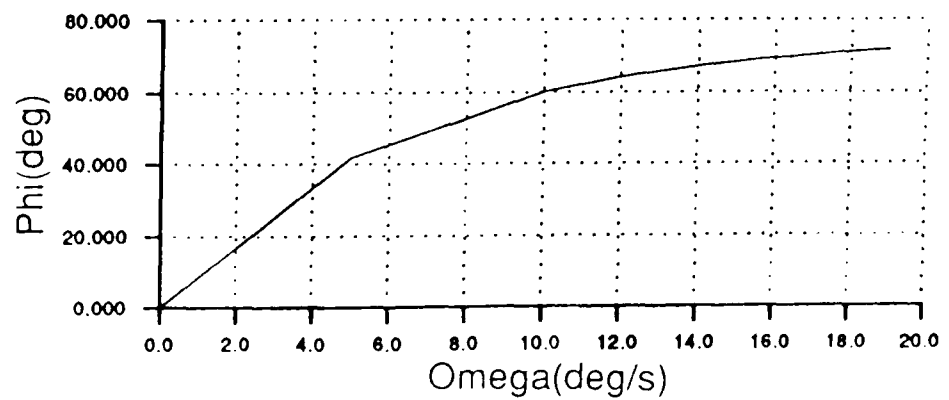
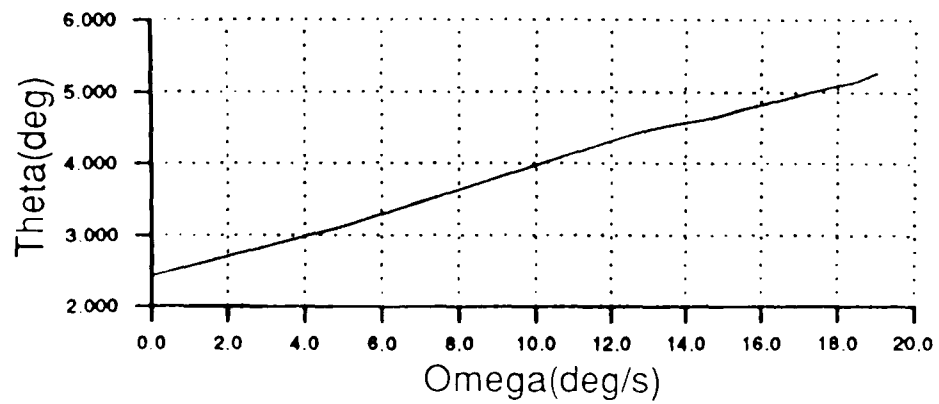
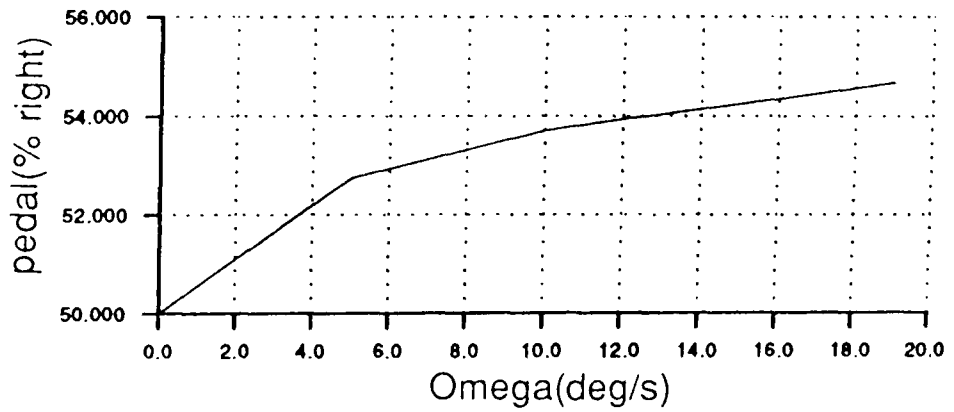
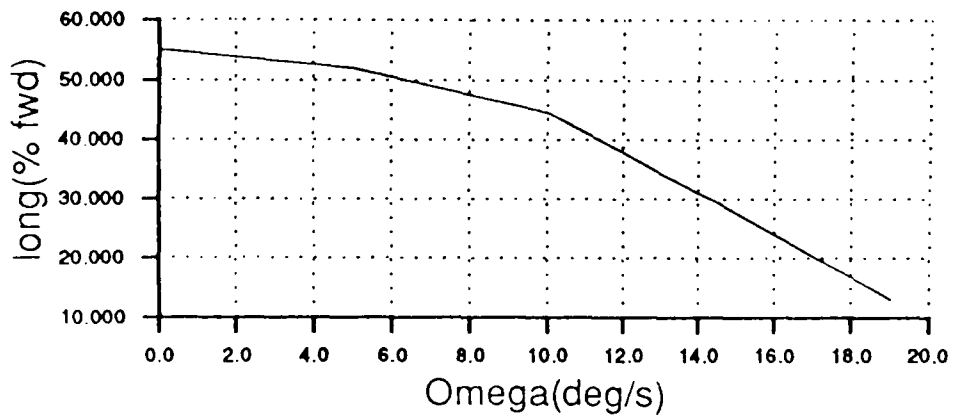
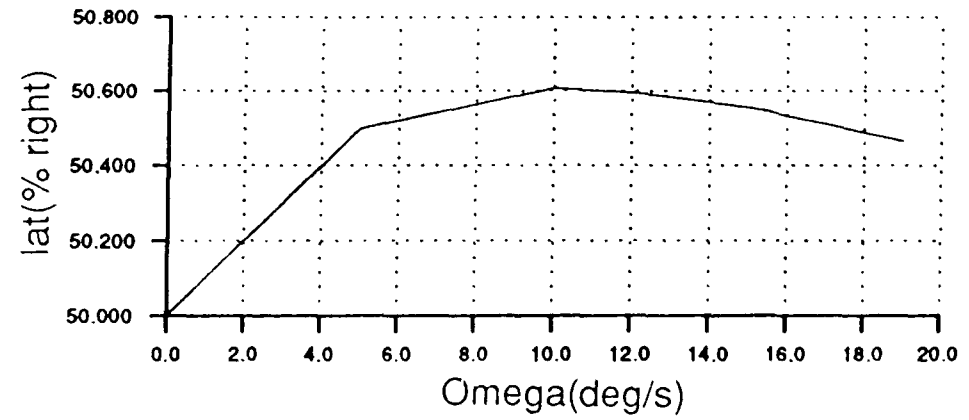
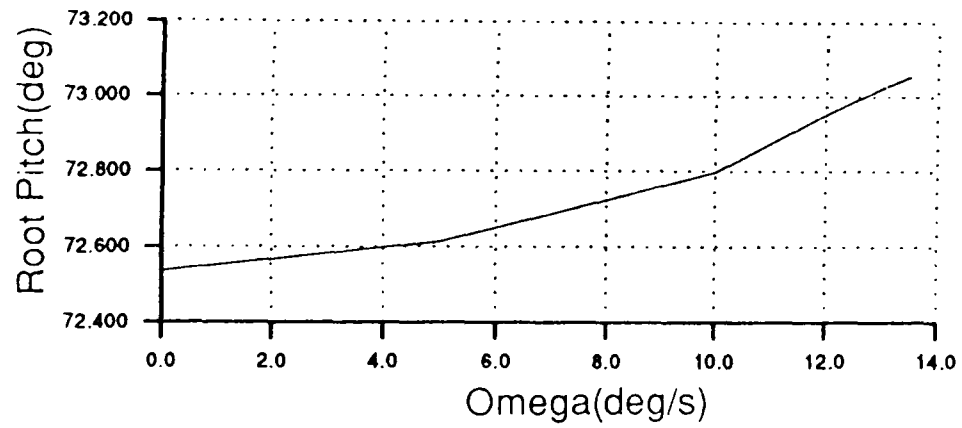


Figure 5.13 Tuning Flight In Aeroplane Mode at 200 Knots
Turn Rates From 0 to 19 Degrees Per Second

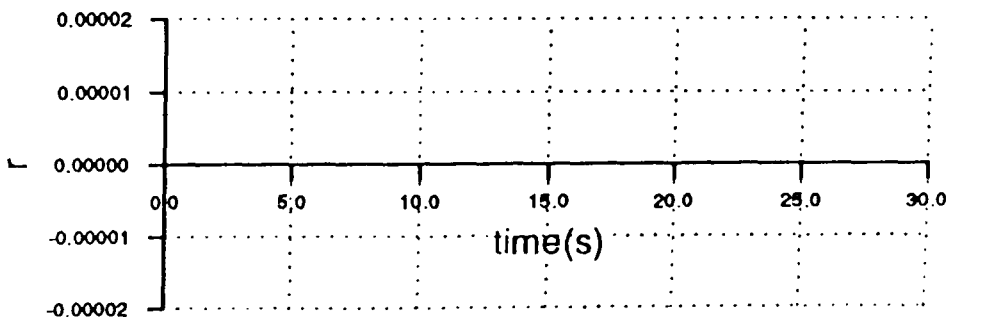
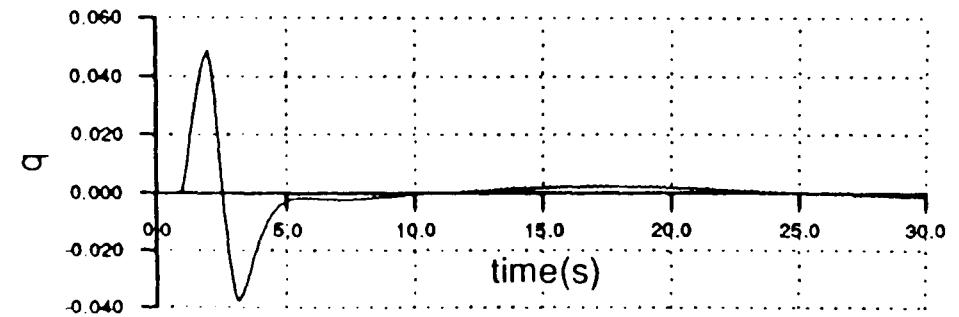
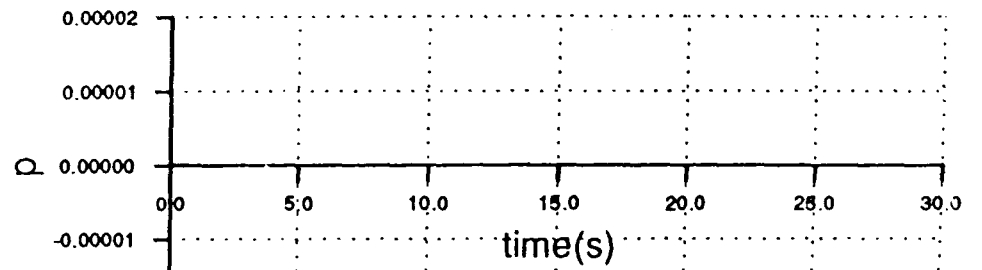
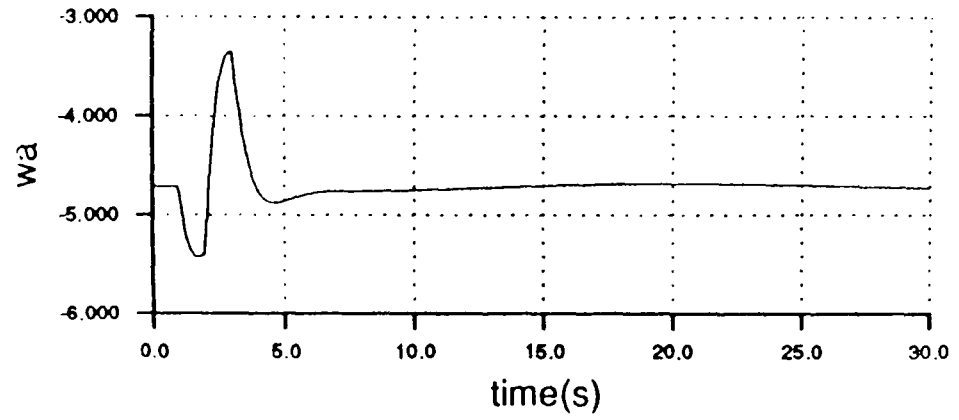
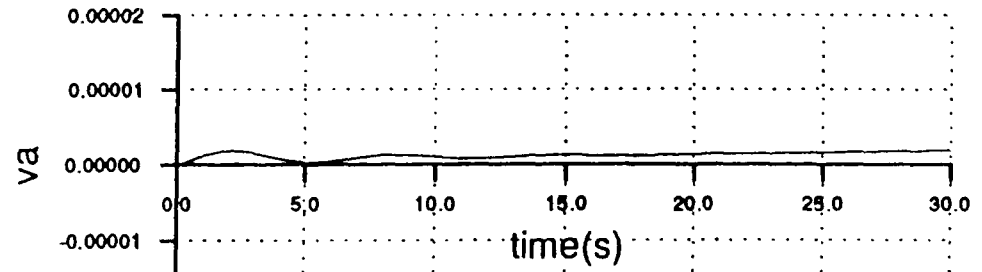
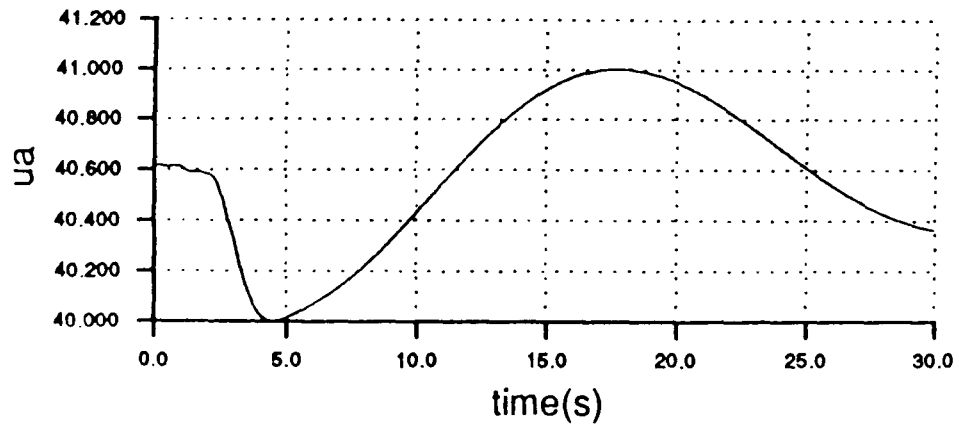


Figure 5.14 Body Axis Flight States Produced when a Doublet is Applied to Combined Collective in Helicopter Mode

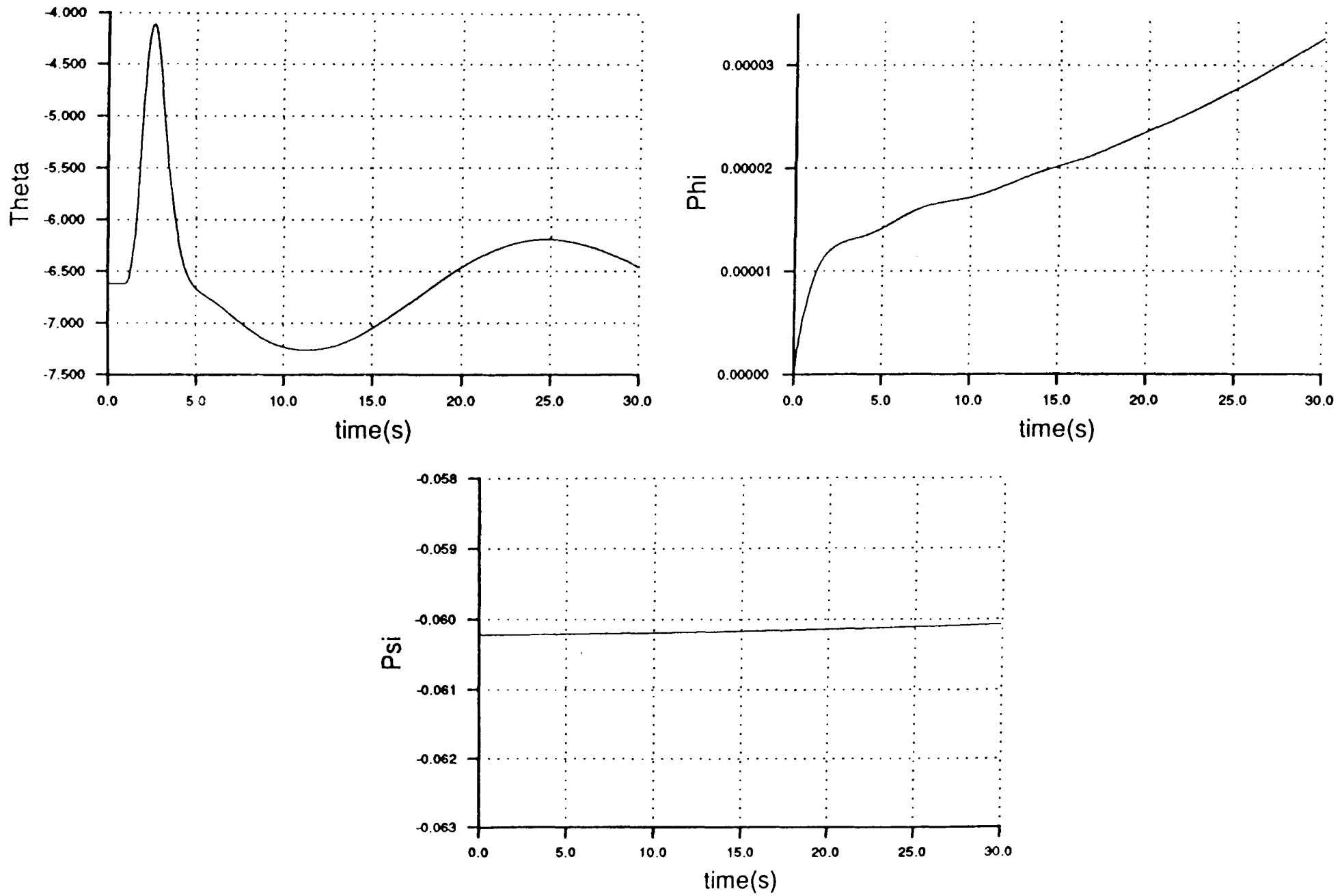


Figure 5.15 Vehicle Attitudes Produced when a Doublet is Applied to Combined Collective in Helicopter Mode

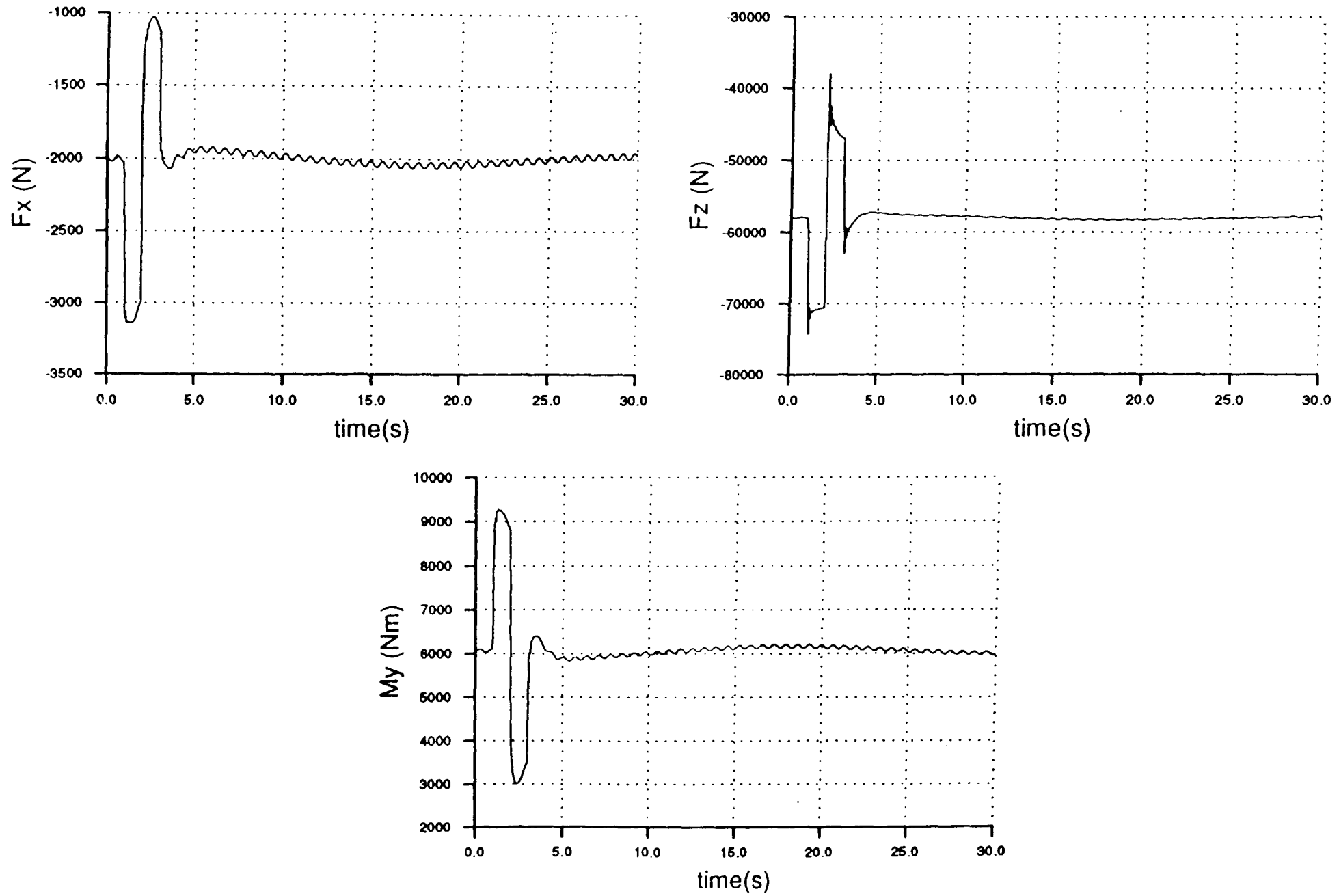


Figure 5.16 Average Forces Produced when a Doublet is Applied to Combined Collective in Helicopter Mode

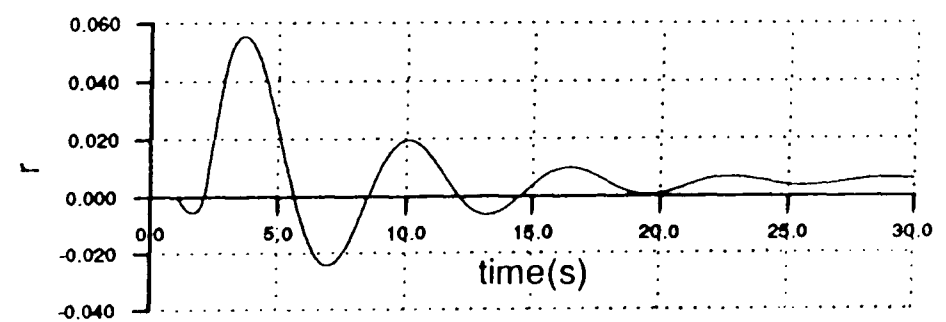
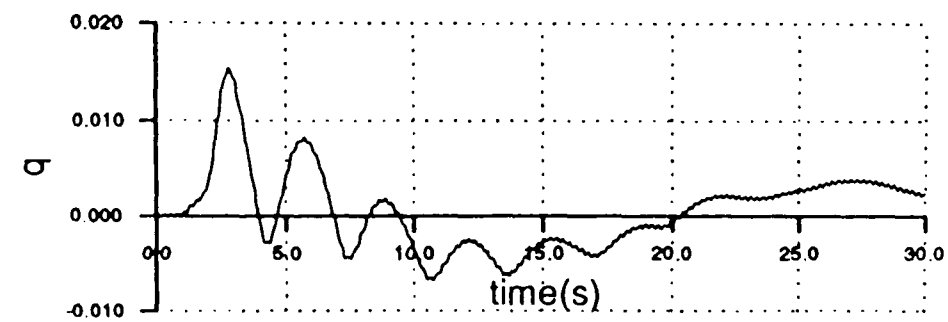
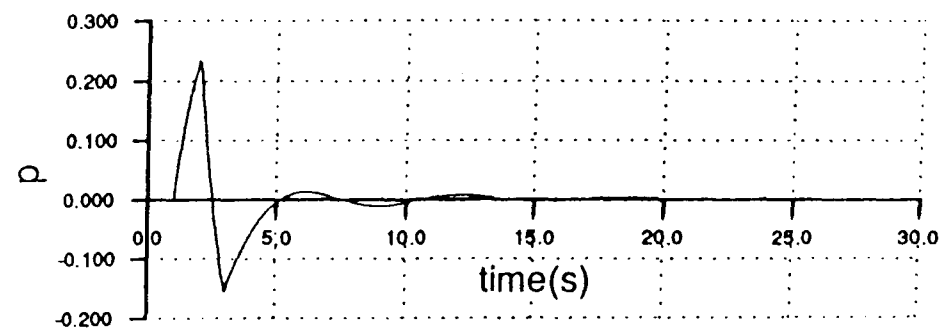
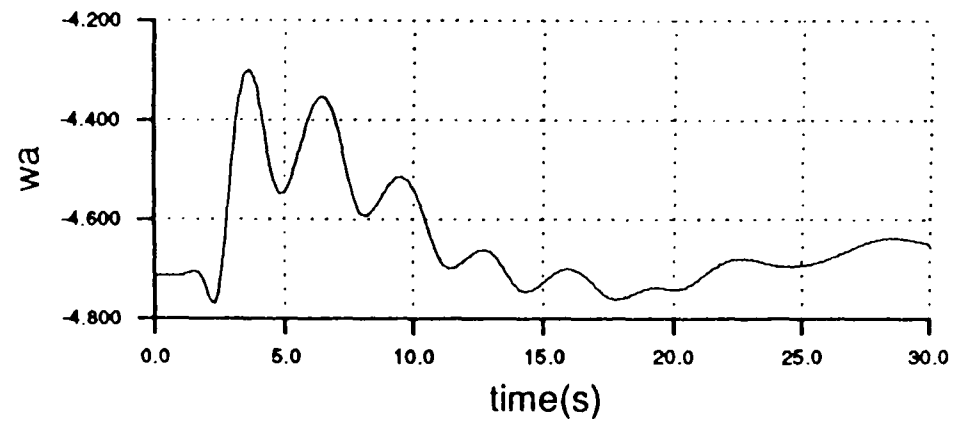
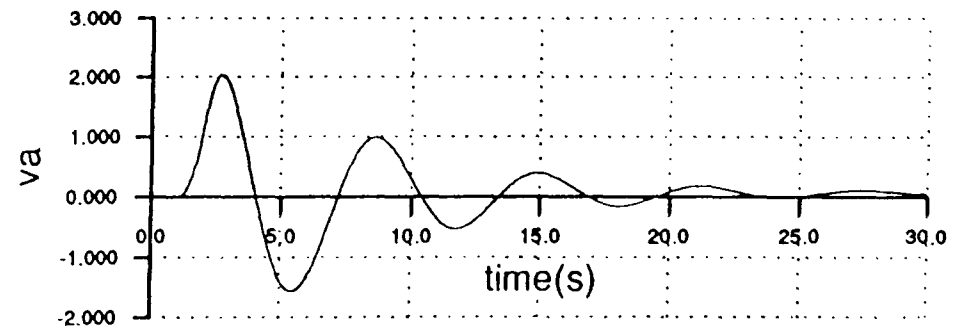
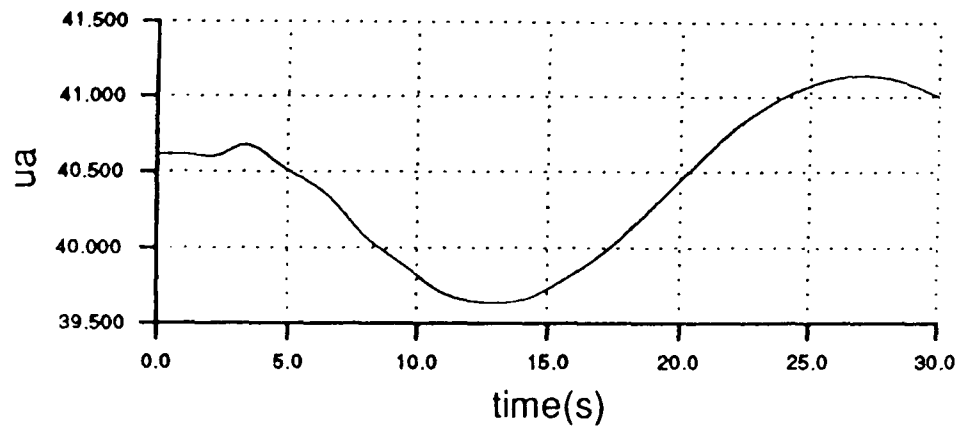


Figure 5.17 Body Axis Flight States Produced when a Doublet is Applied to Lateral Stick in Helicopter Mode

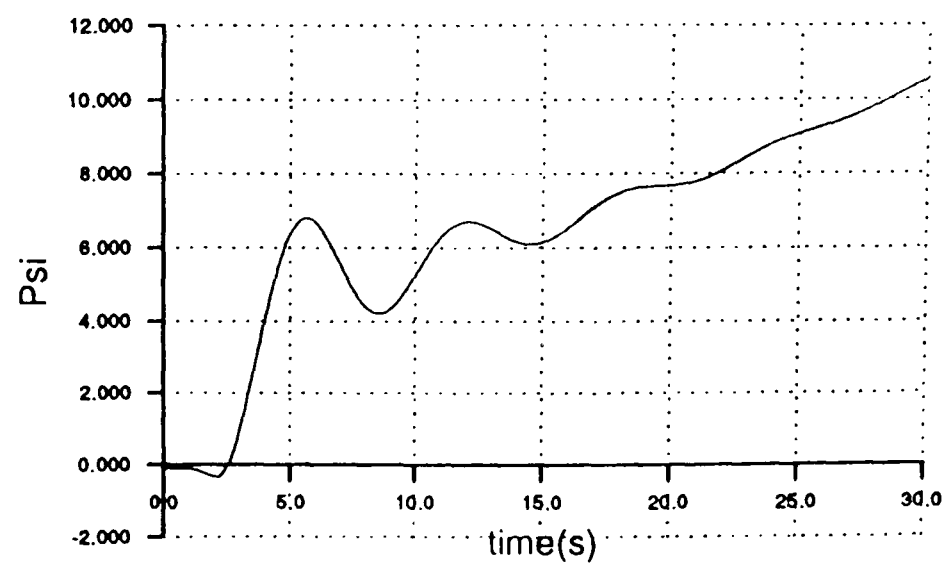
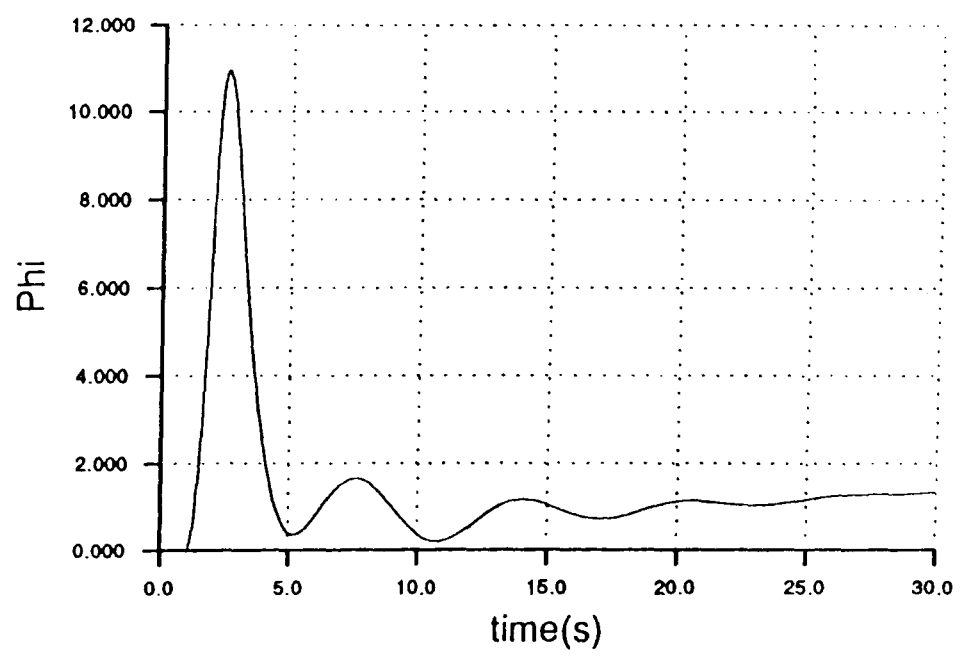
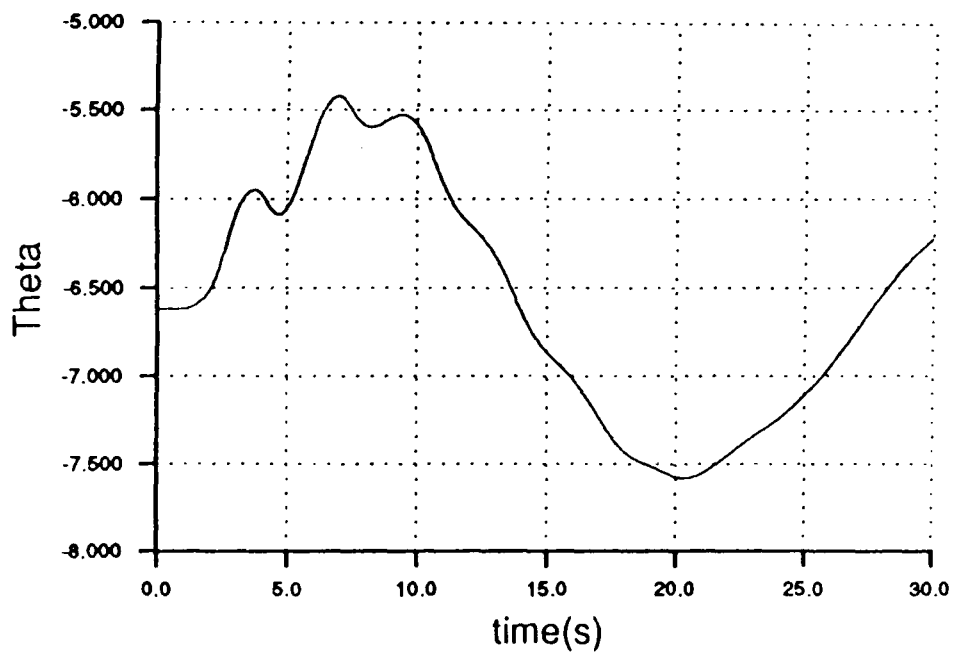


Figure 5.18 Vehicle Attitudes Produced when a Doublet is Applied to Lateral Stick in Helicopter Mode

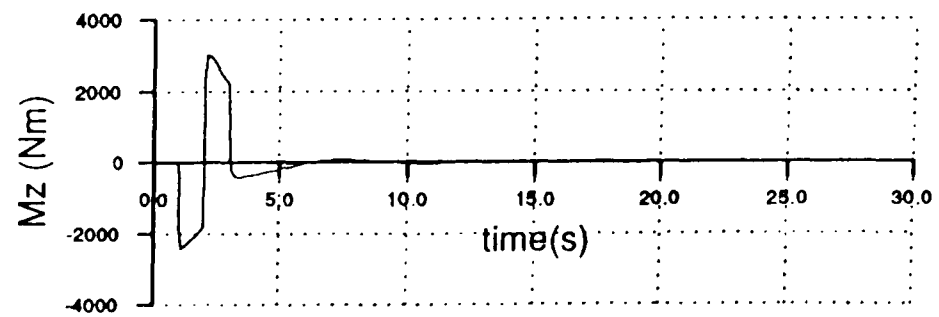
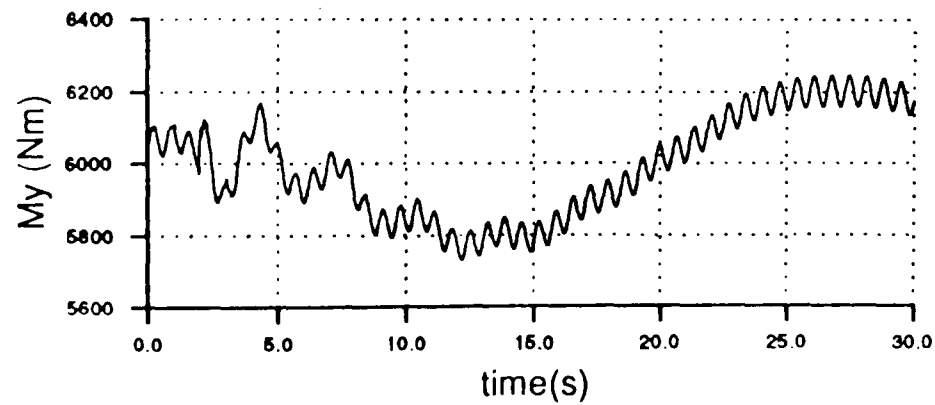
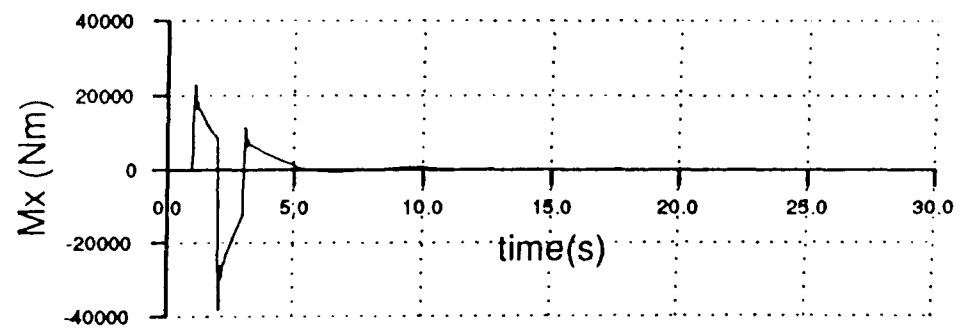
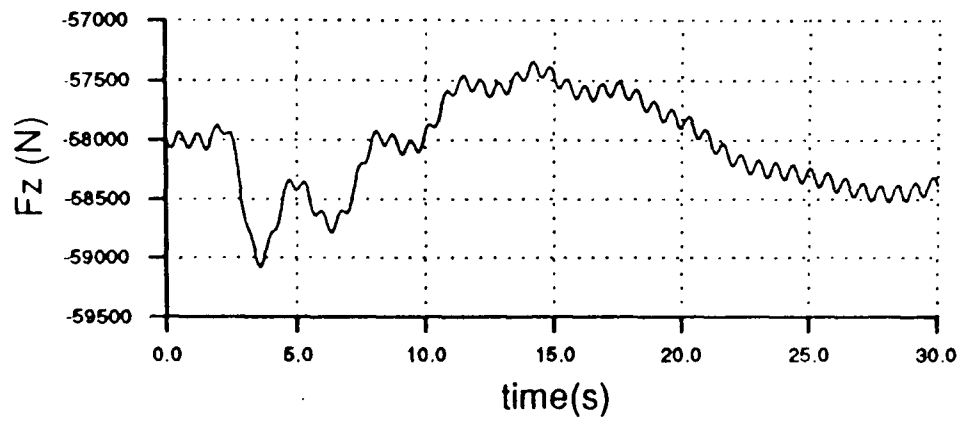
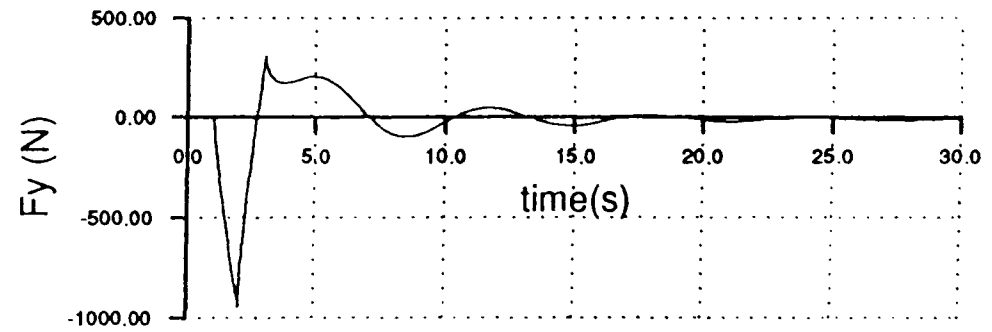
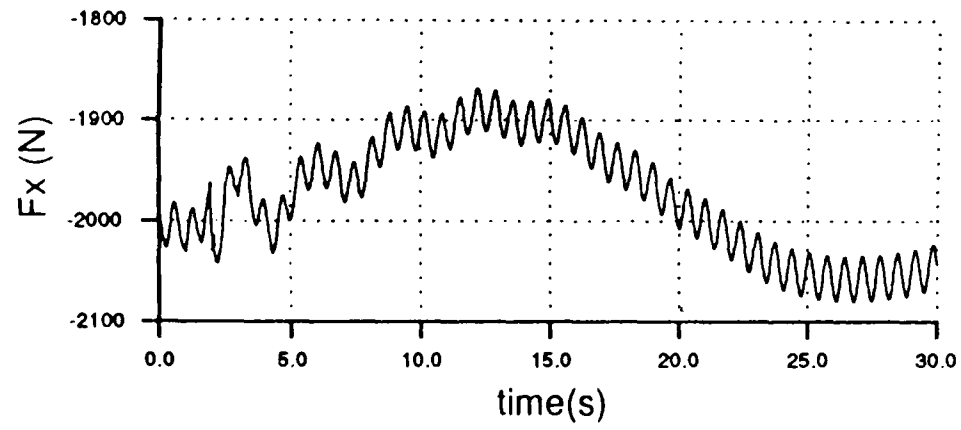


Figure 5.19 Average Rotor Forces Produced when a Doublet is Applied to Lateral Stick in Helicopter Mode

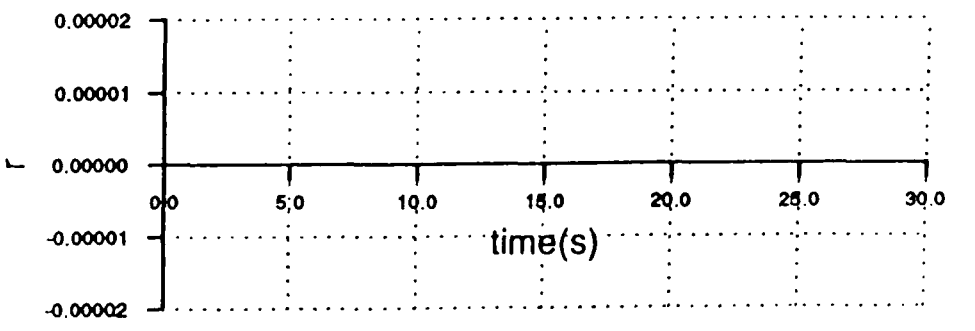
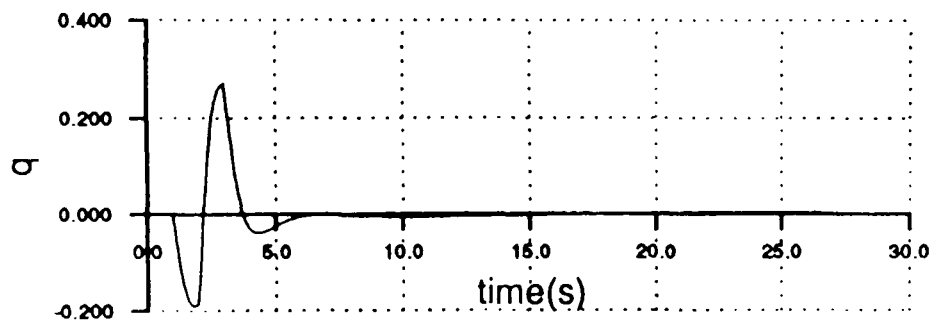
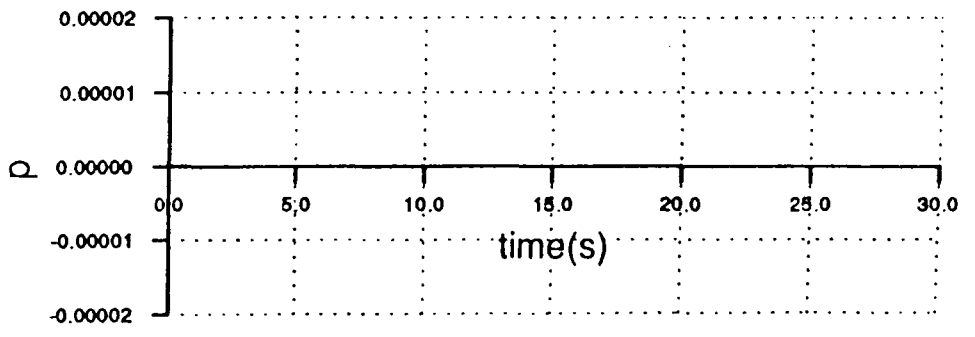
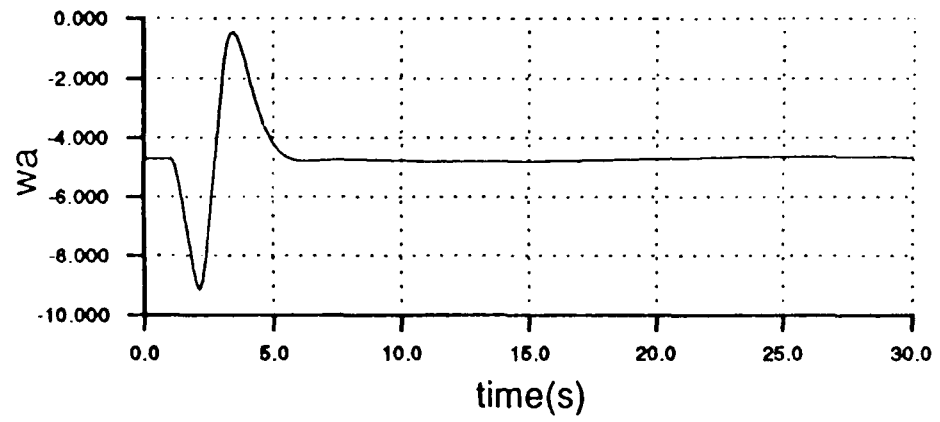
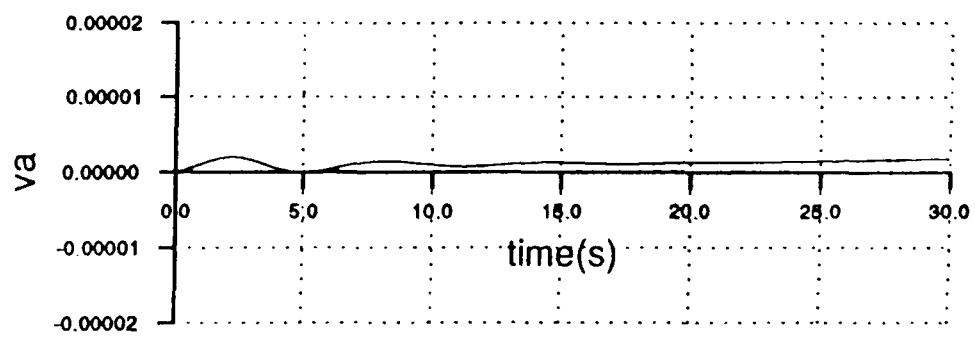
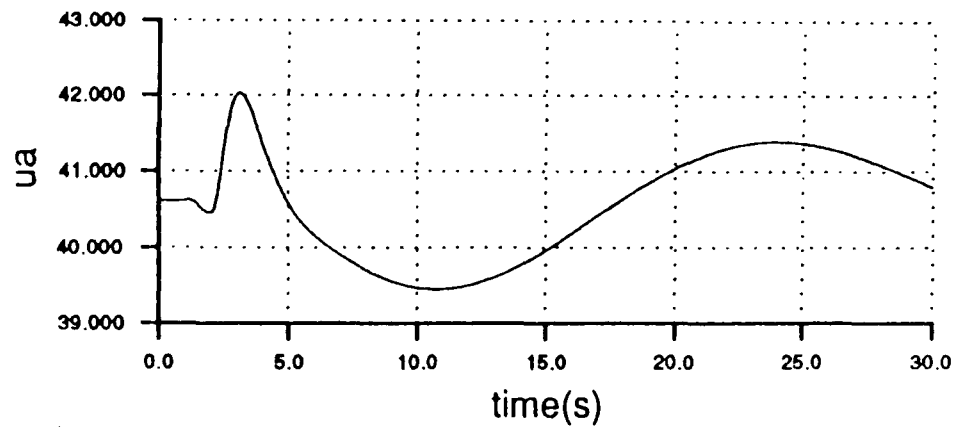


Figure 5.20 Body Axis Flight States Produced when a Doublet is Applied to Longitudinal Stick in Helicopter Mode

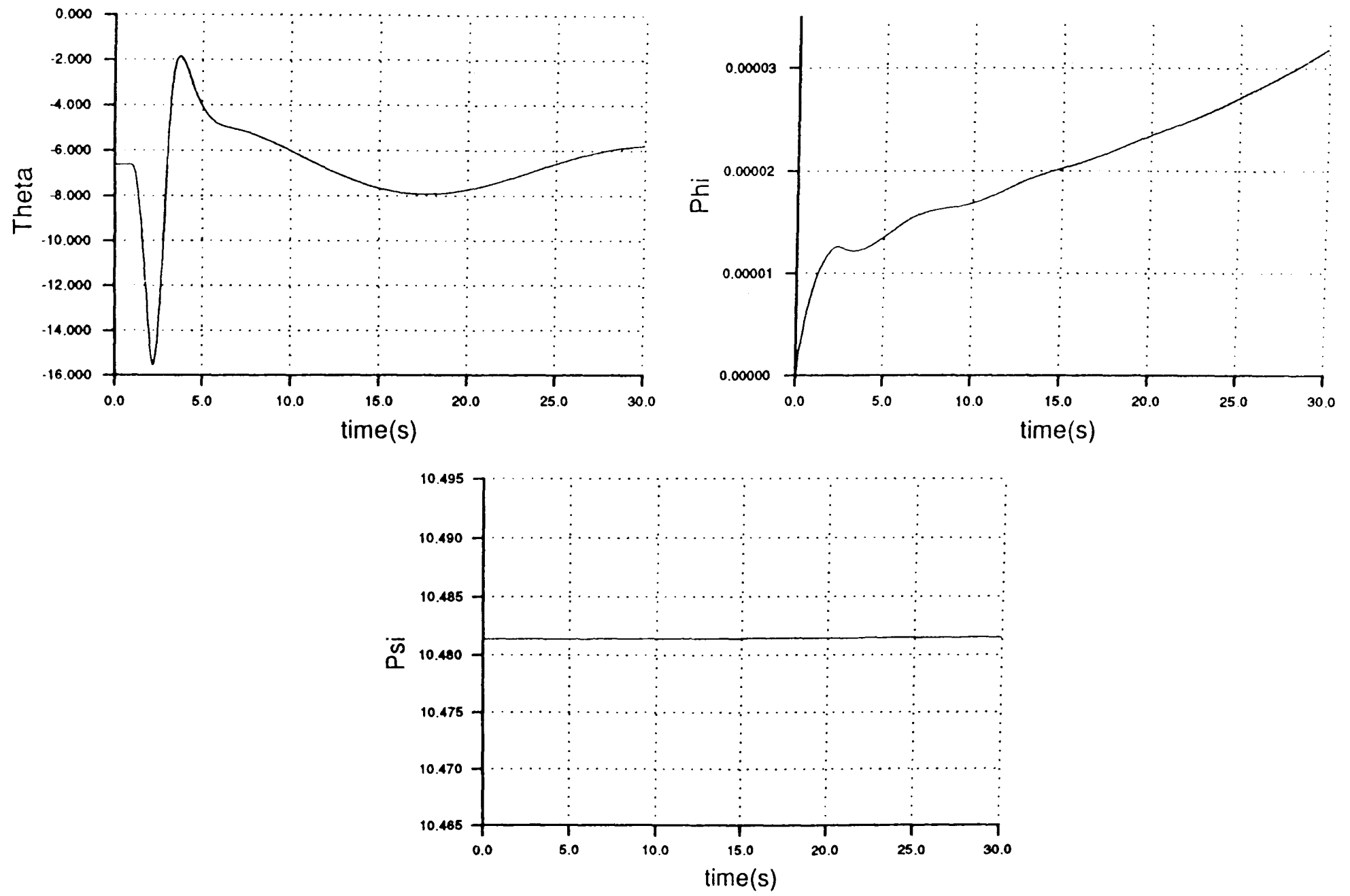


Figure 5.21 Vehicle Attitudes Produced when a Doublet is Applied to Longitudinal Stick in Helicopter Mode

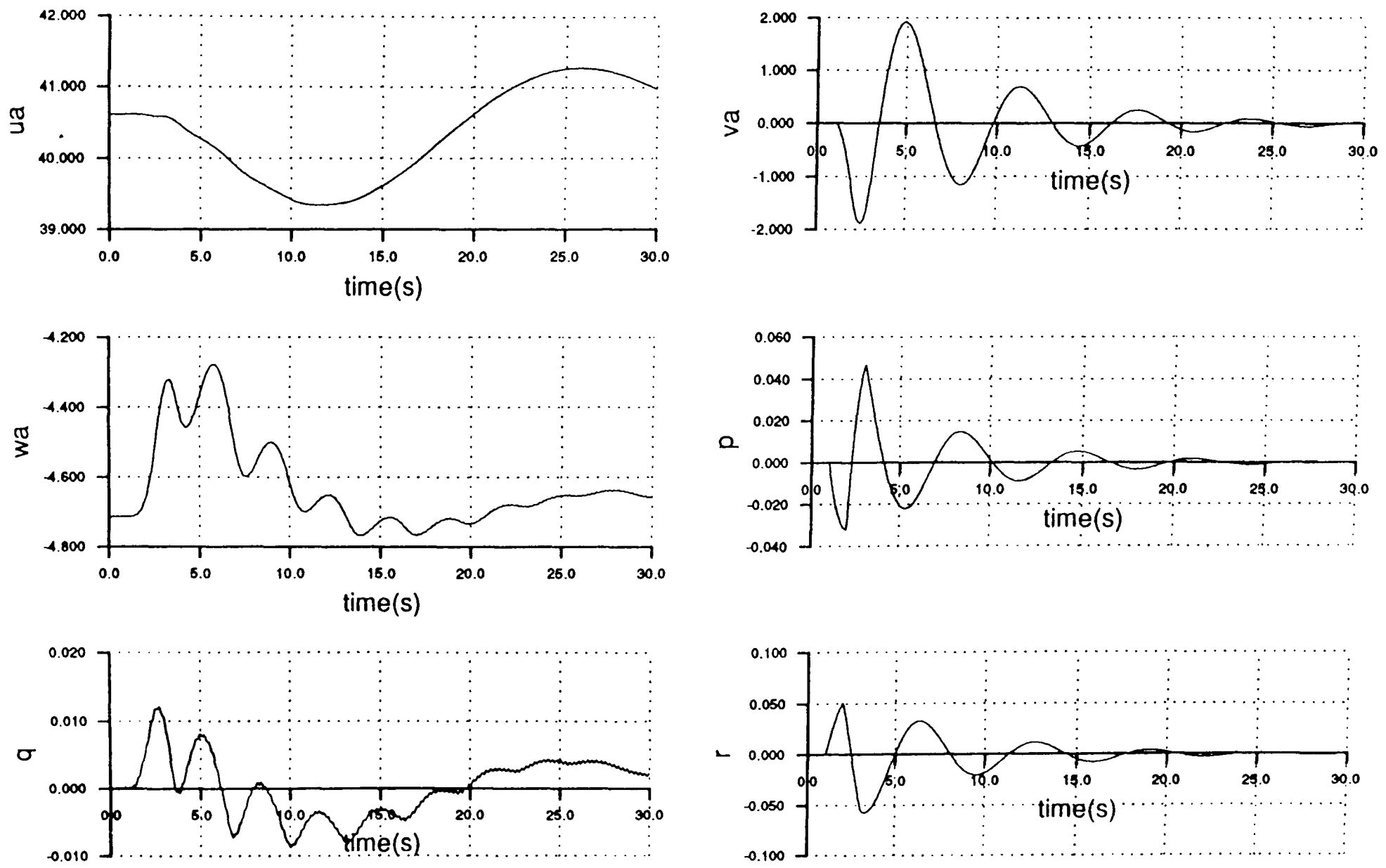


Figure 5.22 Body Axis Flight States Produced when a Doublet is Applied to Pedal in Helicopter Mode

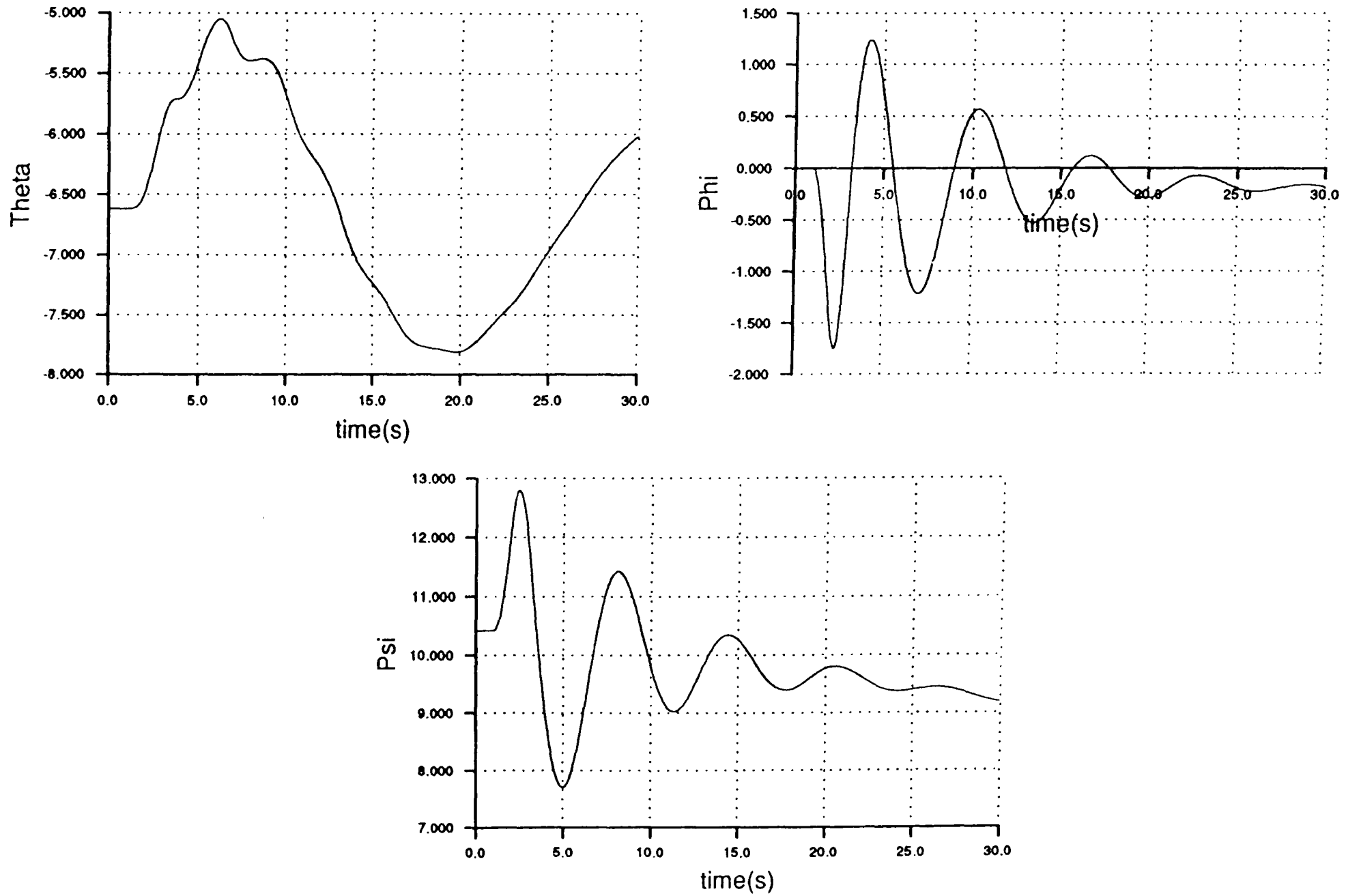


Figure 5.23 Vehicle Attitudes Produced when a Doublet is Applied to Pedal in Helicopter Mode

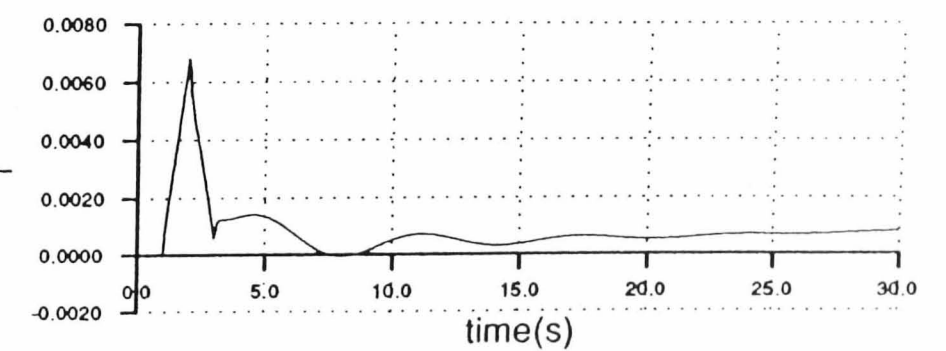
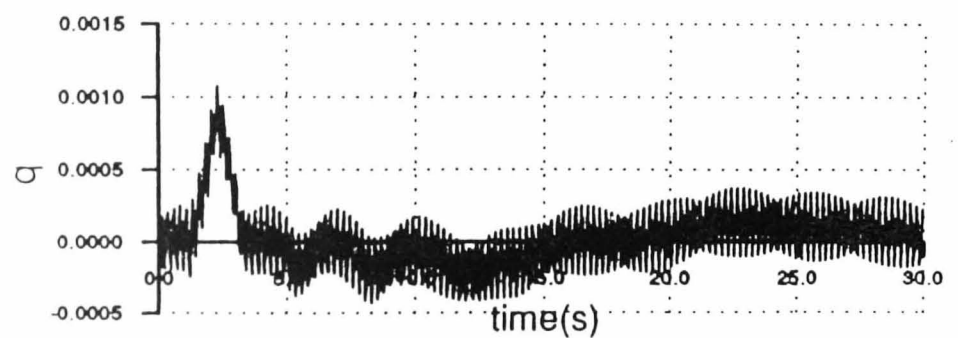
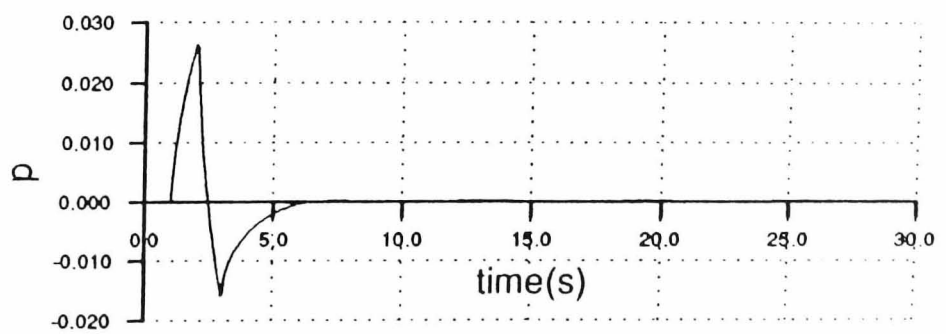
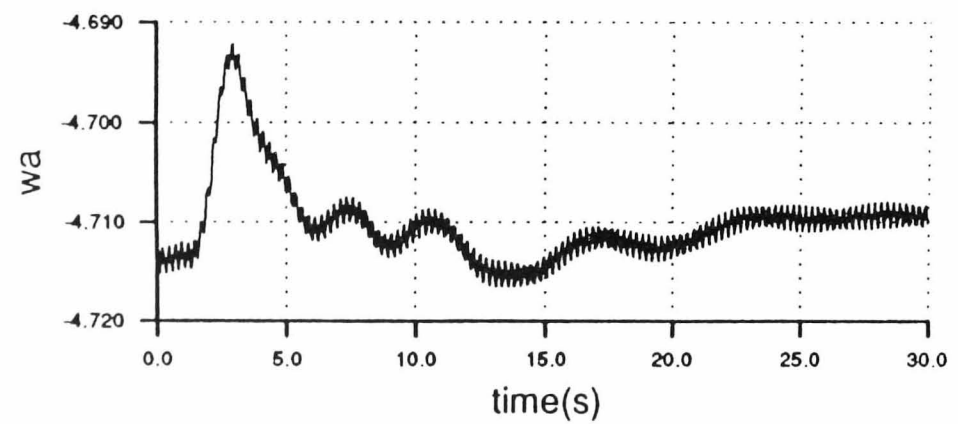
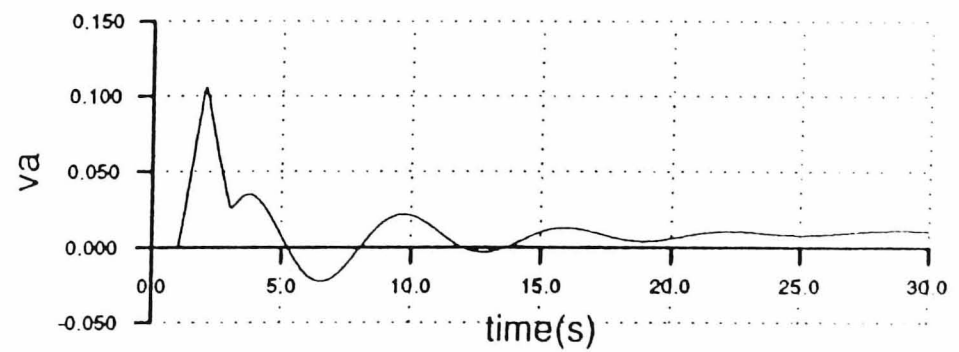
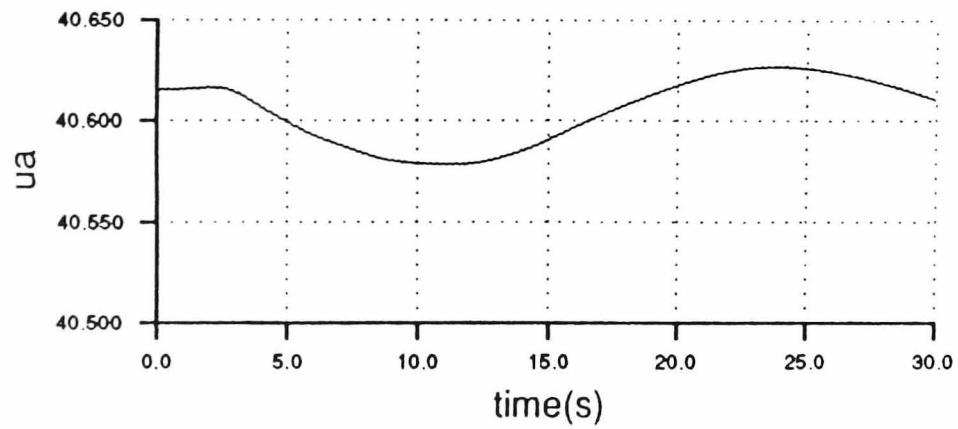


Figure 5.24 Body Axis Flight States Produced when a Doublet is Applied to Combined Lateral Cyclic in Helicopter Mode

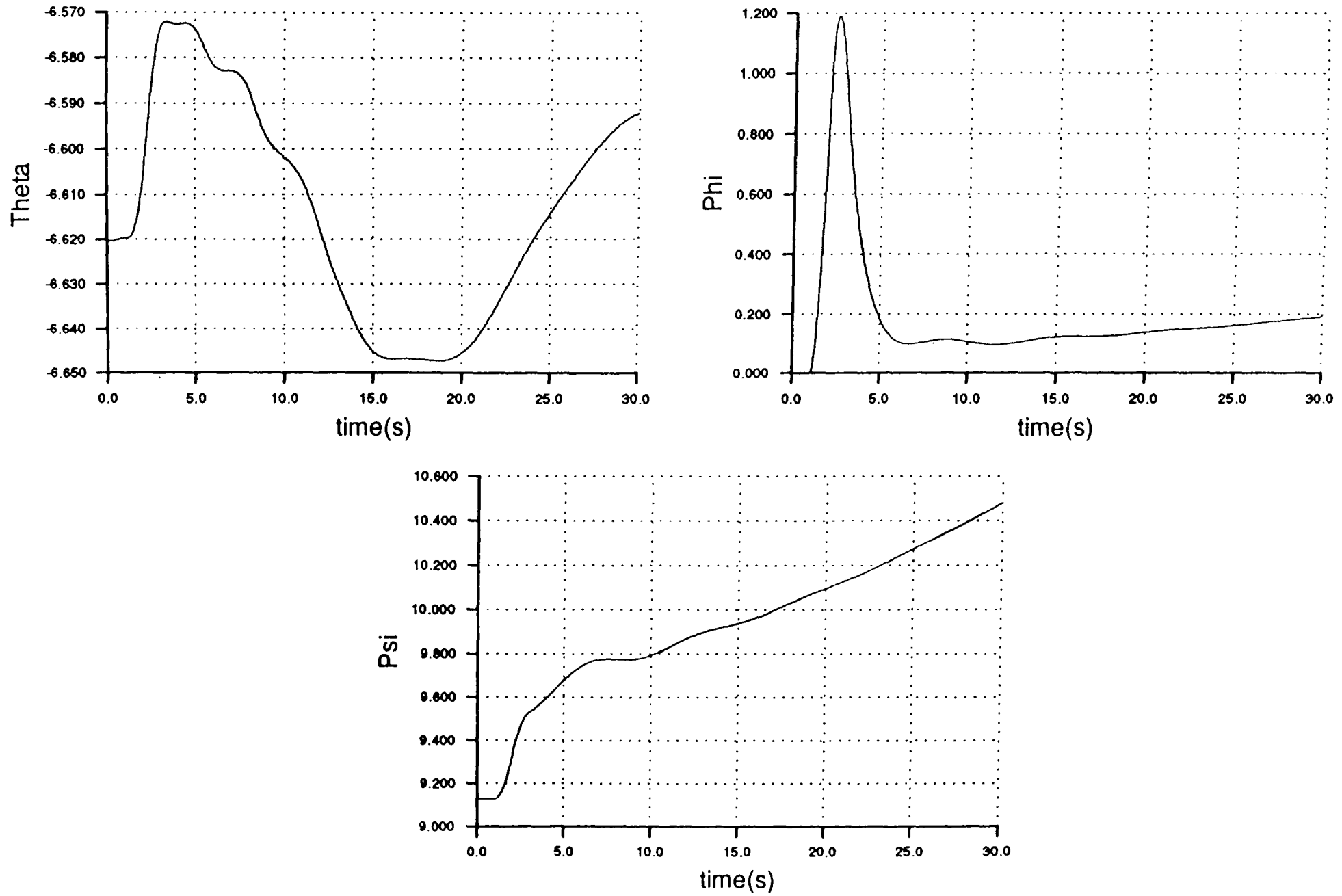


Figure 5.25 Vehicle Attitudes Produced when a Doublet is Applied to Combined Lateral Cyclic in Helicopter Mode

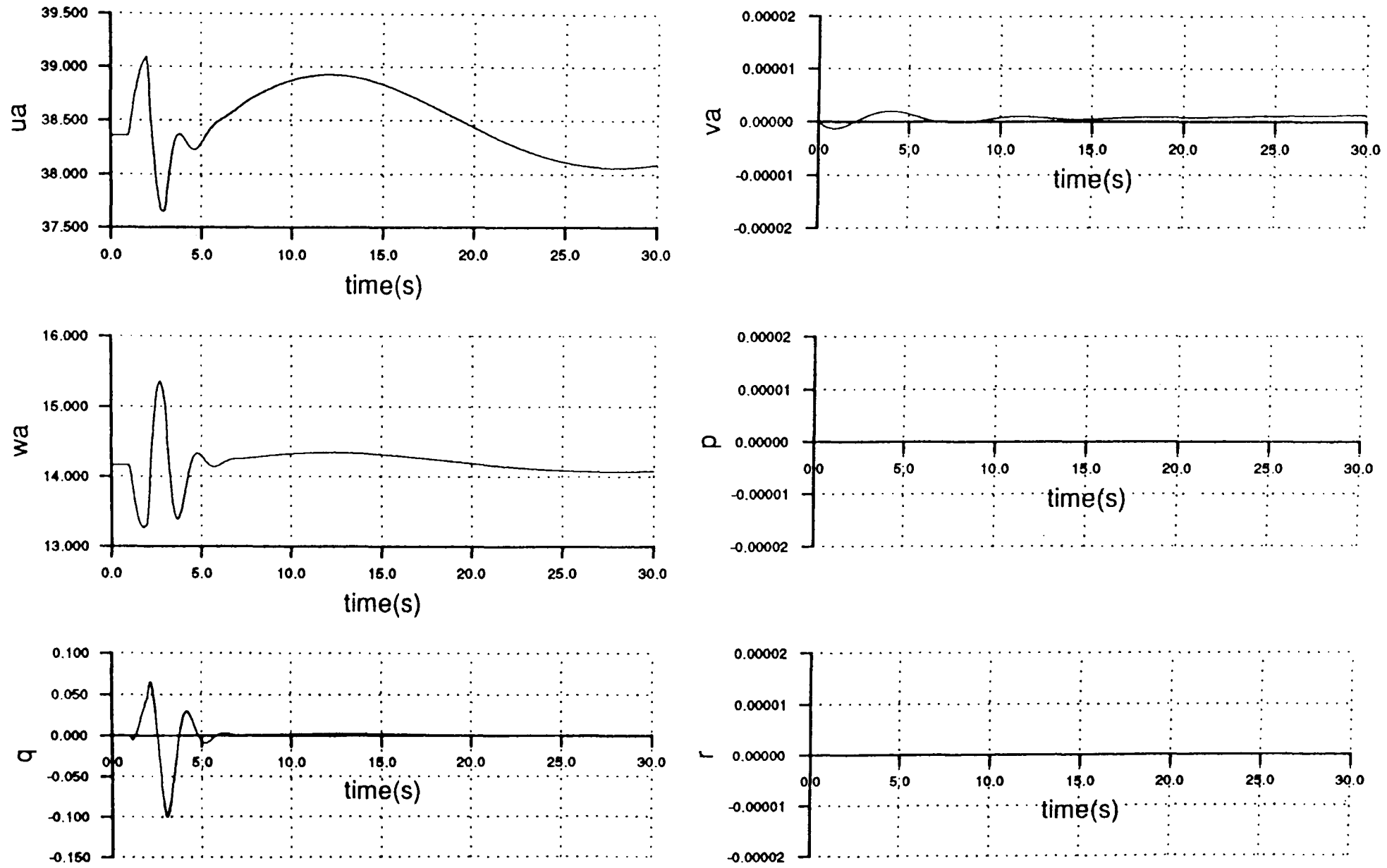


Figure 5.26 Body Axis Flight States Produced when a Doublet is Applied to Combined Collective when Flying with 45 Degrees Nacelle Angle

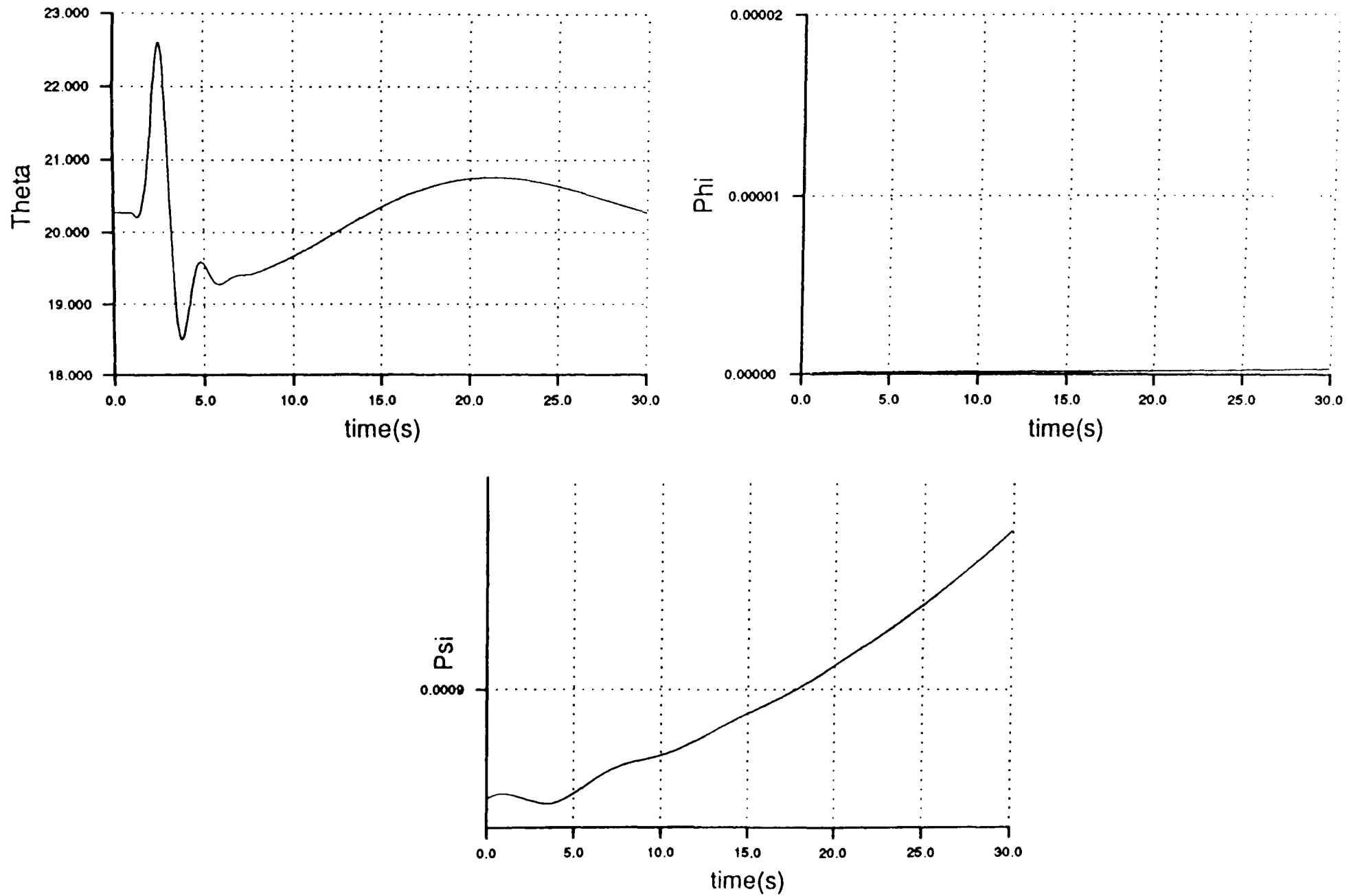


Figure 5.27 Vehicle Attitudes Produced when a Doublet is Applied to Combined Collective when Flying with 45 Degrees Nacelle Angle

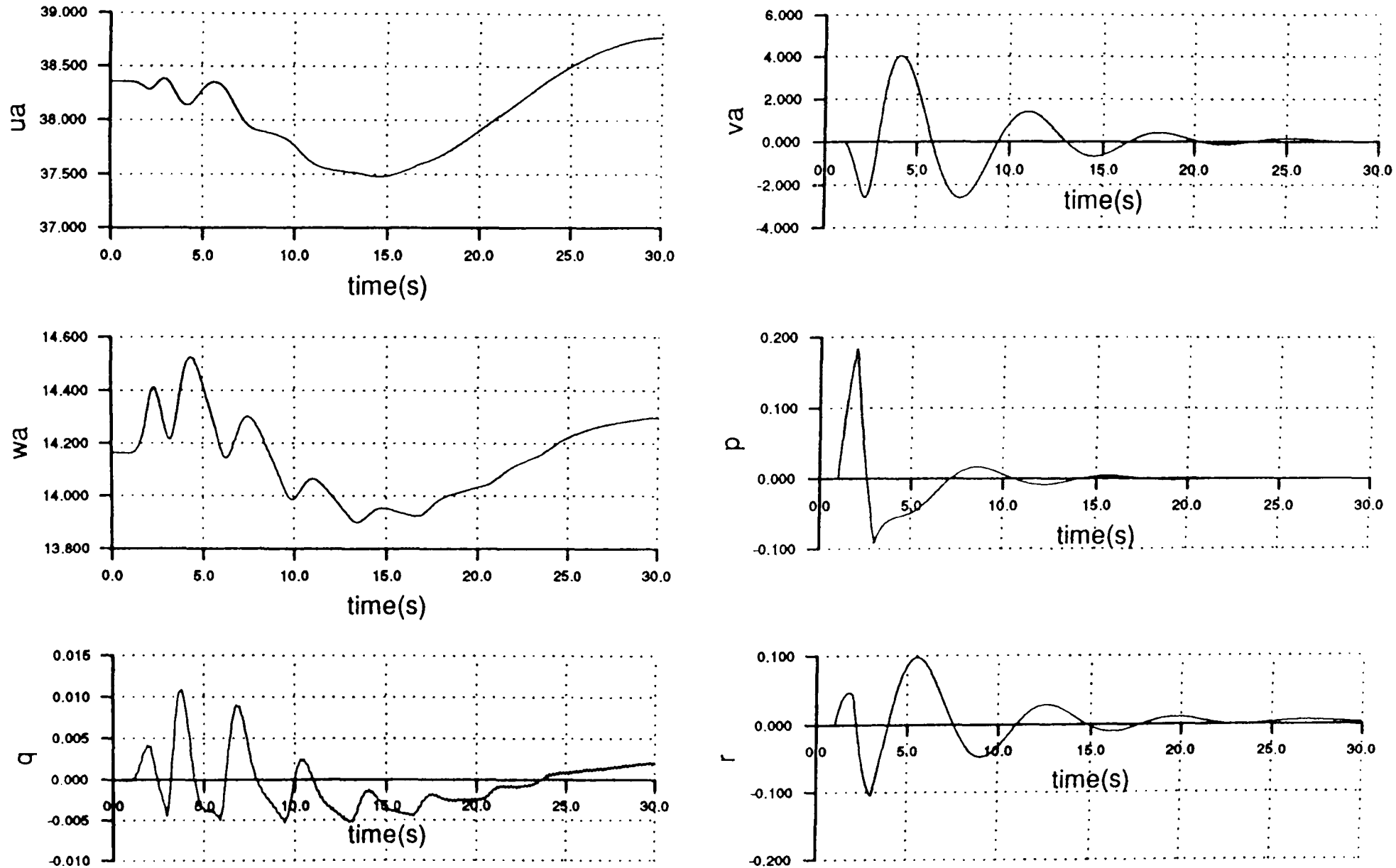


Figure 5.28 Body Axis Flight States Produced when a Doublet is Applied to Lateral Stick when Flying with 45 Degrees Nacelle Angle

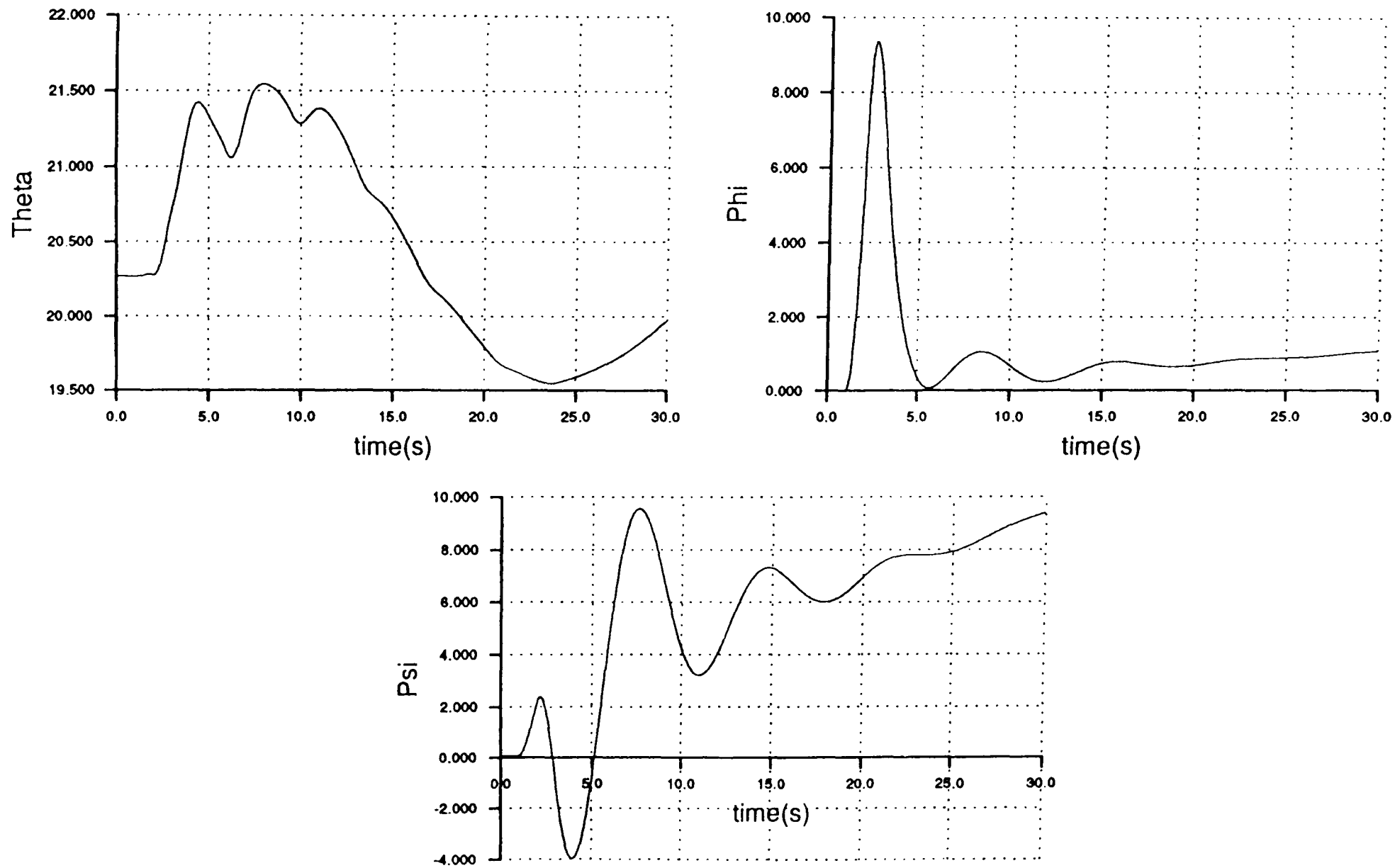


Figure 5.29 Vehicle Attitudes Produced when a Doublet is Applied to Lateral Stick when Flying with 45 Degrees Nacelle Angle

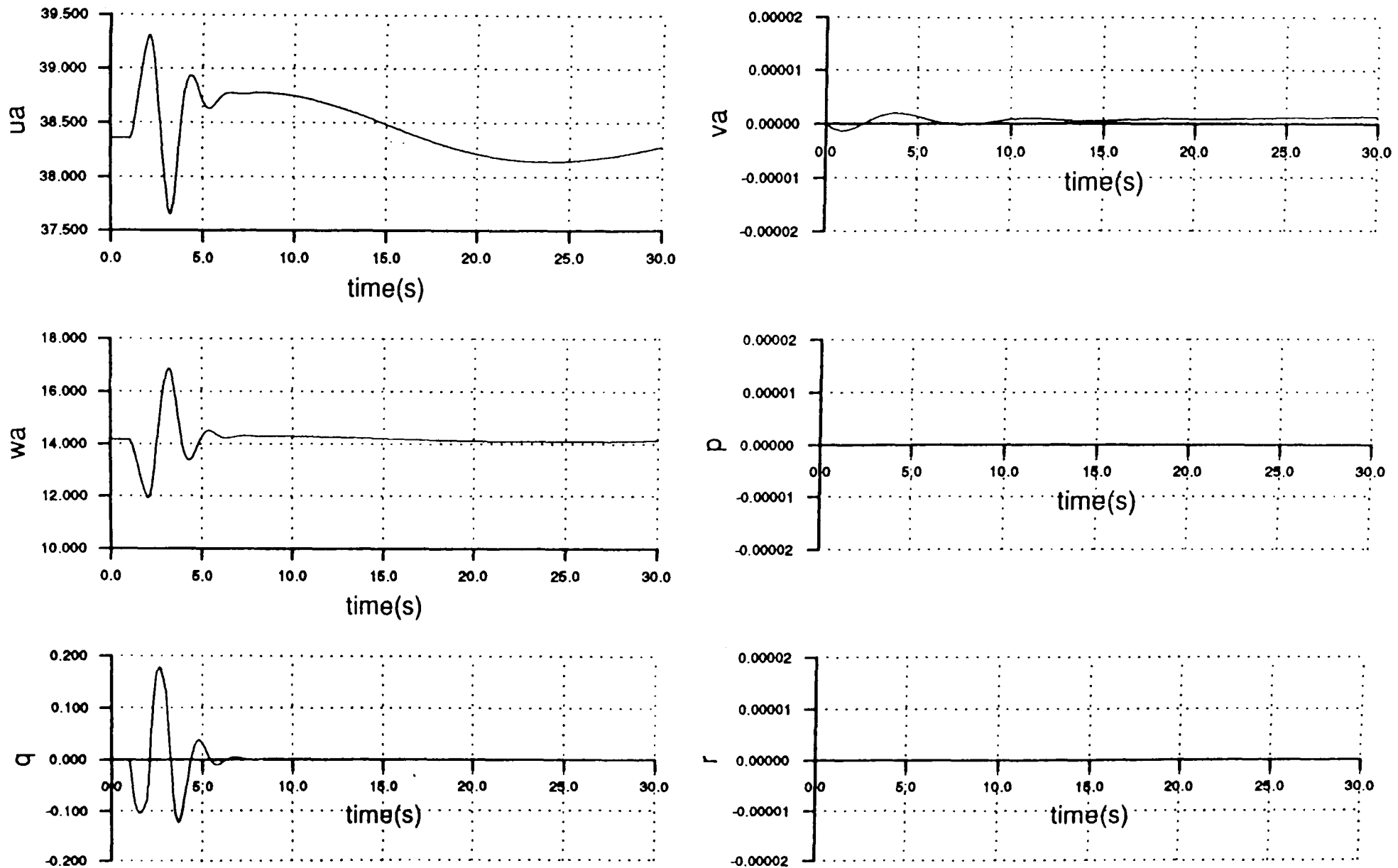


Figure 5.30 Body Axis Flight States Produced when a Doublet is Applied to Longitudinal Stick when Flying with 45 Degrees Nacelle Angle

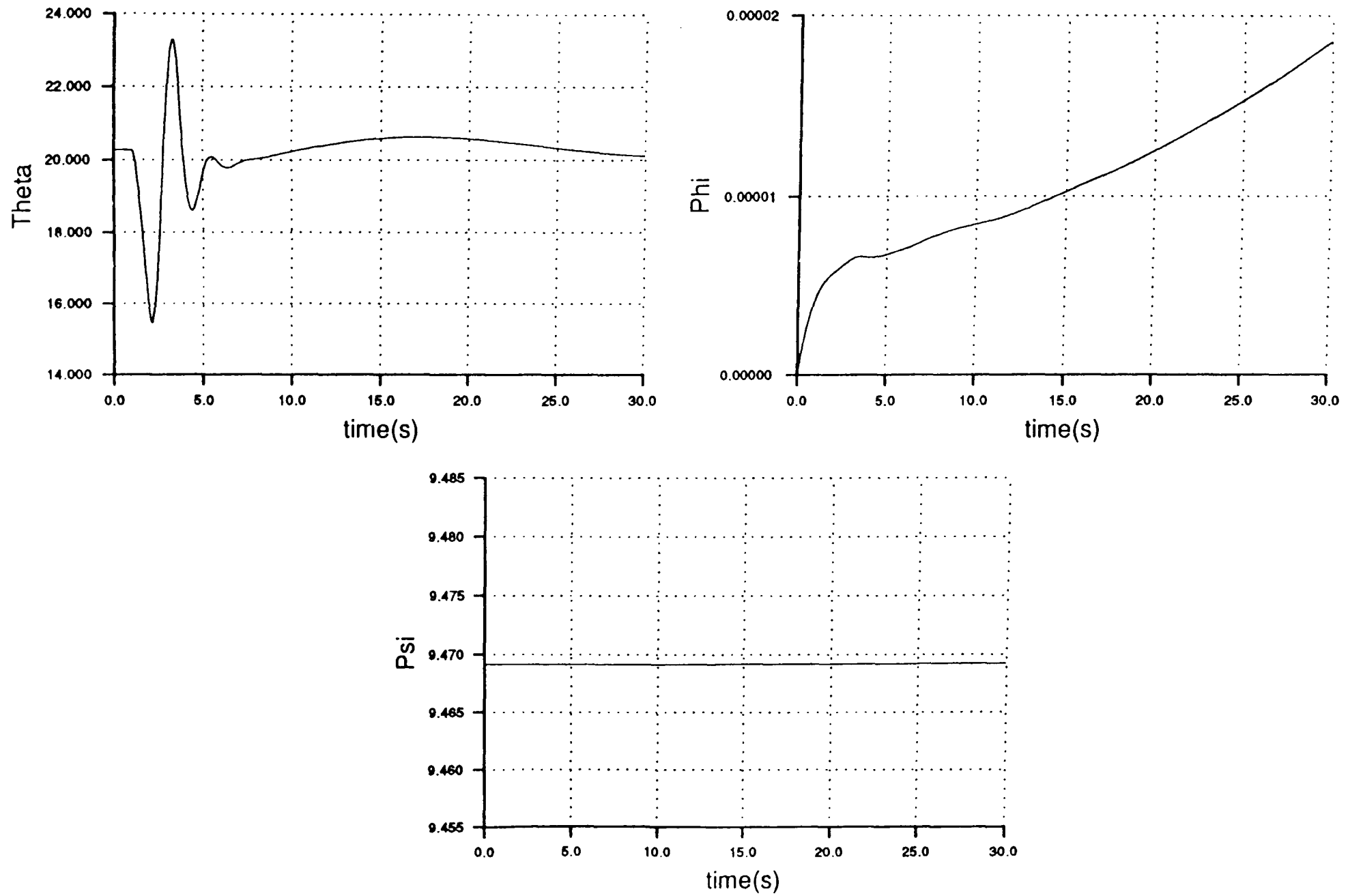


Figure 5.31 Vehicle Attitudes Produced when a Doublet is Applied to Longitudinal Stick when Flying with 45 Degrees Nacelle Angle

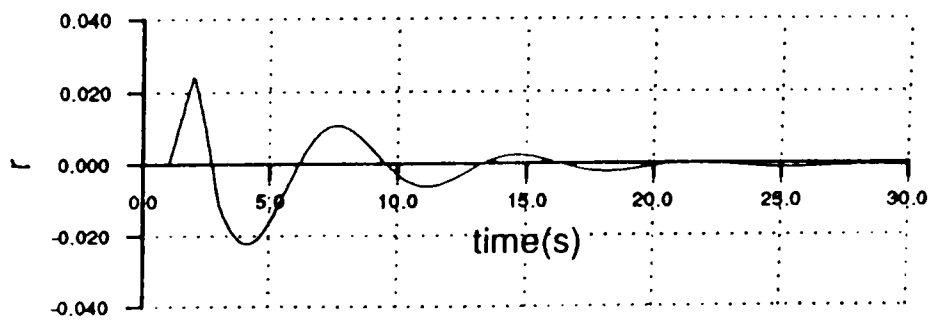
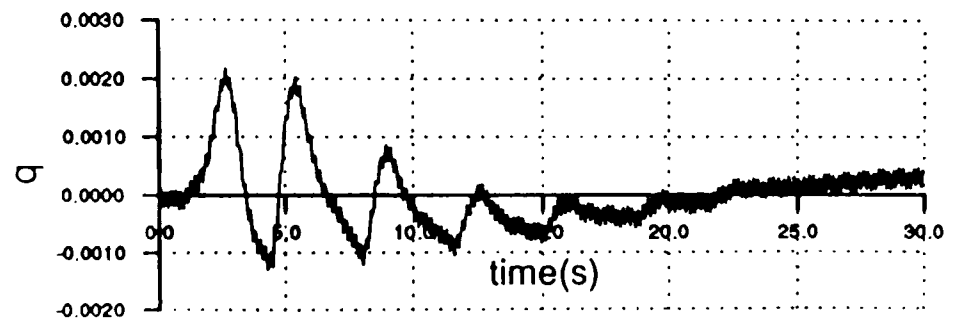
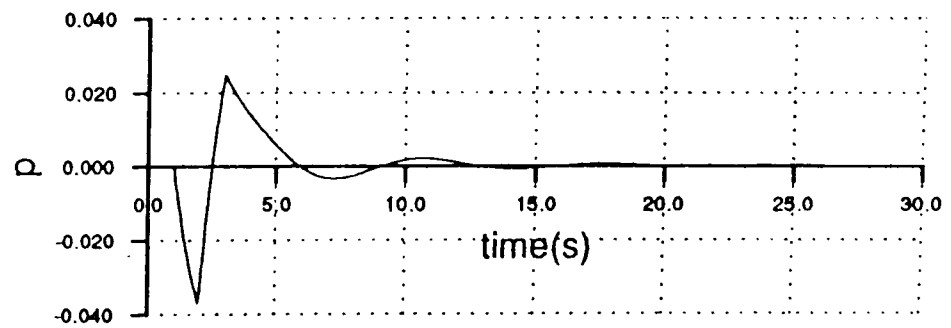
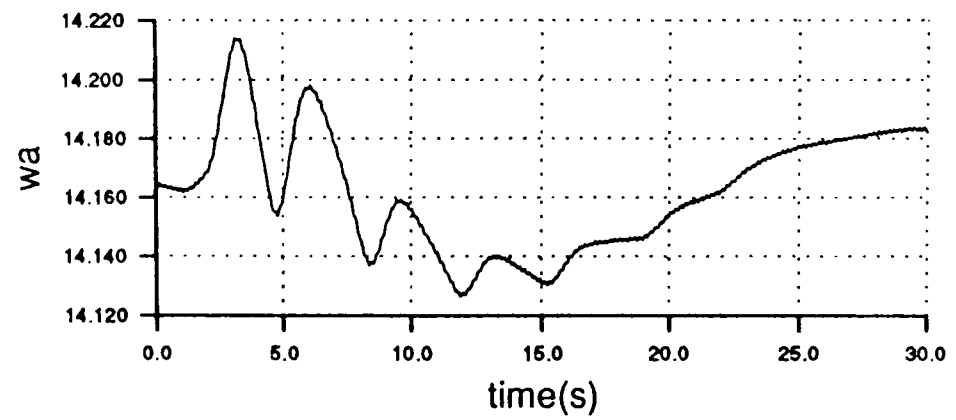
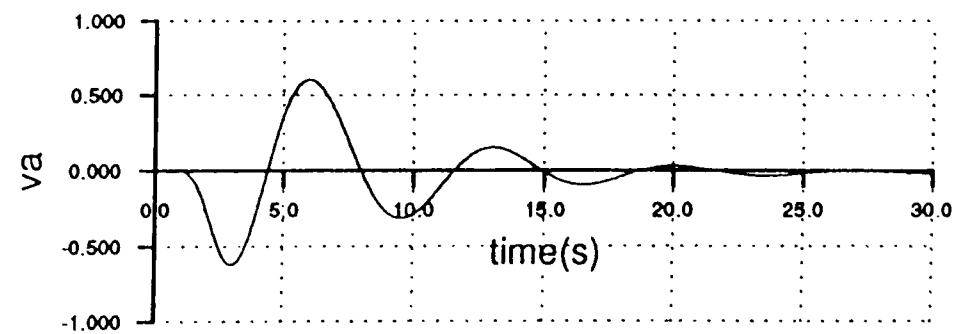
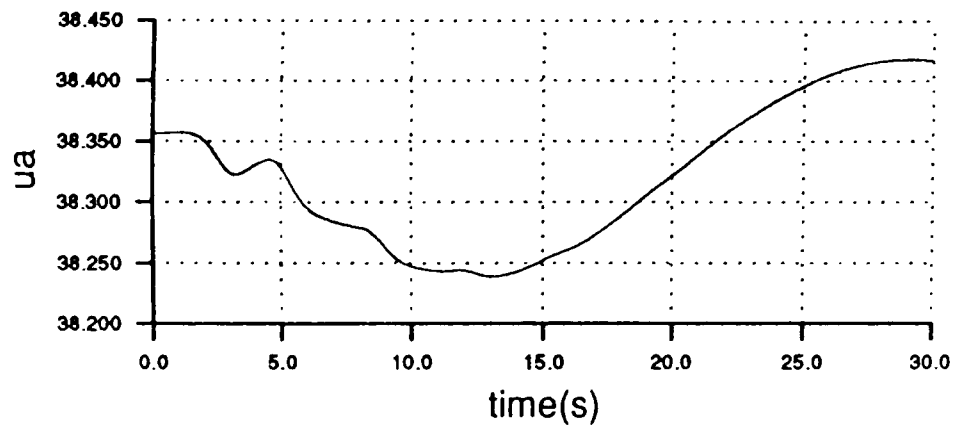


Figure 5.32 Body Axis Flight States Produced when a Doublet is Applied to Pedal when Flying with 45 Degrees Nacelle Angle

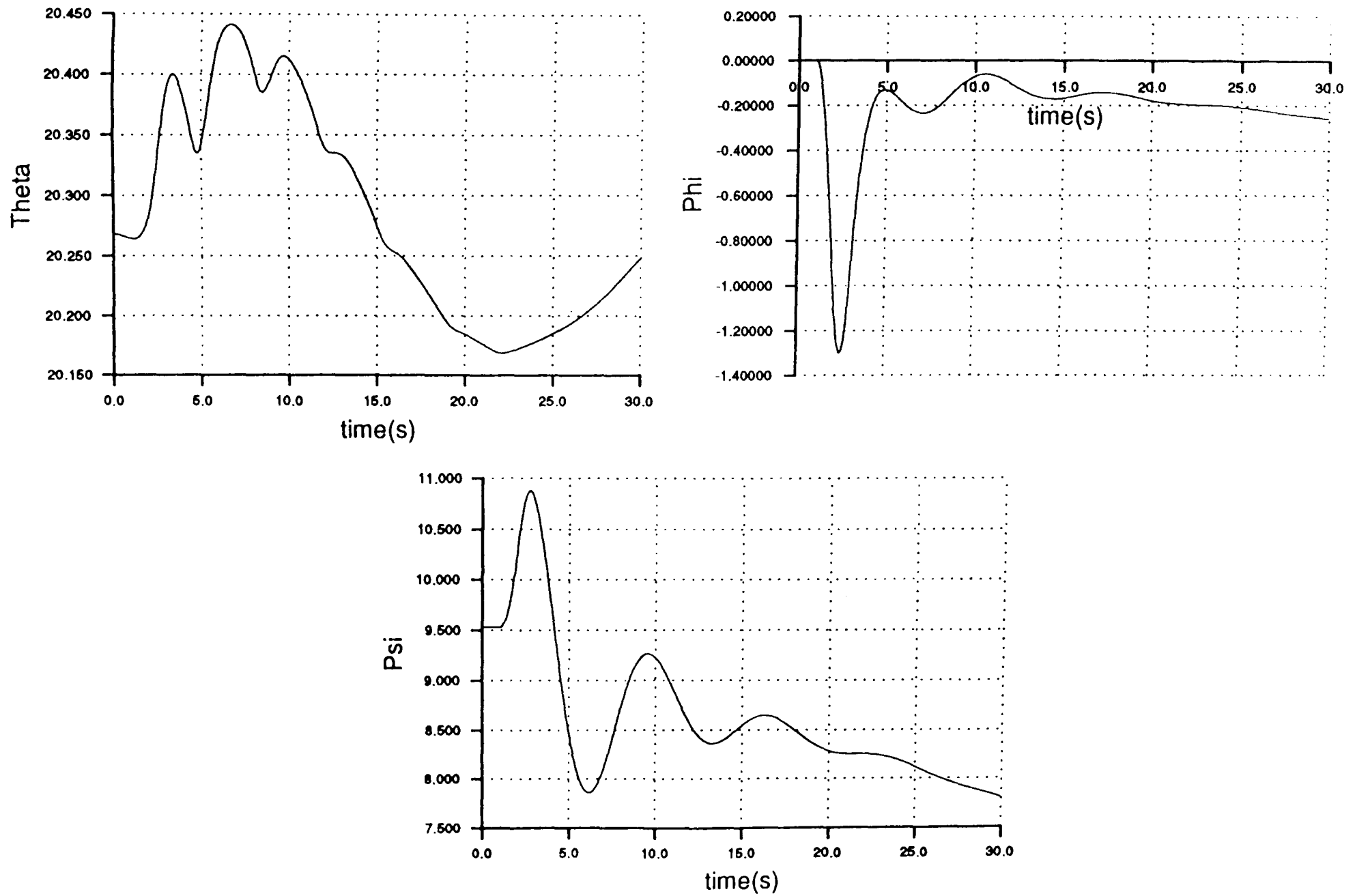


Figure 5.33 Vehicle Attitudes Produced when a Doublet is Applied to Pedal when Flying with 45 Degrees Nacelle Angle

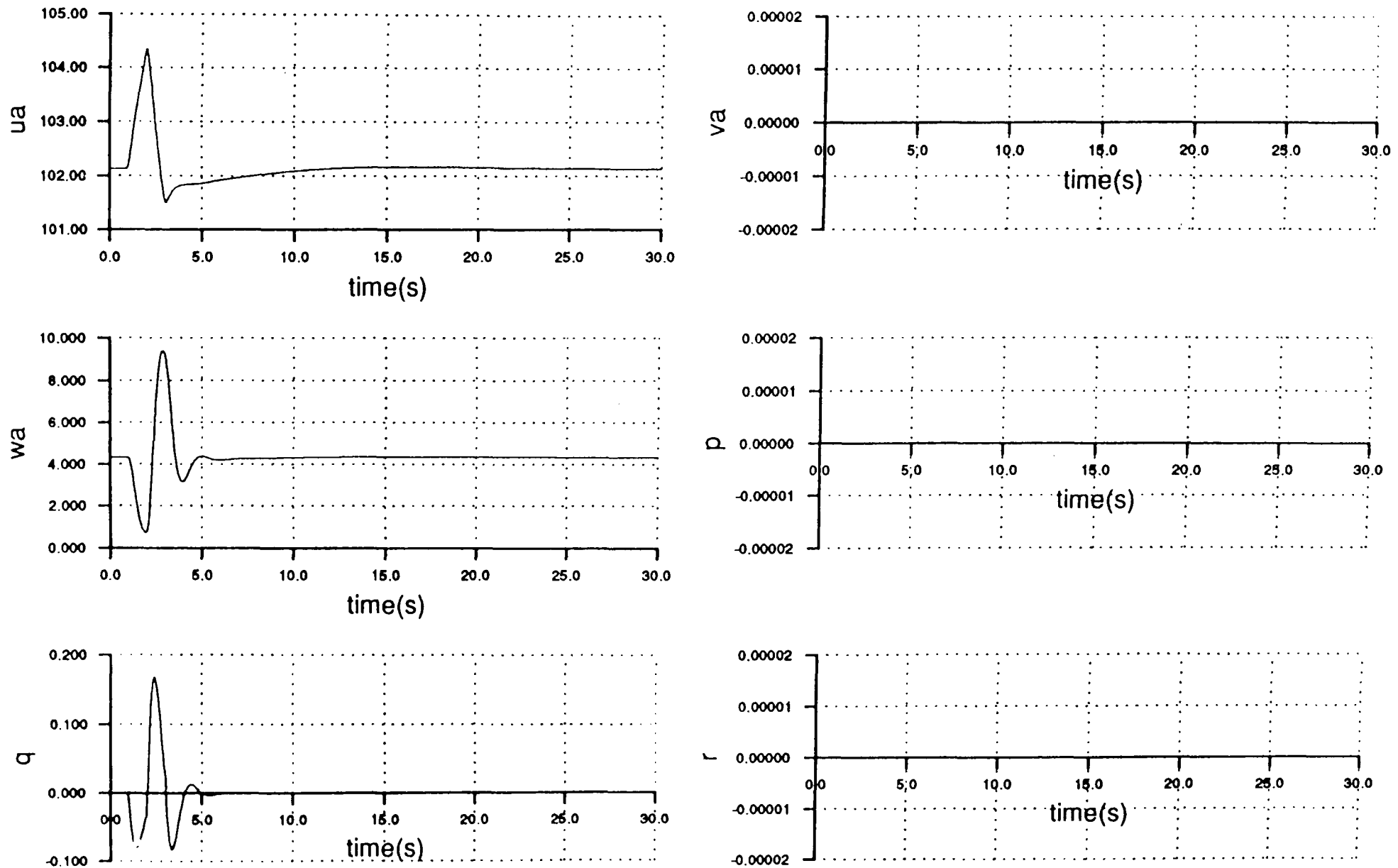


Figure 5.34 Body Axis Flight States Produced when a Doublet is Applied to Combined Collective in Aeroplane Mode

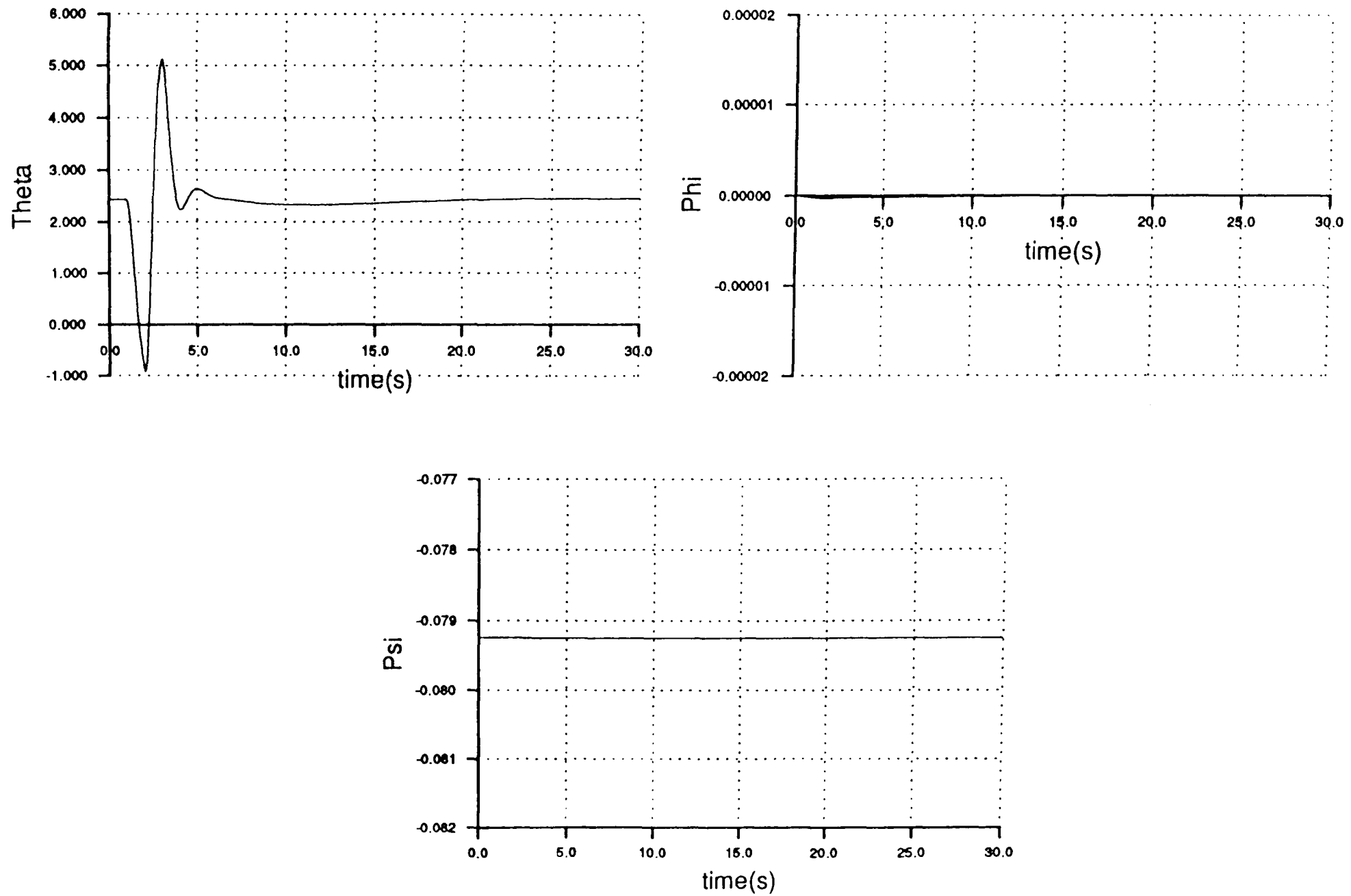


Figure 5.35 Vehicle Attitudes Produced when a Doublet is Applied to Combined Collective in Aeroplane Mode

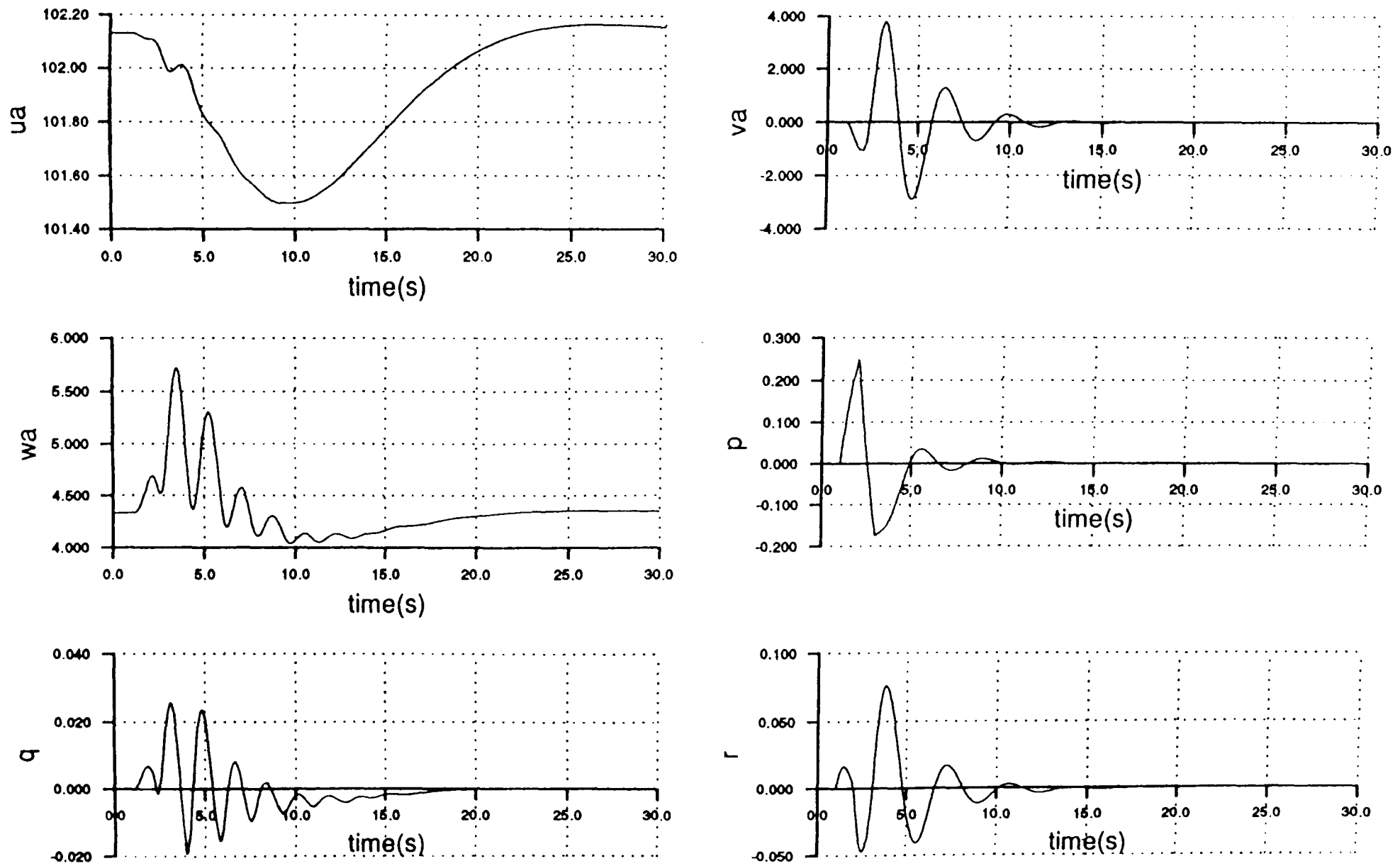


Figure 5.36 Body Axis Flight States Produced when a Doublet is Applied to Lateral Stick in Aeroplane Mode

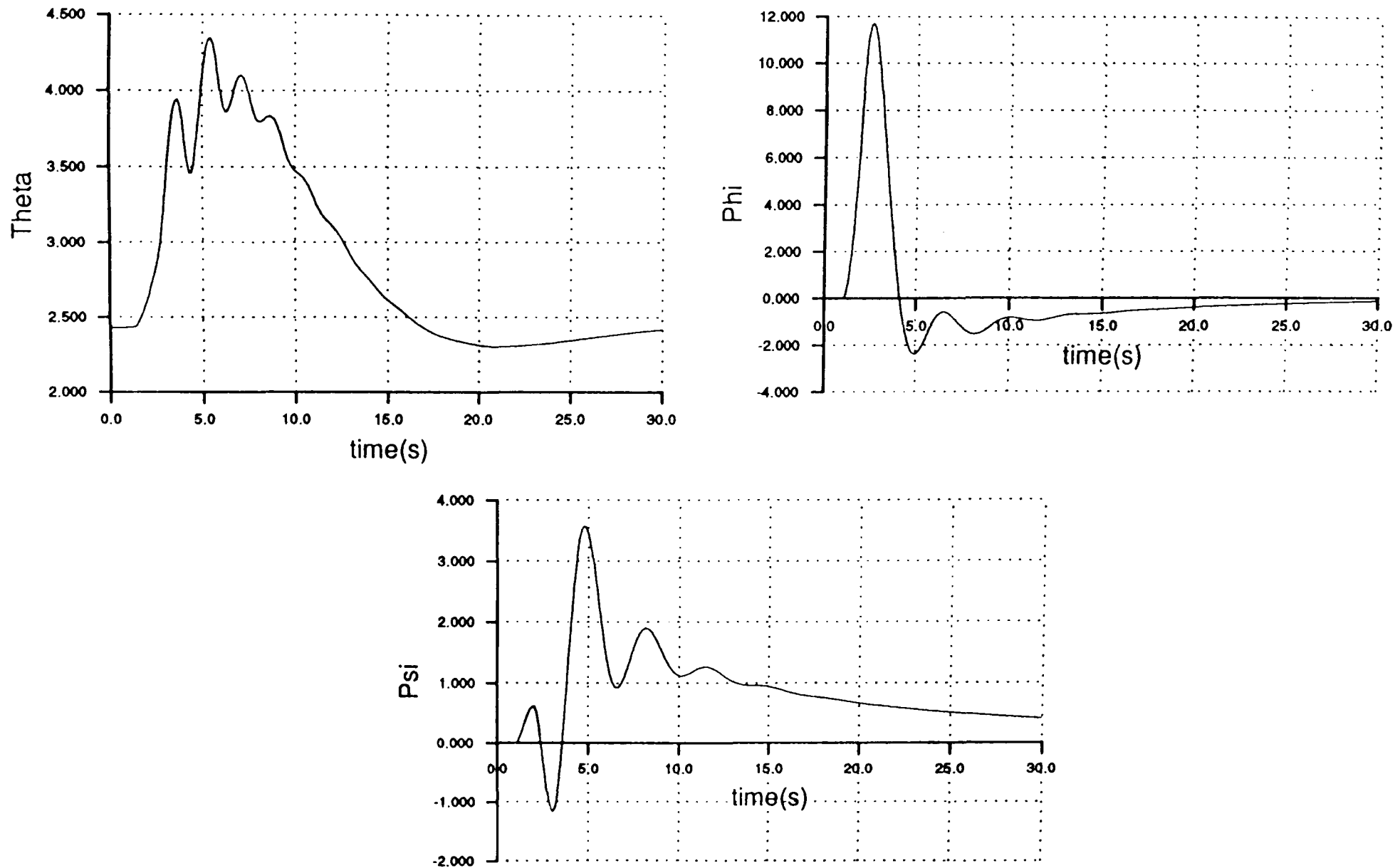


Figure 5.37 Vehicle Attitudes Produced when a Doublet is Applied to Lateral Stick in Aeroplane Mode

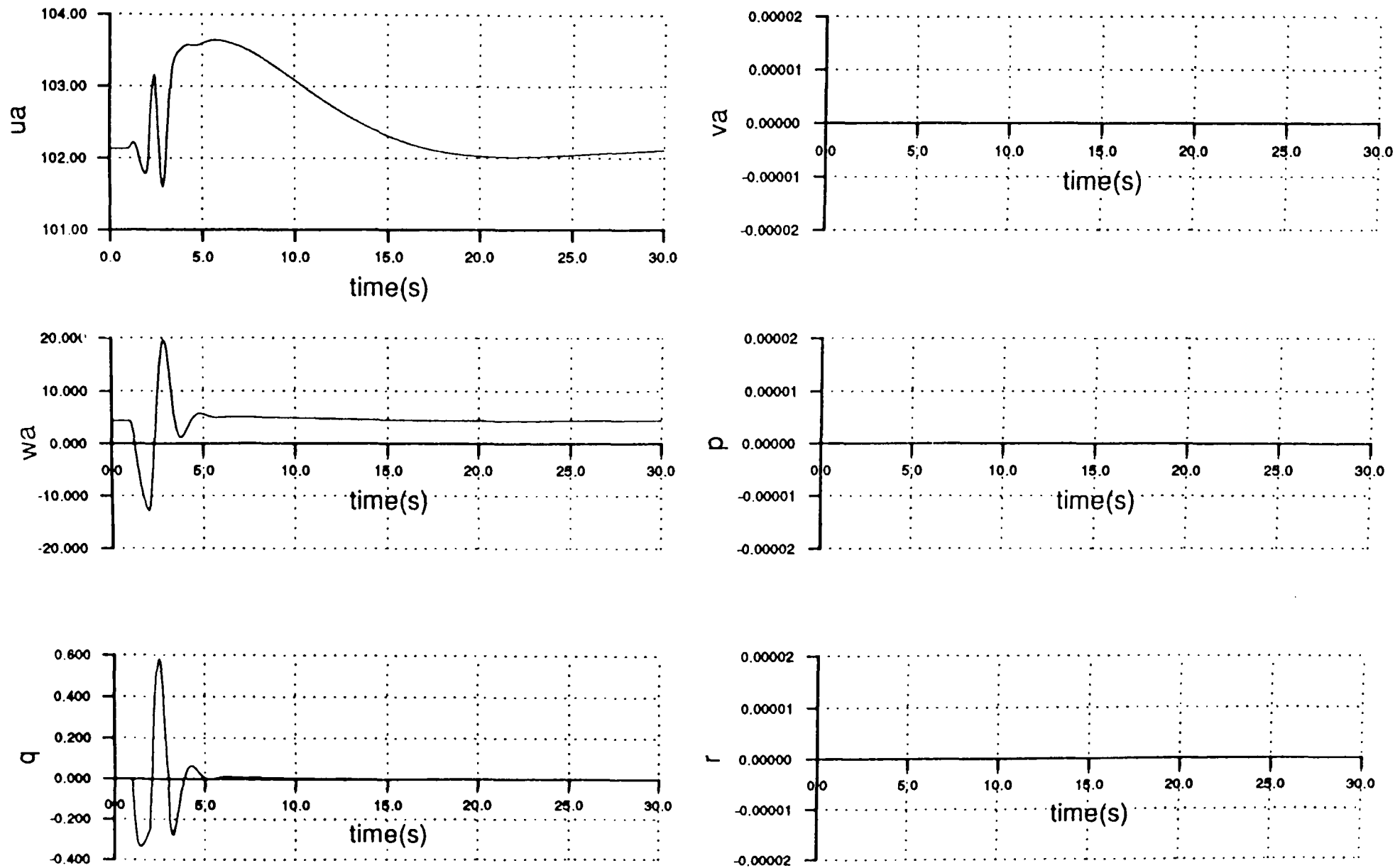


Figure 5.38 Body Axis Flight States Produced when a Doublet is Applied to Longitudinal Stick in Aeroplane Mode

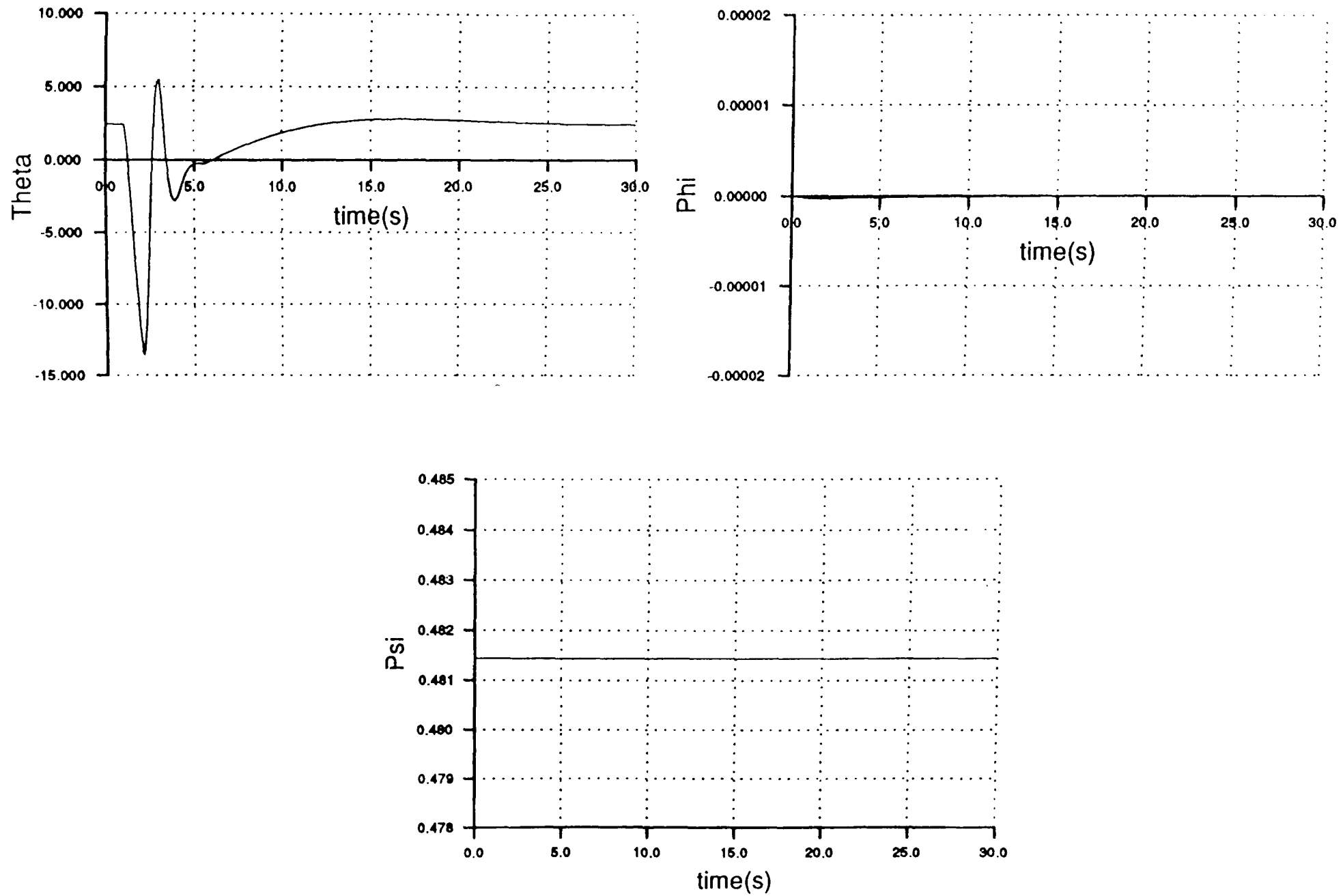


Figure 5.39 Vehicle Attitudes Produced when a Doublet is Applied to Longitudinal Stick in Aeroplane Mode

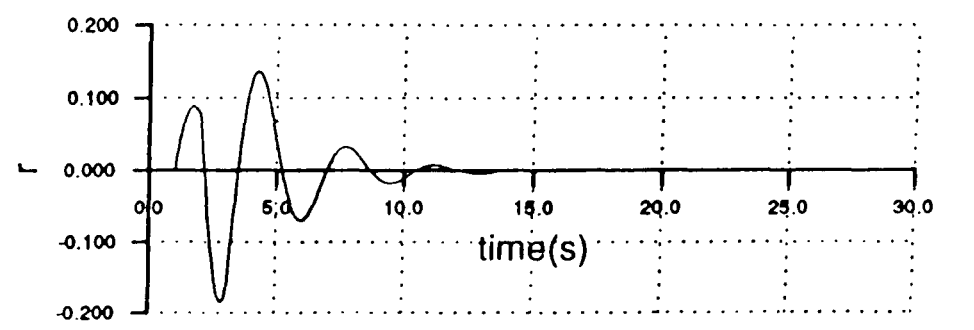
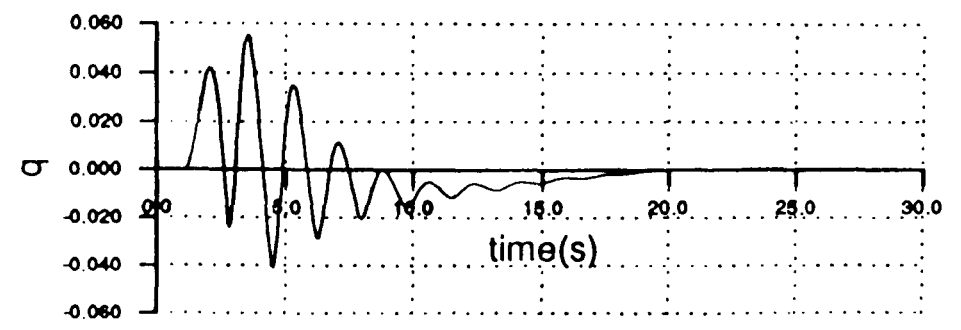
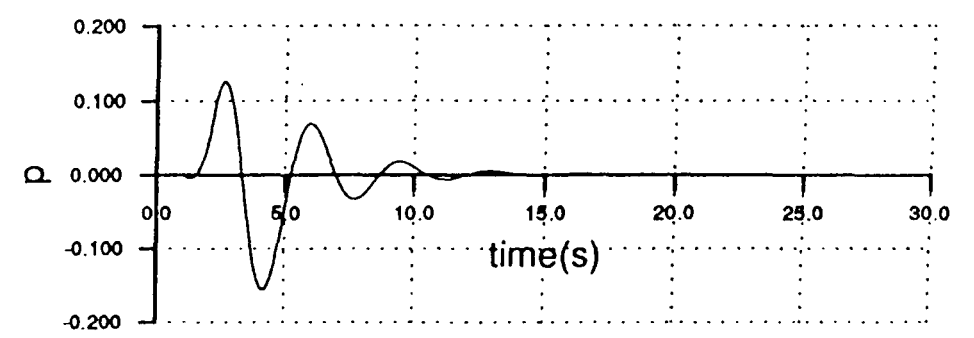
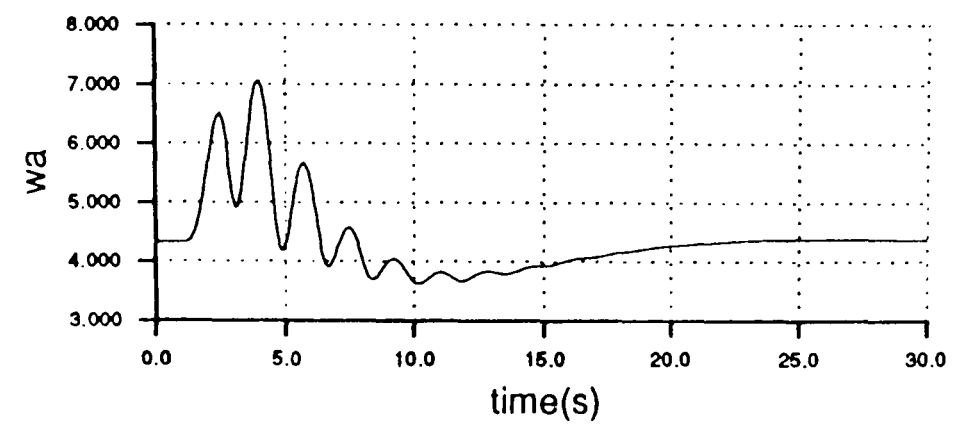
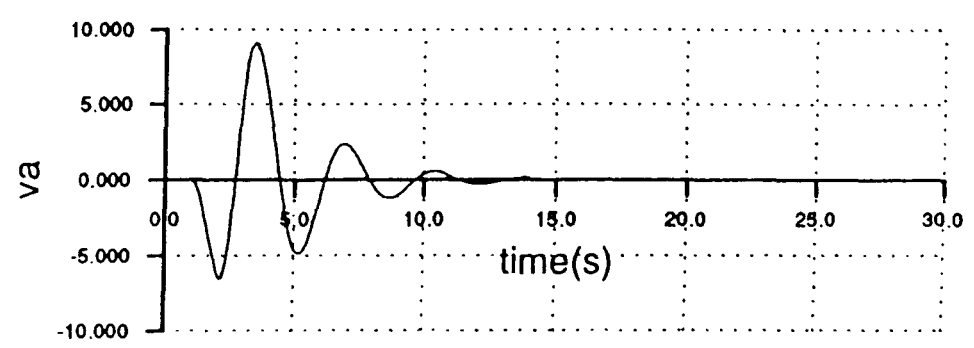
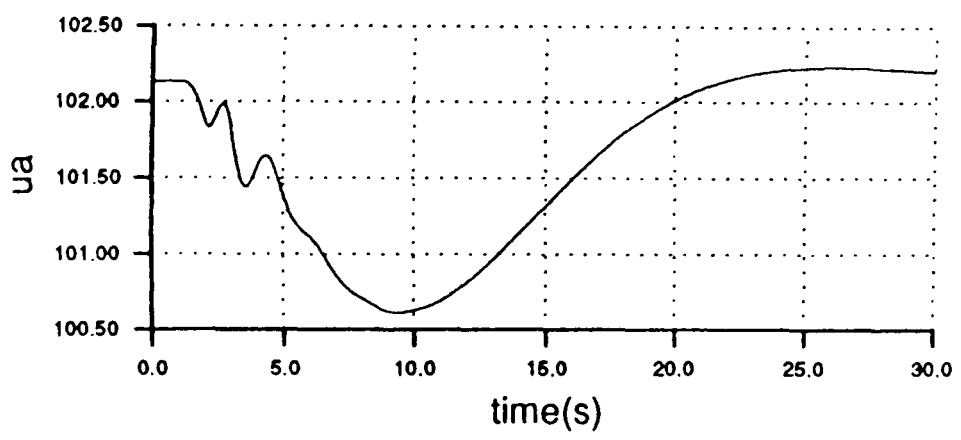


Figure 5.40 Body Axis Flight States Produced when a Doublet is Applied to Pedal in Aeroplane Mode

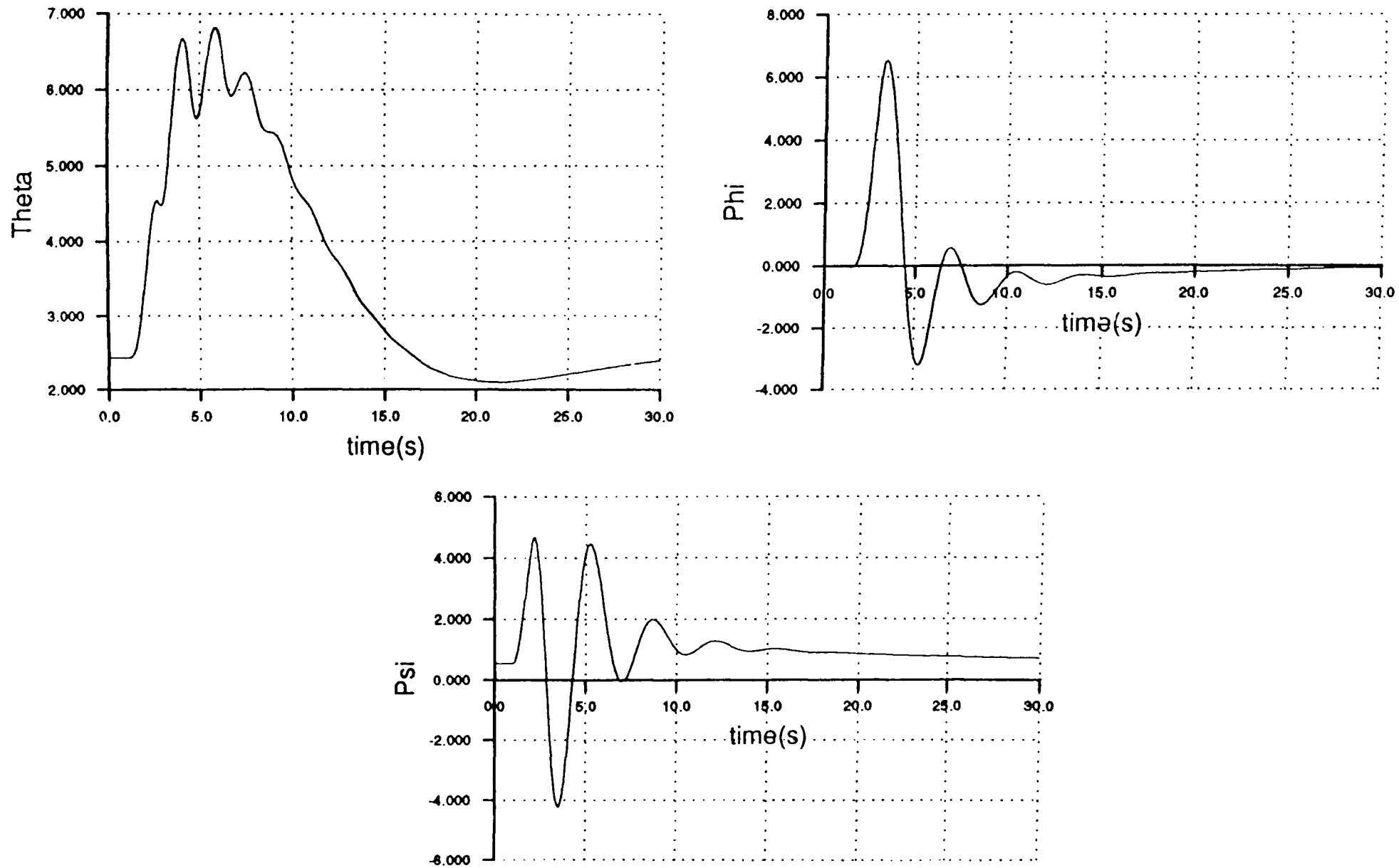


Figure 5.41 Vehicle Attitudes Produced when a Doublet is Applied to Pedal in Aeroplane Mode

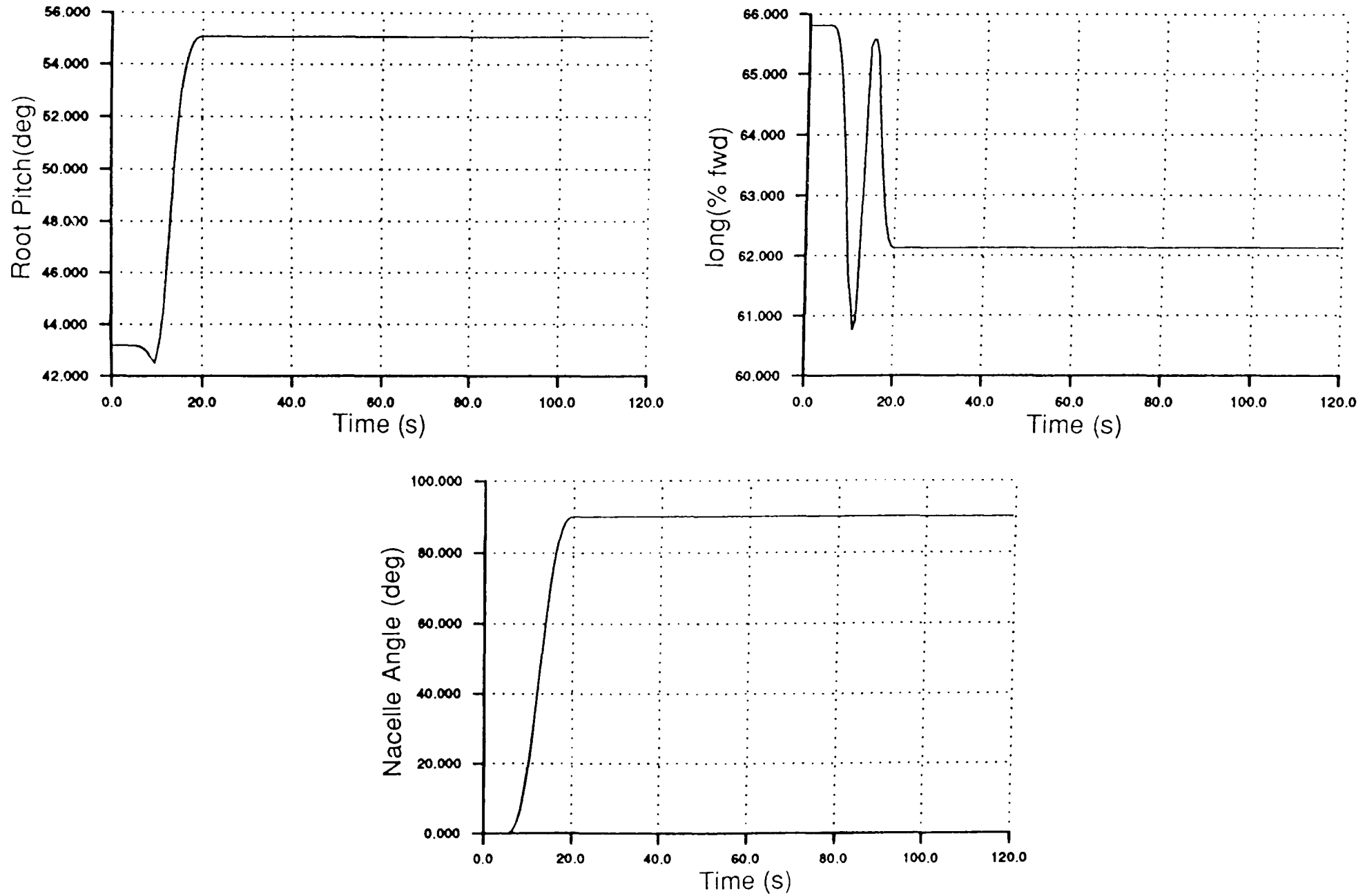


Figure 5.42 Predicted Trim Map of Control Displacements Necessary to Produce a 15 Second Level Flight Transition from Helicopter Mode to Aeroplane Mode

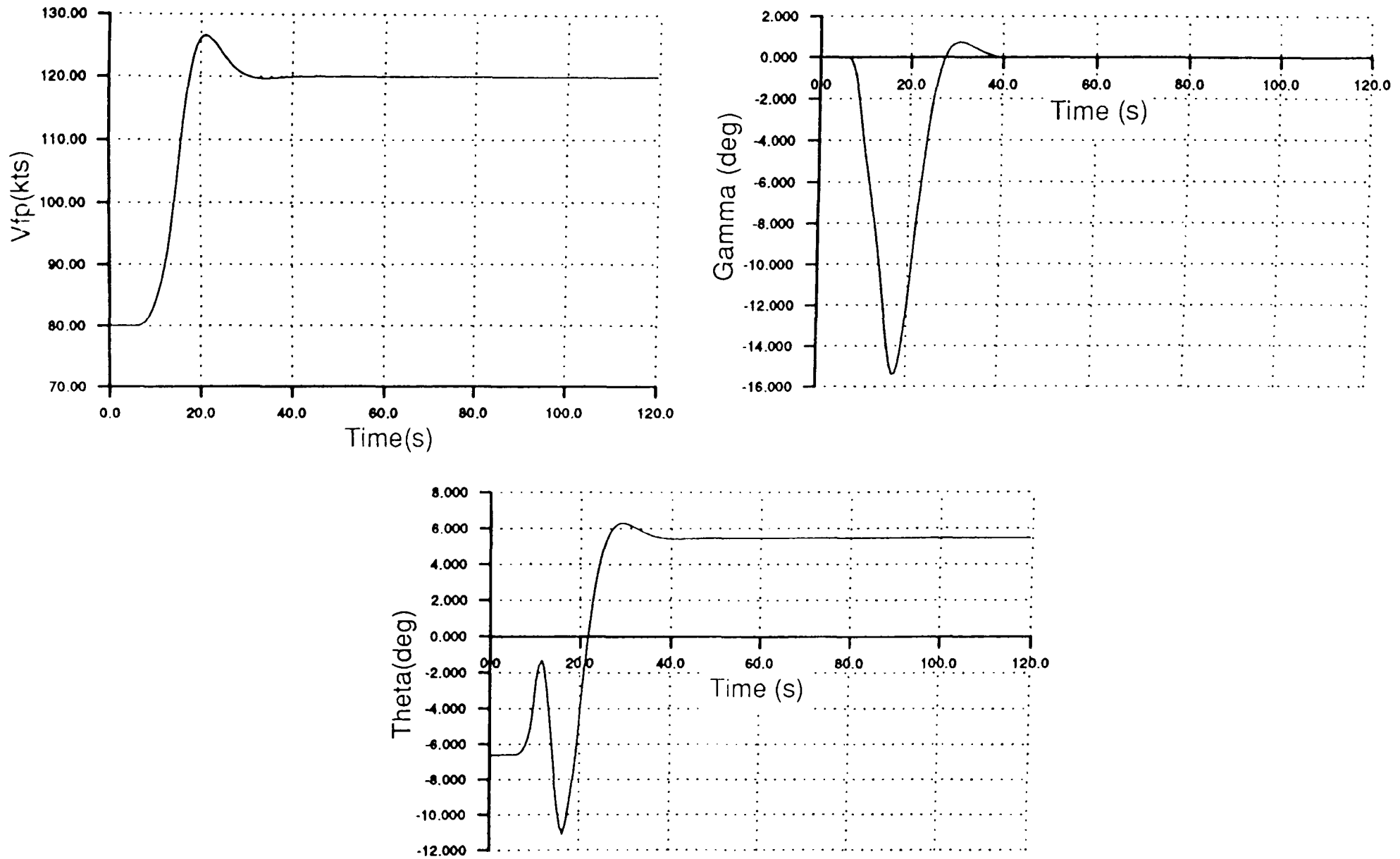


Figure 5.43 Flight Path Produced when Performing a 15 second Transition from Helicopter to Aeroplane Mode Using Control Displacements as Described by a Trim Map

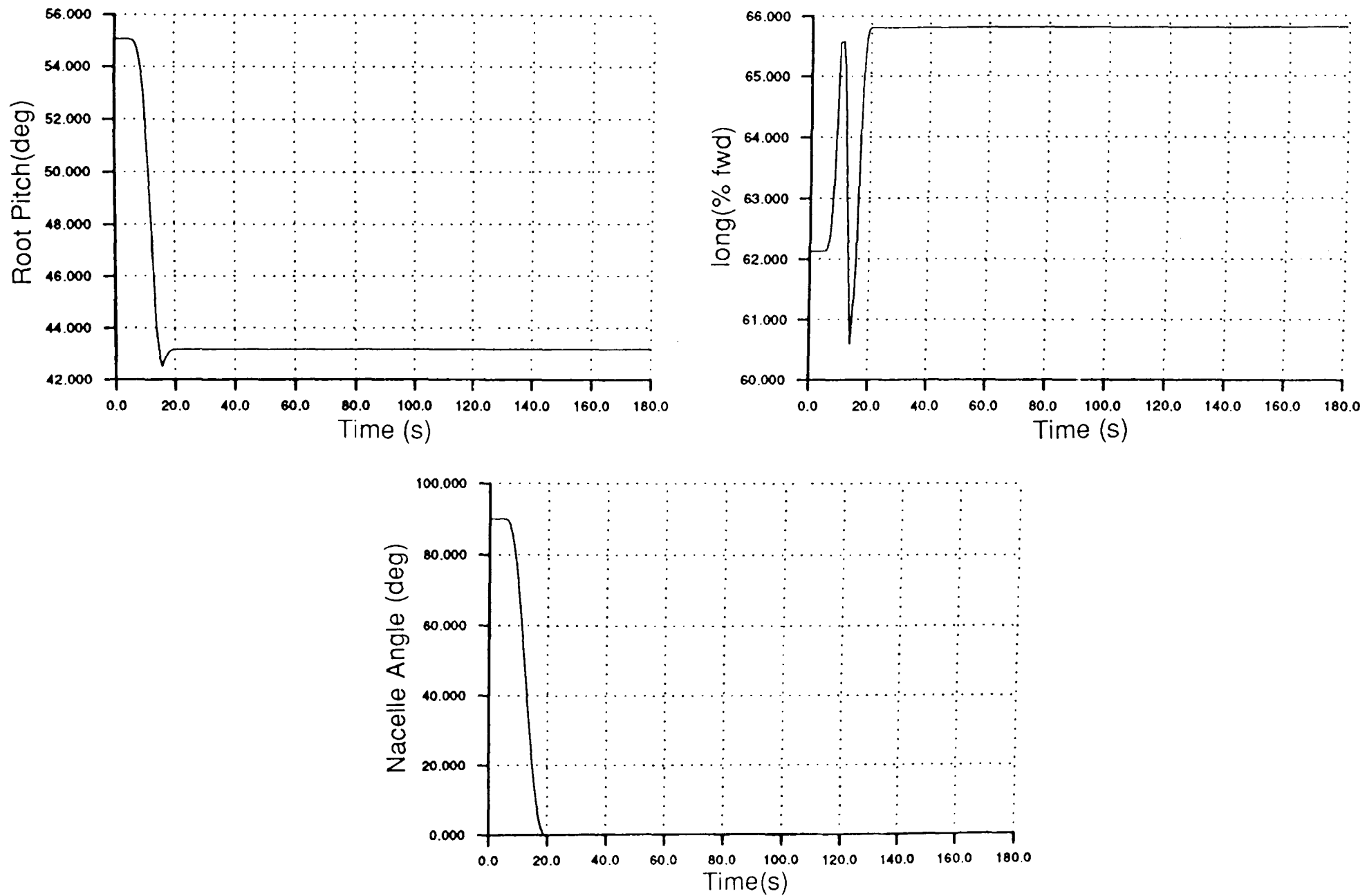


Figure 5.44 Predicted Trim Map of Control Displacements Necessary to Produce a 15 Second Level Flight Transition from Aeroplane Mode to Helicopter Mode

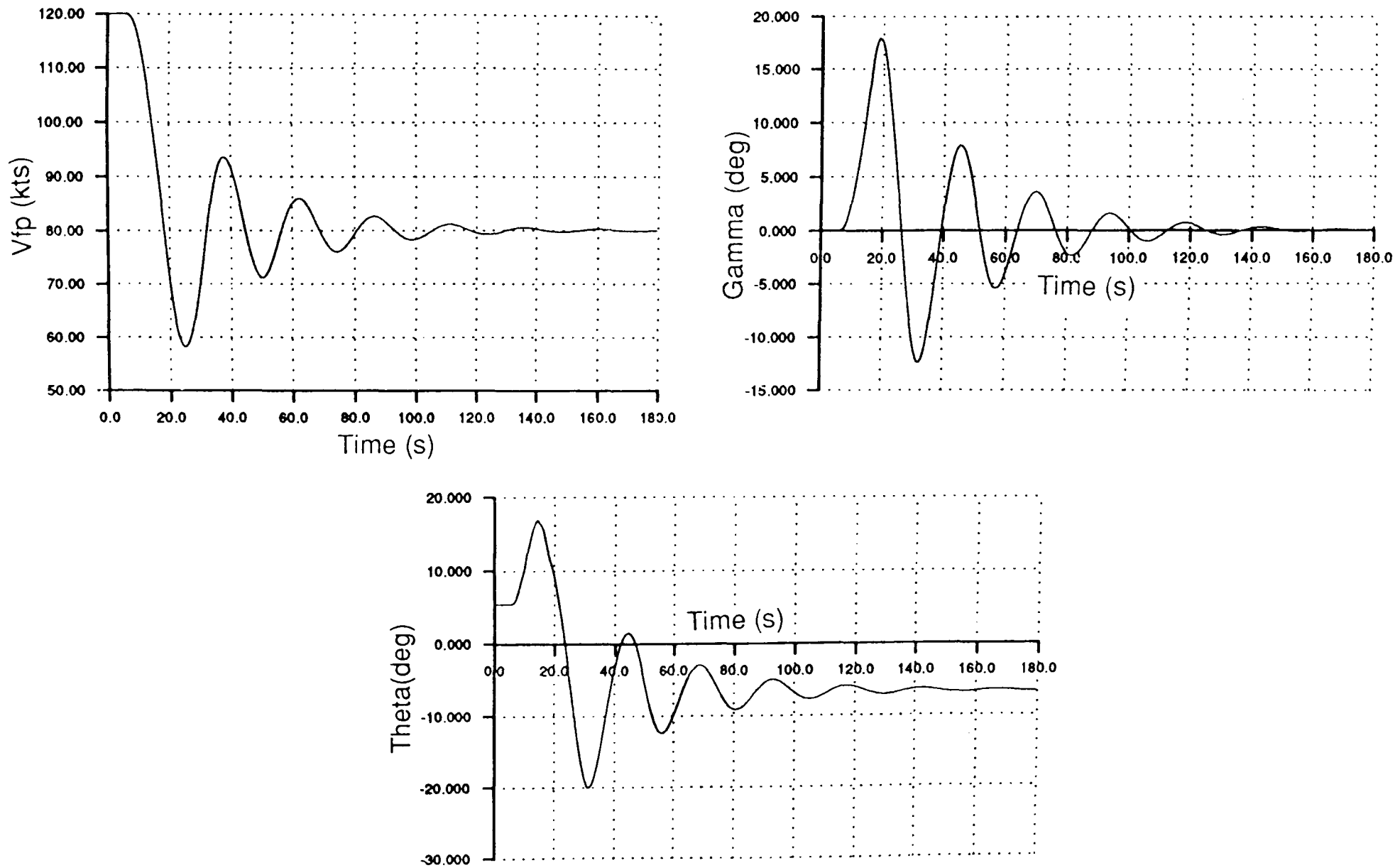


Figure 5.45 Flight Path Produced when Performing a 15 second Transition from Aeroplane to Helicopter Mode Using Control Displacements as Described by a Trim Map

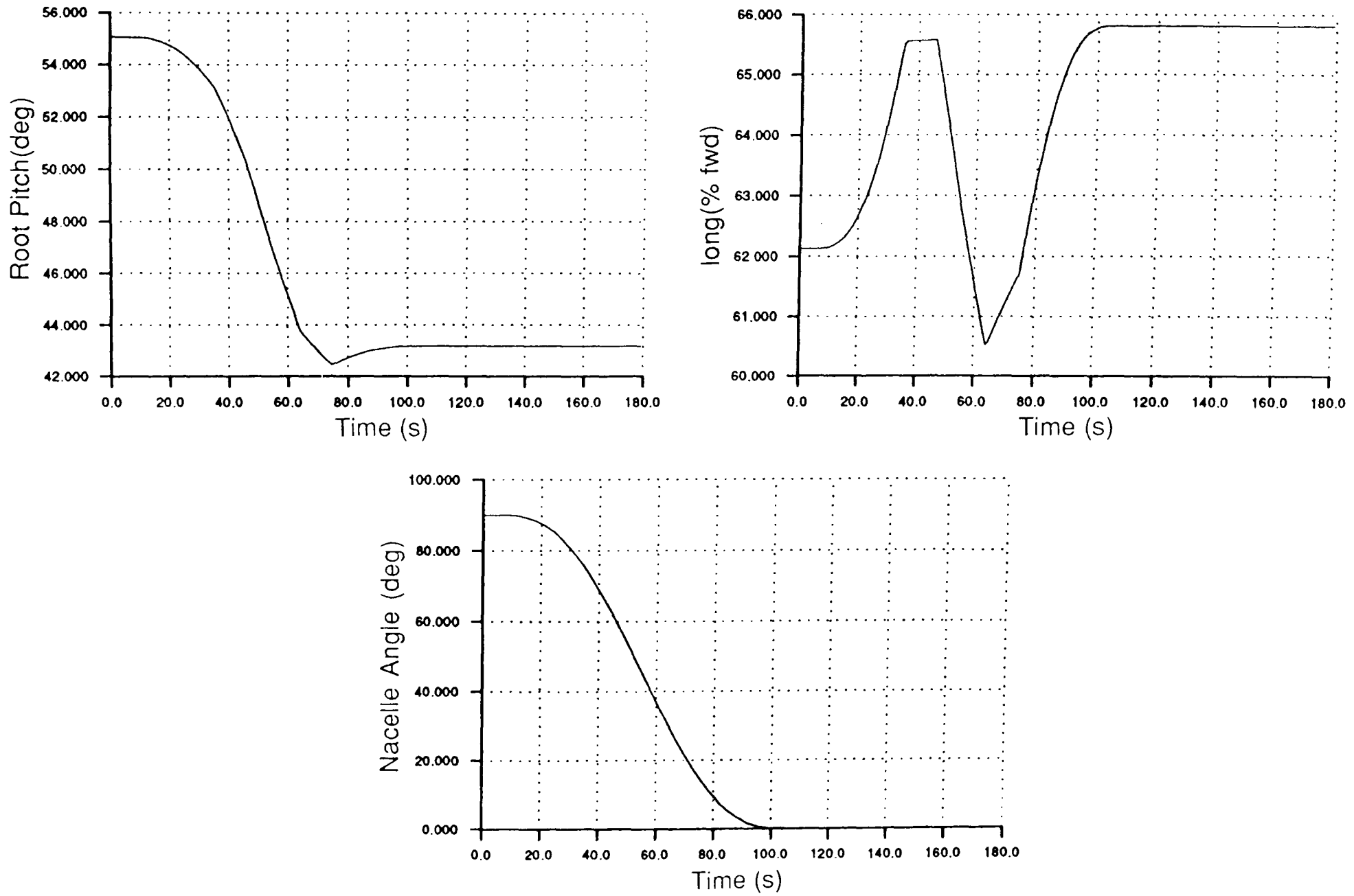


Figure 5.46 Predicted Trim Map of Control Displacements Necessary to Produce a 100 Second Level Flight Transition from Aeroplane Mode to Helicopter Mode

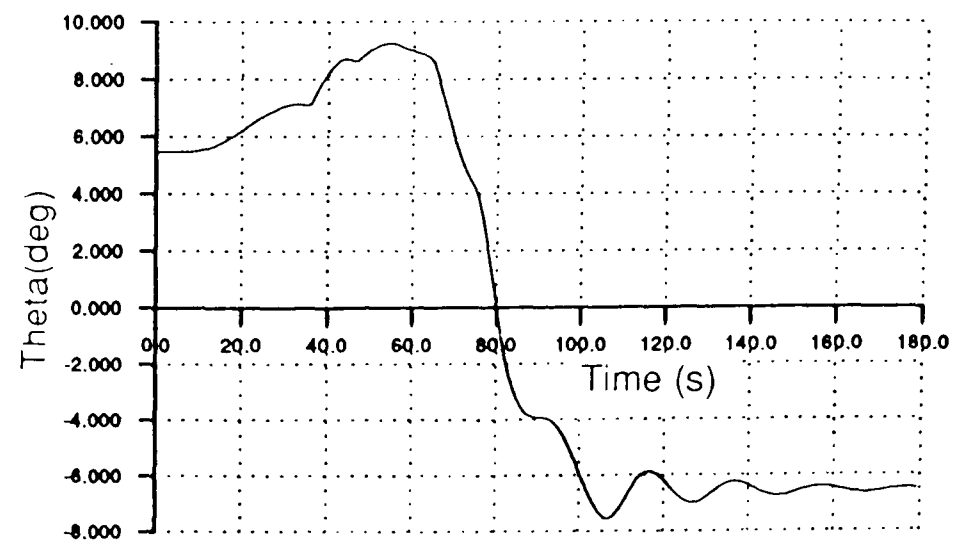
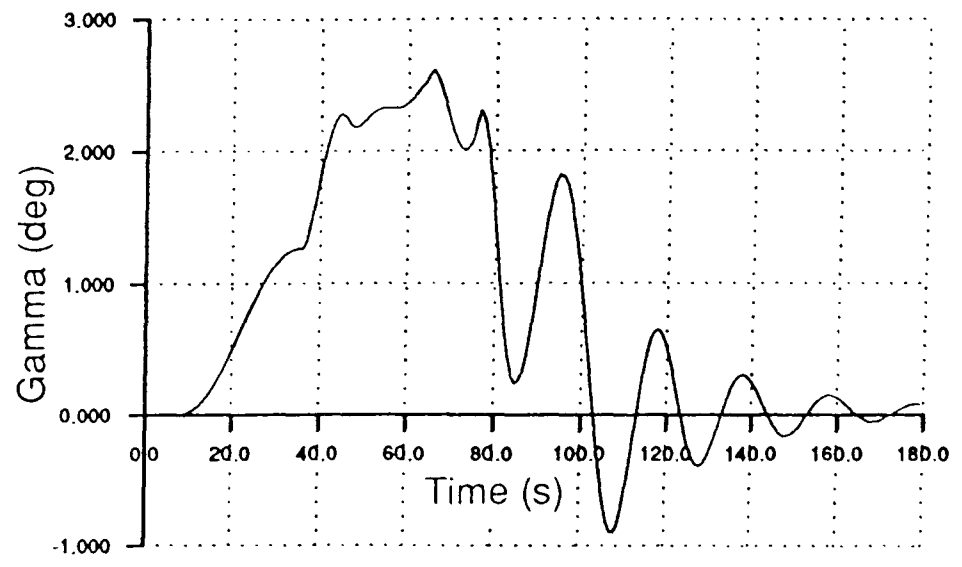
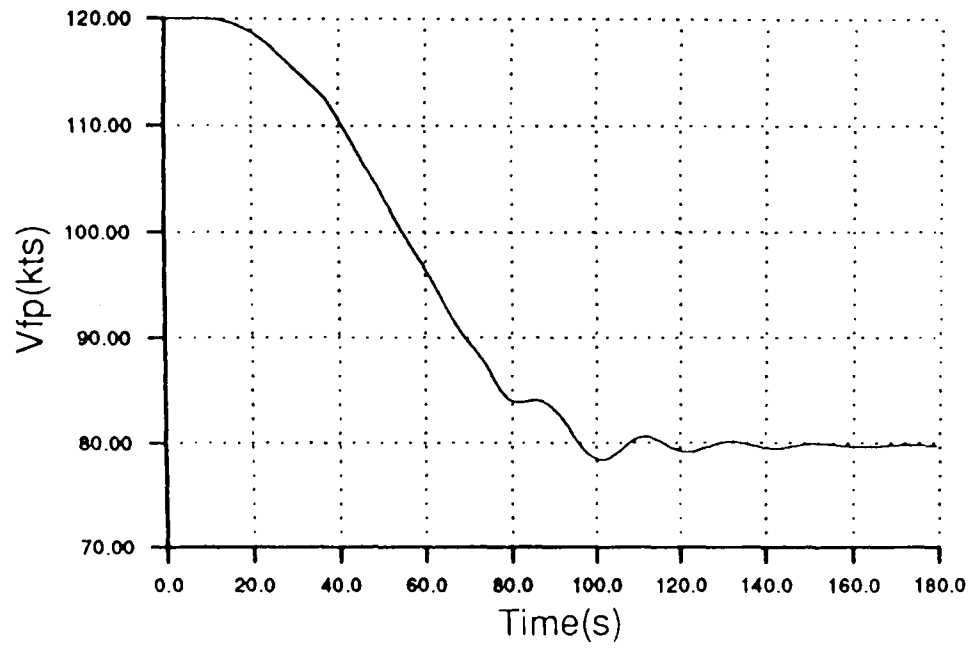


Figure 5.47 Flight Path Produced when Performing a 100 second Transition from Aeroplane to Helicopter Mode Using Control Displacements as Described by a Trim Map

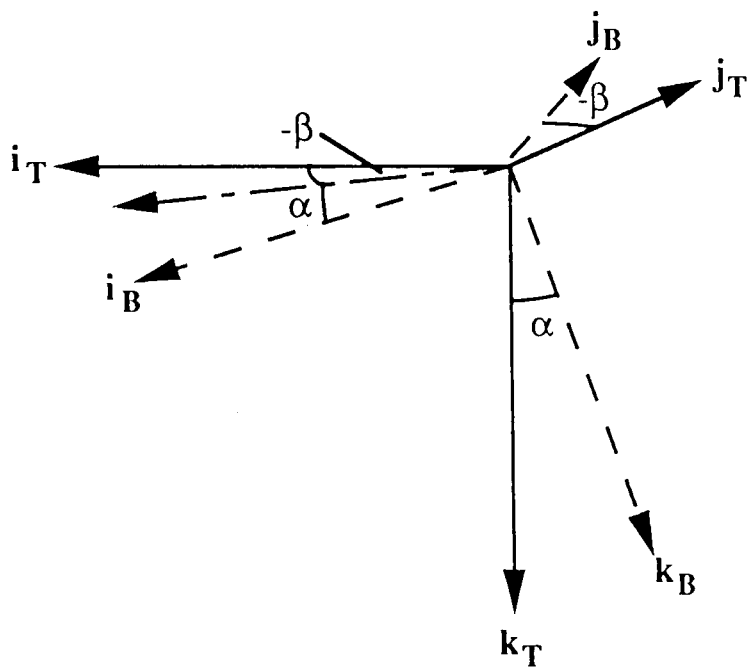


Figure A3.1 Axis Transformation from Local Trajectory Axis to Body Axis